

The effect of iron on the stability, water content and compressibility of mantle silicates - Implications for a hydrous Martian interior

Von der Fakultät für Biologie, Chemie und Geowissenschaften
der Universität Bayreuth

zur Erlangung der Würde eines
Doktors der Naturwissenschaften
- Dr. rer. nat. -

genehmigte
Dissertation

vorgelegt von
Diplom-Geologin Geertje Ganskow
aus Jena

Bayreuth, 2010

Diese Dissertation wurde am Bayerischen Geoinstitut, Universität Bayreuth im Zeitraum von Oktober 2006 bis März 2010 unter der Betreuung von Prof. Dr. Falko Langenhorst angefertigt.

Vollständiger Abdruck der von der Fakultät für Chemie, Biologie und Geowissenschaften der Universität Bayreuth genehmigten Dissertation zur Erlangung des Grades eines Doktors der Naturwissenschaften (Dr. rer. nat.).

Date of submission: 17. März 2010

Date of defence (disputation): 18. Mai 2010

Prüfungsausschuss:

Prof. Dr. Ludwig Zöllner (Vorsitzender)

Prof. Dr. Falko Langenhorst (1. Gutachter)

Prof. Dr. David Rubie (2. Gutachter)

Prof. Dr. Leonid Dubrovinsky

Prof. Dr. Jürgen Senker

Dedicated
to my Parents and my Family

Acknowledgements

I would like to acknowledge Prof. Dr. F. Langenhorst for his trust and patience during the supervision of this research project. Furthermore, I thank Dan Frost, Guðmundur Guðfinnsson, Tiziana Boffa Ballaran, Nobuyoshi Miyajima and Hans Keppler for the scientific support and their aid during measurements and experimental work, respectively. The work benefit from the the careful sample preparation done by Hubert and Uwe. I thank also Detlef for the support during microprobe measurements and the explanations to let me work independently. In particular, thanks to the secretaries for the help in administrative questions and the entire BGI staff.

I highly appreciate the support of my friends and colleagues, with special thank to my closest friends for simply everything.

Last but not least, I would like to thank my family for the support and help in the past 27 years.

Contents

List of Figures	v
List of Tables	ix
Summary	xi
Zusammenfassung	xiv
1 Introduction	1
1.1 The accretion and evolution of Mars	2
1.2 Earth's and Mars' mineralogical structure	4
1.3 Wadsleyite and Ringwoodite	10
1.4 Dense hydrous magnesium silicates (DHMS)	16
1.5 Motivation	22
1.6 Aims of the study	24
2 Multi anvil technique	25
3 Characterisation methods	31
3.1 EPMA and Raman spectroscopy	31
3.2 Fourier transform infrared spectroscopy	36
3.3 TEM and EELS	39
3.4 Single-crystal x-ray diffraction method	43
4 Hydrous Fo₅₀ system	47
4.1 Starting material and experimental conditions	47
4.2 General description of experimental run products	49
4.3 Results	55
4.3.1 Ringwoodite	55

CONTENTS

4.3.1.1	Microprobe analyses	55
4.3.1.2	TEM examination	59
4.3.1.3	FTIR spectroscopy	62
4.3.1.4	Single-crystal x-ray diffraction	66
4.3.2	Dense hydrous Mg-Fe silicates	74
4.3.3	Characterisation of oxide phases	83
4.4	Discussion and conclusions	87
4.4.1	Effect of H and Fe substitution on the ringwoodite structure	87
4.4.2	Effect of Fe-substitution on the O-H stretching mode of hydrous ringwoodite	88
4.4.3	Effect of H and Fe substitution on the compressibility of ringwoodite	89
4.4.4	Water substitution mechanisms and water contents of ferroan ringwoodite	92
4.4.5	The stability, iron partitioning and point defect chemistry of DHMS	96
5	Hydrous Martian mantle composition	103
5.1	Starting material and experimental conditions	103
5.2	General description of experimental run products	106
5.3	Results	114
5.3.1	Olivine, wadsleyite and ringwoodite	114
5.3.2	Pyroxene, garnet and akimotoite	122
5.3.3	Stability and characteristics of DHMS	128
5.3.4	Point defect chemistry of nominally anhydrous mantle minerals	133
5.4	Discussion	137
5.4.1	Water substitution mechanisms and water contents of iron-bearing nominally anhydrous minerals	137
5.4.2	Dense hydrous Mg-Fe silicates in the Martian mantle	143
5.5	Conclusions	144
6	General conclusions	147
	References	159

List of Figures

1.1	Thermal evolution models of the Martian mantle temperatures as a function of time	3
1.2	Mineralogical Structure of the upper 1000 km Earth's mantle . . .	5
1.3	Comparison of the structures of the interiors of (a) Earth and (b) Mars	6
1.4	Mineralogical Model and thermal gradients (areotherm) of the Martian interior (Bertka and Fei 1997)	7
1.5	Model of the Martian thermal gradient	8
1.6	Pressure-composition diagram of the Mg_2SiO_4 - Fe_2SiO_4 solid solution at geotherm conditions	11
1.7	Hydrous Mg-wadsleyite	12
1.8	Hydrous wadsleyite II	12
1.9	Ringwoodite structure	14
1.10	Possible proton positions in hydrous Mg-ringwoodite and associated defects	14
1.11	Preliminary Reference Earth Model	15
1.12	Molar ternary diagram of the dense hydrous magnesium silicates .	16
1.13	Crystal structure of phase D	17
1.14	Crystal structure of superhydrous B	18
1.15	Crystal structure of phase A	19
1.16	Phase relations for the $Mg_2SiO_4 + 5$ wt% H_2O (a), $Mg_2SiO_4 + 11$ wt% H_2O (b) and $Mg_2SiO_4 + 15$ wt% H_2O (c) bulk composition .	20
2.1	Schematic configuration and two stage principal of multi anvil technique	26
2.2	Schematic cross section of the 10/4 octahedron	27
2.3	Schematic illustration of the Multi anvil principal	28

LIST OF FIGURES

3.1	Spectrometer geometry for wavelength dispersive x-ray analysis (Johannson geometry)	33
3.2	Range of the elements that can be analysed by the spectrometer crystals	33
3.3	Schematic illustration of Raman scattering effect	34
3.4	Schematic illustration of the Michelson interferometer of Fourier-transform infrared spectrometer	36
3.5	Correlation of the integrated molar absorption coefficient ε_i of OH stretching bands as a function of the wavenumber	38
3.6	Schematic illustration of TEM sample preparation	39
3.7	Prepared sample for TEM analyses	40
3.8	Fe $L_{2,3}$ -edge Electron energy-loss near-edge structure (ELNES) spectra of natural a garnet	42
3.9	Single-crystal x-ray diffractometer	43
3.10	Diamond anvil cell	45
4.1	Backscattered electron image of single phase ringwoodite (a) and the three-phase assemblage (b)	51
4.2	Ternary diagram of MgO(FeO), SiO ₂ and H ₂ O	54
4.3	Mg ₂ SiO ₄ fraction of ringwoodite as a function of pressure	56
4.4	Electron diffraction patterns of ringwoodite	59
4.5	High resolution TEM image of Mg,Fe-ringwoodite	60
4.6	Iron $L_{2,3}$ electron energy-loss near-edge structure (ELNES) spectra of Mg,Fe-ringwoodite	61
4.7	Infrared absorption spectra of four Mg,Fe-ringwoodite samples	63
4.8	Infrared spectra of hydrous ferroan ringwoodites	66
4.9	Unit cell volume of dry and hydrous ringwoodite as a function of magnesium content	68
4.10	M-O distances (a) and T-O distances (b) of hydrous ringwoodite as a function of magnesium number	70
4.11	Variations of the unit-cell volumes of ferroan ringwoodites as a function of pressure	71
4.12	Plot of Eulerian strain f versus normalized stress F	73
4.13	Stabilities of dense hydrous Mg-Fe silicates as a function of pressure and temperature	74
4.14	Composition of dense hydrous Mg-Fe silicates	76
4.15	Indexed electron diffraction pattern of phase A	77

4.16 Indexed electron diffraction pattern of superhydrous B	79
4.17 Iron $L_{2,3}$ electron energy-loss near-edge structure (ELNES) spectra of superhydrous B and Phase D	79
4.18 Water substitution mechanisms of phase D	80
4.19 Composition of phase D	81
4.20 Indexed electron diffraction pattern of phase D	82
4.21 Phase diagram of the joint Mg_2SiO_4 - Fe_2SiO_4 as a function of pressure (Presnell 1995)	83
4.22 High-resolution TEM image of magnetite	86
4.23 Bright-field TEM image of magnesiowüstite	86
4.24 Correlation between the OH-stretching wavenumber and the O-O distance of the octahedral shared edge	89
4.25 Water content of Mg- and MgFe-ringwoodite	93
4.26 Schematic illustration of the water storage capacity of nominally anhydrous minerals	94
4.27 Phase assemblages as a function of pressure and temperature . . .	97
4.28 Phase relations for the $Mg_2SiO_4 + 11 \text{ wt}\% \text{ H}_2\text{O}$ bulk composition	98
4.29 Water substitution mechanisms of phase D	100
4.30 Iron partitioning between ringwoodite and dense hydrous magnesium silicates as a function of Fe_2SiO_4 mole fraction of ringwoodite	101
5.1 Model of the Martian thermal gradient	105
5.2 Backscattered electron images of run products	107
5.3 Ternary diagram showing the compositions of run products	114
5.4 Raman spectra of olivine	116
5.5 Raman spectra of coexisting mineral phases	117
5.6 Infrared spectra of wadsleyite	118
5.7 High-resolution TEM image of wadsleyite	119
5.8 Iron $L_{2,3}$ electron energy-loss near-edge structure (ELNES) spectra of Mg,Fe-wadsleyite	119
5.9 Infrared spectra of ringwoodite	120
5.10 Iron $L_{2,3}$ electron energy-loss near-edge structure (ELNES) spectra of Mg,Fe-ringwoodite	121
5.11 Iron $L_{2,3}$ electron energy-loss near-edge structure (ELNES) spectra of pyroxene	122

LIST OF FIGURES

5.12	Chemical composition of garnet (pyrope with up to 31% almandine) as a function of pressure	125
5.13	Iron $L_{2,3}$ electron energy-loss near-edge structure (ELNES) spectra of garnet/majoritic-garnet	126
5.14	Raman spectra of Akimotoite	127
5.15	Water substitution mechanisms of phase D	129
5.16	Iron $L_{2,3}$ electron energy-loss near-edge structure (ELNES) spectra of superhydrous B and Phase D	129
5.17	Ternary diagram of composition of phase D and superhydrous B .	130
5.18	Chemical composition of ferroan superhydrous B	132
5.19	Ferric iron fraction versus water content (McCammon et al. 2004)	140
5.20	Ferric iron (wt%) versus water content (wt%) of ringwoodite and wadsleyite	141
5.21	Model of the Martian thermal gradient	143
5.22	Mineralogical model of a hydrous Martian interior	144
5.23	MgSiO ₃ Ilmenite-perovskite transition boundary as a function of pressure and temperature	145
6.1	Backscattered electron image of sample GG 4377	148
6.2	Stability regions of dense hydrous magnesium silicates as function of pressure and temperature	149
6.3	Water contents of ringwoodite as a function of the iron content . .	150
6.4	Iron partitioning coefficient K_D between ringwoodite and coexisting melt as well as garnet and coexisting melt	152
6.5	Aluminium partitioning between garnet and melt as function of pressure	154
6.6	Density of a hydrous Martian melt and ringwoodite as function of pressure at 2170 K	155

List of Tables

2.1	Multi anvil assemblies used in this study.	27
2.2	Pressure calibration for multi anvil technique (Keppler and Frost 2005)	29
3.1	Calibration and measurement details for microprobe analyses. . .	32
3.2	Density factor X_i for water concentration determination	38
3.3	Reference data used for TEM microstructural analyses and phase identification.	41
4.1	Calculated bulk composition of the $\text{MgFeSiO}_4+\text{H}_2\text{O}$ starting material.	47
4.2	Experimental run conditions.	48
4.3	Relative phase abundances (modal%) of recovered samples containing ringwoodite and dense hydrous Mg-Fe silicates.	50
4.4	Average composition of experimental run products based on EPMA measurements	52
4.5	Application of Gibbs' phase rule to observed phase assemblages. .	53
4.6	EPMA data of ringwoodite (1σ standard deviation in parenthesis) 57	
4.7	Mg,Fe-ringwoodite samples used for the determination of water concentration; synthesis conditions, wavenumber of maximum absorption and measured water concentration	64
4.8	Chemical analyses of ringwoodite based on electron microprobe analyses, electron energy loss and IR spectroscopy (Standard deviations are in parentheses).	67
4.9	Structure refinement data for the two ringwoodite samples of this study.	69
4.10	Unit-cell parameter measured as a function of pressure.	72
4.11	EPMA data of DHMS (1σ standard deviation in parenthesis) . . .	75

LIST OF TABLES

4.12	EPMA data of magnesiowüstite with magnesioferrite and magnetite components (1σ standard deviation in parenthesis) . . .	84
4.13	Compressibility of ringwoodite and spinel phases.	91
4.14	Correlation of composition (Fe^{3+} -content) and water-content of ringwoodite	92
5.1	Bulk composition of the starting material - hydrous FMAS.	104
5.2	Experimental run conditions - hydrous FMAS.	105
5.3	EPMA data of quenched melt fraction (selected samples)	106
5.4	Relative mineral phase abundances (modal%) of recovered samples	108
5.5	Application of Gibbs' phase rule to observed phase assemblages .	109
5.6	Mass balance calculation - sample GG 4389 (exemplary for presented data)	111
5.7	Mineral formulae calculation of wadsleyite (wd), superhydrous B (SHyB) and phase D (exemplary for presented data)	112
5.8	Mineral formulae calculation of majoritic-garnet (maj-gt) and pyroxene (exemplary for presented data)	113
5.9	EPMA data of olivine, wadsleyite and ringwoodite (1σ standard deviation in parenthesis)	115
5.10	EPMA data of akimotoite, garnet and pyroxene (1σ standard deviation in parenthesis)	123
5.11	Garnet-melt partitioning ratios of Fe and Al	124
5.12	EPMA data of phase D and superhydrous B (1σ standard deviation in parenthesis)	131
5.13	Calculated oxygen defects in majoritic-garnet and associated water contents	134
5.14	Calculated oxygen defects in pyroxene and associated water content	135
5.15	Estimated water content of a saturated Martian mantle.	146
6.1	Density and iron content calculation of ringwoodite (rw) at 2170 K.	156

Summary

In the scope of this research study two independent sets of experiments were carried out using $\text{MgFeSiO}_4+\text{H}_2\text{O}$ starting composition and a simple Martian mantle bulk composition (hydrous FMAS). This thesis addresses three different effects of iron on the properties of nominally anhydrous transition minerals and dense hydrous magnesium silicates. Furthermore, the potential presence of dense hydrous Mg-Fe silicates in the Martian interior and the water storage potential of a hydrous Martian mantle is evaluated.

1. The effect of iron on the water storage capacity of ringwoodite

The results show that the water storage capacities of iron-rich ringwoodites of about 0.4-0.7 wt% H_2O are considerably reduced compared to pure Mg-ringwoodite. Thus, the ringwoodite samples show an inverse correlation of iron- and water content, implying that the water storage capacity of ringwoodite decreases towards the Fe-endmember. The magnesium-site octahedra represent the favoured protonation site in ferroan ringwoodites corresponding to the $\text{Mg}^{2+} = 2\text{H}^+$ water substitution mechanism. In addition, ferric iron diminishes the water content of ringwoodites due to the reduction of potential protonation sites. This is caused by the creation of Mg-site vacancies by the oxidation of iron and the occupation of octahedral sites by Fe-atoms, which are probably not involved in water substitution mechanism. These results indicate that less water can be stored in nominally anhydrous mantle silicates of iron-rich planetary mantles.

2. The effect of iron on the compressibility of hydrous ferroan ringwoodite

The compressibility of mantle minerals is a decisive parameter that is needed to understand the seismic structure of planetary interiors, observed by geophysical analyses. The knowledge of the effect of iron on the compressibility of ringwoodite is particularly important for the interpretation of the structure of iron-rich planetary interiors such as the Martian mantle. Measurements at ambient conditions yield to unit-cell lattice parameters of $a = 8.1597(6) \text{ \AA}$ and $V = 543.28(13) \text{ \AA}^3$ (run 3854) and $a = 8.1384(3) \text{ \AA}$ and $V = 539.03(7) \text{ \AA}^3$ (run 4218). The P-V data were fitted with a second-order Birch-Murnaghan equation of state.

The first pressure derivative of the bulk modulus, K' , was fixed to the value of 4 yielding to the following refined equation of state parameters: $V_0 = 543.32(7) \text{ \AA}^3$ and $K_{T0} = 186.5(9) \text{ GPa}$ (run 3854) and $V_0 = 539.01(5) \text{ \AA}^3$ and $K_{T0} = 184.1(7) \text{ GPa}$ (run 4218). Structural refinements indicate the presence of significant octahedral vacancies in sample 4218 due to the presence of 0.1 ferric iron atoms per formula unit and the substitution of $\sim 0.37 \text{ wt\% H}_2\text{O}$. However, the values of bulk modulus of $(\text{Mg,Fe})_2\text{SiO}_4$ -ringwoodites found in this study are very similar to that of the Mg- and Fe-endmember ringwoodite, suggesting therefore that the Fe substitution has little effect on the compressibility of ringwoodite. This also suggests therefore that the close-packing of oxygens of the spinel structure is the major factor in determining its compressibility. This cannot be affected by the presence of up to 0.1 atoms per formula unit of vacancies.

3. The effect of iron on the stability of hydrous mantle silicates

The results of the experiments obtained on the two different bulk compositions show that the stability of ringwoodite is extended down to 9 GPa at 750°C ($\text{MgFeSiO}_4 + \text{H}_2\text{O}$) and the transformation pressure of olivine to wadsleyite (simple Martian mantle composition) is lowered by 2 GPa. The shifts of stability fields toward lower pressures are possibly caused by the presence of ferric iron and water. The shift of the olivine-wadsleyite transition would result in an extended upper mantle transition zone, compared to the anhydrous mantle, and consequently yield an increased water storage potential of the Martian mantle. The dense hydrous Mg-Fe silicates, phase D and superhydrous B show stabilities up to 1300°C at 23 GPa (phase D, $\text{MgFeSiO}_4 + \text{H}_2\text{O}$ bulk composition) and for the simple Martian mantle composition up to 1450°C at 20.5 GPa (phase D and superhydrous B), which represents a higher stability of DHMS than previously reported. This suggests that phase D and superhydrous B are relevant dense hydrous Mg-Fe silicates in iron-rich mantles of planetary systems.

4. The potential presence of dense hydrous Mg-Fe silicates in the Martian interior and the water storage potential of a hydrous Martian mantle

The experimental study of hydrous Martian mantle silicates indicates that the Martian mantle consists basically of upper mantle with olivine, garnet and pyroxene as well as upper and lower transition zone build up by wadsleyite and ringwoodite together with pyroxene and majoritic-garnet, respectively. The water contents of wadsleyite with 0.6 wt% H₂O and ringwoodite with 1.1 wt% H₂O are reduced compared to the Mg-endmembers. The Martian transition zone, however, shows the largest water storage capacity since the upper mantle mineral olivine accommodates up to 0.3 wt% H₂O. Pressure and temperature conditions at the core-mantle boundary are insufficient to reach the perovskite stability field, i.e. a lower Martian mantle cannot be expected based on the results presented in this study. Nevertheless, these results imply that significant amounts of water can be stored in the Martian transition zone as well as the upper mantle. In addition, dense hydrous Mg-Fe silicates would be stable up to 1450°C at 20.5 GPa in a hydrous Martian mantle model. On the basis of thermal evolution models of the Martian mantle, provided in the literature, and iron partitioning data between mineral phases and melt it is discussed that dense hydrous Mg-Fe silicates may form in the Martian interior at P-T conditions corresponding to the lower Martian transition zone.

Zusammenfassung

Im Rahmen dieser Doktorarbeit wurden zwei unabhängige Serien von Experimenten mit einer $\text{MgFeSiO}_4+\text{H}_2\text{O}$ Gesamtzusammensetzung und einer vereinfachten Mars-Mantel Gesamtzusammensetzung (wasserhaltiges FMAS System) durchgeführt.

In dieser Arbeit werden drei verschiedene Effekte des Eisens auf die Eigenschaften von nominell wasserfreien Mineralphasen und dichten wasserhaltigen Magnesiumsilikaten behandelt (DHMS). Des Weiteren wird die Möglichkeit des Auftretens dichter wasserhaltiger Magnesiumsilikate im Inneren des Mars und die potenzielle Wasseraufnahmefähigkeit eines wasserhaltigen Marsmantels diskutiert.

1. Der Einfluss des Eisens auf die Wasseraufnahmefähigkeit von Ringwoodit

Die Ergebnisse zeigen, dass die Wasseraufnahmefähigkeiten von eisenreichen Ringwooditen (0.4-0.7 gew% H_2O) im Vergleich zu dem reinen Mg-Endglied deutlich reduziert sind. Ringwoodit zeigt demnach eine negative Korrelation zwischen Eisen- und Wassergehalt, so dass eine sehr niedrige Wasseraufnahmefähigkeit des Fe-Endglieds zu erwarten ist. Magnesium-Oktaeder stellen die bevorzugten Protonierungspositionen in eisenhaltigen Ringwooditen dar, entsprechend der Substitution $\text{Mg}^{2+} = 2\text{H}^+$. Eisen reduziert vermutlich die Anzahl möglicher Protonierungspositionen auf zwei Arten, zum einen durch die Bildung von Mg-Leerstellen, als Folge der Eisenoxidation. Zum anderen scheint Eisen nicht direkt an den Wassereinbaumechanismen beteiligt zu sein, so dass der Einbau von Fe grundsätzlich die Anzahl der Protonierungsstellen reduziert. Daher ist zusätzlich zu beobachten, dass der Wassergehalt durch dreiwertiges Eisen erniedrigt wird. Diese Resultate deuten an, dass weniger Wasser in eisenreichen planetaren Mänteln durch nominell wasserfreie Silikate gespeichert werden kann.

2. Der Einfluss des Eisens auf die Kompressibilität von wasser- und eisenhaltigem Ringwoodit

Die Kompressibilität von Mantelmineralen ist ein entscheidender Faktor, welcher zur Interpretation geophysikalischer Daten und seismischer Strukturen von Planeteninneren benötigt wird. Das Wissen über den Einfluss des Eisens

auf die Kompressibilität von Ringwoodit ist insbesondere wichtig für die Interpretation der Struktur von eisenreichen planetaren Mänteln, wie zum Beispiel des Marsmantels. Die Messungen bei Umgebungsbedingungen haben die Elementarzellen-Parameter $a = 8.1597(6) \text{ \AA}$ und $V = 543.28(13) \text{ \AA}^3$ (Exp. 3854) und $a = 8.1384(3) \text{ \AA}$ und $V = 539.03(7) \text{ \AA}^3$ (Exp. 4218) ergeben. Die Druck-Volumen-Daten wurden mit einer Birch-Murnaghan-Zustandsgleichung zweiter Ordnung angepasst. Die erste Ableitung des Kompressionsmoduls nach dem Druck, K' , wurde auf den Wert von 4 festgelegt, was folgende verfeinerte Zustandsgleichungsparameter ergibt: $V_0 = 543.32(7) \text{ \AA}^3$ und $K_{T0} = 186.5(9) \text{ GPa}$ (Exp. 3854) and $V_0 = 539.01(5) \text{ \AA}^3$ und $K_{T0} = 184.1(7) \text{ GPa}$ (Exp. 4218). Strukturverfeinerungen deuten die Anwesenheit von erheblichen Oktaeder-Leerstellen in der Probe 4218 an, welche durch die Oxidation von zweiwertigem Eisen und den Einbau von $\sim 0.37 \text{ gew\% H}_2\text{O}$ entstehen. Die ermittelten Kompressionsmodule von $(\text{Mg,Fe})_2\text{SiO}_4$ Ringwooditen sind vergleichbar mit den Werten des Fe- und Mg-Endglieds, was darauf hinweist, dass die Eisensubstitution keinen nachweisbaren Einfluss auf die Kompressibilität von Ringwoodit hat. Des Weiteren lässt sich schlussfolgern, dass die dichteste Kugelpackung der Sauerstoffatome in der Spinell-Struktur im wesentlichen die Kompressibilität von Ringwoodit bestimmt. Selbst bei 0.1 a.p.f.e. Oktaeder-Leerstellen konnte keine Änderung des Kompressionsmoduls festgestellt werden.

3. Der Einfluss des Eisens auf die Stabilität von wasserhaltigen Mantelsilikaten

Die Ergebnisse der Experimente, welche mit den zwei verschiedenen Gesamtzusammensetzungen durchgeführt wurden, zeigen, dass die Stabilität von Ringwoodit bei niedrigen Temperaturen (750°C) zu niedrigerem Druck von 9 GPa erweitert ist ($\text{MgFeSiO}_4 + \text{H}_2\text{O}$ Gesamtzusammensetzung). Des Weiteren ist der Transformationsdruck des Olivin-Wadsleyit-Übergangs für die vereinfachte Marsmantel-Gesamtzusammensetzung um 2 GPa verringert. Diese Stabilitätsverschiebungen zu niedrigerem Druck sind vermutlich durch die Gegenwart von dreiwertigem Eisen und Wasser bedingt. Die Verschiebung des Olivin-Wadsleyit-Übergangs würde im Vergleich zum wasserfreien System in einer ausgedehnteren oberen Übergangszone des Marsmantels resultieren, was einer erhöhten Wasseraufnahmefähigkeit des Marsmantels entsprechen würde. Die dichten wasserhaltigen Magnesiumsilikate, Phase D und

Superhydrous B, sind bis zu Temperaturen von 1300°C bei 23 GPa (Phase D, $\text{MgFeSiO}_4 + \text{H}_2\text{O}$ Gesamtzusammensetzung) und 1450°C bei 20.5 GPa (vereinfachte Marsmantel-Gesamtzusammensetzung) stabil. Dies stellt eine erhöhte Stabilität von dichten wasserhaltigen Magnesiumsilikaten in Hinsicht auf vorhergehende Literaturdaten dar. Demnach kann angenommen werden, dass Phase D und Superhydrous B in eisenreichen Mänteln von planetaren Systemen auftreten könnten.

4. Das potenzielle Auftreten von dichten wasserhaltigen Magnesiumsilikaten im Inneren des Mars und die Wasseraufnahmefähigkeit eines wasserhaltigen Marsmantels

Die experimentelle Studie von wasserhaltigen Silikaten in einem Mars-ähnlichen System zeigt, dass der Marsmantel hauptsächlich aus einem oberen Mantel mit Olivin, Granat und Pyroxen und einer Übergangszone besteht, welche aus Wadsleyit und Ringwoodit sowie Pyroxen und Majorit-Granat aufgebaut ist. Die Wassergehalte von Wadsleyit (0.6 Gew% H_2O) und Ringwoodit (1.1 Gew% H_2O) sind im Vergleich zu dem Mg-Endglied verringert. Dennoch zeigt die Übergangszone des Marsmantels die höchste Wasseraufnahmefähigkeit, da Olivin nur bis zu 0.3 Gew% H_2O im oberen Mantel aufnimmt. Die Druck-Temperatur-Bedingungen an der Kern-Mantel-Grenze sind nicht ausreichend, um Perowskit zu stabilisieren, d.h. ein unterer Marsmantel ist aufgrund der vorliegenden Resultate nicht vorstellbar. Dennoch zeigen diese Ergebnisse, dass bedeutende Mengen an Wasser in der Übergangszone und dem oberen Mantel des Mars gespeichert werden können. Zusätzlich ist zu beobachten, dass die dichten wasserhaltigen Magnesiumsilikate, Phase D und Superhydrous B, bis 1450°C und 20.5 GPa stabil sind. Daher wurde auf der Grundlage von thermischen Evolutionsmodellen und Eisenverteilungsdaten zwischen Mineralphasen und Schmelze das potenzielle Auftreten von dichten wasserhaltigen Magnesiumsilikaten im Marsinneren erörtert. Diese dichten wasserhaltigen Magnesiumsilikate könnten im Marsmantel unter Temperatur-Druck-Bedingungen gebildet werden, die der unteren Übergangszone des Mantels entsprechen.

Chapter 1

Introduction

Our blue planet Earth, is unique in the solar system. Earth experienced several random incidences during its evolution which made life possible. Formed at a convenient distance from the sun, the collision with a smaller planet which resulted in the formation of the moon, and tilting of the Earth's rotation axis provided a proper rotation velocity to cause balanced temperature distribution and seasons on Earth. Water is believed to be essential for the origin of life, and according to our knowledge, Earth is the only planet that fulfills the essential conditions to retain fluid water on its surface over geological time.

On planet Mars surface features have been observed that are similar to fluvial structures found on Earth, raising the question of whether fluid water was once present on Mars. Observations of surface features and geochemistry of Mars provide evidences for liquid water in previous epochs in Mars' history. Geological features like large outflow channels and transported material associated with sedimentation present on the Martian surface provide the evidence that water was released from within the crust. The atmospheric and climatic conditions on Mars do not allow liquid water on the surface, therefore quickly released large quantities of water are necessary to form these channels and to flow certain distances before freezing (Jakosky and Phillips 2001). The water was probably once stored in the Martian interior and then liberated to the surface. To understand this process, knowledge of Martian mantle structure and stability of hydrous phases is required.

1.1 The accretion and evolution of Mars

The origin of water on Mars

The origin of water on terrestrial planets is assumed to result from the water content of about 12 wt% H₂O of the chondrite material that accreted during planet formation (Dreibus et al. 1997). Later, additional water was delivered to terrestrial planets by impacts during the “late veneer phase”. Clear evidence is found for an existence of water on Mars such as hydrated minerals on the surface and fluvial outflow channels, however the water liberation processes, and the water storage potential remain unknown.

The Martian evolution after accretion including differentiation, and thermal evolution, is uncertain and different models exist. Elkins-Tanton (2008) proposed a model of magma ocean solidification, which shows the progressive solidification of a magma ocean and the subsequent overturning to form the crust, and a stably stratified mantle with respect to density. As the magma ocean crystallises, denser crystals will sink, and less dense crystals float. During this fractional crystallisation the residual melt will be enriched in iron and volatiles such as water. Thus, even small initial water contents may result in significant amounts of water in the Martian mantle stored by the nominally anhydrous mantle minerals.

The thermal evolution of Mars

Thermal evolution models of the Martian interior depend essentially on model parameters and as a result different thermal evolution paths are reasonable for Mars. The Martian thermal gradient and the P-T conditions at the core-mantle boundary are determined by the physical state, and the size and the composition of the Martian core. These parameters are still unconstrained and the thermal structure of the Martian interior remains uncertain. Nevertheless, different thermal evolution models were presented by Spohn et al. (2001), who showed that the mantle temperatures depend strongly on the mantle heat transfer connected to particular environments such as plate tectonics, or the development and constitution of the lithosphere. According to the different thermal history models, the mantle temperatures are assumed to be between 1500 K and 2000

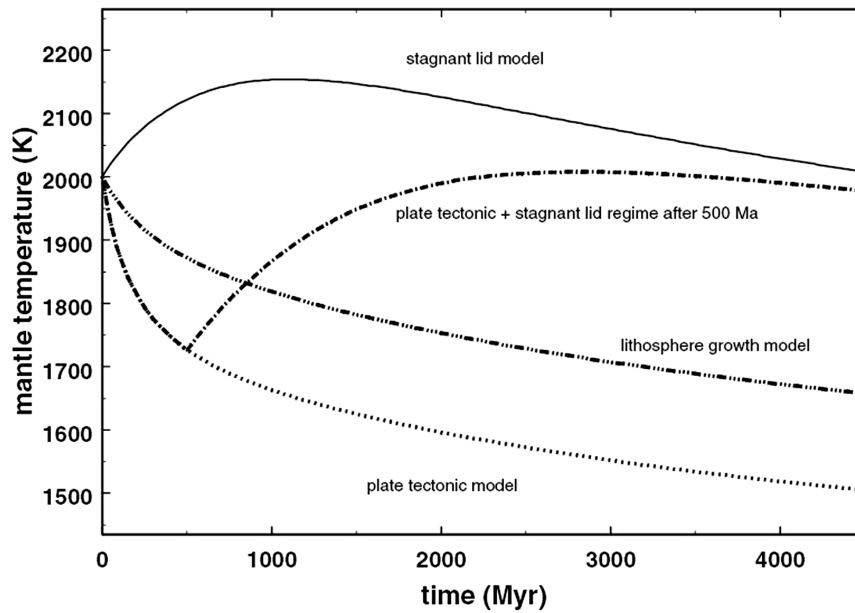


Figure 1.1: Thermal evolution models of the Martian mantle temperatures as a function of time - showing the different mantle temperatures due to different heat transfer models connected to particular environments (from Spohn et al. 2001).

K (plate tectonic model and stagnant lid model, respectively, Figure 1.1).

The current areotherm (Martian thermal gradient, Figure 1.5) was experimentally determined by Fei and Bertka (2005), based on the melting relations in a model Martian core composition, and the physical state of the core. The P-T conditions at the Martian core-mantle boundary are assumed to be ~ 1800 K for an entirely liquid core at 23 GPa (Williams and Nimmo 2004).

1.2 Earth and Mars - Mineralogical structure of planetary interiors

I. Earth's mineralogical inner structure

According to the current static model, planet Earth is composed of several shells - crust, upper mantle, transition zone, lower mantle, outer and inner core - each of which consist of different mineral assemblages (Figures 1.2, 1.3). The upper mantle mainly consists of olivine accompanied by smaller fractions of garnet, clino- and orthopyroxene. With increasing pressure and temperature, i.e. increasing depth in planetary interiors, mineral phases undergo phase transformations, which result in changes of structural and physical properties such as density and compressibility. First of all the density, but also the compressibility of mineral phases determine the velocity of compressional waves travelling through planetary interiors. Relatively sharp phase transformations, which result in density changes, cause jumps in seismic wave velocities that are detected by geophysical observations, the so called seismic discontinuities. At approximately 14 GPa olivine transforms to a denser high-pressure polymorph wadsleyite with a higher density and bulk modulus $K \sim 170$ GPa (Jacobsen 2006). Because of the lower compressibility than olivine ($K \sim 130$ GPa, Jacobsen 2006), this results in increasing elastic-wave velocities at the upper mantle-transition zone boundary. This phase transformation marks the beginning of the mantle transition zone and the 410 km seismic discontinuity. At higher pressure, wadsleyite transforms to denser cubic ringwoodite at 17.5 GPa. Garnet, clino- and orthopyroxene are stable at upper mantle conditions, while orthopyroxene starts to breakdown and is accommodated as the majorite component in the garnet structure. Clinopyroxene also enters the garnet structure at higher pressure. The incorporation of orthopyroxene and clinopyroxene components increases with increasing pressure and temperature such that the majoritic component increases in garnet until almost pure majorite exists in the transition zone (Frost 2008).

Wadsleyite and ringwoodite, the high pressure polymorphs of olivine, dominate the transition zone together with majorite-garnet down to a depth of 660 km. The decomposition of ringwoodite and the transformation of majorite-garnet into the lower mantle mineral assemblage of magnesium silicate perovskite, ferropericlae and calcium silicate perovskite results in another major

1.2 Earth's and Mars' mineralogical structure

seismic discontinuity at 660 km depth (Figures 1.2, 1.3). The lower mantle region extends down to the core-mantle-boundary at 2,900 km depth (Figure 1.3). The Earth's core is subdivided into a molten outer core made of iron with 10% of light elements (S, C or O) and a solid inner core consisting of Fe-Ni alloy (Lodder & Fegley 1998). An important issue is the global water cycle in order to understand the dynamics of the Earth's interior and to interpret geophysical observations. Subduction zones are crucial for the transport of water to deep mantle regions. Hydrated minerals in subduction slabs undergo either phase transformations to form the "Dense hydrous magnesium silicates" at lower temperature, or decompose with the release of water at higher temperature. Several experimental studies at high P-T showed that the nominally anhydrous mantle minerals have the potential to store the water released by the decomposition of hydrated minerals. The largest amount of accommodated water of up to 2.4 - 3.3 wt% H₂O was determined for ringwoodite and wadsleyite (Kudoh et al. 1996; Kohlstedt et al. 1996; Smyth et al. 2005). These results demonstrate that there is an enormous water storage capacity for the Earth's upper mantle and transition zone (Smyth & Jacobsen 2006).

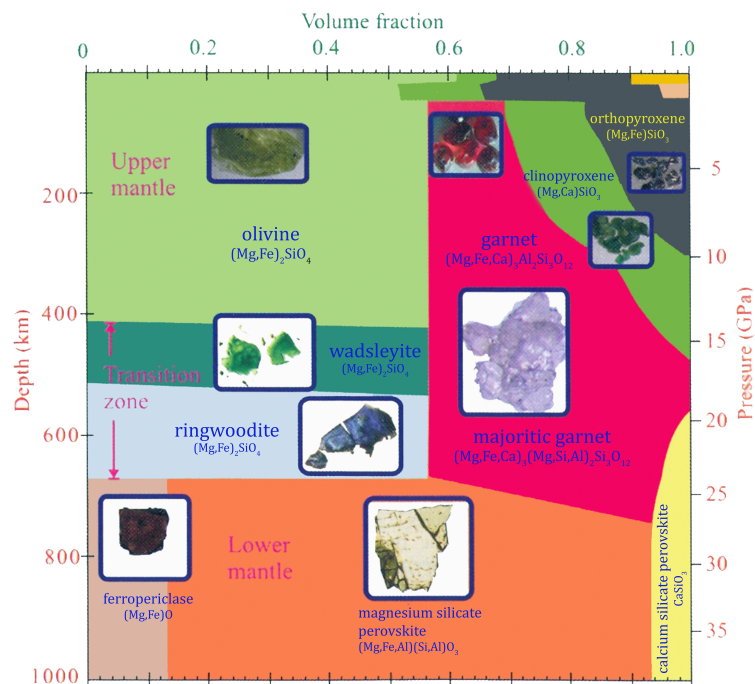


Figure 1.2: Mineralogical Structure of the upper 1000 km Earth's mantle - Mineral assemblages of pyrolitic mantle along the oceanic geotherm (small yellow and beige in the upper right corner represent feldspar and spinel stabilities); from Frost (2008).

1. INTRODUCTION

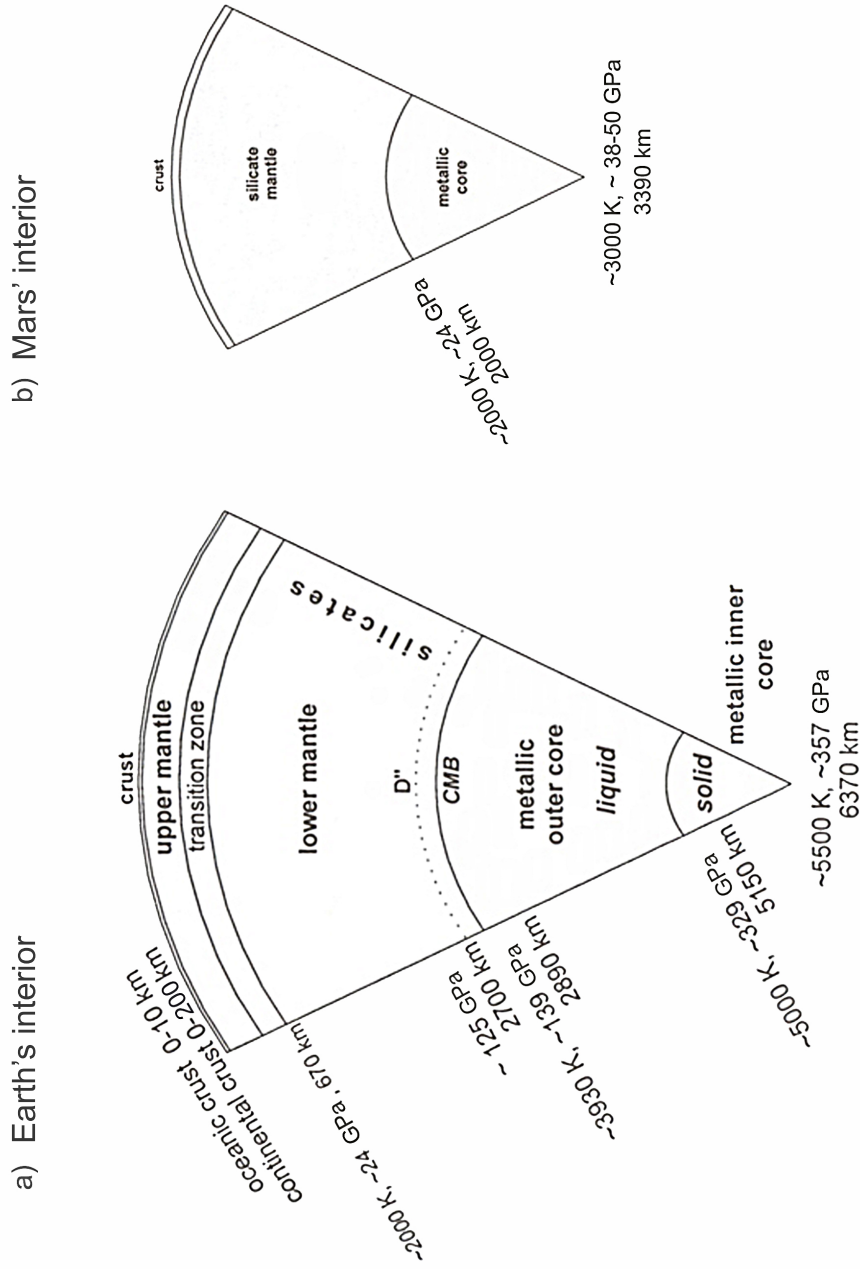


Figure 1.3: Comparison of the structures of the interiors of (a) Earth and (b) Mars - from Lodders and Fegley (1998), Martian core mantle boundary data after Fei et al. (1995).

II. Mars' mineralogical inner structure

Mars is the outermost planet of the terrestrial planets in our solar system. Mars, with a radius of 3390 km, has almost half the size of Earth (Figure 1.3). Fundamental knowledge on Mars was gained by Martian missions, and meteorite examinations. Dreibus and Wänke (1985) derived a compositional model for the Martian mantle based on element correlations between the measured element ratios of SNC meteorites (Martian meteorites), and chondritic element abundances. This method to derive the model composition is independent of Mars' moment of inertia, which makes this model suitable as basis for experimental studies of planet Mars.

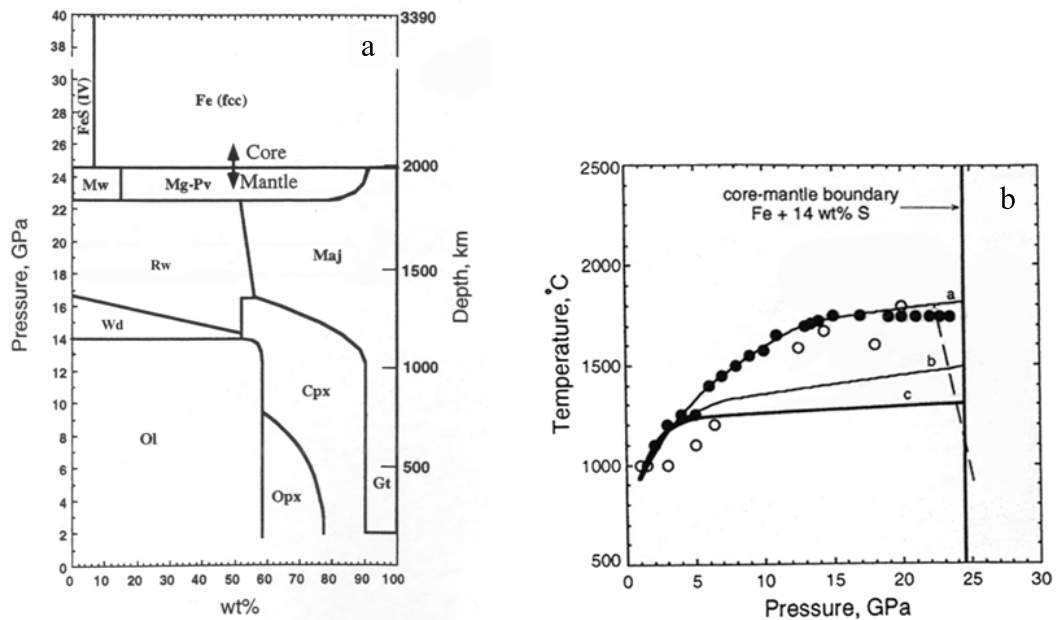


Figure 1.4: Mineralogical Model and thermal gradients (areotherm) of the Martian interior (Bertka and Fei 1997) - (a) Relative mineral phase abundances as a function of pressure along the areotherm of Mars indicated by line a (1.4b); (b) Thermal gradients of the Martian interior assuming a liquid Martian core after Longhi et al. (1992) - line a; assuming a solid core after Longhi et al. (1992) - line b; assuming liquid core after Fei & Bertka (1996) - line c; black circles - experiments by Bertka & Fei 1997 (Dreibus and Wänke (1985) Martian mantle composition), Core-mantle boundary after Fei et al. (1995), silicate-perovskite transition boundary after Ito & Takahashi (1989)(dashed line).

1. INTRODUCTION

Experimental data by Bertka and Fei (1997) concerning the determination of Martian mantle mineralogy is based on the Dreibus & Wänke (1985) compositional Martian mantle model. This model depends on geochemical and geophysical assumptions, while all models predict that the mantle bulk composition is more iron-rich than the Earth's mantle. Mars is considered to have a layer structure, like Earth, consisting of crust, silicate mantle and core. Figure 1.3 shows a simplified structure of the Martian interior since the actual position of the upper mantle - transition zone boundary and the presence of a lower mantle are still poorly constraint because the depth of these boundaries depends on the assumed thermal gradient. Mantle mineralogy is predicted to be similar to that of Earth (Figure 1.4). Bertka and Fei (1997) constrained the model mineralogy as a function of pressure on the basis of their experiments along the modeled areotherm, assuming a liquid Martian core after Longhi et al. (1992) with sulfur-rich compositions (Figure 1.4). More recent publications by Stevenson (2001) and Yoder et al. (2003), however, point out that the current Martian core is potentially divided into outer liquid and inner solid core. Further publications suggest the occurrence of the core-mantle boundary (CMB) at 23 GPa and 1800 K (Fei and Bertka 2005, Williams and Nimmo 2004).

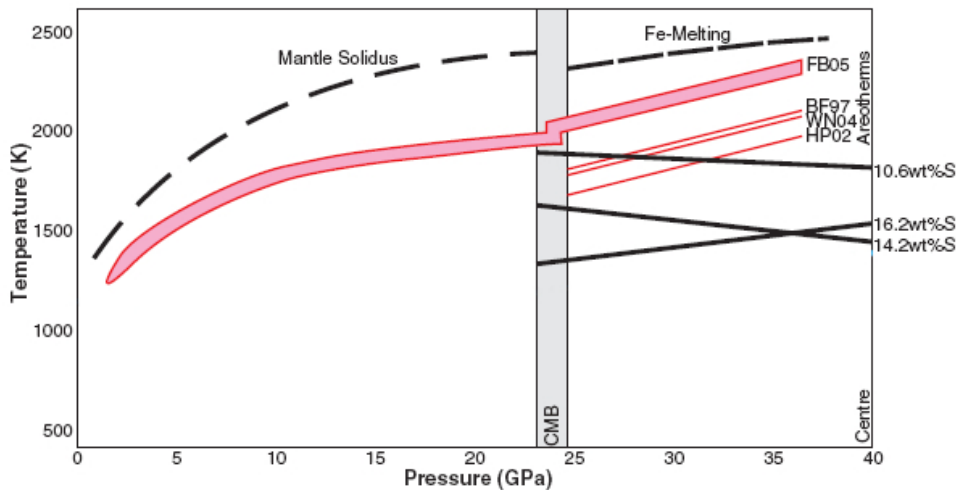


Figure 1.5: Model of the Martian thermal gradient - Core-mantle boundary (CMB) after Fei and Bertka (2005), thermal gradients (areotherms) after Fei and Bertka (2005)(FB05); black solid line - temperatures of liquidus loop intersections for sulfur contents of the core (Stewart et al. 2007); red solid lines - core areotherms of Bertka and Fei (1997)(BF97), Williams and Nimmo (2004)(WN04), Hauck and Phillips (2002)(HP02)

1.2 Earth's and Mars' mineralogical structure

Figure 1.5 shows a recent thermal gradient of the Martian interior, which supports an areotherm similar to the thermal gradient indicated by line b in figure 1.4b. On the basis of the current mineralogical structure of Mars (Bertka and Fei 1997), the Martian upper mantle is interpreted to be dominated by olivine (58%) and minor fractions of ortho- and clinopyroxene (18 and 14%) as well as garnet (10%). At ~ 10 GPa, corresponding to 800 km depth, orthopyroxene (opx) enters as the majorite-component into the garnet (gt). Olivine (ol) transforms to its high pressure polymorph wadsleyite (wd) at 14 GPa. With increasing pressure up to 17 GPa, wadsleyite transforms to ringwoodite (rw) and clinopyroxene (cpx) enters the garnet structure by creating majoritic-garnet (Maj). According to the model of Bertka and Fei (1997), the Martian mantle transition zone is composed of 50-60 wt% ringwoodite and 50-40 wt% majoritic garnet between 17 - 22 GPa (1300 - 1800 km depth). Both mineral phases transform to Mg-perovskite and magnesiowüstite at 22 GPa, forming a thin lower mantle (Figure 1.4).

1.3 Wadsleyite and Ringwoodite - Nominally Anhydrous Minerals in the Earth's and Martian transition zones

The mineral phases of the Earth's transition zone, such as wadsleyite and ringwoodite, came into special focus after Smyth (1987) showed that water can be accommodated in their structures. Smyth (1996) suggested that about 4 times the amount of present-day ocean water can be stored in the transition zone, if ringwoodite and wadsleyite were fully hydrated. The water is accommodated by certain cation substitution mechanisms, resulting in defect structures of the nominally anhydrous minerals (NAMs).

I. Wadsleyite

At 14 GPa and 1200°C, forsterite transforms to Mg_2SiO_4 -Wadsleyite, which has an orthorhombic structure, space group *Imma*. This transition corresponds right to the conditions for the 410 km discontinuity. Olivine with 20 mole% Fe_2SiO_4 transforms at about 13 GPa and 1600°C into a mixture of wadsleyite and olivine, with olivine Mg-richer than wadsleyite. Along the Mg_2SiO_4 - Fe_2SiO_4 solid solution, with an increasing Fe_2SiO_4 fraction > 40 mole % Fe_2SiO_4 , wadsleyite becomes instable and olivine transforms to a mixture of olivine and ringwoodite (Figure 1.6). The maximum iron content of wadsleyite is about 40 mole% Fe_2SiO_4 at Earth's geotherm conditions (~ 13 GPa and $\sim 1700^\circ\text{C}$, Figure 1.6). The crystal structure of wadsleyite consists of three octahedral sites with alternating M1 and M2 edge-sharing octahedra stacked along the b-axis and M3 double chains parallel to the a-axis. Octahedra-chains are corner-linked to Si_2O_7 -dimers parallel to the b-axis (Figure 1.7). The iron-substitution in wadsleyite occurs preferentially in the M1 and M3 octahedral site while Fe is depleted in M2 octahedral sites (Finger et al. 1993). Potential hydration sites of Mg-wadsleyite are possible for all oxygen atoms. Hydroxyl ions are highly disordered in wadsleyite with >0.8 wt% H_2O and occupy at least 14 distinct atomic environments (Kohn et al. 2002). Four potential hydration positions can be assigned for wadsleyite with lower water content (<0.8 wt% H_2O), connected to O1, O2, O3 and O4 sites. Hydration of wadsleyite is mainly arranged by protonation of the O1 atom of the M3 site (Figure 1.7), an unusual non-silicate oxygen atom, which is charge balanced by cation vacancies, mainly by Mg-vacancies (M3 site) and

subordinately by Si-vacancies. Full hydration of the O1 site corresponds to a theoretical water content of up to 3.3 wt% H₂O (Smyth 1987; Smyth et al. 1997). The O2 oxygen atom is also a possible protonation position with two potential hydrogen sites (Downs 1989). Further possible sites for hydrogen are the O3 and O4 oxygen atoms if nearby Mg-sites are vacant (Ross et al. 2003). Synthesised Mg₁₀₀-wadsleyite contains up to 3.1 wt% H₂O (Inoue et al. 1995), whereas Fe₉₀-wadsleyite accommodates up to 2.4 wt% H₂O (Kohlstedt et al. 1996). In addition, ordering of vacancies with divalent cations and Si in two non-equivalent M3 octahedral sites may lead to a deviation from orthorhombic symmetry resulting in a monoclinic structure of hydrous wadsleyite, space group *I2/m* (Smyth et al. 1997). However, Smyth et al. (1997) suggested that this monoclinic structure of hydrous wadsleyite is limited to an iron content of <8 mole% Fe₂SiO₄, thus the orthorhombic structure of hydrous wadsleyite, space group *Imma*, is more likely in iron bearing systems like Earth and Mars (Figure 1.8). Smyth and Kawamoto (1997) reported a second structure for hydrous Fe₉₀-wadsleyite, wadsleyite II, with orthorhombic *Imma* structure. Unit cell parameters as a- and c-axes are similar to wadsleyite while the b-axis is 2.5 times that of wadsleyite (~29 Å). Wadsleyite II contains up to 2.8 wt% H₂O, and was synthesized at 18 GPa and 1400°C (Smyth and Kawamoto 1997).

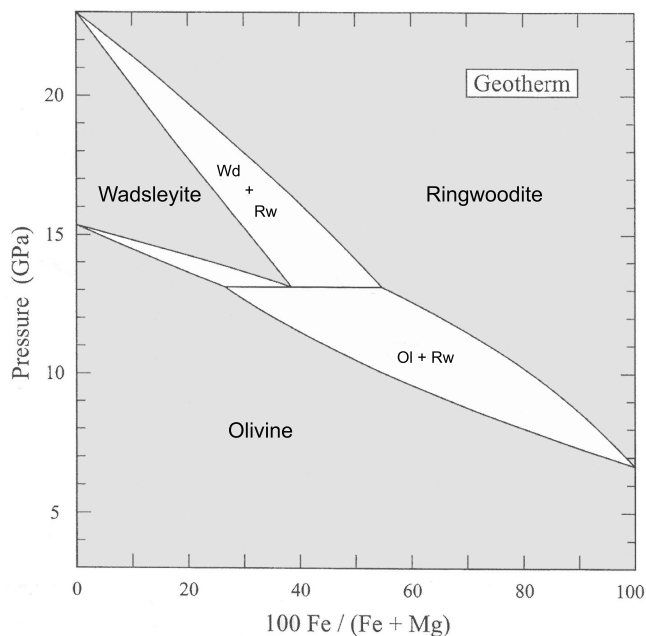


Figure 1.6: Pressure-composition diagram of the Mg₂SiO₄-Fe₂SiO₄ solid solution at geotherm conditions - (Gasparik 2003).

1. INTRODUCTION

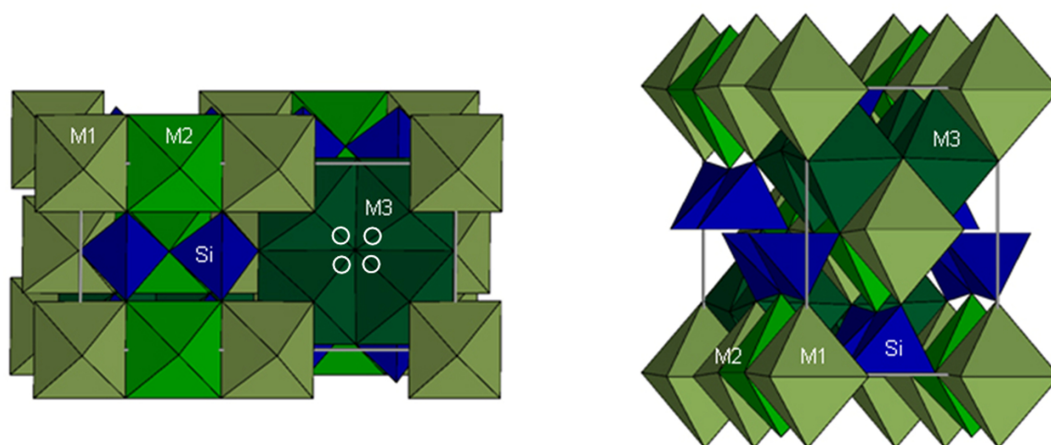


Figure 1.7: Hydrous Mg-wadsleyite - orthorhombic *Imma* structure, with three octahedral sites M1, M2 and M3 as well as tetrahedral site Si; left - c-axis normal to paper plane with a-axis vertical and b-axis horizontal (in paper plane), right - c-axis vertical and a-b plane horizontal; white circles indicate protonation of the O1 site of M3 double chains (Smyth 2006).

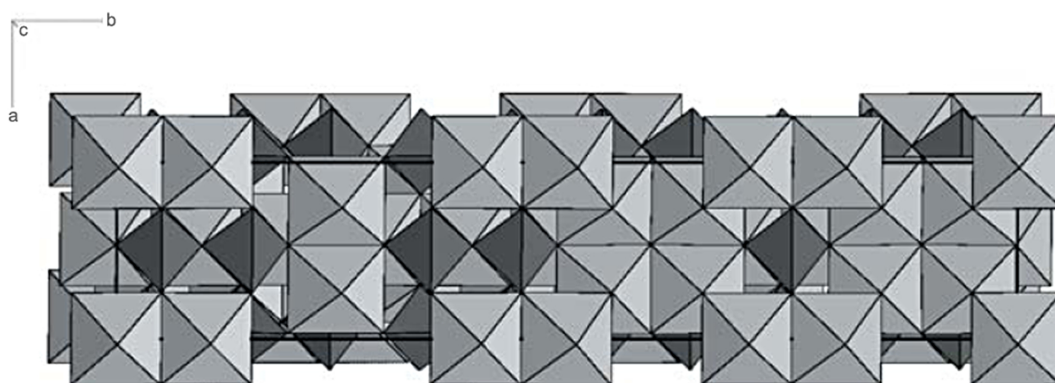


Figure 1.8: Hydrous wadsleyite II - orthorhombic *Imma* structure with a- and c-axes similar to wadsleyite, b-axis is 2.5 times that of wadsleyite ($\sim 29 \text{ \AA}$) and contains isolated SiO_4 as well as Si_2O_7 groups (Smyth 2006).

II. Ringwoodite

Ringwoodite the highest pressure polymorph of olivine, has a cubic normal spinel structure, space group $Fd\bar{3}m$, with one distinct crystallographic site for each element. The ringwoodite structure is build up by sequences of OT-layers (MgO_6 octahedron and SiO_4 tetrahedron) and O-layers (MgO_6 octahedron) stacked along the [111] direction (Figure 1.9). The oxygen atoms are arranged in cubic close packing (ccp) with silicon occupying the tetrahedral interstitial site and magnesium the octahedral interstitial site, respectively (Blanchard et al. 2009). The wadsleyite to ringwoodite transformation occurs at 20 GPa and 1600°C for the Mg-endmember composition. Ringwoodite forms a solid solution between the Mg- and Fe-endmember. With increasing iron fraction along the Mg_2SiO_4 - Fe_2SiO_4 solid solution the transformation pressure for ringwoodite is shifted toward lower pressure (see also Koch et al. 2004). Hydrous Mg-ringwoodite possesses the same cubic structure $Fd\bar{3}m$ as the anhydrous analogue. Ringwoodite accommodates up to 2.7 wt% H_2O (Kohlstedt et al. 1996). The major protonation mechanism of Mg- and $(\text{Mg}_{0.89}\text{Fe}_{0.11})$ -ringwoodite are octahedral site vacancies (Smyth et al. 2003). However, hydration occurs for both octahedral and tetrahedral edges (Kudoh et al. 2000; Kohlstedt et al. 1996), while protonation of the fully occupied tetrahedral site requires partial occupancy of the tetrahedral site by magnesium, thus hydrous ringwoodite potentially shows Mg-Si disorder (Kudoh 2000; Smyth et al. 2004). Density functional theory calculations predict possible proton positions in hydrous Mg-ringwoodite (Blanchard et al. 2009) these include cation vacancies and Mg-Si disorder (Figure 1.10). Four defect configurations are suggested involving $[\text{V}_{\text{Mg}}(\text{OH})_2]^x$, Mg-vacancies with protons bound to opposite oxygen atoms of the vacancy, $[\text{V}_{\text{Si}}(\text{OH})_4]^x$, Si-vacancies with OH-bonds close to the tetrahedral edges, $[\text{Mg}_{\text{Si}}(\text{OH})_2]^x$, Mg-substitution for Si in the tetrahedral site compensated by two protons and $[\text{V}_{\text{Mg}}(\text{OH})_2\text{Mg}_{\text{Si}}\text{Si}_{\text{Mg}}]^x$, Mg-Si disorder with nearby Mg-vacancy causing protonation of two octahedral oxygen atoms.

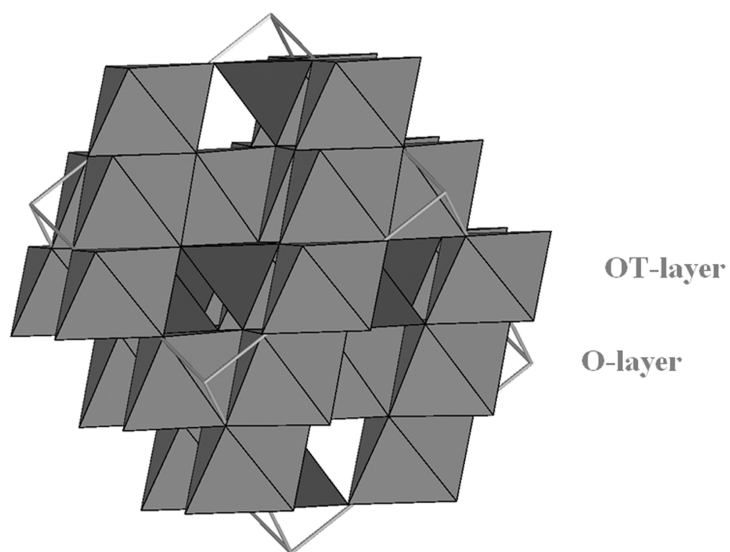


Figure 1.9: Ringwoodite structure - dark gray - Si-tetrahedron, gray - Mg-octahedron arranged in OT and O-layers stacked along [111].

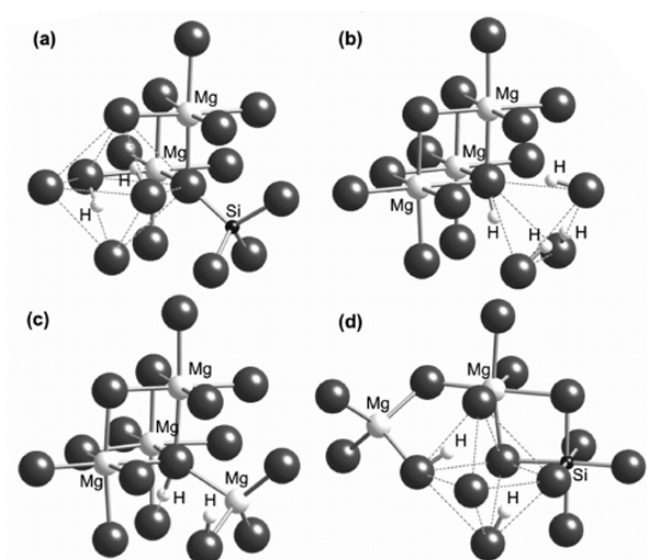


Figure 1.10: Possible proton positions in hydrous Mg-ringwoodite and associated defects - (a) $[V_{Mg}(OH)_2]_x$, (b) $[V_{Si}(OH)_4]_x$, (c) $[Mg_{Si}(OH)_2]_x$, (d) $[V_{Mg}(OH)_2Mg_{Si}Si_{Mg}]_x$; unlabeled atom denote oxygen atoms (Blanchard et al. 2009).

The density and compressibility of ringwoodite determine the characteristics of the lower part of the mantle transition zone e.g. compressional wave velocities (Figure 1.11). Anhydrous and hydrous Mg_2SiO_4 ringwoodites have been studied intensively using different techniques like Brillouin spectroscopy, ultrasonic interferometry and X-ray diffraction (Hazen 1993; Inoue et al. 1998; Jackson et al. 2000; Yusa et al. 2000; Li 2003; Sinogeikin et al. 2003; Wang et al. 2003; Jacobsen et al. 2004; Manghnani et al. 2005; Jacobsen and Smyth 2006). Jackson et al. (2000) and Li (2003) determined an isothermal bulk modulus, K_{T0} , of 185 GPa for dry Mg-ringwoodite using Brillouin spectroscopy and ultrasonic interferometry, respectively. Anhydrous iron-bearing ringwoodite with up to 10 mol% iron appears to have a slightly higher bulk modulus ($K_{T0} = 188(3)$ GPa) than the pure Mg-endmember (Sinogeikin et al. 2003), although given the uncertainties, the difference is negligible. Anhydrous pure iron-endmember ringwoodite measured in DACs shows a distinctly higher bulk modulus of 207(3) GPa (Hazen 1993). In contrast, hydrous Mg-ringwoodite with 2.3 wt% H_2O has a smaller isothermal bulk modulus with K_{T0} ranging between 155(4) and 165.8(5) GPa (Inoue et al. 1998, Wang et al. 2003a). Powder X-ray diffraction data of hydrous Mg-ringwoodite with 2.8 wt% H_2O also resulted in a significantly smaller bulk modulus of 148(1) GPa (Yusa et al. 2000). Isothermal bulk modulus of hydrous ferroan ringwoodite (~ 11 atom% iron) was determined using ultrasonic interferometry and powder X-ray diffraction and ranges from 175(3) to 177(4) GPa (Manghnani et al. 2005; Jacobsen et al. 2004; Jacobsen and Smyth 2006). Thus data suggests, that water and iron-substitution into ringwoodite has opposite effects on the compressibility.

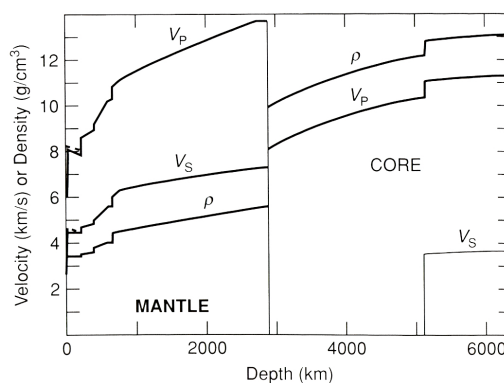


Figure 1.11: Preliminary Reference Earth Model - illustrating the density and seismic wave velocities as a function of depth (Anderson 2007 after Dziewonski and Anderson 1981).

1.4 Dense hydrous magnesium silicates (DHMS) - the Alphabet phases

At temperatures below the normal geothermal gradient dense hydrous magnesium silicates have been synthesised in high-pressure experiments (Figure 1.12). These phases are referred to as the “alphabet phases”. Alphabet phases may play an important role for water transport into the mantle, if temperatures in subducted slabs are well below the geothermal gradient. In such a case, the phases called superhydrous B and phase D are most important for water transport into the transition zone and even into the lower mantle, because these hydrous phases show the highest pressure stability (Shieh et al. 1998). Therefore, superhydrous B (SHyB) and phase D are a focus of this study. However, SHyB and phase D form at ~ 16 GPa by transformation from other hydrous phases such as phase A. Therefore, phase A represents also an important component for the potential water transport in subduction slabs at lower pressures.

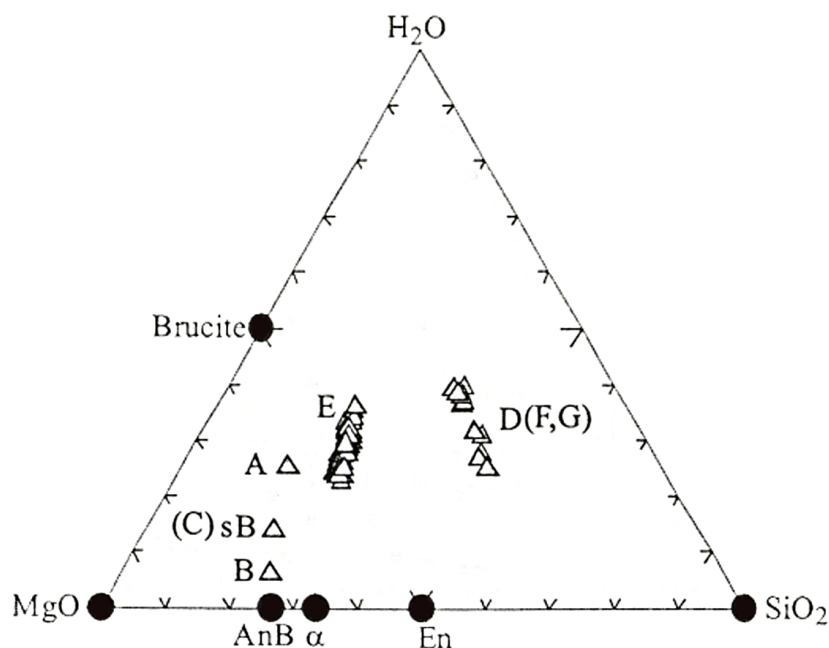


Figure 1.12: Molar ternary diagram of the dense hydrous magnesium silicates - showing compositions and their variations; abbreviations are AnB - anhydrous B, sB - superhydrous B, En - enstatite, α - olivine (Frost 1999).

I. Phase D

Phase D was first observed by Yamamoto & Akimoto (1977) and Liu (1986) in high-pressure studies of the MgO-SiO₂-H₂O system. The ideal formula of phase D is MgSi₂H₂O₆, but it can show variable compositions and water contents of 10-18 wt% H₂O (Yang et al. 1997). The crystal structure described by Yang et al. (1997) consists of hexagonal close packed oxygens (hcp) with silicon and magnesium occupying octahedral interstitial sites. Phase D has trigonal symmetry, space group $P\bar{3}1m$, with unit-cell parameter $a = 4.7453(4) \text{ \AA}$, $c = 4.3450(5) \text{ \AA}$ and $V = 84.74(2) \text{ \AA}^3$. SiO₆ and MgO₆ octahedra are arranged in two separate layers stacked along the c-axis. One layer is built up by edge-sharing SiO₆ octahedra to form a brucite-like layer, in which one of three octahedral sites is vacant. The second layer bridges between the SiO₆ layers and is made of MgO₆ octahedra, with two of three octahedral sites vacant. The MgO₆ octahedron is located above and below the vacancies of the SiO₆ layer (Figure 1.13). The O-H bonds occur exclusively in the MgO₆ layer. Phase D is stable from 15 up to 50 GPa (Frost & Fei 1998, Frost 1999) with a maximum thermal stability of 1300°C at 23 GPa (Ohtani et al. 2000) for the Mg₂SiO₄ + 15 wt% H₂O bulk composition.

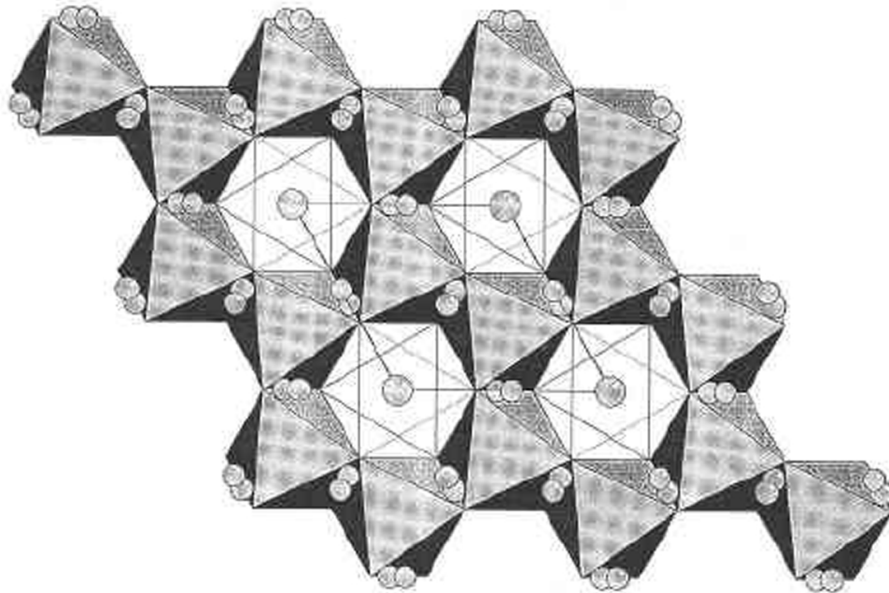


Figure 1.13: Crystal structure of phase D - view along c-axis; small spheres - Hydrogen-atoms, large spheres - Magnesium-atoms, shaded octahedron - SiO₆, unshaded octahedron - MgO₆ (Yang et al. 1997).

II. Superhydrous B

Superhydrous B (SHyB) was first observed by Gasparik (1990) and has been synthesised between 15 - 23 GPa and 800-1400°C. SHyB crystallises in the orthorhombic space group $Pnmm$, with the mineral formula $Mg_{10}Si_3H_4O_{18}$ containing 5.8 wt% H_2O , and unit-cell parameters $a = 5.0894(6) \text{ \AA}$, $b = 13.968(7) \text{ \AA}$ $c = 8.6956(2) \text{ \AA}$ and $V = 618.15 \text{ \AA}^3$ (Pacalo and Parise 1992). The structure consists of an ordered intergrowth of two layers alternating along the b-axis (Figure 1.14). One layer is made of Mg-octahedra and Si-tetrahedra, consequently called OT-layer. The other layer is called O-layer and is exclusively made up of Mg and Si in octahedral coordination. Two OT-layers are interconnected by one O-layer, while the H is located in the OT-layer bonded to the oxygen atoms around Mg (Pacalo and Parise 1992).

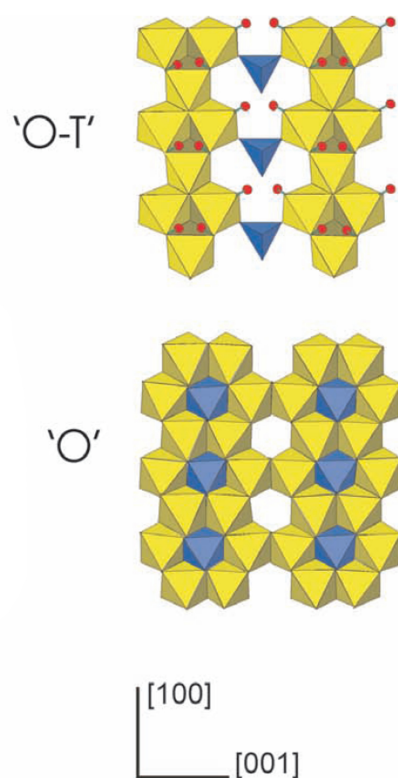


Figure 1.14: Crystal structure of superhydrous B - showing protonation (red spheres) of the OT-layer and O-layer with blue shaded Si-sites and yellow shaded Mg-sites (Crichton and Ross 2005).

III. Phase A

Yamamoto and Akimoto (1974) determined the mineral formula, $\text{Mg}_7\text{Si}_2\text{H}_6\text{O}_{14}$ (12 wt% H_2O), of a hydrous phase designated “phase A” by Ringwood and Major (1967). It crystallises in hexagonal space group $P6_3$, with unit-cell parameters $a = 7.8603(2) \text{ \AA}$, $c = 9.5730(2) \text{ \AA}$ and $V = 512.22 \text{ \AA}^3$ (Horiuchi et al. 1979). The stability field of phase A extends from 3-17 GPa with the maximum temperature of 1100°C at 11 GPa. The structure of phase A consists of slightly distorted ABCB packing of anions (O^{2-} and OH^-) with Mg occupying 50% of the octahedral sites and Si filling $1/14^{\text{th}}$ of the tetrahedral sites. Two distinct layers are stacked along the c -axis (Horiuchi et al. 1979). In the first layer one M(2) octahedron shows edge-sharing with another M(2) octahedron forming a M_3O_{13} group. These groups are linked to one another by the M(3) octahedron. The Si(1) tetrahedra is located in the interstices of this network sharing corners with M(2). The second layer is build up by M_3O_{13} groups of three edge-sharing M(1) octahedra (Figure 1.15). These groups are interconnected by sharing corners with Si(2) tetrahedra (Horiuchi et al. 1979). Kagi et al. (2000) identified two hydrogen positions connected to O2 and O4 positions in the M(1) layer of phase A.

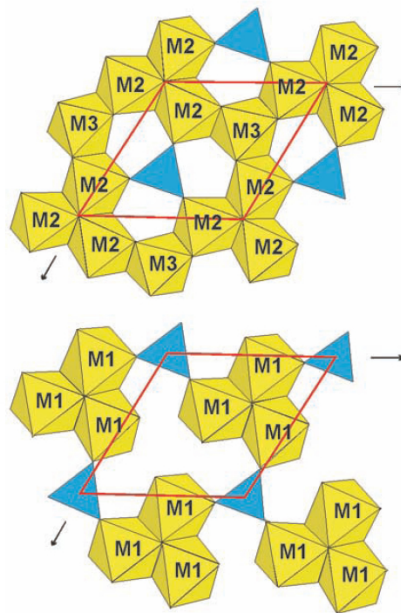


Figure 1.15: Crystal structure of phase A - two alternating layers along the c -axis: $\text{M}_2\text{M}_3\text{O}_{13}$ groups are centered around the edges of the unit cell (upper), blue shaded - Si-tetrahedra, yellow shaded - Mg-octahedra (Crichton and Ross 2005).

IV. Stabilities of Dense hydrous magnesium silicates

The pressure-temperature stability of superhydrous B and phase D depends on the water content of the bulk composition. Ohtani et al. (1995) and Kanzaki (1991) showed that phase D forms at pressures of 15 GPa for a $\text{Mg}_2\text{SiO}_4 + 20 \text{ wt}\% \text{ H}_2\text{O}$ bulk composition. The stability of phase D is shifted to higher pressure with decreasing water content of the bulk composition (Ohtani et al. 2000). The formation temperature of phase D decreases from $\sim 1400^\circ\text{C}$ to $< 600^\circ\text{C}$ between 19 and 24 GPa with decreasing water content of the bulk composition. Superhydrous B shows less variations of the stability and is stable at higher temperatures than phase D. Figure 1.16 shows the phase relations for the $\text{Mg}_2\text{SiO}_4 + 5 \text{ wt}\% \text{ H}_2\text{O}$, $\text{Mg}_2\text{SiO}_4 + 11 \text{ wt}\% \text{ H}_2\text{O}$ and $\text{Mg}_2\text{SiO}_4 + 15 \text{ wt}\% \text{ H}_2\text{O}$ bulk compositions as a function of pressure and temperature. The occurrence of phase D and superhydrous B based on experimental data is also plotted.

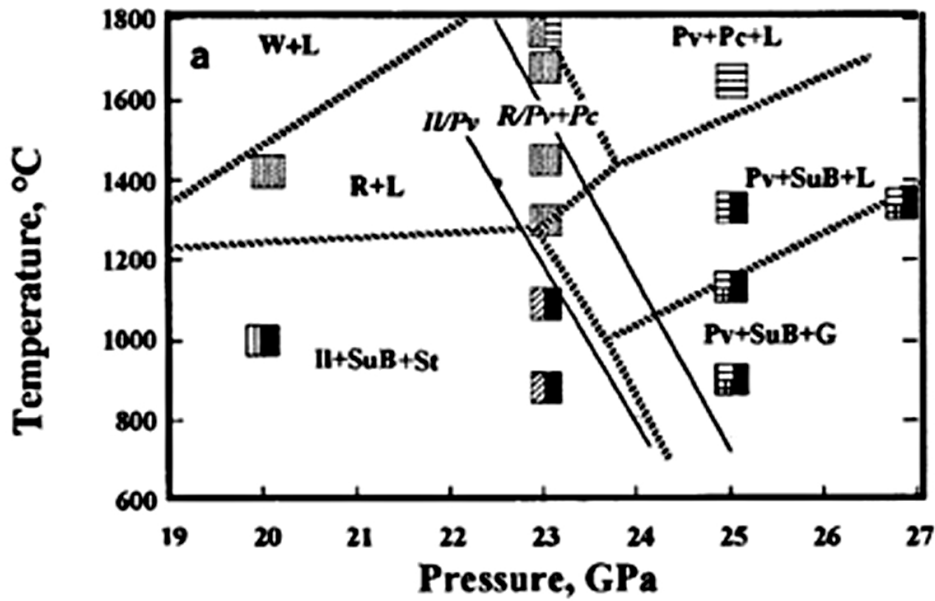


Figure 1.16: Phase relations for the $\text{Mg}_2\text{SiO}_4 + 5 \text{ wt}\% \text{ H}_2\text{O}$ (a), $\text{Mg}_2\text{SiO}_4 + 11 \text{ wt}\% \text{ H}_2\text{O}$ (b) and $\text{Mg}_2\text{SiO}_4 + 15 \text{ wt}\% \text{ H}_2\text{O}$ (c) bulk composition - abbreviations are L - liquid, E - phase E, St - stishovite, Pv - perovskite, R - ringwoodite, W - wadsleyite, Pc - periclase, Il - ilmenite, G - phase D (also referred to phase G/F), SuB - superhydrous B and Bc - brucite (from Ohtani et al. 2000).

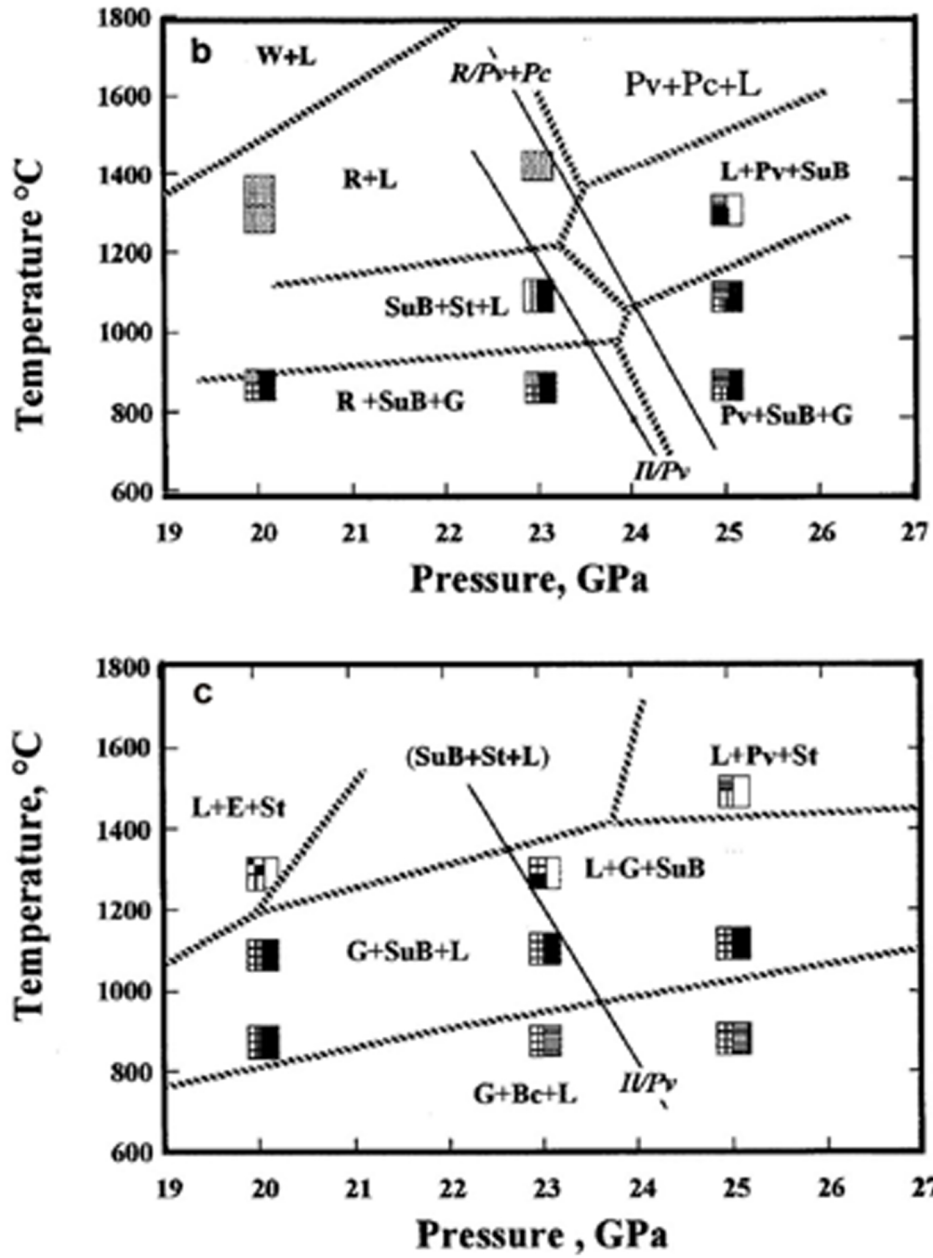


Figure 1.16 (continued)

1.5 Motivation

Wadsleyite and ringwoodite, the high pressure polymorphs of olivine, are supposed to be the most abundant mineral phases in the Earth's mantle transition zone. Both minerals have been studied intensively due to their potential importance for the global water cycle. Although ringwoodite and wadsleyite are nominally anhydrous minerals, they are able to accommodate up to 2.4 - 3.3 wt% H₂O (Kudoh et al. 1996; Kohlstedt et al. 1996; Smyth et al. 2005), implying that Earth's transition zone has an enormous water storage capacity.

Present knowledge about mineral properties and crystallographic details, however, are based on experimental data obtained on magnesium-rich or pyrolytic compositions relevant for the Earth. Comparably little is known about phases, their stabilities and water contents in iron-rich systems that are more relevant for planet Mars. As previously mentioned, wadsleyite shows a limited stability with increasing Fe₂SiO₄-fraction, however the incorporation of Fe³⁺ stabilises wadsleyite to iron-richer compositions. This effect of the valence state of iron on the stability of spinelloid phases was studied by Koch et al. (2004). An increasing iron-fraction lowers transformation pressures, i.e. the transition from upper mantle to transition zone, as well as the seismic discontinuity, would be located at shallower depth in iron-rich planetary systems. The transition zone-lower mantle boundary remains unchanged with increasing Fe₂SiO₄-fraction. Thus, the transition zone would be extended for iron-rich mantles, which leads to larger amounts of water that may be stored in the associated transition zone.

The primary aim of this thesis is to address three different effects of iron on nominally anhydrous transition minerals and dense hydrous magnesium silicates: [1.] A set of experiments was conducted on MgFeSiO₄+H₂O bulk composition in order to study the effect of iron on the structure of nominally anhydrous mineral phases and their water storage capacity. As reported for hydrous wadsleyite, iron-rich compositions can result in the formation of superstructures such as wadsleyite II. Thus, structural microanalyses using transmission electron microscopy were aimed at the exploration of potential superstructures of ringwoodite, or wadsleyite with iron-rich compositions. The stabilisation of mineral phases to higher pressure and temperature may relate to structural features of superstructures such as octahedral silica, as suggested by Smyth and Kawamoto (1997). Furthermore, iron and particularly ferric iron affects the stability of mineral phases in respect of transformation pressures and compositions in case of wadsleyite, as mentioned before. Thus, an important

part of this study is the determination of the effect of iron on the stabilities of dense hydrous Mg-Fe silicates.

[2.] Because the actual position of the upper mantle - transition zone boundary and the presence of a lower mantle in a hydrous Martian interior are still uncertain, a second set of experiments was performed with simple hydrous Mars-like bulk composition. These experiments were aimed at the synthesis of hydrous Martian mantle silicates using the thermal model of Fei and Bertka (2005). The synthetic hydrous mineral phases represent the basis to estimate the potential water storage capacity of a hydrous Martian mantle and to derive the mineralogical structure of a hydrous Martian interior. The effect of hydration on the Martian mantle structure can be estimated from such model, for which derivation mass balance calculations are used. Dense hydrous Mg-Fe silicates are high-pressure phases stable at lower temperatures and represent important components of planetary water cycles as reported for the Earth. Because Earth-like subduction is absent on Mars, element partitioning between mantle mineral phases and coexisting melt was used to estimate the potential presence of DHMS in the Martian interior.

[3.] High-pressure and high-temperature experiments yield fundamental knowledge on physical properties of mineral phases in Earth's interior such as density and compressibility. These properties are essential to understand mantle dynamics and to interpret seismic data. Water and iron substitutions into the ringwoodite structure appear to have opposite effects on its compressibility. Therefore, to constrain better the results, a single-crystal X-ray diffraction compressibility study was performed at room temperature using well-characterized ringwoodite samples having different iron and H concentrations. Knowledge of the effect of iron on the compressibility of ringwoodite is particularly important for the interpretation of the structure of iron-rich planetary mantles like Mars.

1.6 Aims of the study

The overall aim of this study is to evaluate how much water can be stored in the Martian interior, and whether DHMS could exist in the Martian mantle. To accomplish this, the following items were investigated:

(1) To experimentally determine the effect of iron on hydration mechanisms, and water contents of nominally anhydrous minerals (NAMs) and dense hydrous magnesium silicates (DHMS), unpolarised infrared spectroscopic analyses of NAMs and microprobe analyses of dense hydrous Mg-Fe silicates were carried out. The related crystal chemistry plays a crucial role in terms of the hydration mechanisms. The ferric iron content is determined using electron energy-loss spectroscopy in order to evaluate its effect on the water contents.

(2) Understanding the phase stabilities and structures related to the iron and water substitutions is essential for the interpretation of geophysical observations and planetary dynamics. The determination of the phase stabilities of NAMs and DHMS were made by performing two series of high pressure and high temperature experiments. By using a simple $\text{MgFeSiO}_4 + \text{H}_2\text{O}$ system the general effect of iron on phase stabilities was estimated. A simple Martian mantle composition was used to relate these findings to a planetary system. Structural properties were assigned by structure refinements and transmission electron microscopy analyses.

(3) Single-crystal x-ray diffraction experiments are performed to determine the effect of iron on the compressibility of hydrous ferroan ringwoodite. This knowledge is important for the interpretation of seismic data and the determination of the density of ringwoodite under mantle conditions.

(4) To determine element partitionings between mineral phases and melts, microprobe analyses were made. Element partitioning data are an indicator for favoured cation substitutions, and essential to interpret chemical compositions of coexisting mineral phases.

Chapter 2

Multi anvil technique - Sample synthesis

Samples were synthesised using two stage 6/8-Kawai type multi anvil presses at Bayerisches Geoinstitut, University of Bayreuth. During high P-T experiments, near-hydrostatic conditions are generated by 3 outer steel anvils located in each of the two guide blocks, which apply forces to 8 tungsten carbide cubes (Figure 2.1). These cubes have corner truncations to form an octahedral cavity, in which a Cr₂O₃-doped MgO pressure medium is placed. The Cr₂O₃-doped (5% Cr₂O₃) MgO-octahedra contain the furnace assembly, the thermocouple and the sample. The octahedron size corresponds to the corner truncations of the WC cubes for a particular assembly, which is chosen according to the desired pressure. Octahedra sizes and corner truncations of the WC cubes for the certain assemblies as well as the maximum reachable pressures are given in Table 2.1. The heating furnace inside the octahedron is made of LaCrO₃. The heater is surrounded by an insulating ZrO₂ sleeve, to avoid reactions of the various units during the experiments. In case of the 18M and 14M assembly this lanthanum-chromate heater is stepped in order to decrease the thermal gradient in the sample capsule. The electrical contact between the furnace and the WC cubes is established with a molybdenum disk and ring at the bottom and top of the furnace, respectively. Magnesium oxide sleeves separate the sample capsule and the thermocouple from the resistance heater.

2. MULTI ANVIL TECHNIQUE

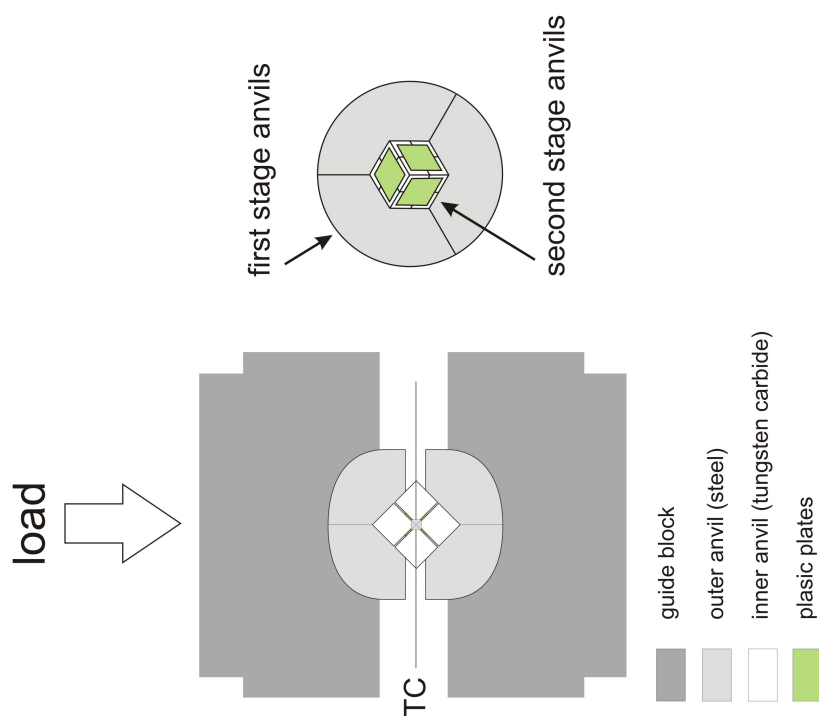


Figure 2.1: Schematic configuration and two stage principal of multi anvil technique - vertical view along piston movement of the press (right), horizontal perspective (left).

During experiments, temperature is monitored by a thermocouple, placed lengthwise inside the furnace in direct contact with the top of the sample capsule. Temperature measurements are accomplished by utilising the Seebeck effect which occurs when two distinct metallic conductors form a closed circuit and the two junctions between the two metals are maintained at different temperatures. This causes an electrical current to flow which is an indicator of the temperature. The thermocouple consists of two wires ($W_{97}Re_3$ and a $W_{75}Re_{25}$ wires 0.13 mm \varnothing for 10/4, 10M and 14M or 0.25 mm \varnothing for 18M), which reside in the 4-hole alumina sleeve and bent at one side to create a junction, which is in contact with the sample capsule. A schematic illustration of the assembly is shown in Figure 2.2.

Table 2.1: Multi anvil assemblies used in this study.

assembly	WC cube	octahedron	max. pressure
	corner truncation	edge length	[GPa]
18M	11 mm	18 mm	12
14M	8 mm	14 mm	16
10M	5 mm	10 mm	20
10/4	4 mm	10 mm	24
7/3	3 mm	7 mm	26

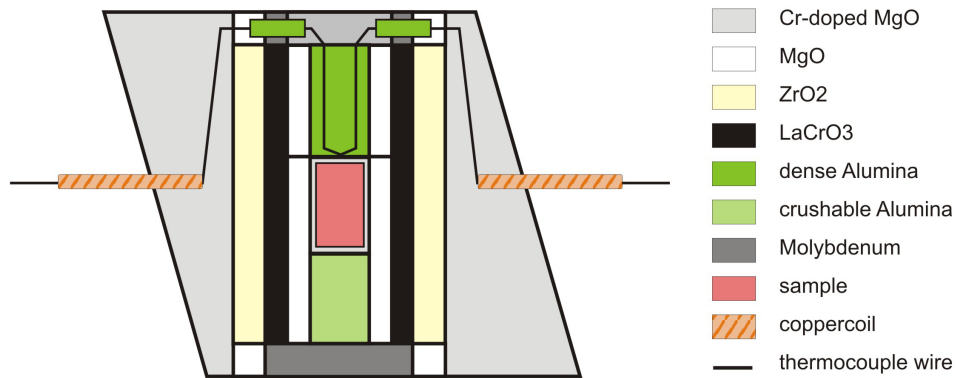


Figure 2.2: Schematic cross section of the 10/4 octahedron - illustrating the different elements of the assembly.

Three gaskets made of pyrophyllite surround each truncation of the WC-cubes, which point toward the octahedral cavity in order to seal the high-pressure region. The WC-cube faces are isolated by card board and teflon tape, which also support the gaskets during pressurisation. These gaskets play an important role in terms

2. MULTI ANVIL TECHNIQUE

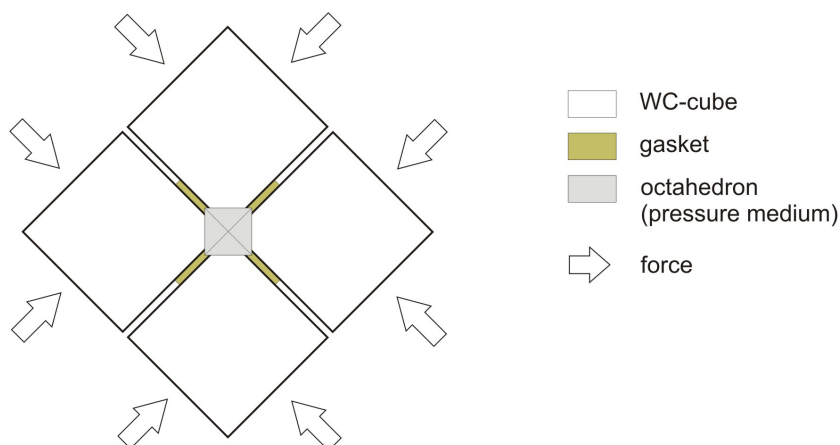


Figure 2.3: Schematic illustration of the Multi anvil principal - indicating the position of the crucial gaskets between the Tungsten-Carbide (WC) cubes are indicated.

of pressure generation since the pyrophyllite will extrude while the WC-cubes move closer together under the applied force (Figure 2.3). This extrusion leads to frictional loss of force and limits the maximum pressure for the particular assemblies (Table 2.1). These effects in combination with the influence of thermal expansion in the assembly determine the effective pressure in the octahedral assembly, which is defined by pressure calibrations. The pressure calibration as a function of applied load and temperature is done using phase transformations at well known pressure / temperature conditions, which were obtained in separate calibration experiments. According to the octahedral assembly and their maximum pressure, respectively, different phase transformations are applied (Table 2.2). As an example, to calibrate the 10/4 assembly the following three phase transformations are used: forsterite to wadsleyite at 1600°C (Morishima et al. 1994), wadsleyite to ringwoodite at 1600°C (Suzuki et al. 2000) and ringwoodite to perovskite plus periclase at 1600°C (Fei et al. 2004b). However, the inaccuracy of the pressure calibration is about 1 GPa. Further information of multi-anvil devices is given by Keppler and Frost (2005).

Table 2.2: Pressure calibration for multi anvil technique (Keppler and Frost 2005)

assembly	phase transformation	reference
18M	quartz - coesite	
	coesite - stishovite	Zhang et al. (1996)
14M	coesite - stishovite	Zhang et al. (1996)
	forsterite - wadsleyite	Morishima et al. (1994)
10M	forsterite - wadsleyite	Morishima et al. (1994)
	wadsleyite - ringwoodite	Suzuki et al. (2000)
10/4	forsterite - wadsleyite	Morishima et al. (1994)
	wadsleyite - ringwoodite	Suzuki et al. (2000)
	ringwoodite - perovskite+periclase	Fei et al. (2004b)
7/3	forsterite - wadsleyite	Morishima et al. (1994)
	wadsleyite - ringwoodite	Suzuki et al. (2000)
	ringwoodite - perovskite+periclase	Fei et al. (2004b)

Chapter 3

Characterisation methods

3.1 Electron probe micro analyses and Raman spectroscopy

Electron Probe Micro Analyses

Chemical analyses were carried out by the electron probe microanalysis technique using a JEOL JXA-8200 electron microprobe at Bayerisches Geoinstitut and CAMECA SX-50 at the Institute of Geoscience / University of Jena. Sample GG 2542 was remeasured with both facilities to verify the data reproducibility, which yielded identical results. Thus, obtained results are comparable even though the sample was measured with two microprobes. Recovered sample capsules were cut into halves and mounted in epoxy-resin. The polished sample surface was carbon coated up to 10 nm thickness in order to avoid charging effects during measurements. Accurate chemical compositions of the mineral phases were quantified by wavelength dispersive analysis (WDX). Acceleration current and high voltage was set to 20 nA and 15 kV for calibration and measurements with counting rates of 20/10 seconds for sample and background, respectively.

Each element such as magnesium, iron, aluminium and silicon was calibrated on an adequate standard (Table 3.1). Movable analyser crystals located in the spectrometer separate the wavelengths of the characteristic x-rays, which are generated by the interaction of the electron beam with the elements in the sample.

3. CHARACTERISATION METHODS

Table 3.1: Calibration and measurement details for microprobe analyses.

element	standard	Analyser crystal		Conditions		Counting time [sec]	
		JEOL	CAMECA	current	HV	peak	background
Si	diopside	PETH	TAP	20 nA	15 kV	20	10
Mg	diopside	TAP	TAP	20 nA	15 kV	20	10
Fe	hematite						
	fayalite (CAMECA)	LIF	LIF	20 nA	15 kV	20	10
Al	spinel	TAP	—	20 nA	15 kV	20	10

LIF - lithiumfluoride $2d = 4.027 \text{ \AA}$
TAP - thallium-acid-pthalate $2d = 25.76 \text{ \AA}$
PET - pentaerythritol $2d = 8.742 \text{ \AA}$

The analyser crystals diffract those characteristic x-rays onto the detector that satisfy the Bragg' equation (3.1):

$$n\lambda = 2d\sin\theta \quad (3.1)$$

with λ -wavelength, d -interplaner spacing, θ -bragg angle.

Sample, analyser crystal and detector are interconnected by the Johannson geometry, where these three components are located upon the Roland circle (Figure 3.1). Thus, wavelengths relevant for measurements are selected and finally collected in the detector (gas detector). Since the Bragg' angle θ range is restricted mechanically to $25 - 130^\circ$ different analyser crystals with distinct interplanar d -spacings are employed to measure the concentration of elements, depending on their atomic number (Figure 3.2). Several corrections such as dead time, background and interference correction are required for quantitative analyses, which are applied to the raw intensities. The matrix effects, which depend on the sample composition, have to be corrected to achieve accurate measurements (ZAF correction; Z - atomic number, A - absorption, F - fluorescence).

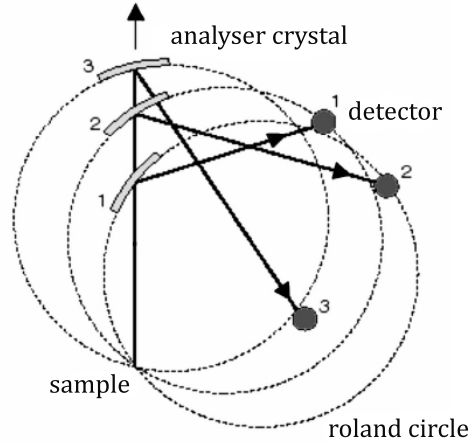


Figure 3.1: Spectrometer geometry for wavelength dispersive x-ray analysis (Johansson geometry) - moveable analyser crystal and detector are located on the imaginary roland circle and create different diffraction conditions in order to filter certain x-ray radiation (from Williams 1987).

	2d (nm)	6 C	14 Si	22 Ti	30 Zn	38 Sr	46 Pd	54 Xe	62 Sm	70 Yb	78 Pt	86 Rn
TAP	2.576	⁸ O	¹⁵ P	²⁴ Cr	⁴¹ Nb	⁴⁶ Pd	⁷⁹ Au					
TAPH	2.576	⁹ F	¹³ Al	²⁴ Cr	³⁵ Br	⁴⁷ Ag	⁷⁰ Yb					
PET	0.8742		¹³ Al	²⁵ Mn	³⁶ Kr	⁶⁵ Tb	⁷⁰ Yb					
PETH	0.8742		¹⁴ Si	²² Ti	³⁷ Rb	⁵⁶ Ba	⁷² Hf					
LIF	0.4027			¹⁹ K	³⁷ Rb	⁴⁸ Cd						
LIFH	0.4027			²⁰ Ca	³¹ Ga	⁵⁰ Sn	⁷⁹ Au					

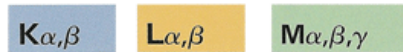


Figure 3.2: Range of the elements that can be analysed by the spectrometer crystals - (reference: JEOL); $K\alpha$ radiation of the elements were used for the quantitative measurements.

Raman spectroscopy

In addition to the chemical analyses, sample characterisation and phase identification were also carried out by Raman spectroscopy using a Jobin-Yvon LABRAM-Raman spectrometer equipped with Olympus BX40 microscope and CCD detector. Measurements were conducted with visible laser (632 nm) to distinguish the polymorphs olivine, wadsleyite and ringwoodite as well as garnet, majorite and pyroxenes. The obtained spectra were compared with reference data provided by databases (RRUFF) and literature data. Generally, samples require no special preparation for Raman spectroscopy, thus mainly the same samples as for microprobe analyses were used. Raman spectroscopy is based on the eponymous Raman-effect, i.e. scattering of incident monochromatic light, which changes energy due to inelastic scattering by vibrating molecular groups. Most of the incident light is scattered elastically without changing energy of the incident and emitted photons (Rayleigh scattering), whereas a fraction of the incident photons may gain or lose small amounts of energy because of inelastic scattering.

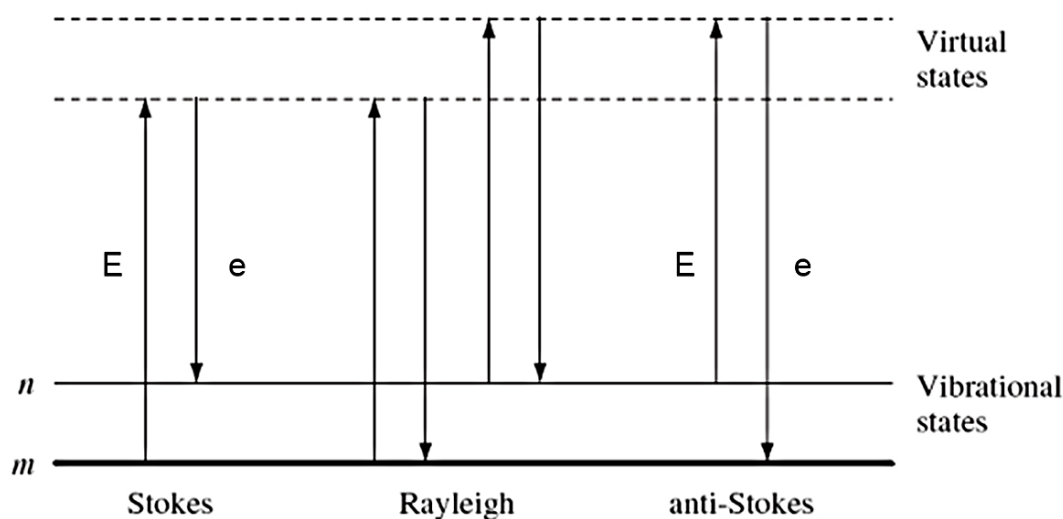


Figure 3.3: Schematic illustration of Raman scattering effect - (from W.E. Smith & G. Dent 2005); E - energy of the incident light, e - energy of the inelastic scattered light.

The change in energy corresponds to the difference of two energy levels of the vibration mode: 1. *stokes scattering* - the vibrational unit is excited to a higher virtual energy level due to interaction with incident photons, i.e. the electron cloud is deformed and polarised by interaction with photons, respectively. The short-lived excitation is followed by the return to the first excitation level n by emitting a photon with lower energy (higher wavelength) than the incident photon (E - energy of the incident light, e - energy of the inelastically scattered light). 2. *anti-stokes scattering* - the vibrational unit is in the first energy level state at the moment of the scattering event. The incident photons induce the excitation of the vibrational unit to another higher virtual energy level before the vibrational unit relaxes to the ground state m by emitting a photon, which is higher in energy, i.e. it has a shorter wavelength than the incident photons (Figure 3.3). The energy difference of incident light and the scattered light is expressed by the Raman shift, given in wavenumbers [cm^{-1}]. In vibrational spectroscopy, the vibration modes are classified in symmetric and asymmetric vibrations. Asymmetric vibrations are Raman inactive and symmetric vibrations are Raman active, when the polarisability, i.e. deformability of the electron cloud of the vibrational unit, changes during the excitation of the vibrational unit by the incident light. Various vibration modes give “fingerprints” of mineral phases expressed as typical Raman spectra.

3.2 Fourier transformed infrared spectroscopy analyses - FTIR analyses

The water contents in nominally anhydrous minerals were determined using Fourier transform Infrared Spectroscopy (BRUKER IFS 120 high resolution FTIR spectrometer with IR microscope equipped with a tungsten source). In a FTIR spectrometer, the generated near infrared radiation ($\lambda = 750 - 2500 \text{ nm}$) travels to the beam splitter of the Michelson-interferometer where 50% of the radiation is transmitted to a moveable mirror and 50% is deflected to a fixed mirror (Figure 3.4). After reflection at the particular mirrors the infrared radiation is recombined at the beam splitter and passes through the sample, while the unabsorbed infrared radiation is finally collected in the narrow-band MCT detector. A Si-coated CaF_2 beam splitter was used in case of water content determination.

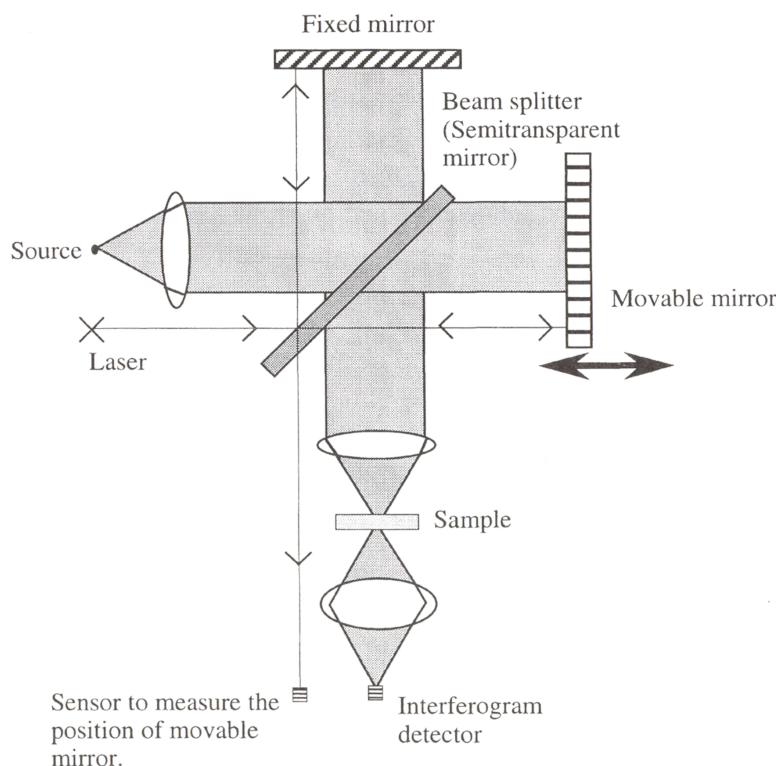


Figure 3.4: Schematic illustration of the Michelson interferometer of Fourier-transform infrared spectrometer - (from textbook "Near-Infrared Spectroscopy", Siesler, H.W., Ozaki, Y., Kawata, S. and Heise, M.H. (2002)).

3.2 Fourier transform infrared spectroscopy

Infrared radiation interacts with the sample and certain IR-frequencies are absorbed, which correspond to the frequencies of certain molecular vibrations. Different functional groups absorb different characteristic IR-radiation frequencies given in wavenumbers [cm^{-1}]. The OH-groups of hydrous minerals absorb in the range 3200 to 3700 cm^{-1} .

Measured samples were in form of single crystals (sample 3854 and 4218) or polished sample thin sections up to a thickness of 25-40 μm . The thickness of the sample including the glue-layer was measured for each sample using a micrometer gauge. For measurements, thin sections were removed from the glass with acetone. Thus, the thickness values of the samples are estimations and introduce a small error on the estimated water concentration values, since the absorption is thickness dependent as outlined in the Lambert-Beer law. The particular OH-groups in minerals such as ringwoodite might be oriented in different directions, thus the spectra of unpolarised measurements may not show the maximum absorption for OH-groups, if oriented inappropriate. Libowitzky and Beran (2004) pointed out that unpolarised infrared analyses may lead to different water concentrations in minerals due to constant absorbance with increasing thickness of the sample, which is contrary to the Lambert-Beer law. Such a discrepancy is evident for sample thicknesses >0.8 mm according to Libowitzky and Beran (2004). This influence was ruled out by using sufficiently thin samples (~ 30 μm thickness) so that absorbance and sample thickness correlate according to the Lambert-Beer law. During the measurements the single crystals or thin sections were placed on a CaF_2 plate. Different apertures were used for the measurements depending on the crystal size in order to avoid mixed analyses and to measure optically clean areas of the particular crystals. The determination of the water concentration of the mineral phases was done by the integration of the obtained absorption band in the region of 2000 to 3780 cm^{-1} applying the following formula (3.2) and the Paterson (1982) calibration (Figure 3.5):

$$C_{OH} = \frac{X_i}{150\zeta} \int \frac{K(\bar{\nu})}{(3780 - \bar{\nu})} d\bar{\nu} \quad (3.2)$$

The concentration of OH is given in ppm wt (parts per million weight); X_i is the density factor (Table 3.2); ζ is the orientation factor, which is 1/3 for unpolarised measurements; $K(\bar{\nu})$ is the absorption coefficient [cm^{-1}] for a given wavenumber.

3. CHARACTERISATION METHODS

The density factor is calculated after the formula $X_i = 10^6(18/2d)$, where 18 is the molar weight of water and d is the density of the mineral phase [g/l]. The correlation of OH-stretching frequency and absorption coefficient for ringwoodite is empirical so that water contents are estimations with accuracy probably between 30-50% (Kohlstedt et al. 1996).

Table 3.2: Density factor X_i for water concentration determination

	density [g/cm ³]	density [g/l]	density factor Xi
Fe,Mg-Ringwoodite	4.204	4204	2141
Fe-Ringwoodite	4.848	4848	1856
Mg-Ringwoodite	3.56	3560	2528
Mg _{1.5} Fe _{0.5} -Wadsleyite	3.83	3830	2350
Forsterite	3.22	3220	2795
Clinoenstatite	3.21	3210	2804
Stishovite	4.287	4287	2099

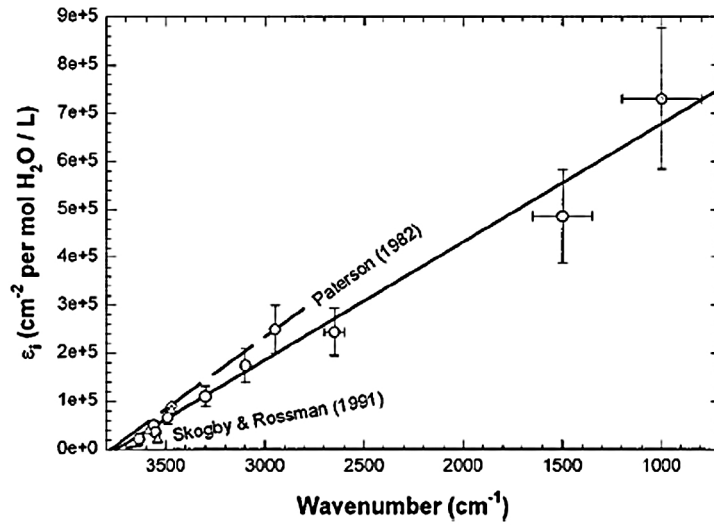


Figure 3.5: Correlation of the integrated molar absorption coefficient ϵ_i of OH stretching bands as a function of the wavenumber - (Libowitzky and Beran 2004).

3.3 Transmission electron microscopy and electron energy loss spectroscopy

Transmission electron microscopy (TEM) was used for the microstructural identification and characterisation of synthesised minerals. For TEM analysis, samples have to be thinned to electron transparency, i.e. to thicknesses in the order of less than 100 nm. The sample thinning was carried out by Argon milling using a GATAN dual ion mill 600. Thin sections of 25 - 50 μm thickness were first glued on 100 μm mesh Molybdenum grids. The grid was then ion-milled at an angle of 13-14° at 4.5 kV high voltage and 1 mA gun current. The milling duration varies with the constitution of the sample and takes around 15-20 hours for 25-30 μm thick samples (Figure 3.6, Figure 3.7). In case of sample GG 2580, GG 3854 and GG 4218 crystals were crushed to powder and placed as ethanol suspension on a holey carbon grid with 200 μm mesh (Lacey grid).

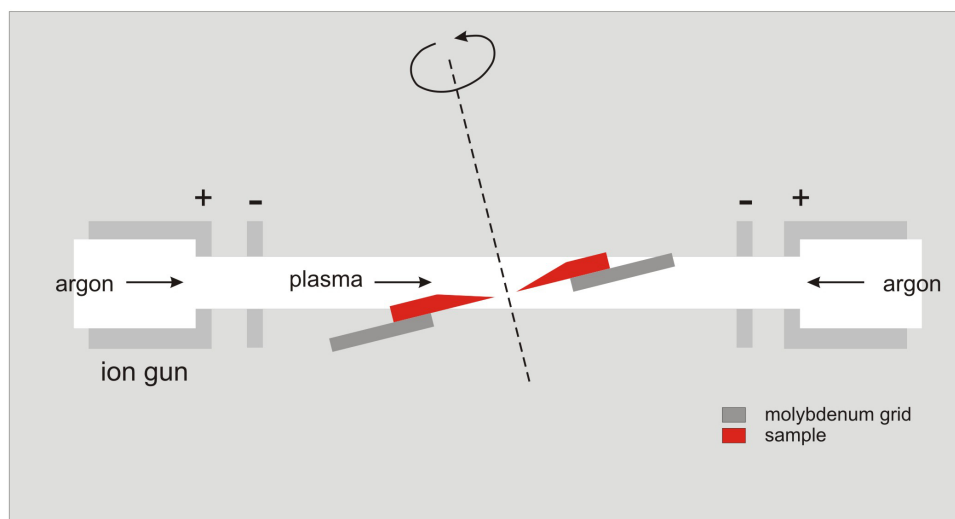


Figure 3.6: Schematic illustration of TEM sample preparation - Argon milling method.

After the milling procedure the samples were carbon coated to ensure electrical conductivity and thus to avoid charge effects during measurements. TEM observations and selected area electron diffraction (SAED) were carried out with a Philips CM20 FEG transmission electron microscope equipped with a GATAN parallel electron energy loss spectrometer (PEELS) 666. Electron diffraction was used to determine the symmetry and interplanar spacings, which is a fingerprint of mineral phases. Obtained diffraction patterns were evaluated by measuring the distances of the diffraction spots in reciprocal space, i.e. spot distances in the

3. CHARACTERISATION METHODS

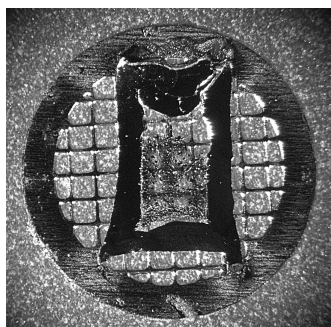


Figure 3.7: Prepared sample for TEM analyses - showing the transparent (wedge shaped) crystals in the middle of the sample capsule glued on molybdenum grid (3 mm \varnothing).

diffraction pattern. Interplanar spacings in real space were calculated applying the formula (3.3):

$$d = \frac{\lambda L}{R} \quad (3.3)$$

where d is the interplanar spacing in real space [\AA]; L is the distance between sample and photo plate; λ is the wavelength of the electrons and R is the distance of the diffraction spots in reciprocal space [mm]. The expression λL is called the camera constant. The calibrated camera constant for the TEM C20 is $\lambda L = 23.85$ with $\lambda = 0.0251$ nm and $L = 950$ nm. Diffraction patterns were indexed and identified by aid of the EDANA program 9.21 (Kogure, T. 2003) by comparison of measured and calculated diffraction spot distances in reciprocal space [mm] and real space [\AA]. For the calculation of diffraction patterns of relevant phases the lattice parameters listed in Table 3.3 were used. Electron diffraction spot distances in reciprocal space which reflect the interplanar distances in real space and even more the angle between sets of lattice planes $h_1k_1l_1$ and $h_2k_2l_2$ of the diffraction pattern are crucial for the determination of structures. Extinction of reflections (“forbidden reflections”) and double diffraction is an important issue concerning the comparison of measured and reference diffraction patterns. The systematic absence of certain reflections is called “forbidden reflections” or extinction of reflections due to destructive interference of scattered electron beams caused by particular crystallographic symmetry. Thick samples as well as strongly diffracting lattice planes, however, may cause the appearance of symmetrically forbidden reflections in the diffraction pattern. This so called “double diffraction” phenomena occurs when electrons are diffracted from one set of lattice planes and act as a primary electron beam for further diffraction from a second set of lattice planes. In order to verify the actual appearance of reflections in the diffraction

patterns, diffraction spots at conditions outside of zone axis were compared with visible reflections in zone axis conditions.

Table 3.3: Reference data used for TEM microstructural analyses and phase identification.

Mineral phase	Reference phase	Space group	Lattice parameter[Å]	Reference
Nominally anhydrous minerals				
Ringwoodite	Fe-ringwoodite	$Fd\bar{3}m$	a = 8.234 a = 5.711	Yagi et al. (1974)
Wadsleyite	Mg-wadsleyite	$Imma$	b = 11.467 c = 8.256	Finger et al. (1993)
Garnet	Pyrope	$Ia\bar{3}d$	a = 11.452	Armbruster et al. (1992)
	Majorite	$I4_1/a$	a = 11.501 c = 11.480	Angel et al. (1989)
	Majorite + 19 mole% Pyrope	$I4_1/a$	a = 11.480 c = 11.475	Heinemann et al. (1994)
Akimotoite	Mg-akimotoite	$R\bar{3}$	a = 4.728 c = 13.559 $\gamma = 120^\circ$	Horiuchi et al. (1982)
Dense hydrous magnesium silicates				
Phase D	Mg-phase D	$P\bar{3}1m$	a = 4.745 c = 4.345	Yang et al. (1997)
Superhydrous B	Mg-SHyB	$Pnmm$	a = 5.089 b = 13.968 c = 8.696	Pacalo & Parise (1992)
			a = 7.868	
Phase A	Mg-phase A	$P6_3$	c = 9.577 $\gamma = 120^\circ$	Kagi et al. (2000)
Oxides				
Magnesiowüstite	Wüstite	$Fm\bar{3}m$	a = 4.311	Hazen (1981)
Magnetite	Magnetite	$Fd\bar{3}m$	a = 8.394	Fleet (1981)

3. CHARACTERISATION METHODS

Interactions of the electron beam and a sample leads also to inelastic scattering events of the electrons whereby the electrons lose certain energy. This energy loss can be measured and corresponds to the energy which is approximately needed to ionise particular atoms in the sample. In case of iron, these electron energy-loss near-edge structure (ELNES) spectra provide information about the valence state. The ferric to total iron ratio was determined following the procedure described by van Aken (1998). It requires the integration over two energy windows of the L_3 and L_2 ionisation edges of iron. The intensity ratio of the L_3 and L_2 ionisation edge yields the ferric to total iron ratio. ELNES spectra were collected using an energy-loss spectrometer (Gatan PEELS 666). Depending on the ferric iron content, the obtained ELNES spectra show a strong double peak at 707.8 eV and 709.5 eV energy loss, which represents the ferrous and ferric iron maxima at the FeL_3 -edge, respectively. The peak shape of the FeL_3 -edge changes according to the relative abundance of ferric and ferrous iron, i.e. an equal ratio of Fe^{2+} and Fe^{3+} results in two equal peaks of the FeL_3 -edge (Figure 3.8).

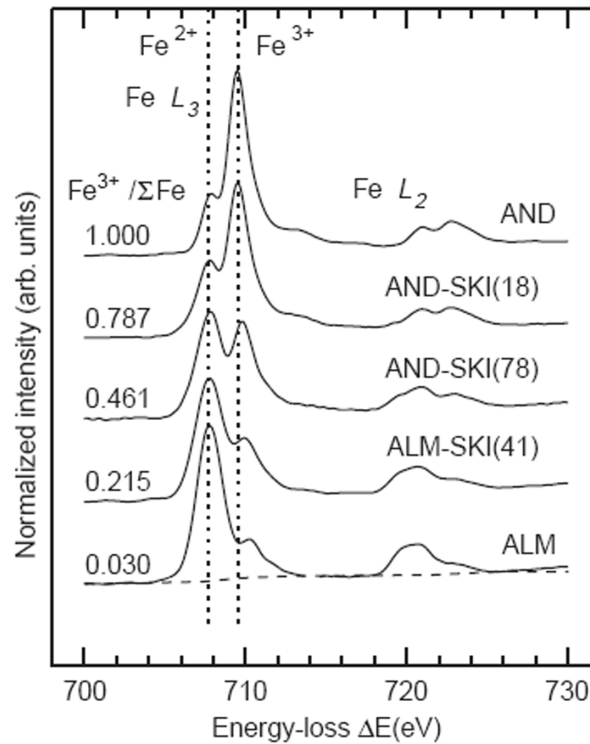


Figure 3.8: $FeL_{2,3}$ -edge Electron energy-loss near-edge structure (ELNES) spectra of natural a garnet - showing the shape of the Fe^{2+} and Fe^{3+} maxima of the FeL_3 -edge for different ferric to total iron ratios (van Aken 1998).

3.4 Single-crystal x-ray diffraction method

Precise determination of lattice parameters of minerals can be achieved by the single-crystal x-ray diffraction method. The basis for acquiring lattice-parameters of minerals is the Bragg law (3.4), which contains information about the parameters of the lattice and diffraction conditions:

$$n\lambda = 2d\sin\theta \quad (3.4)$$

with λ -wavelength of the incident x-ray, n - order of interference, d -interplaner distance, which is a function of the lattice parameter a , b , c , α , β , γ and θ -Bragg angle. Reflections which fulfill the conditions of the Bragg equation by constructive interference are detected and essentially required for orientation measurements and structure refinements. Combination of the diamond-anvil cell technique and single-crystal x-ray diffraction enables determinations of the lattice parameters as a function of pressure and the calculation of the equation of state of mineral phases.

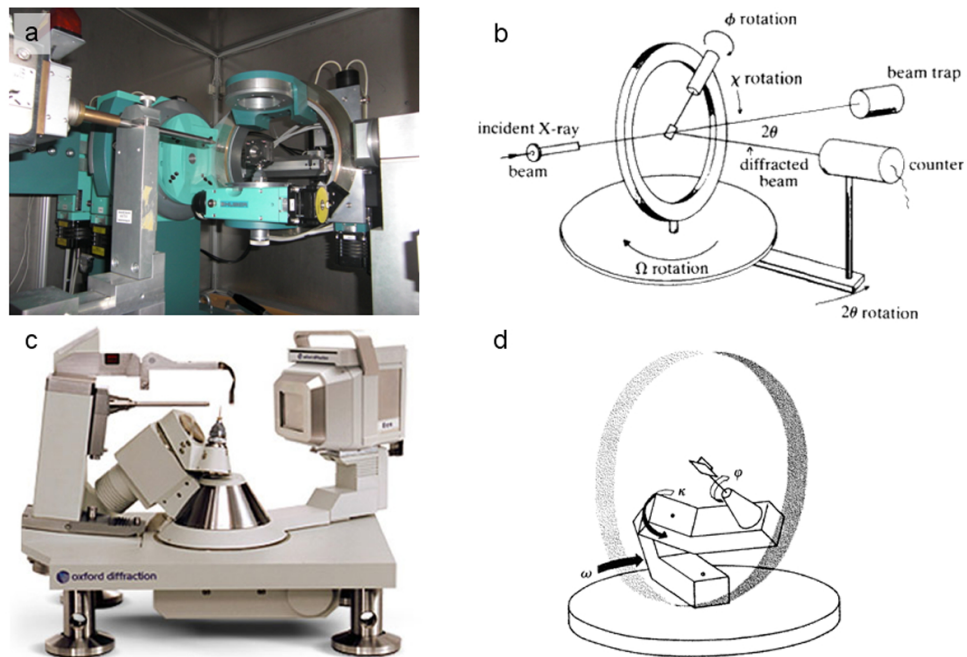


Figure 3.9: Single-crystal x-ray diffractometer - (a) Huber four-circle diffractometer (b) schematic illustration of four-circle diffractometer principle (c) Xcalibur diffractometer (Oxford Diffraction) (d) schematic illustration of diffractometer principle.

X-ray single-crystal diffraction at room pressure

Two ferroan hydrous ringwoodite single-crystals, one for each run-product were selected for the high-pressure X-ray diffraction experiments. Prior to the measurements in the diamond anvil cell, intensity data were collected at ambient conditions using an Xcalibur diffractometer equipped with a CCD detector and a graphite monochromator (Figure 3.9c,d). For measurements MoK α radiation operated at 50 kV and 40 mA was used. The single crystals were mounted on a glass fiber during x-ray single-crystal diffraction at room pressure. Combined omega and phi scans were chosen to obtain a coverage of half reciprocal sphere up to $2\theta_{\max} = 80^\circ$ for sample 4218 and up to $2\theta_{\max} = 90^\circ$ for sample 3854. The exposure time was 15 s/frame. Lorentz and polarization factors as well as an analytical absorption correction based on the crystal shape were taken into account for the correction of the reflection intensities using the CrysAlis package (Oxford Diffraction 2006). Structure refinements were performed based on F^2 (structure factor F_{hkl} , which is closely related to the intensity of the reflection it describes) using the SHELX97 program package (Sheldrick 1997) in the WinGX 1.70.01 System (Farrugia 1999) with space group $Fd\bar{3}m$ and anisotropic displacement parameters following a similar procedure as described by Smyth et al. (2003). Fully ionized scattering curves (Ibers and Hamilton 1974) were used for all cations. Since the cation occupancies of light elements like Si and Mg depends on the scattering curve used for oxygen, at the initial state of the refinements the distributed scattering factor of the oxygen atom between the atomic scattering curve and the scattering curve of O^{2-} (Tokonami 1965) was refined together with the cation occupancies. This procedure resulted in a similar scattering distribution for both samples of 50% O and 50% O^{2-} . This value was then fixed during the last cycles of refinements. The iron content from the microprobe analysis was constrained to be at the octahedral site. Mg and Si occupancies were refined at the octahedral and at the tetrahedral sites, respectively, without any constraint. Unit-cell parameters, data collection and refinement details, fractional atomic coordinates, equivalent thermal parameters, and polyhedral bond lengths obtained in this study are reported in Table 4.9.

High-pressure experiments

The two ringwoodite single crystals studied at room conditions and having dimensions: 120x100x30 μm (sample 3854) and 100x50x30 μm (sample 4218) were loaded into two diamond-anvil cells (DAC) with diamond culets of 600 μm in diameter (Figure 3.10). Steel gaskets preindented to 90 μm thickness with 250 μm \varnothing holes and a 4:1 mixture of methanol:ethanol as pressure transmitting medium were used. Ruby crystals were also loaded into the DACs for pressure determination (Mao et al. 1986) during the high-pressure experiments. Unit-cell parameters were measured as a function of pressure with a Huber four-circle single-crystal diffractometer equipped with a point detector and a graphite monochromator at the Bayerisches Geoinstitut operating with $\text{MoK}\alpha$ radiation at 50 kV and 40 mA. During data collection, the crystal is rotated in 4 angles, θ , ω , χ , ϕ in order to center the peak positions of the reflections (Figure 3.9 a,b). Peak positions were determined using the eight-position centering method (King and Finger 1979) in order to minimize experimental aberrations. Unit-cell parameters measured up to ~ 9 GPa were obtained using vector-least-square refinements (Ralph and Finger 1982). The unit-cell parameters of the hydrous ferroan ringwoodites at different pressures are given in Table 4.10.

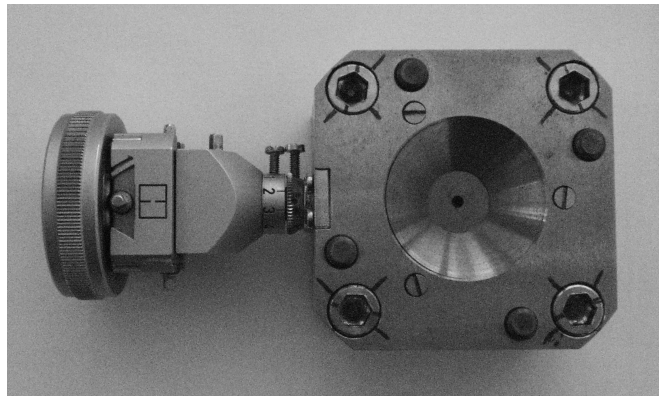


Figure 3.10: Diamond anvil cell - with goniometer-head for high-pressure experiments.

Chapter 4

Experimental study of hydrous iron-bearing mantle silicates in the $\text{MgFeSiO}_4\text{-H}_2\text{O}$ system

4.1 Starting material and experimental conditions

The experiments were conducted using a nominal Forsterite 50 ($\text{Fo}_{50}\text{Fa}_{50}$) + H_2O bulk composition as starting material. The powder starting material was made from a synthetic fayalite (Fe_2SiO_4) and a 2:1 molar mixture of brucite and quartz ($2 \text{Mg}(\text{OH})_2 + \text{SiO}_2$). The two components were mixed in a 1:1 ratio to obtain the stoichiometric $\text{MgFeSiO}_4\text{+H}_2\text{O}$ bulk composition. Water was added only in the form of brucite, which yields a starting material with 9.5 wt% H_2O (Table 4.1). The dried and powdered components were ground together under ethanol in an agate mortar. Fractions of the starting material were loaded into platinum capsules, which were previously sealed one-sided by electrical welding and finally closed by cold welding after loading the powder.

Table 4.1: Calculated bulk composition of the $\text{MgFeSiO}_4\text{+H}_2\text{O}$ starting material.

		hydrous Fo_{50}
SiO_2	wt%	31.58
MgO	wt%	21.19
FeO	wt%	37.77
H_2O	wt%	9.46
Σ	wt%	100

4. HYDROUS FO₅₀ SYSTEM

Experiments were conducted over a broad pressure range at various temperatures in order to investigate the stability of nominally anhydrous and hydrous phases up to the pressure limit of the multi-anvil technique of about 25 GPa (Table 4.2). The run conditions varied from 9 to 25 GPa and 750 to 1500°C, whereby most of the experiments in this temperature range were performed between 15 to 25 GPa. One experiment was repeated with a different heating duration (30 minutes GG 2542 and 8 hours GG 4236) in order to identify influences of the run time on the sample synthesis. It turned out that the heating duration has no influence on the phase assemblages but the run conditions may become more oxidizing due to the loss of hydrogen from the system by the dissociation of water. Thus, the ferric iron content may be increased by longer heating durations. A single experiment at 23 GPa and 1400°C was performed using platinum/rhodium (PtRh) alloy as capsule material to test the effect of capsule material on phase assemblages. Despite the different capsule material (PtRh-capsule), the same mineral phases were synthesised as in experiments at similar conditions using platinum capsules.

Table 4.2: Experimental run conditions.

Sample	Pressure	Temperature	Heating duration	Capsule	Starting composition
GG 2615	6 GPa	500°C	6 h	platinum	hy Fo 50
GG 3975	6 GPa	750°C	5 h	platinum	hy Fo 50
GG 2580	9 GPa	750°C	2 h	platinum	hy Fo 50
GG 2895	10 GPa	750°C	8 h	platinum	hy Fo 50
GG 2539	15 GPa	750°C	3 h	platinum	hy Fo 50
GG 3853	15 GPa	950°C	1 h	gold*	hy Fo 50
GG 3854	15 GPa	1150°C	0.5 h	gold*	hy Fo 50
GG 2540	18 GPa	750°C	2 h	platinum	hy Fo 50
GG 2541	18 GPa	950°C	1 h	platinum	hy Fo 50
GG 2542	18 GPa	1150°C	0.5 h	platinum	hy Fo 50
GG 4236	18 GPa	1150°C	8 h	platinum	hy Fo 50
GG 2827	20.5 GPa	950°C	4 h	platinum	hy Fo 50
GG 2737	20.5 GPa	1150°C	8 h	platinum	hy Fo 50
GG 2795	20.5 GPa	1300°C	5 h	platinum	hy Fo 50
GG 4218	20.5 GPa	1400°C	3.5 h	platinum	hy Fo 50
GG 2613	23 GPa	950°C	1 h	platinum	hy Fo 50
GG 2736	23 GPa	1150°C	8 h	platinum	hy Fo 50
GG 2793	23 GPa	1300°C	8 h	platinum	hy Fo 50
GG 4327	23 GPa	1400°C	1.5 h	PtRh	hy Fo 50
GG 2800	23 GPa	1500°C	5 h	platinum	hy Fo 50
GG 2801	25 GPa	1500°C	4 h	platinum	hy Fo 50
GG 4374	18 GPa	1200°C	2 h	platinum foil & tube	hy Fo50 dry Fo50

* gold capsules to avoid iron loss to the capsule by absorption since gold is inert in respect to iron (Merrill & Wyllie 1973)

4.2 General description of experimental run products and calculation fundamentals for presented data

The relative phase abundances (modal%) of the recovered samples were determined using ImageJ programme (Table 4.3). The ringwoodite crystals developed as single phase are either elongated prismatic with quenched melt regions (GG 3854, GG 2541) or fine grained isometric with cavities between the crystals, which indicates the presence of a fluid during the experiment (GG 3853, Figure 4.1a). Ringwoodite crystals are also isometric and fine grained as well as massive in samples with coexisting dense hydrous Mg-Fe silicates. Generally, the run products are fine grained crystals when neither fluid nor quenched melt were observed. Traces of brucite (the so called quench-brucite) are present in almost all run products and possibly formed during quench when fluid exsolves from the melt. The size of the quench crystals gives a relative estimation of the viscosity of the melt, i.e. crystals are larger in low viscosity melts. At 18 GPa and 1150°C quench crystals are up to 15 μm large, whereas at 20.5 and 1400°C as well as 23 GPa and 1500°C quench crystal size decreases to about 5 μm which implies that the viscosity of the melt increases, which can be correlated with an increasing silica content of the melt.

The data obtained by EPMA¹ measurements, infrared spectroscopy and EELS² were used to determine the average mineral composition and to derive the mineral formulae as provided in Table 4.4. The iron partitioning coefficient K_D between ringwoodite and magnesiowüstite was determined on the basis of the equation:

$$K_D = \frac{X_{\text{Mg}}^{\text{ringwoodite}} X_{\text{Fe}}^{\text{magnesiowüstite}}}{X_{\text{Mg}}^{\text{magnesiowüstite}} X_{\text{Fe}}^{\text{ringwoodite}}}, \quad (4.1)$$

where $X_{\text{Mg}}^{\text{ringwoodite}}$ is the molar Fe/(Mg+Fe) ratio. The absorption of iron by platinum capsules was observed in every experimental run, whereas the starting composition was still retained in several experiments and at elevated temperature iron-rich magnesiowüstite is formed. This implies that the amount of absorbed iron is rather small.

¹electron probe micro analysis

²electron energy-loss spectroscopy

Table 4.3: Relative phase abundances (modal%) of recovered samples containing ringwoodite and dense hydrous Mg-Fe silicates.

Sample	Pressure/Temp.	Dominant phase	Secondary phase	Accessory phase ($\leq 5\%$)	Melt	Porosity
2580	9 GPa/750°C	phase A ringwoodite	brucite	11.4%	—	—
2895	10 GPa/750°C	phase A ringwoodite	brucite	17.8%	—	—
2539	15 GPa/750°C	ringwoodite	phase A	24.1%	—	36.2%
3853	15 GPa/950°C	ringwoodite	—	—	—	37.4%
3854	15 GPa/1150°C	ringwoodite	—	—	62.2%	—
2540	18 GPa/750°C	ringwoodite	phase D	28.8%	—	4.9%
2541	18 GPa/950°C	ringwoodite	—	—	45%	—
2542	18 GPa/1150°C	ringwoodite	—	stishovite magnesiowüstite	2.3% 2.9%	—
4236	18 GPa/1150°C	ringwoodite magnesiowüstite	stishovite	8.2%	brucite	16.1%
2827	20.5 GPa/950°C	superhydrous B phase D	magnesiowüstite	14.0	—	—
2737	20.5 GPa/1150°C	phase D superhydrous B	ringwoodite magnesiowüstite	20.3% 19.0%	—	—
2795	20.5 GPa/1300°C	ringwoodite	phase D	34.6%	brucite	—
4218	20.5 GPa/1400°C	ringwoodite	magnesiowüstite	18.4%	—	3.1%
2613	23 GPa/950°C	brucite phase D	stishovite superhydrous B magnesiowüstite	8.8% 13.3% 7.2%	magnesiowüstite	4.4% 60.9%
2736	23 GPa/1150°C	ringwoodite	phase D magnesiowüstite	29.6% 21.1%	brucite	—
2793	23 GPa/1300°C	ringwoodite magnesiowüstite	phase D brucite	18.6% 11.4%	—	16.8%
4327	23 GPa/1400°C	ringwoodite magnesiowüstite	stishovite	13.7%	magnetite	n.a. 29.7%
2800	23 GPa/1500°C	ringwoodite	stishovite magnesiowüstite	14.0% 8.7%	—	43.2%

relative phase abundances measured with ImageJ program;
 phases were distinguished by different gray scales in backscattered electron images

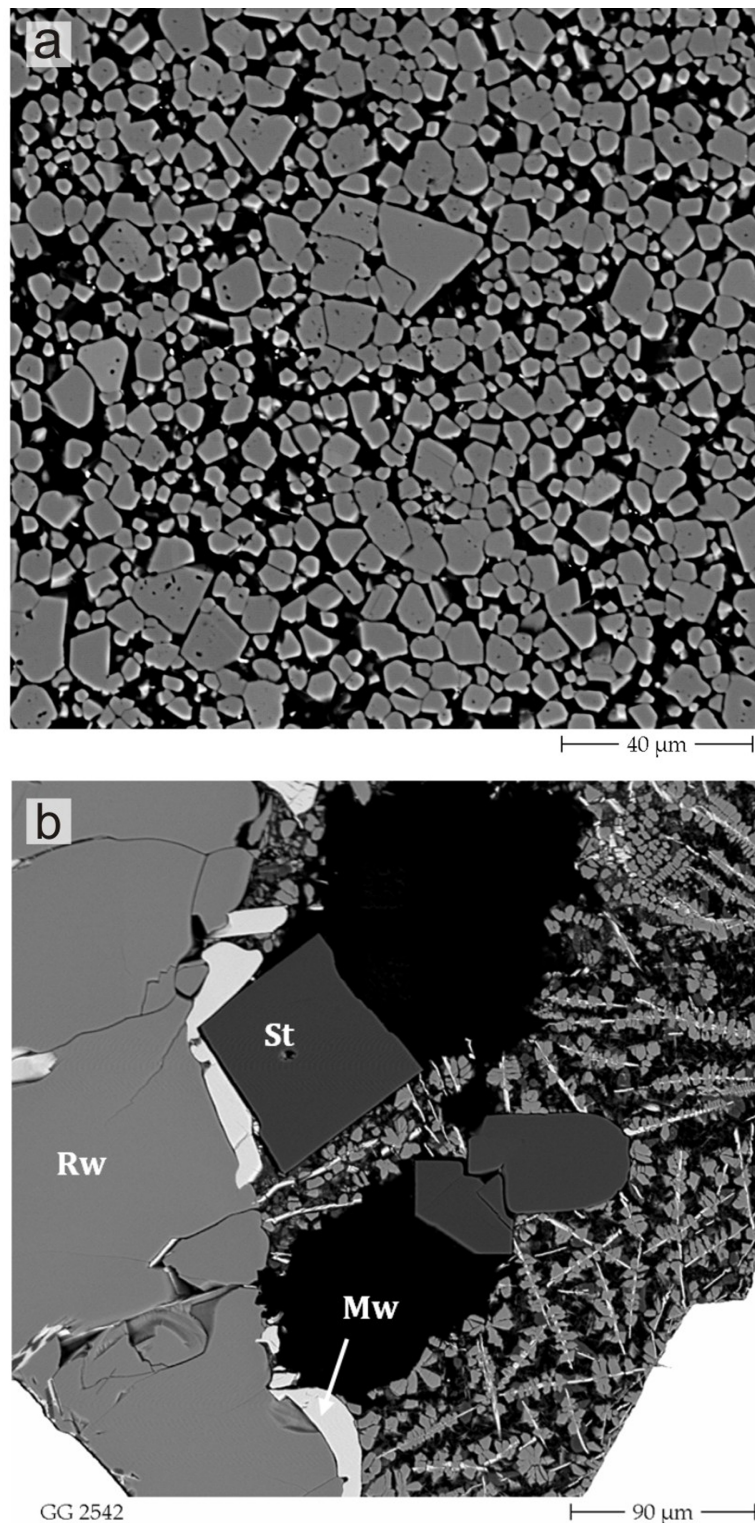


Figure 4.1: Backscattered electron image of single phase ringwoodite (a) and the three-phase assemblage (b) - sample GG 3853, 15 GPa and 950°C (a), sample GG 2542, 18 GPa and 1150°C; Rw - ringwoodite, Mw - magnesiowüstite, St - stishovite (b).

Table 4.4: Average composition of experimental run products based on EPMA measurements

	GG 2542	GG 2737	GG 2580	GG 2737
	rw	phase D	phase A	SHyB
	(24 pts.)	(22 pts.)	(10 pts.)	(16 pts.)
SiO ₂	[wt%] 34.6(1)	58(2)	24.2(3)	26.0(9)
MgO	[wt%] 22.7(1)	26(1)	46.9(5)	47.7(8)
FeO	[wt%] 39.5(3)	2.0(1)	17.5(5)	15.8(9)
Fe ₂ O ₃ [†]	[wt%] 3.30(2)	3.4(4)	n.a.	7.2(8)
H ₂ O [*]	[wt%] 0.5	10.6(2.0) [‡]	11.4(8) [‡]	3.3(6) [‡]
Σ	[wt%] 100.6(4)	100	100	100
Cation based on	4 O	6 O	14 O	18 O
Si ⁴⁺	0.98	1.79	1.98	3.01
Fe ³⁺	—	0.08	—	—
*Mg ²⁺	—	0.13	—	—
Fe ³⁺	0.07	—	—	0.62
Mg ²⁺	0.96	1.04	5.73	8.22
Fe ²⁺	0.93	0.05	1.20	1.53
H	0.09	2.17	6.22	2.56
Σ	3.03	5.26	15.13	15.94
Mg/Si	0.98	0.65	2.89	2.73

Si ⁴⁺	0.98	0.98	1.98	3.01
Fe ³⁺	—	0.08	—	—
*Mg ²⁺	—	0.13	—	—
Fe ³⁺	0.07	—	—	0.62
Mg ²⁺	0.96	1.04	5.73	8.22
Fe ²⁺	0.93	0.05	1.20	1.53
H	0.09	2.17	6.22	2.56
Σ	3.03	5.26	15.13	15.94
Mg/Si	0.98	0.65	2.89	2.73

[‡] estimated water contents based on low microprobe totals
[†] Electron energy-loss spectroscopy
^{*} Unpolarised infrared analyses
^{*} Mg-Si disorder

4.2 General description of experimental run products

The observed phase assemblages are in agreement with Gibbs' phase rule $F = C - P + 2$, with C - minimum number of components to create the present (mineral) phases, P - number of (mineral) phases, F - degree of freedom which is the number of intensive properties (e.g. pressure and temperature) that are independent of other intensive parameters. The observed brucite phase is probably a result of experiment quenching. The fluid phase, which formed brucite upon quenching, was dissolved in the melt during the experiment, thus brucite and quenched material (observed in some experimental runs) are assumed as the same phase. The minimum number of components, number of observed phases and the resulting degrees of freedom are given in Table 4.5.

Table 4.5: Application of Gibbs' phase rule to observed phase assemblages.

Component system	Present phases (P)	Sample	Number of components (C)		Degrees of freedom (F)*
A	ringwoodite fluid [†]	GG 3854	2	MgFeSiO ₄ H ₂ O	2
B	ringwoodite phase A brucite	GG 2539	3	Fe ₂ SiO ₄ SiO ₂ Mg(OH) ₂	2
	ringwoodite phase D brucite	GG 2540	3	Fe ₂ SiO ₄ SiO ₂ Mg(OH) ₂	2
C*	ringwoodite magnesiowüstite stishovite melt	GG 2800	4	SiO ₂ MgO FeO Mg(OH) ₂	2

* $F = C - P + 2$ Gibbs' phase rule

* applicable also to phase D + SHyB + brucite + mw (sample GG 2827, GG 2736)

[†] cavities are referred to a fluid phase present during the experiment

observed run products are given in table 4.3, note that brucite + melt are considered as same phase

The number of components involves the components which are needed to produce the present phases of the run product.

The MSH (M - MgO, S - SiO₂, H - H₂O) diagram displays the composition of every observed mineral phases (Figure 4.2). For the sake of clarity, the Mg-endmembers are considered in order to point out the correlation of run products and the choice of the component system (brucite refers also to melt or fluid). During the experiment, temperature and pressure (intensive parameter) were constant, thus Gibbs' phase rule was fulfilled and chemical equilibrium was probably reached in every experiment ($F = 0$).

4. HYDROUS FO₅₀ SYSTEM

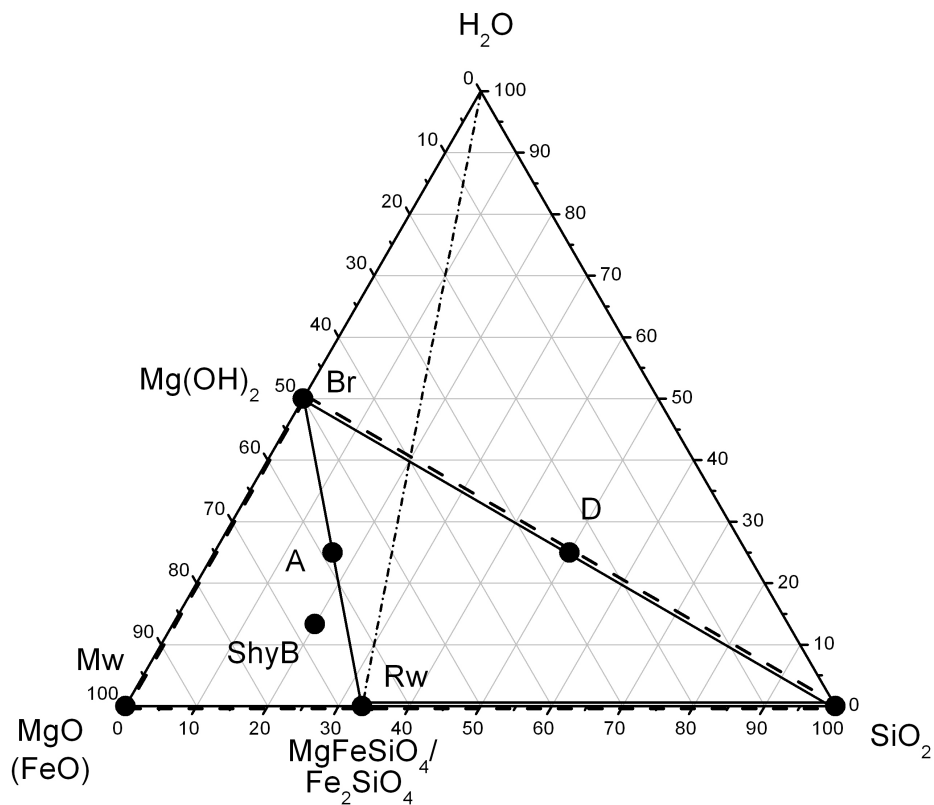


Figure 4.2: Ternary diagram of MgO(FeO), SiO₂ and H₂O - showing the Mg-endmember compositions of phase D (D), phase A (A), superhydrous B (ShyB), ringwoodite (Rw, MgFeSiO₄ / Fe₂SiO₄), magnesiowüstite (Mw), stishovite (SiO₂), brucite (Br, Mg(OH)₂) and water (fluid, H₂O); dash dotted line - component system A, solid line - component system B, dashed line - component system C.

4.3 Results on the particular mineral phases

4.3.1 Ringwoodite

Ringwoodite, one of the nominally anhydrous transition zone minerals, is the dominant high pressure polymorph of olivine covering a broad range of pressure-temperature conditions (9-23 GPa and 750-1500°C, this study).

4.3.1.1 Microprobe analyses - Compositional variations of ringwoodite and the coexisting phases

Within the pressure-temperature conditions of 9-23 GPa and 750-1500°C ringwoodite appears as a single phase and with coexisting dense hydrous magnesium silicates (alphabet phases) or together with stishovite and magnesiowüstite (Figure 4.1b, Table 4.3). When occurring as single phase, ringwoodite retains the starting composition with approximately 50 mole% Fe_2SiO_4 (sample GG 3854, GG 3853 and GG 2541; Table 4.6). When coexisting with the dense hydrous magnesium silicate “phase A” in the pressure range from 9 to 15 GPa at 750°C, ringwoodite shows enhanced iron contents varying from 52.5 to 65 mole% Fe_2SiO_4 (GG 2580, GG 2895, GG 2539). Other dense hydrous magnesium silicates such as “phase D” and “superhydrous B” coexist with ringwoodite in the low temperature region (750-1300°C) at pressures between 18 and 23 GPa. Ringwoodite is the dominant phase in sample GG 2540 together with coexisting “phase D”. The iron fraction of ringwoodite of 55 mole% Fe_2SiO_4 deviates slightly from the starting composition. In sample GG 2737, ringwoodite with ~ 38 mole% Fe_2SiO_4 is the second most abundant phase together with magnesiowüstite among the dominant dense hydrous magnesium silicates “phase D” and “superhydrous B”. The relative phase abundances of present mineral phases as well as the relative melt fraction are listed in Table 4.3. The three phase assemblage ringwoodite + stishovite + magnesiowüstite appears at 18 GPa and 1150°C as well as in the P-T- space between 20-23 GPa and 1400-1500°C (Figure 4.1b). Ringwoodite is the dominant phase in those samples, whereas the relative abundance of the concomitant phases varies. Ringwoodites show strong variations in iron fractions between 51-25.5 mole% Fe_2SiO_4 , which is a result of the varying modal fraction of magnesiowüstite, i.e. iron partitions preferentially into magnesiowüstite ($K_D^{\text{rw}/\text{mw}} = 0.02-0.07$, Table 4.6), and into the coexisting melt. The compositional variations are also an effect of pressure, as is obvious from the three-phase assemblage loop (Figure 4.3, 4.21). In the samples GG

4. HYDROUS FO₅₀ SYSTEM

2580, GG 2895, GG 2539 and GG 2540, which lie below the 50 mole% Mg₂SiO₄ starting composition, magnesiowüstite is absent and the abundance as well as the magnesium contents of coexisting phase A and phase D cause the increased iron fraction in ringwoodite (Figure 4.3).

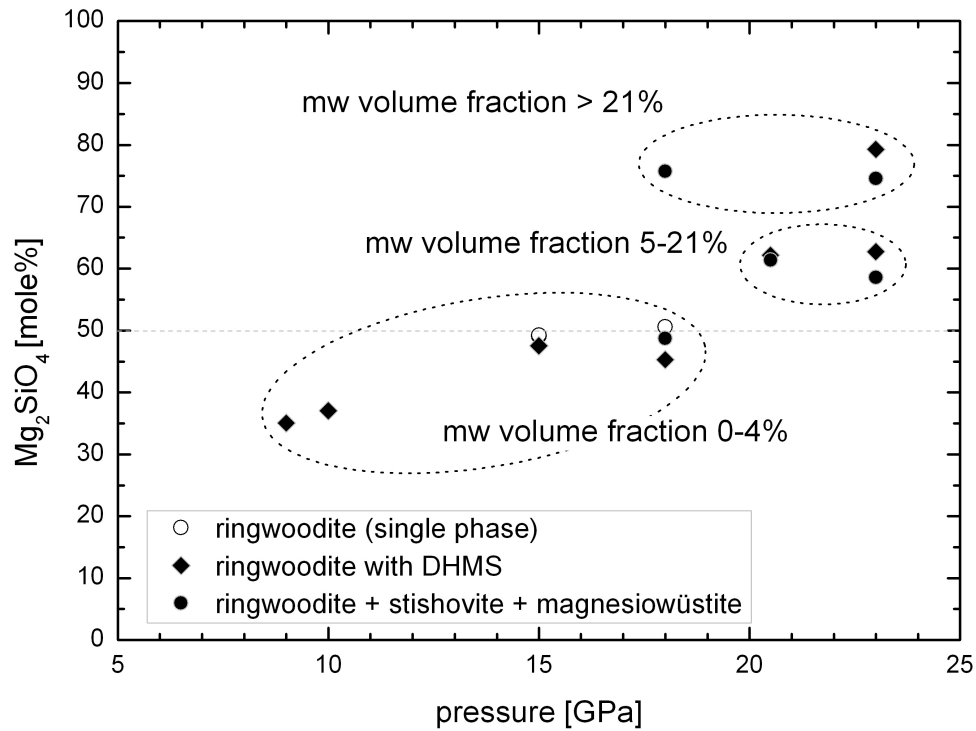


Figure 4.3: Mg₂SiO₄ fraction of ringwoodite as a function of pressure - indicated are the coexisting modal fractions of magnesiowüstite, dashed line - starting composition, abbreviation: mw - magnesiowüstite.

Table 4.6: EPMA data of ringwoodite (1σ standard deviation in parenthesis)

Sample	P, T	pts.	MgO [wt%]	SiO ₂ [wt%]	FeO [wt%]	Fe ₂ O ₃ [†] [wt%]	H ₂ O* [wt%]	Total	Mg# [mole%]	‡K _D ^{r/w/mw}	Mineral formula
GG 2580	(9 GPa, 750°C)	08	15.9(5)	32.9(4)	52.3(7)	n.a.	n.a.	101.1(6)	35.08	—	
GG 2895	(10 GPa, 750°C)	31	17.0(7)	32.9(3)	51.5(8)	n.a.	n.a.	101.4(4)	37.05	—	
GG 2539	(15 GPa, 750°C)	47	22.1(6)	34.7(2)	43.5(8)	n.a.	n.a.	100.3(4)	47.55	—	
GG 3853	(15 GPa, 950°C)	55	23.2(2)	35.4(2)	43.0(5)	n.a.	n.a.	101.6(5)	49.06	—	
GG 3854	(15 GPa, 1150°C)	53	23.3(2)	35.1(2)	42.4(3)	0.475(3)	0.71	102.0(4)	49.28	—	(Mg _{0.97} Fe ²⁺ _{0.99} Fe ³⁺ _{0.01}) _{1.97} Si _{0.98} H _{0.13} O ₄
GG 2540	(18 GPa, 750°C)	47	20.8(7)	34.6(3)	44.8(6)	n.a.	n.a.	100.2(3)	45.29	—	
GG 2541	(18 GPa, 950°C)	53	24(1)	35.6(3)	42(1)	n.a.	n.a.	101.3(4)	50.62	—	
GG 2542	(18 GPa, 1150°C)	24	22.7(1)	34.6(1)	39.5(3)	3.30(2)	0.5	100.6(4)	48.72	0.070(3)	(Mg _{0.96} Fe ²⁺ _{0.93} Fe ³⁺ _{0.07}) _{1.97} Si _{0.98} H _{0.09} O ₄
GG 4236	(18 GPa, 1150°C)	34	39.3(4)	38.5(5)	22.5(7)	n.a.	0.35	100.6(5)	75.74	0.04(1)	(Mg _{1.51} Fe _{0.48}) _{1.99} Si _{0.98} H _{0.06} O ₄
GG 4374	(18 GPa, 1150°C)	9	23.5(6)	35.2(1)	43.0(7)	n.a.	n.a.	101.7(3)	49.03	—	(Mg _{0.99} Fe _{1.01}) ₂ Si _{1.00} O ₄
*GG 4374	(18 GPa, 1150°C)	22	42.2(2)	39.4(2)	18.8(2)	n.a.	n.a.	100.5(3)	80.00	—	(Mg _{1.60} Fe _{0.40}) ₂ Si _{1.00} O ₄
GG 2737	(20.5 GPa, 1150°C)	16	31.0(6)	36.3(7)	34(1)	n.a.	n.a.	101.0(6)	62.20	0.03(2)	
GG 2795	(20.5 GPa, 1300°C)	03	44(1)	39.1(0)	19(1)	n.a.	n.a.	101.3(0)	80.61	0.020(4)	
GG 4218	(20.5 GPa, 1400°C)	30	30.2(3)	36.0(2)	29.4(4)	4.88(6)	0.37	100.9(3)	61.40	0.06(2)	(Mg _{1.21} Fe ²⁺ _{0.66} Fe ³⁺ _{0.10}) _{1.97} Si _{0.97} H _{0.07} O ₄
GG 2736	(23 GPa, 1150°C)	20	31.5(8)	36.7(0)	33.3(6)	n.a.	n.a.	101.5(0)	62.75	0.03(2)	
GG 2793	(23 GPa, 1300°C)	10	42(2)	39.0(4)	20(2)	n.a.	n.a.	101.1(3)	79.28	0.03(1)	
GG 4327	(23 GPa, 1400°C)	66	39(2)	38.9(4)	23(2)	0.8(1)	0.62	102.5(7)	74.58	0.05(1)	(Mg _{1.47} Fe ²⁺ _{0.49} Fe ³⁺ _{0.02}) _{1.98} Si _{0.98} H _{0.10} O ₄
GG 2800	(23 GPa, 1500°C)	19	29(2)	36.5(5)	36(3)	n.a.	0.38	101.5(5)	58.60	0.07(1)	(Mg _{1.17} Fe _{0.83}) ₂ Si _{0.98} H _{0.07} O ₄

Mg# = (Mg/(Mg+Fe))*100

* anhydrous MgFeSiO₄ system

† Electron energy-loss spectroscopy

* Unpolarised infrared analyses

ringwoodite mineral formulae are shown for samples measured with IR-spectroscopy

‡ K_D defined as (Fe/Mg)_{ringwoodite}/(Fe/Mg)_{iron oxide} as in equ. 4.1

4. HYDROUS FO₅₀ SYSTEM

The occurrence of the three-phase assemblage at 20 GPa and 1400°C as well as 23 GPa and 1500°C is in agreement with previous studies, whereas the low temperature (1150°C) experiment at 18 GPa is in contradiction with data presented for similar temperatures by Fei et al. (1991). The experiments of this study, however, are reproducible and in order to address the reason for the occurrence of the rw + mw + st assemblage in the hydrous MgFeSiO₄ system the experimental run at 18 GPa and 1150°C was repeated with an anhydrous nominal Fo₅₀ starting composition (run GG 4374). The three-phase assemblage is also developed at 18 GPa and 1150°C in the anhydrous MgFeSiO₄ system but with distinct ringwoodite and magnesiowüstite compositions of Fo₈₀-ringwoodite and (Mg_{0.13}Fe_{0.87})O. Thus, the addition of water can be excluded as explanation for the observation of the three phase assemblage at lower pressure. This observation is probably the result of different redox conditions during the experiment, which can be due to the dissociation of water in the hydrous system (reaction 4.2) and the absorption of iron by the platinum capsule material (reaction 4.3). The oxygen, which is provided by both reactions, decomposes fayalite to form stishovite and a ferric iron compound such as magnetite (reaction 4.4). However, the Mg in the system may also form a magnesiowüstite and magnesioferrite component together with magnetite. Nevertheless, the occurrence of the three-phase assemblage at lower pressure is caused by the oxidation of iron.



4.3.1.2 TEM examination - Structural properties of ringwoodite and the valence state of iron at different pressure and temperature conditions

Different zone axis diffraction patterns of ferroan ringwoodite were taken using TEM and indexed with EDANA program to determine the symmetry and d-spacings of ringwoodite. On the basis of these diffraction patterns, and observed absences of reflections, it is confirmed that hydrous iron-rich ringwoodite has the cubic spinel structure, space group $Fd\bar{3}m$. Two different indexed diffraction patterns of hydrous ferroan ringwoodite are shown in Figure 4.4.

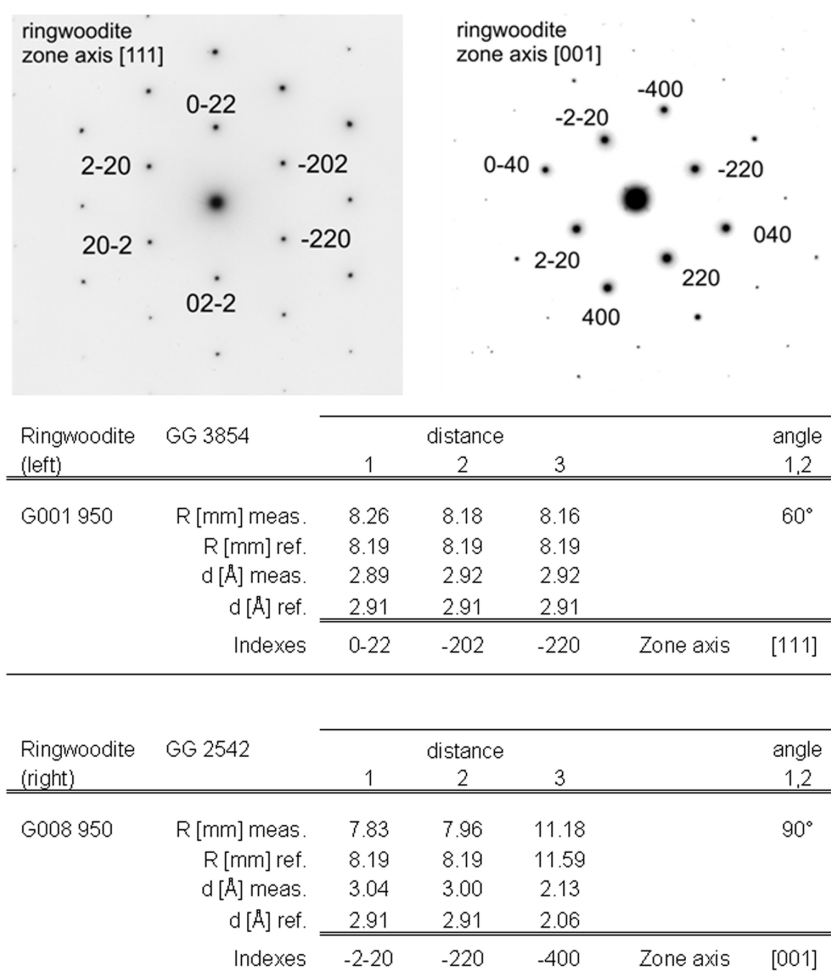


Figure 4.4: Electron diffraction patterns of ringwoodite - GG 3854 (left), GG 2542 (right), Tables show measured and reference (Fe-ringwoodite) distances of the diffraction pattern.

4. HYDROUS FO₅₀ SYSTEM

High resolution images show a defect-free ringwoodite structure (Figure 4.5), even the typical {110} stacking faults were not observed in any ringwoodite sample. These stacking faults are commonly formed by the martensitic solid-state transformation from olivine to ringwoodite (Kerschhofer et al. 1996), while Smyth et al. (2003) reports the absence of the typical {110} stacking faults of synthetic ringwoodite.

Electron energy-loss spectroscopy was combined with structural analyses in order to determine the ferric iron fraction incorporated into ringwoodite. Electron energy-loss near-edge structure (ELNES) spectra show a strong peak at 707.8 eV energy loss with a small shoulder at 709.5 eV, which represent the ferrous and ferric iron maxima at the FeL₃-edge, respectively. The peak shape of the FeL₃-edge changes corresponding to the relative abundances of ferric and ferrous iron (Chapter 3.3). The Fe²⁺ maximum of the FeL₃-edge is clearly dominant in four analysed ringwoodite samples, indicating dominantly ferrous iron. A small Fe³⁺-fraction in ringwoodite was observed for sample GG 2542 and GG 4218, which is shown by an evolving peak at 709.5 eV of the FeL₃-edge. The integration of the FeL_{2,3} edge intensities yield Fe³⁺/ΣFe ratios of 0.01(5) to 0.13(5) for ringwoodite (Figure 4.6).

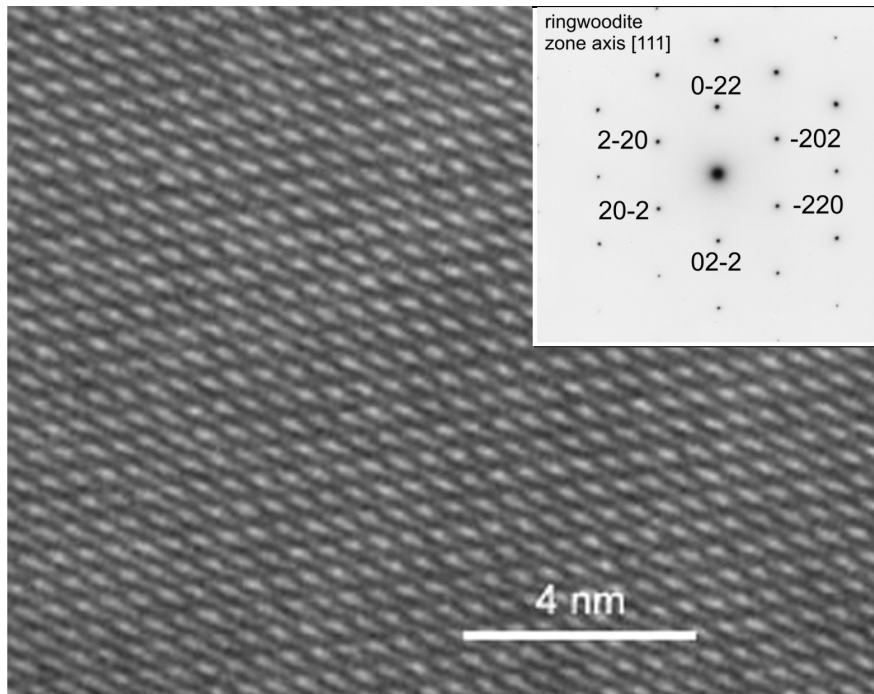


Figure 4.5: High resolution TEM image of Mg,Fe-ringwoodite - zone axis [111], sample GG 3854 (15 GPa, 1150°C).

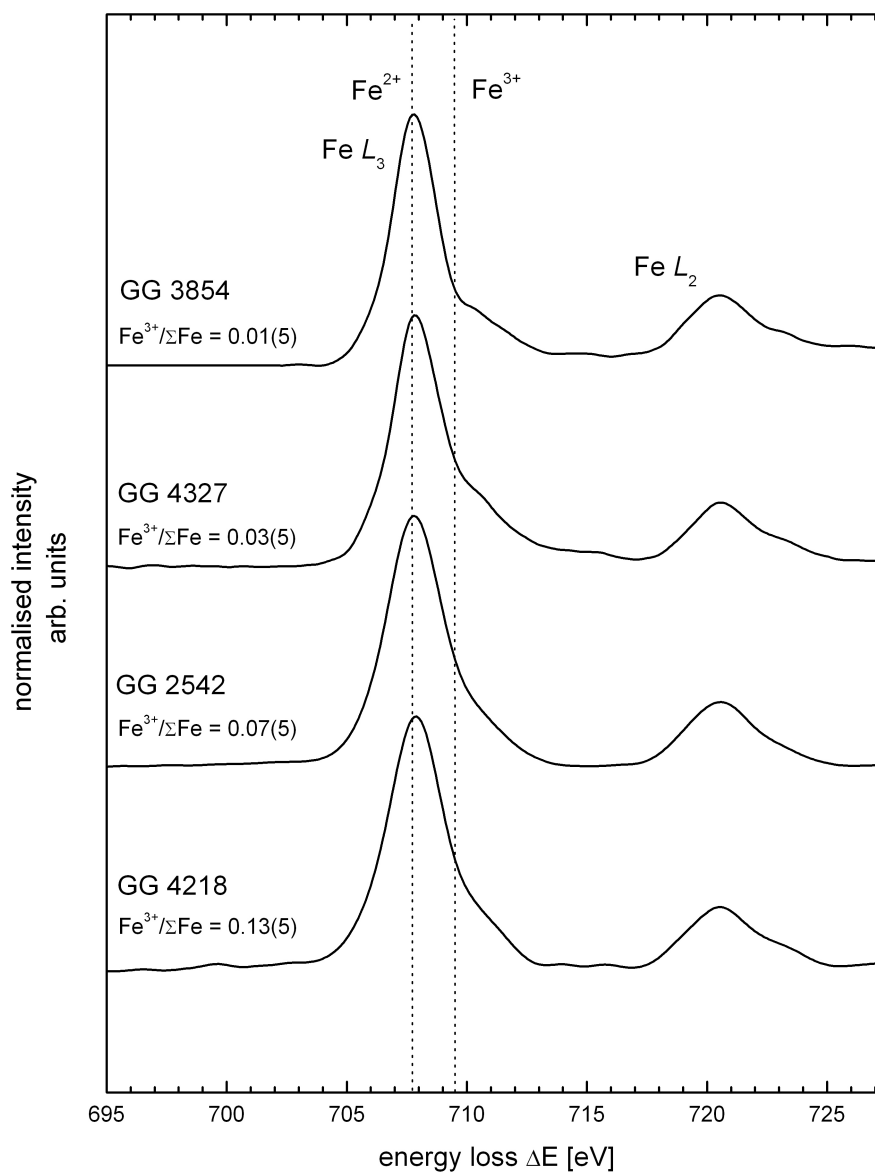


Figure 4.6: Iron $L_{2,3}$ electron energy-loss near-edge structure (ELNES) spectra of Mg,Fe-ringwoodite - synthesised at distinct P-T conditions; GG 3854 (15 GPa, 1150°C), GG 4327 (23 GPa, 1400°C), GG 2542 (18 GPa, 1150°C), GG 4218 (20.5 GPa, 1400°C).

4.3.1.3 FTIR spectroscopy - Water storage capacity and associated point defect chemistry of iron-bearing ringwoodite

I. Water storage capacity of iron-bearing ringwoodite

Fourier transformed infrared spectroscopy was performed to determine the concentration of H₂O (in form of OH-groups) in the nominally anhydrous mineral ringwoodite. Six samples synthesised at different pressure-temperature conditions were selected and measured as described in Characterisation methods, subchapter 3.2. The results and spectra of four representative samples are shown in Table 4.7 and Figure 4.7. The OH-absorption band of ringwoodite appears to be very broad in all spectra from about 2000 to 3800 cm⁻¹ with slightly varying absorbance maxima at 3200 cm⁻¹ to 3300 cm⁻¹ and smaller peaks at lower and higher wavenumbers. The absorption band is broader (FWHM ~800 cm⁻¹, sample GG 3854) than reported for Mg-ringwoodite (FWHM ~410 cm⁻¹, Bolfan-Casanova et al. 2000), which may be due to different atomic environments of hydroxyl groups in ferroan ringwoodite. The particularly weak absorption features at lower (2700 cm⁻¹) and higher (3700 cm⁻¹) wavenumbers are assigned to different types of OH-groups (Bolfan-Casanova et al. 2000). Therefore the entire absorption feature in the range from 2000 to 3800 cm⁻¹ was integrated for water content estimations, although Bolfan-Casanova et al. (2000) as well as Chamorro Pérez et al. (2006) suggest that the lower energy band may be due to overtones of the in-plane X-OH. These vibrational features appear in the IR-spectra of every sample, while the absorption band at 3700 cm⁻¹ is not visible for sample GG 3854 probably because of the broad main absorption band. The IR-spectrum of sample GG 3854 shows two additional absorption bands at 2900 cm⁻¹, which are likely due to some residual methanol-ethanol (pressure transmitting medium, see chapter 3.4) on the crystal surface. Obtained spectra were corrected for thickness and background was subtracted in order to integrate the absorption band using equation 3.2 in the region of 2000 to 3780 cm⁻¹ (Figure 4.7). The calibration of Paterson (1982) was used to estimate the H-content in ringwoodite, which is shown in Table 4.7. The water content of ringwoodite synthesised in the MgFeSiO₄ system ranges from ~0.4 to ~0.7 wt% H₂O.

Obtained data represent the water storage capacity, the maximum mass fraction of H₂O retained in ferroan ringwoodite at different pressure and temperature conditions. The concept of water storage capacity of nominally anhydrous minerals is explained in Hirschmann et al. (2005) who pointed out that the

maximum water concentration in minerals changes with mineral composition and water fugacity, which in turn depends on the assemblage of coexisting mineral phases and composition of the coexisting fluids, respectively. Thus, water storage capacity does not necessarily display the maximum water solubility of a mineral phase, which indeed requires water activity to be unity (water present as H₂O-rich fluid). The water, which is in excess of the water storage capacity of existing mineral phases, is present as H₂O- or silicate-rich fluid (Hirschmann et al. 2005), i.e. filling cavities between crystals or represented by quenched material. Despite the observed porosity, there is no clear evidence that points to the presence of molecular water or water-rich fluid during the experiments so that the water activity is assumed to be below unity.

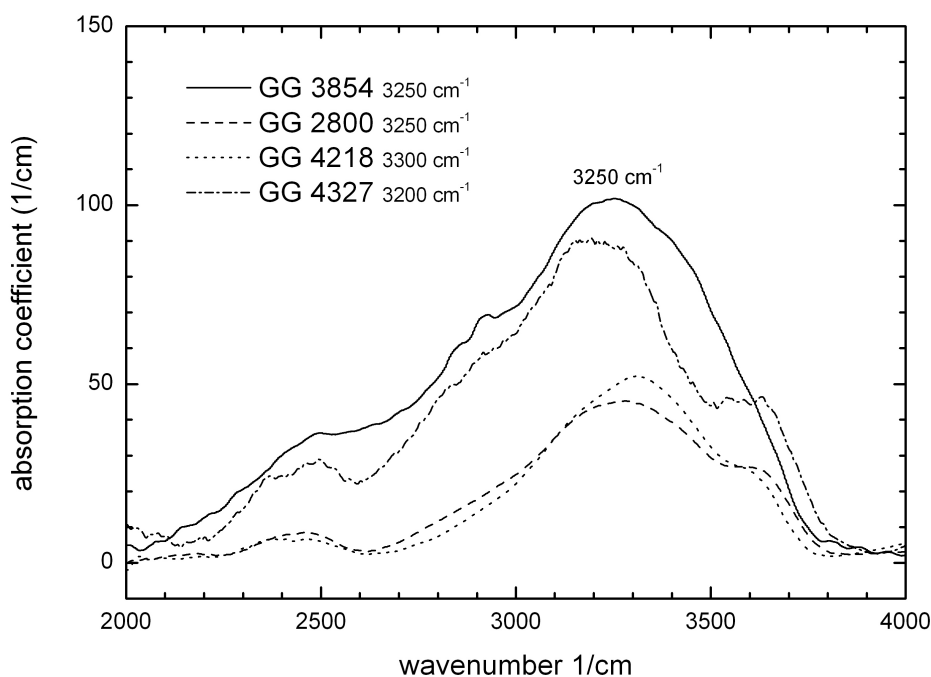


Figure 4.7: Infrared absorption spectra of four Mg,Fe-ringwoodite samples - wavenumbers represent maximum absorption peaks of the spectra; GG 3854 (15 GPa, 1150°C), GG 4218 (20.5 GPa, 1400°C), GG 4327 (23 GPa, 1400°C), GG 2800 (23 GPa, 1500°C).

4. HYDROUS FO₅₀ SYSTEM

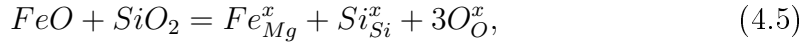
Table 4.7: Mg,Fe-ringwoodite samples used for the determination of water concentration; synthesis conditions, wavenumber of maximum absorption and measured water concentration

Sample	Thickness	Pressure	Temp.	Absorption Maximum	H ₂ O concentration [ppm] and [wt%]
GG 3854	30 μm	15 GPa	1150°C	3250 cm-1	6656 - 7521 ppm average 7088 ppm \equiv 0.71 wt%
GG 2800	25 μm	23 GPa	1500°C	3250 cm-1	3485 - 4115 ppm average 3800 ppm \equiv 0.38 wt%
GG 4218	30 μm	20.5 GPa	1400°C	3300 cm-1	3587 - 3905 ppm average 3746 ppm \equiv 0.37 wt%
GG 4327	30 μm	23 GPa	1400°C	3200 cm-1	5282 - 7067 ppm average 6175 ppm \equiv 0.62 wt%

II. Point defect chemistry of iron-bearing ringwoodite

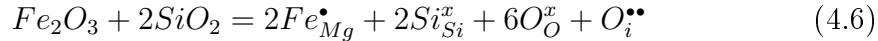
The incorporation of ferrous and ferric iron in the ringwoodite structure is achieved by substitution predominantly into the Mg-site, since Fe-Si disorder is predicted to be less than 1%, i.e. less than 0.01 a.p.f.u. of iron (Hazen et al. 1993). Thus, the substitution mechanisms for ferric and ferrous iron into the magnesium site of ringwoodite are as follows (for notation see Kröger and Vink 1956)³:

Fe²⁺ in Mg-site



which represents the common Fe-Mg substitution of the solid solution between Mg- and Fe-endmember of ringwoodite.

Fe³⁺ in Mg-site



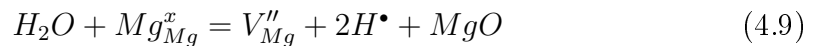
³Mg_{Mg}^x - Mg in Mg-site, O_i^{••} - O²⁻ on an interstitial site, Fe'_{Si} - ferric iron in Si-site, V''_{Mg} - Mg-vacancy, Fe_{Mg}[•] - ferric iron in Mg-site; ^x - neutral site, ' - positive undercharge, • - negative undercharge

The Mg-site vacancy gives in combination with the interstitial oxygen of equation 4.6 the resulting equation 4.8, i.e. creation of octahedral-site vacancies without hydration:

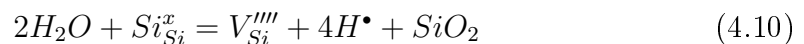


Further possible substitution mechanisms to incorporate water in ringwoodite involve cation vacancies and cation disorder charge balanced by hydrogen substitution (Hazen et al. 1993; Blanchard et al. 2009), whereas no clear evidence was found for Mg-Si disorder in the ringwoodite samples:

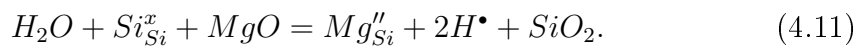
Mg-site vacancies



Si-site vacancies



Mg-Si disorder



The water substitution mechanisms of hydrous ferroan ringwoodite and the correlation of the water content and the iron content will be discussed in chapter 4.4 III.

4.3.1.4 Single-crystal x-ray diffraction - Equation of state and structure refinements of hydrous ferroan ringwoodite

I. Sample characterisation

Two samples of hydrous ferroan ringwoodite synthesised from a stoichiometric MgFeSiO₄ starting mixture (Fe₂SiO₄ + Mg(OH)₂ + SiO₂) at 15 GPa and 1150°C (run 3854) as well as at 20.5 GPa and 1400°C (run 4218) were analysed by single-crystal x-ray diffraction to determine their compressibility. Ringwoodite was the only phase present in the synthesis product of run 3854, whereas it was the dominant phase coexisting with stishovite and magnesiowüstite in run 4218. Results of the chemical analyses are given in Table 4.8. Electron energy-loss near-edge structure (ELNES) spectra were collected for both samples. Quantification of Fe³⁺/ΣFe ratio was done following the procedure described by van Aken (1998). Integration of the two peaks of the iron L₃ and L₂ ionisation edge in the spectra yields Fe³⁺/ΣFe = 0.01(5) for run 3854 and Fe³⁺/ΣFe = 0.13(5) for run 4218. Water concentration of hydrous ringwoodite was determined by means of Fourier transform infrared spectroscopy. Obtained spectra were corrected for thickness and the region from 2000 - 3730 cm⁻¹ was integrated using the calibration of Paterson (1982) to estimate the H₂O content in wt% (Table 4.8). The resulting formulae of hydrous ringwoodites are as follows: (Mg_{0.97}Fe²⁺_{1.00})_{1.97}Si_{0.98}H_{0.13}O₄ (run 3854) and (Mg_{1.21}Fe²⁺_{0.66}Fe³⁺_{0.10})_{1.97}Si_{0.97}H_{0.07}O₄ (run 4218).

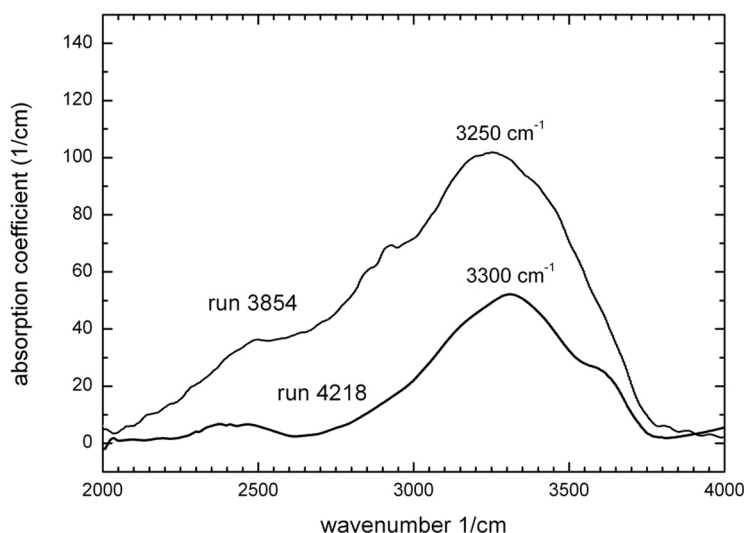


Figure 4.8: Infrared spectra of hydrous ferroan ringwoodites - sample GG 3854 (15 GPa, 1150°C) and sample GG 4218 (20.5 GPa, 1400°C)

Table 4.8: Chemical analyses of ringwoodite based on electron microprobe analyses, electron energy loss and IR spectroscopy (Standard deviations are in parentheses).

oxides [wt%]*	run 4218	run 3854
SiO ₂	36.0(2)	35.2(2)
MgO	30.2(3)	23.3(2)
FeO	29.4(4)	42.8(3)
Fe ₂ O ₃	4.9(1)	—
H ₂ O	0.37	0.71
Σ	100.9(3)	102.0(4)
cations based on 4 oxygen atoms		
Si	0.97	0.98
Mg	1.21	0.97
Fe ²⁺	0.66	1.00
Fe ³⁺	0.10	—
H#	0.07	0.13
Σ	3.01	3.08
Mg/(Mg+Fe)	0.62	0.49
water content based on IR spectra		
peak maximum	3300 cm ⁻¹	3250 cm ⁻¹
H ₂ O [wt%]	~0.37	~0.71
*Average of 30 (4218) and 55 (3854) microprobe measurements		
# from IR spectroscopy measurements		
Fe ³⁺ from EELS analyses		

II. Structure refinements of hydrous Fe-bearing ringwoodites

In general, the unit-cell volume of ringwoodite increases with increasing Fe-content (Figure 4.9). There is some evidence that water substitution also increases the unit-cell volume of ringwoodite (Smyth et al. 2003) as suggested by the fit of the hydrated samples which all lie above the linear trend between the anhydrous end-members (dotted and solid lines, respectively reported in Figure 4.9). Octahedral, M-O, and tetrahedral, T-O, bond distances obtained from the structural refinements of our samples are compared with those reported in the literature for ringwoodites having different Mg/(Mg+Fe) ratios and water contents (Figure 4.10a,b). The M-O bond distance increases with increasing Fe-content of ringwoodite (Figure 4.10a), whereas the T-O bond distance slightly decreases with increasing Fe-content (Figures 4.10b). Anhydrous Mg_2SiO_4 ringwoodite has M-O distances comparable to those of hydrous Mg-ringwoodite (Figure 4.10a) whereas increasing water content seems to increase the T-O bond distances (Figure 4.10b).

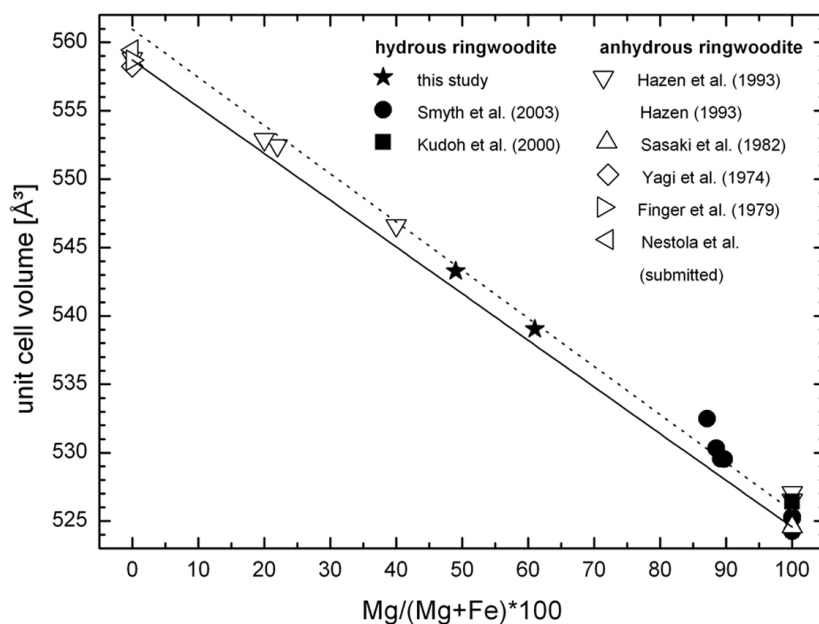


Figure 4.9: Unit cell volume of dry and hydrous ringwoodite as a function of magnesium content - solid symbols - hydrous ringwoodite (Kudoh et al. [2000] 2 wt% H_2O ; Smyth et al [2003] 0.74 wt% H_2O Fo_{100} -ringwoodite, 0.86 wt% H_2O Fo_{90} -ringwoodite, 1.07 wt% H_2O Fo_{87} -ringwoodite); open symbols - anhydrous ringwoodite; solid line - linear fit of anhydrous samples, dotted line - linear fit of hydrous samples.

Table 4.9: Structure refinement data for the two ringwoodite samples of this study.

Sample	run 4218	run 3854
N_{meas}	12420	15250
N_{unique}	104	136
N_{obs}	76	111
R_{int}	0.0476	0.0299
R	0.0391	0.0291
R_w ($F > 4\sigma$)	0.0212	0.02
$wR2$	0.0602	0.0565
Goof	0.862	1.019
Nr. Parameters	10	10
a (Å)	8.1384 (3)	8.1597 (6)
V (Å ³)	539.07 (7)	543.28 (13)
octahedral site		
Mg occ	0.540 (3)	0.496 (2)
Fe occ	0.381 (1)	0.495 (1)
Total occupancy	0.921	0.991
U ₁₁	0.0073 (3)	0.00649 (15)
U ₁₂	-0.0004 (2)	-0.00016 (10)
U _{eq}	0.0073 (3)	0.00649 (15)
M-O (Å)	2.0972 (14)	2.1045 (9)
O-M-O (°)	86.73 (7)	86.64 (4)
O-M-O (°)	93.27 (7)	93.36 (4)
O-O (non-shared)	2.880 (4)	2.888 (2)
O-O (shared)	3.050 (4)	3.062 (2)
tetrahedral site		
Si occ	0.9904 (7)	1.0007 (4)
U ₁₁ (=U _{eq})	0.0080 (4)	0.0064 (3)
Si-O (Å)	1.657 (2)	1.6580 (15)
O-O (Å)	2.705 (4)	2.708 (2)
O atom site		
x	0.24253 (16)	0.24231 (11)
U ₁₁	0.0084 (6)	0.0070 (3)
U ₁₂	0.0011 (5)	-0.0001 (2)
U _{eq}	0.0084 (6)	0.0070 (3)

U_{eq} represent the isotropic equivalent of the anisotropic temperature factors

4. HYDROUS FO₅₀ SYSTEM

The Fe substitution also has a strong effect on the OH-stretching mode of hydrous ringwoodite. Unpolarised infrared spectra of the two samples (Figure 4.8) show broad OH-absorption bands with the largest absorption peaks at about 3250 and 3300 cm⁻¹ for samples 3854 and 4218, respectively. These bands are clearly at larger wavenumbers than the OH bands of hydrous Mg₂SiO₄ and iron-bearing ringwoodite with 12 mole% Fe whose absorbance peaks are centered at 3105 cm⁻¹ and 3140 cm⁻¹, respectively (Smyth et al. 2003).

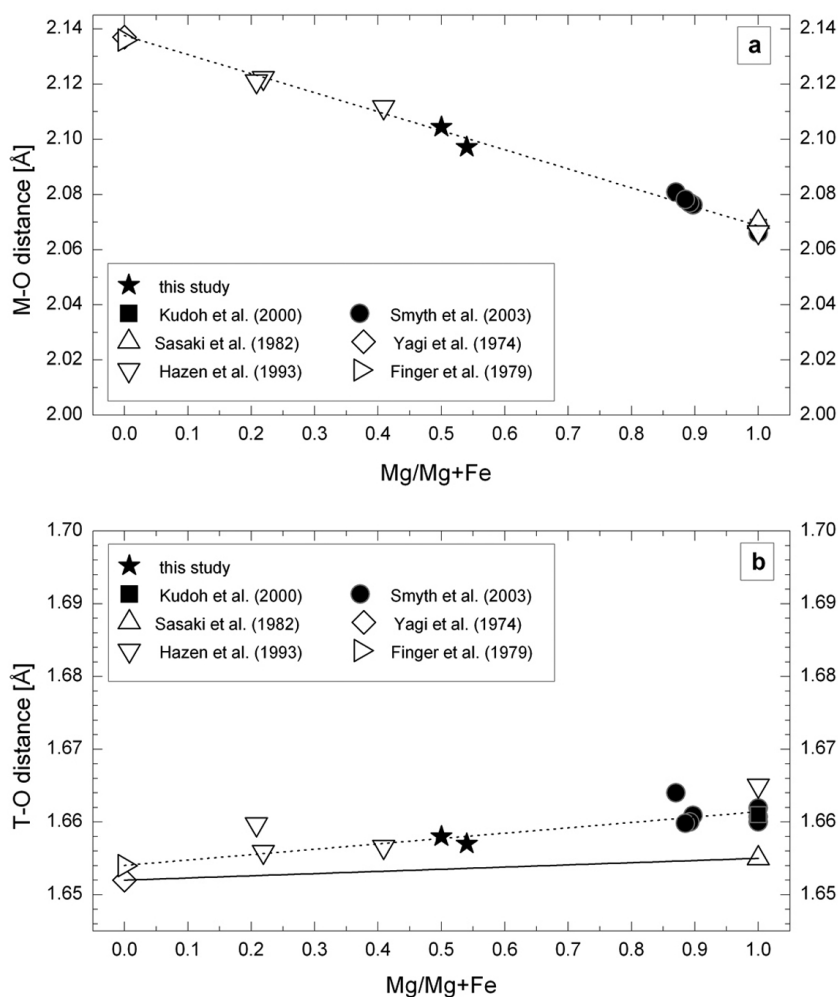


Figure 4.10: M-O distances (a) and T-O distances (b) of hydrous ringwoodite as a function of magnesium number - solid symbols - hydrous ringwoodite (Kudoh et al. [2000] 2 wt% H₂O; Smyth et al [2003] 0.74 wt% H₂O Fo₁₀₀-ringwoodite, 0.86 wt% H₂O Fo₉₀-ringwoodite, 1.07 wt% H₂O Fo₈₇-ringwoodite); open symbols - anhydrous ringwoodite; solid line - linear fit of anhydrous samples, dotted line - linear fit of hydrous samples.

III. Equations of state

The variations of the unit-cell volumes of samples 3854 and 4218 are shown in Figure 4.11 as a function of pressure. The continuous trend of the compression data indicates that no phase transition occurs for both samples in the investigated pressure range. The plot of normalised stress $F_E = P/3f_E(1+2f_E)^{5/2}$ vs. Eulerian strain $f_E = [(V_0/V)^{2/3}-1]/2$ (Angel 2000) (Figs. 4.12a,b) has a horizontal slope indicating that the first pressure derivative of the bulk modulus, K' , has a value of about 4. Accordingly, the P-V data were fitted with a second-order Birch-Murnaghan EoS using the EOSFIT 5.2 program (Angel 2002) refining simultaneously the room pressure unit-cell volume, V_0 , and the bulk modulus, K_{T0} . The refined EoS parameters are: $V_0 = 543.32(8) \text{ \AA}^3$ and $K_{T0} = 186.5 (9) \text{ GPa}$ for run 3854 and $V_0 = 539.01(5) \text{ \AA}^3$ and $K_{T0} = 184.1 (7) \text{ GPa}$ for run 4218. A 3rd-order Birch-Murnaghan EoS fit of the P-V data yields the same results given the uncertainties, i.e. $V_0 = 543.2 (7) \text{ \AA}^3$, $K_{T0} = 189 (4) \text{ GPa}$ and $K' = 3.4 (8)$ for run 3854 and $V_0 = 539.01 (6) \text{ \AA}^3$, $K_{T0} = 185 (3) \text{ GPa}$ and $K' = 3.9 (7)$ for run 4218. The discussion of the results is given in chapter 4.4.

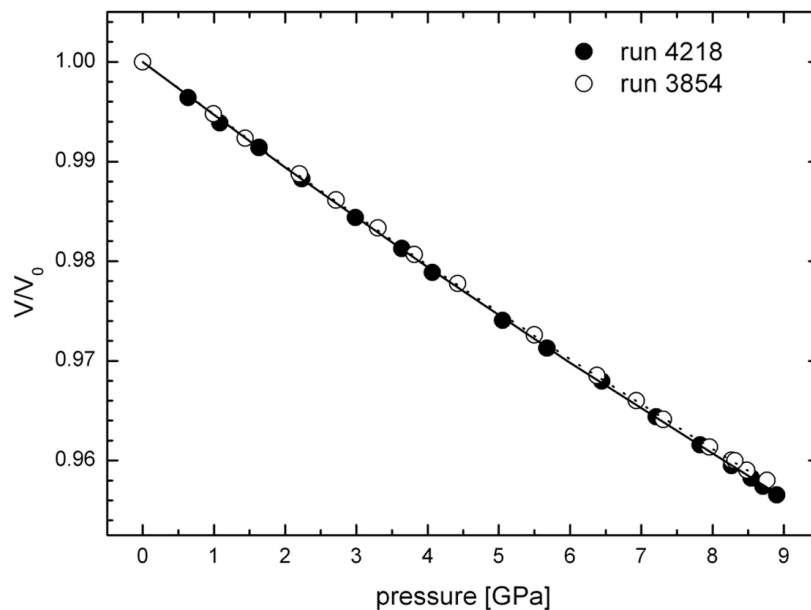


Figure 4.11: Variations of the unit-cell volumes of ferroan ringwoodites as a function of pressure - The values have been normalized with respect to the measured volumes at room pressure; solid line - fitted equation of state run 4218, dotted line - fitted equation of state run 3854.

4. HYDROUS FO₅₀ SYSTEM

Table 4.10: Unit-cell parameter measured as a function of pressure.

run 4218		
Pressure (GPa)	a (Å)	V (Å ³)
0.000(6)	8.1384(3)	539.03(7)
0.64(1)	8.1286(4)	537.10(8)
1.08(5)	8.1217(3)	535.73(7)
1.63(2)	8.1150(3)	534.40(6)
2.23(1)	8.1064(3)	532.70(7)
2.99(0)	8.0957(3)	530.61(6)
3.64(2)	8.0872(3)	528.93(6)
4.07(3)*	8.0806(4)	527.63(7)
5.05(4)*	8.0674(5)	525.05(10)
5.68(0)	8.0597(3)	523.55(7)
6.44(4)	8.0505(5)	521.76(9)
7.21(3)	8.0460(4)	519.83(9)
7.83(3)	8.0328(4)	518.32(7)
8.27(0)	8.0269(3)	517.19(6)
8.54(1)	8.0235(3)	516.52(6)
8.71(2)	8.0211(4)	516.07(8)
8.90(3)	8.0188(3)	515.61(6)
run 3854		
Pressure (GPa)	a (Å)	V (Å ³)
0.0001(1)	8.1597(6)	543.28(13)
0.990(9)	8.1455(3)	540.45(6)
1.44(3)	8.1388(3)	539.11(6)
2.20(2)	8.1290(3)	537.17(7)
2.71(1)	8.1218(4)	535.75(8)
3.30(4)	8.1141(3)	534.23(7)
3.81(1)	8.1068(3)	532.79(6)
4.42(1)	8.0988(4)	531.20(8)
5.50(0)	8.0845(3)	528.40(6)
6.38(0)	8.0732(4)	526.19(7)
6.93(0)	8.0662(3)	524.82(7)
7.31(4)	8.0609(3)	523.79(7)
7.96(1)	8.0532(3)	522.28(6)
8.27(1)	8.0495(3)	521.57(7)
8.31(2)*	8.0494(4)	521.54(8)
8.48(2)	8.0467(3)	521.02(6)
8.77(2)	8.0438(3)	520.47(6)

* data points measured during decompression

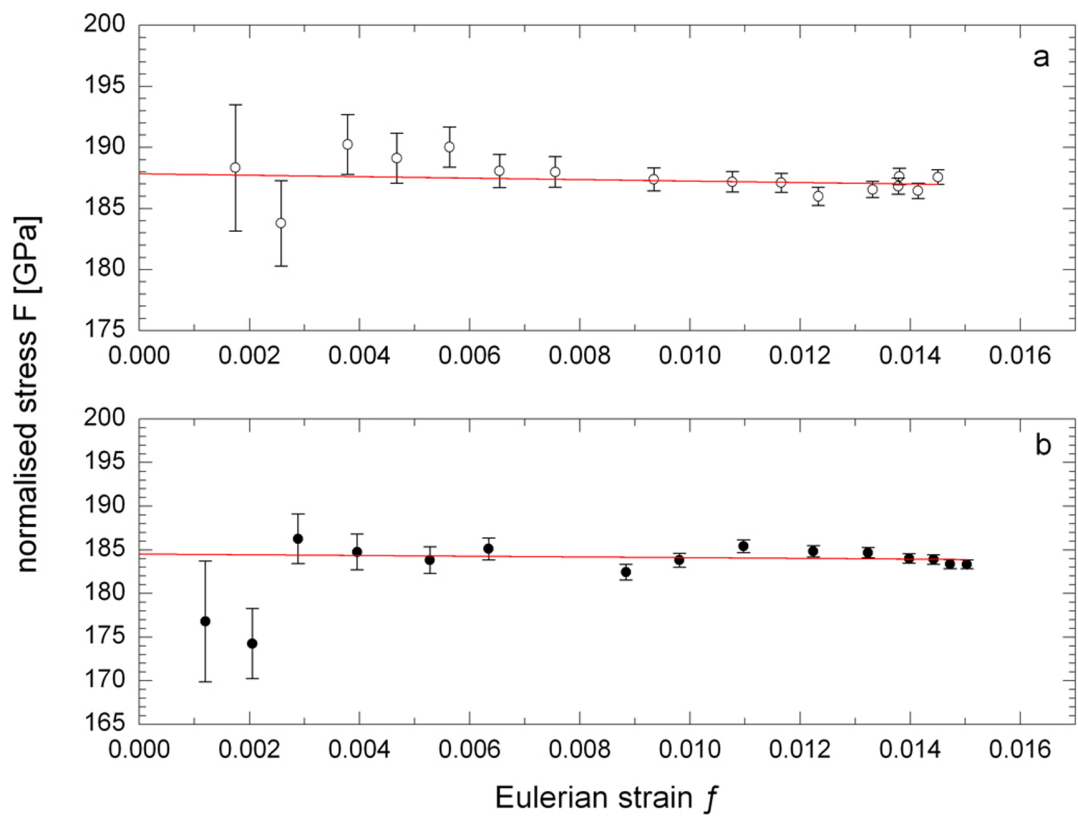


Figure 4.12: Plot of Eulerian strain f versus normalized stress F - The solid line represents a linear regression fit of data with the zero-pressure bulk modulus given by the F -axis interception at zero-pressure (a) run 3854, interception at 187.9 GPa (b) run 4218, interception at 184.5 GPa.

4.3.2 Dense hydrous Mg-Fe silicates in iron-rich systems - stabilities and mineral phase characteristics

Dense hydrous magnesium silicates, also referred to as “alphabet phases”, were studied intensively in the MgO-SiO₂-H₂O system relevant for the Earth because of their potential importance for the global water cycle. DHMS are stable at lower temperatures < 1300°C and high pressures up to 44 GPa (Shieh et al. 1998) and may serve as water carriers in the mantle. Recovered samples from experimental runs at 750°C in the pressure range 9 to 15 GPa contain the hydrous “phase A” coexisting with ringwoodite, while at 18 GPa so called “phase D” coexists with ringwoodite marking the maximum stability of phase A to be between 15 and 18 GPa (Figure 4.13). At 20 GPa phase D coexists with superhydrous B (shyB) and magnesiowüstite up to 1150°C. With increasing temperature superhydrous B decomposes at first by forming the assemblage ringwoodite - phase D - magnesiowüstite followed by the decomposition of phase D beyond 1300°C, which causes the occurrence of melt due to the excess of water. Superhydrous B and phase D are stable up to 1150°C and 1300°C, respectively, denoting that phase D represents the dominant dense hydrous magnesium silicate at elevated pressure and temperature in the MgFeSiO₄ system (Figure 4.13).

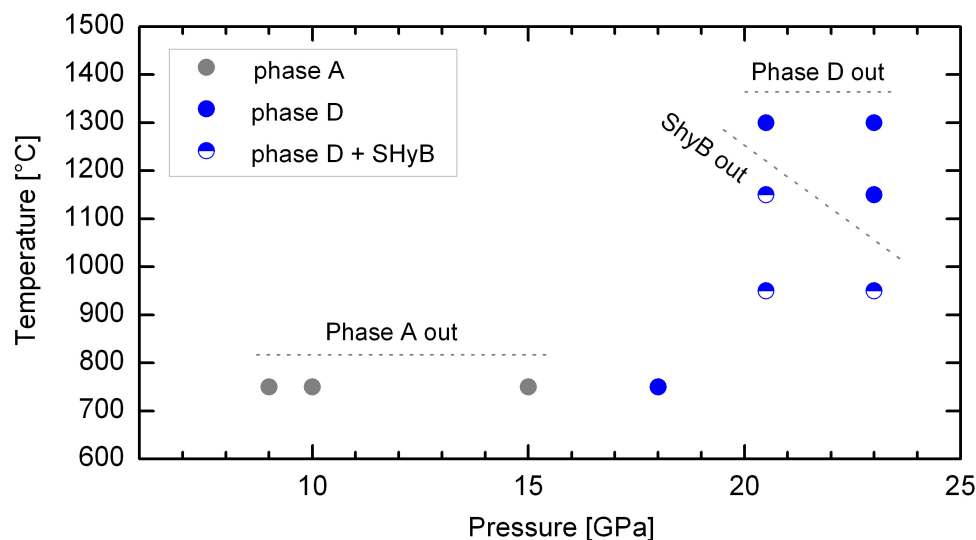


Figure 4.13: Stabilities of dense hydrous Mg-Fe silicates as a function of pressure and temperature - applying MgFeSiO₄ + 9.5 wt% H₂O bulk composition; dashed line - stability (maximum temperature) of superhydrous B (ShyB), Phase A and Phase D.

Table 4.11: EPMA data of DHMS (1σ standard deviation in parenthesis)

Sample	P, T	pts.	MgO [wt%]	SiO ₂ [wt%]	FeO [wt%]	Fe ₂ O ₃ [†] [wt%]	Total	Mineral formula
phase A - ideal formula Mg ₇ Si ₂ H ₆ O ₁₄								
GG 2580	(9 GPa, 750°C)	10	46.9(5)	24.2(3)	17.5(5)	n.a.	88.6(8)	(Mg _{5.73} Fe _{1.20}) _{6.93} Si _{1.98} H _{6.22} O ₁₄
GG 2895	(10 GPa, 750°C)	49	47.3(6)	24.0(4)	17.6(6)	n.a.	88.9(5)	(Mg _{5.80} Fe _{1.21}) _{7.01} Si _{1.97} H _{6.09} O ₁₄
GG 2539	(15 GPa, 750°C)	30	49.0(8)	24.3(2)	14.4(7)	n.a.	87.7(5)	(Mg _{5.86} Fe _{0.97}) _{6.83} Si _{1.95} H _{6.56} O ₁₄
superhydrous B - ideal formula Mg ₁₀ Si ₃ H ₄ O ₁₈								
GG 2827	(20.5 GPa, 950°C)	21	48.0(3)	25.7(3)	20.4(4)	n.a.	94.8(6)	(Mg _{8.12} Fe ²⁺ _{1.95}) _{10.07} (Mg _{0.06} Si _{2.94}) ₃ H _{3.99} O ₁₈
GG 2613	(23 GPa, 950°C)	02	54.1(7)	27.0(1)	10.1(7)	4.6(5)	95.8(2)	(Mg _{8.92} Fe ²⁺ _{0.93} Fe ³⁺ _{0.36}) _{10.21} (Fe ³⁺ _{0.02} Si _{2.98}) ₃ H _{3.23} O ₁₈
GG 2737	(20.5 GPa, 1150°C)	16	47.7(8)	26.0(9)	15.8(9)	7.2(8)	96.7(6)	(Mg _{8.22} Fe ²⁺ _{1.53} Fe ³⁺ _{0.63}) _{10.37} Si _{3.01} H _{2.56} O ₁₈
phase D - ideal formula MgSi ₂ H ₂ O ₆								
GG 2540*	(18 GPa, 750°C)	20	23(1)	53(2)	6(1)	n.a.	82.2(9)	(Mg _{0.86} Fe ²⁺ _{0.14}) ₁ (Mg _{0.14} Si _{1.56}) _{1.70} H _{3.48} O ₆
GG 2827	(20.5 GPa, 950°C)	20	25.7(6)	55.4(9)	4.7(3)	n.a.	86.1(7)	(Mg _{0.82} Fe ²⁺ _{0.12}) _{0.94} (Mg _{0.33} Si _{1.67}) ₂ H _{2.78} O ₆
GG 2613	(23 GPa, 950°C)	08	27(1)	57(2)	1.8(1)	3.0(2)	89(2)	(Mg _{1.10} Fe ²⁺ _{0.05}) _{1.15} (Mg _{0.15} Fe ³⁺ _{0.07} Si _{1.76}) ₂ H _{2.17} O ₆
GG 2737	(20.5 GPa, 1150°C)	22	26(1)	58(2)	2.0(1)	3.4(4)	89(2)	(Mg _{1.04} Fe ²⁺ _{0.05}) _{1.09} (Mg _{0.13} Fe ³⁺ _{0.08} Si _{1.79}) ₂ H _{2.17} O ₆
GG 2736	(23 GPa, 1150°C)	12	23(2)	60(2)	5.7(7)	n.a.	89(2)	(Mg _{0.87} Fe ²⁺ _{0.14}) _{1.02} (Mg _{0.17} Si _{1.83}) ₂ H _{2.32} O ₆
GG 2795	(20.5 GPa, 1300°C)	06	23.7(9)	58.7(8)	5.0(2)	n.a.	87.8(6)	(Mg _{0.85} Fe ²⁺ _{0.13}) _{0.98} (Mg _{0.22} Si _{1.78}) ₂ H _{2.49} O ₆
GG 2793	(23 GPa, 1300°C)	09	22.0(5)	60(1)	5.4(2)	n.a.	87.4(7)	(Mg _{0.79} Fe ²⁺ _{0.14}) _{0.93} (Mg _{0.20} Si _{1.80}) ₂ H _{2.54} O ₆

water contents estimated based on low microprobe totals, i.e. deviation from 100% represents the amount of water

* dominant MgSi_{2-x}H_{2+4x}O₆ substitution mechanism (see Figure 4.18)

† Electron energy-loss spectroscopy

4. HYDROUS FO₅₀ SYSTEM

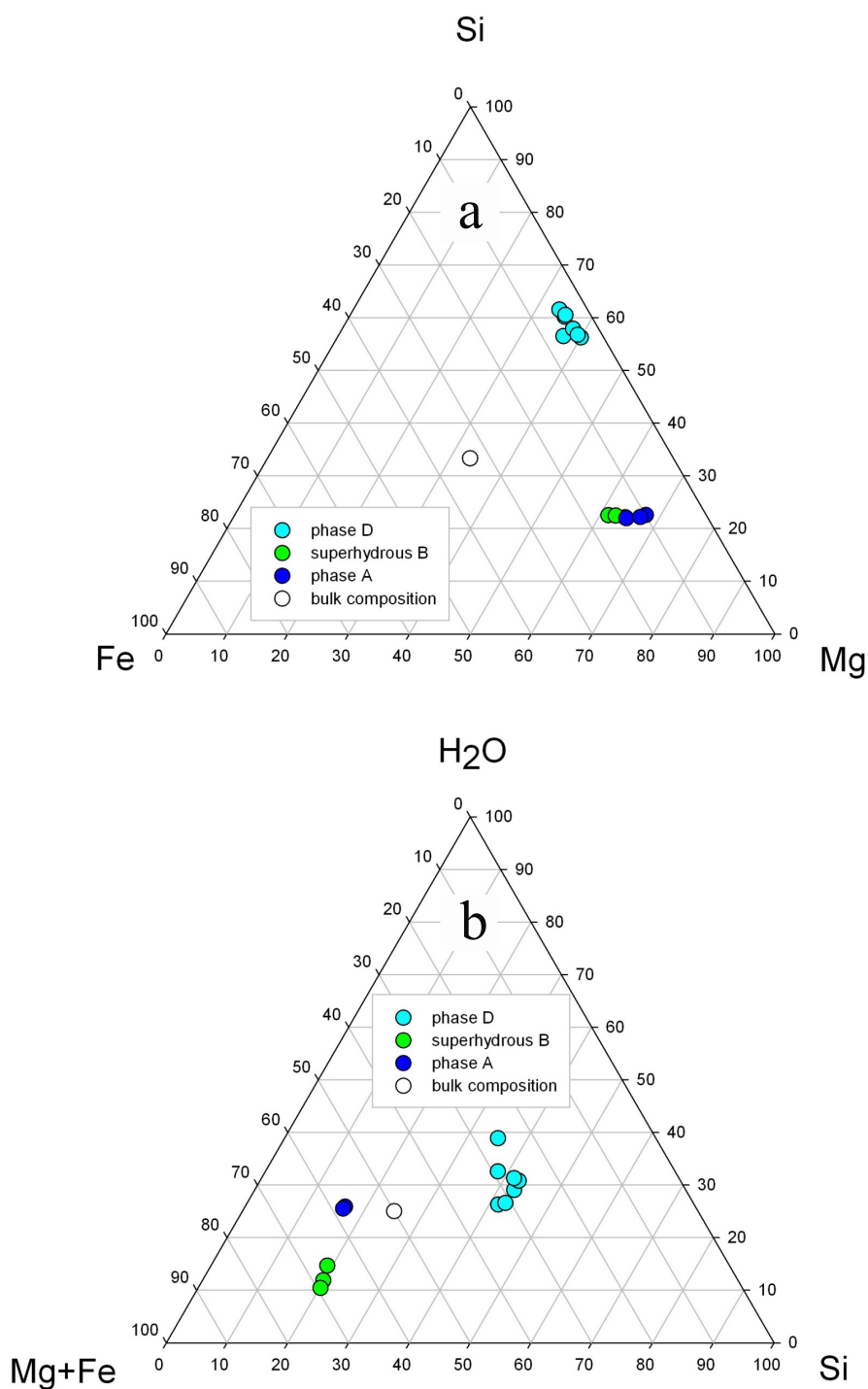


Figure 4.14: Composition of dense hydrous Mg-Fe silicates - a) ternary diagram showing compositional variations [mole%] in the Fe-Mg-Si triangle, b) ternary diagram displaying composition of hydrous phases [mole%] in the Fe+Mg-Si-H₂O system.

Mineral formulae including the water content of dense hydrous magnesium silicates are determined on the basis of deviations of microprobe totals from 100%.

I. Phase A

Phase A, $\text{Mg}_{5.73}\text{Fe}_{1.20}\text{Si}_{1.98}\text{H}_{6.22}\text{O}_{14}$ (ideal formula $\text{Mg}_7\text{Si}_2\text{H}_6\text{O}_{14}$, Yamamoto and Akimoto 1974), contains ideally 12 wt% H_2O which is also reflected by the lower microprobe analyses totals (Table 4.11). Maximal ~ 18 wt% FeO is incorporated in phase A by Mg-Fe substitution, which causes small scatter in compositional data (Figure 4.14). Structural analyses of phase A using transmission electron microscopy show a hexagonal structure with space group $P6_3$. For example, zone axes $[010]$ and $[011]$ recorded by electron diffraction patterns can be indexed in consistence with the assumed space group (Figure 4.15). Unit cell parameters $a, b = 7.896(1) \text{ \AA}$, $c = 9.595(2) \text{ \AA}$, $\alpha, \beta = 90^\circ$, $\gamma = 120^\circ$ and $V = 518.1(1) \text{ \AA}^3$ determined using single-crystal X-ray diffraction (automated four-cycle diffractometer) at Bayerisches Geoinstitut are increased in comparison to the values reported by Kagi et al. (2000) of $a, b = 7.8563(2) \text{ \AA}$, $c = 9.5642(5) \text{ \AA}$ and $V = 511.23(2) \text{ \AA}^3$. This expansion of cell parameters could be attributed to the iron-substitution.

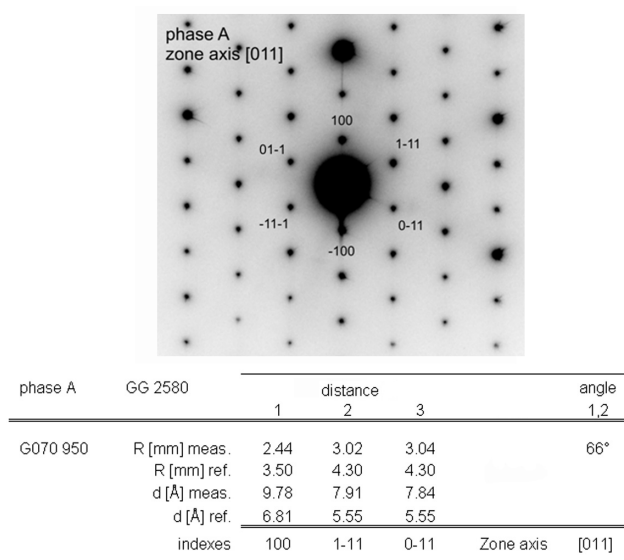


Figure 4.15: Indexed electron diffraction pattern of phase A - zone axis $[011]$; the Table displays measured and reference distances of diffraction spots in reciprocal space and interplanar distances in real space, as well as corresponding diffraction spot indices and angles between first and second measured direction.

II. Superhydrous B

Superhydrous B (SHy B) was observed in three recovered samples synthesised at 20 GPa and 950-1150°C as well as 23 GPa and 950°C. The microprobe totals are slightly variable for SHyB with an average water content of 4.3 wt%, which is less compared to the ideal water content of Mg-SHyB of 5.8 wt% H₂O. Superhydrous B contains $\text{Fe}^{3+}/\Sigma\text{Fe} = 0.29(5)$ determined by electron energy-loss spectroscopy (Figure 4.17). Thus, the determined mineral formulae of superhydrous B diverges from the ideal mineral formula $\text{Mg}_{10}\text{Si}_3\text{H}_4\text{O}_{18}$.

Obtained mineral formula $(\text{Mg}_{8.22}\text{Fe}^{2+}_{1.53}\text{Fe}^{3+}_{0.62})_{10.37}\text{Si}_{3.01}\text{H}_{2.56}\text{O}_{18}$ (sample GG 2737), however, suggest the incorporation of ferric iron by Mg-Fe³⁺- as well as Si-Fe³⁺-substitution and ferrous iron is accommodated in superhydrous B by Mg-Fe substitution with a maximum ferrous and ferric iron fraction of ~16 wt% FeO and ~7 wt% Fe₂O₃. Compositional variations of superhydrous B are not reported in the literature while slight scatter in the composition of SHyB is evident in Figure 4.14. The cation substitution mechanisms as well as creation of cation vacancies due to the accommodation of ferric iron likely causes the compositional variations. The structural properties of SHyB were investigated by analysis of diffraction patterns obtained by transmission electron microscopy. Evaluation of the zone axis $[1\bar{1}1]$ pattern of sample GG 2737 (Figure 4.16) reveals d-spacings that are, within the error limits, compatible with reference data of Mg-endmember superhydrous B.

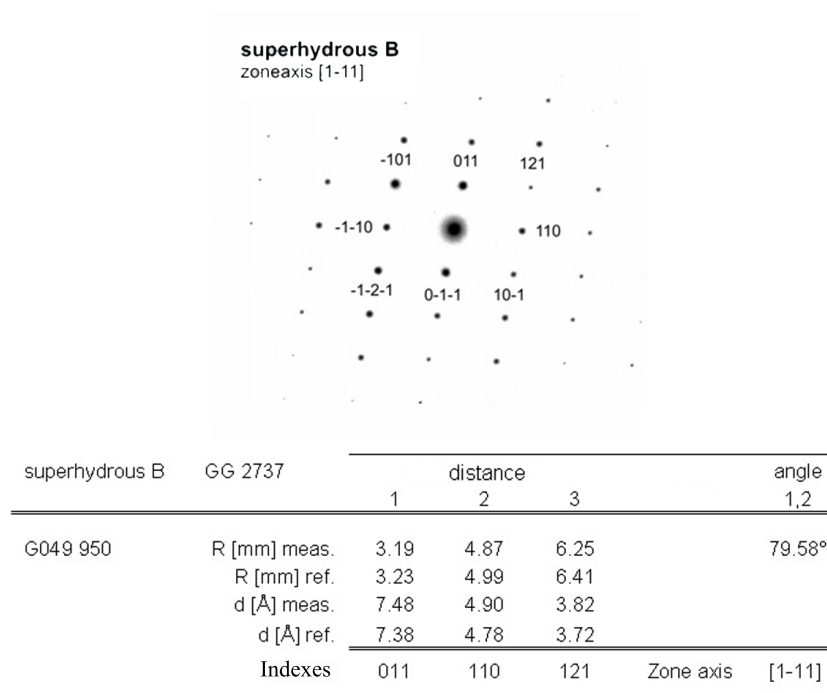


Figure 4.16: Indexed electron diffraction pattern of superhydrous B - zone axis $[1\bar{1}1]$; the Table displays measured and reference distances of diffraction spots in reciprocal space and interplanar distances in real space, as well as corresponding diffraction spot indices and angles between first and second measured direction.

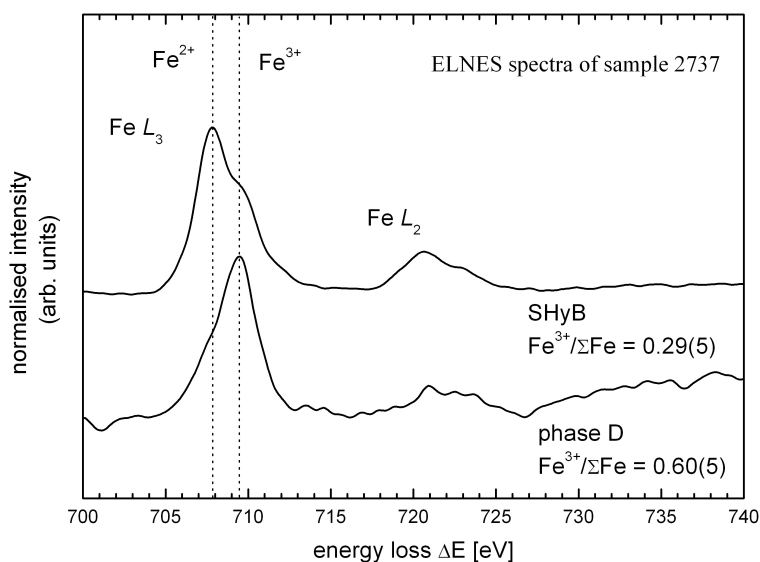


Figure 4.17: Iron $L_{2,3}$ electron energy-loss near-edge structure (ELNES) spectra of superhydrous B and Phase D - sample 2737 (20.5 GPa, 1150°C).

III. Phase D

Phase D, $\text{MgSi}_2\text{H}_2\text{O}_6$ (ideal formula) has variable compositions caused by different water contents resulting for example in Mg-endmember mineral formula $\text{Mg}_{1.11}\text{Si}_{1.89}\text{H}_{2.22}\text{O}_6$ (Yang et al. 1997). Microprobe totals of Fe-bearing phase D range from 82-89 wt% displaying the variable water content as reported for the pure Mg-endmember. Phase D is the dense hydrous magnesium silicate, which incorporates the lowest amount of total iron among the DHMS phases of about ~ 6 wt% Fe_{total} , which within error limits remains constant throughout the different samples. The ferric iron content of phase D determined by electron energy-loss spectroscopy is about $\text{Fe}^{3+}/\Sigma\text{Fe} = 0.60(5)$ (Figure 4.17). The resulting mineral formula of phase D is as follows, $(\text{Mg}_{1.04}\text{Fe}^{2+}_{0.05})_{1.09}(\text{Mg}_{0.13}\text{Fe}^{3+}_{0.08}\text{Si}_{1.79})_2\text{H}_{2.17}\text{O}_6$ (sample GG 2737). Merely the Mg- and Si-fractions vary strongly even within each sample, which is indicated by the standard deviations of the analyses given in parentheses in Table 4.11. Thus, the variable water contents and the incorporation of iron are mainly charge balanced by silicon (Si-vacancies and Si-Mg disorder) as indicated by the variations along the Si-Mg joint (Figure 4.14) and the decreasing values of Si [pfu], while Mg [pfu] and Fe [pfu] remain relatively constant (Figure 4.19). Figure 4.18 shows that Mg-Si disorder is present in most of the samples, which enables along with Fe^{3+} in the Si-site the accommodation of additional water.

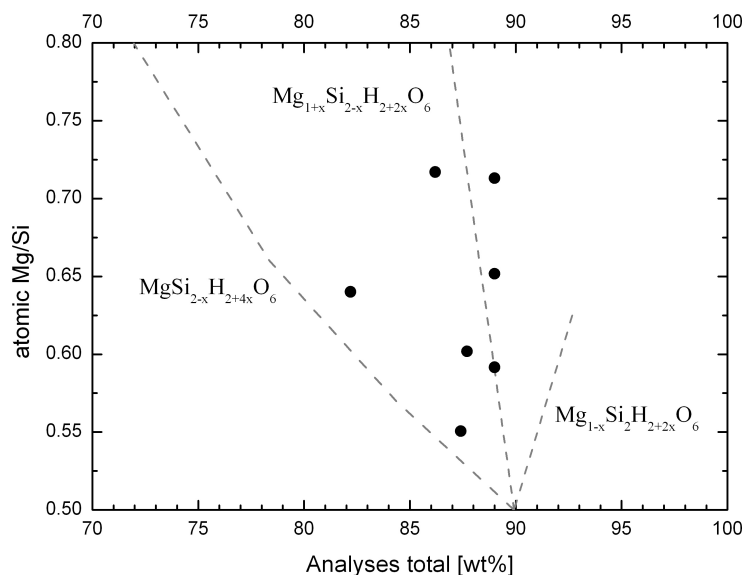


Figure 4.18: Water substitution mechanisms of phase D - dashed lines represent water substitution mechanisms.

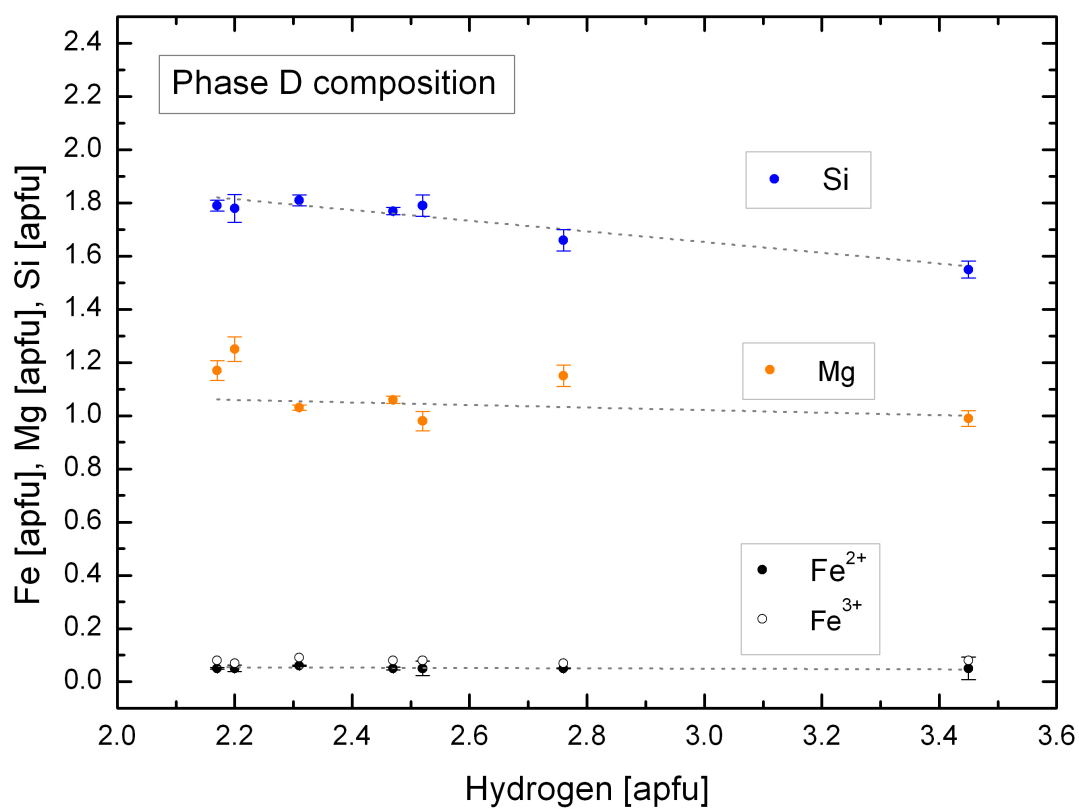
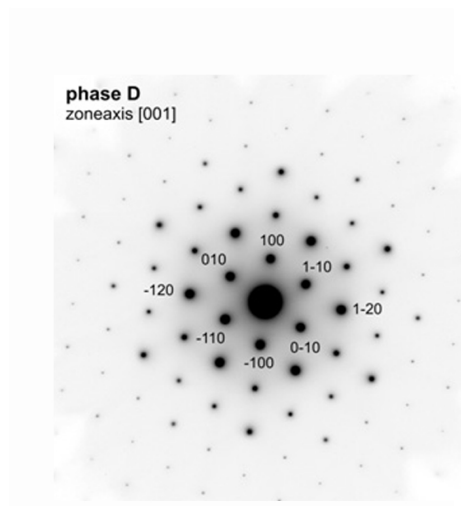


Figure 4.19: Composition of phase D - Iron, magnesium and silicon atoms per formula unit (apfu) as a function of water content (hydrogen atoms per formula unit); dashed lines - linear fit of data; water content estimations are based on the low microprobe totals.

4. HYDROUS FO₅₀ SYSTEM

The structure of phase D was investigated by electron diffraction indicating no major differences to the reference data of pure Mg-phase D. For example, zone axes [001] and [112] were indexed for sample GG 2793 and GG 2737, which are consistent with the Mg-endmember phase D (Figure 4.20).



phase D	GG 2793	distance			angle 1,2
		1	2	3	
M893 950	R [mm] meas.	5.77	5.70	5.77	60°
	R [mm] ref.	5.80	5.79	5.77	
	d [Å] meas.	4.14	4.18	4.13	
	d [Å] ref.	4.11	4.12	4.14	
	Indexes	100	1-10	0-10	Zone axis [001]

Figure 4.20: Indexed electron diffraction pattern of phase D - zone axis [001]; Table displays measured and reference distances of diffraction spots in reciprocal space and interplanar distances in real space, as well as corresponding diffraction spot indices and angles between first and second measured direction.

4.3.3 Characterisation of oxide phases - stishovite and iron oxides

The anhydrous Mg_2SiO_4 - Fe_2SiO_4 phase diagram shows that oxide phases such as magnesiowüstite and stishovite appear at elevated pressures > 20 GPa and coexist with ringwoodite (Figure 4.21). Experimental runs at 18 GPa and 1150°C as well as 20 - 23 GPa and 1400 - 1500°C yield the three phase assemblage ringwoodite (rw) + stishovite (st) + magnesiowüstite (mw). More details are mentioned in subchapter 4.3.1.1.

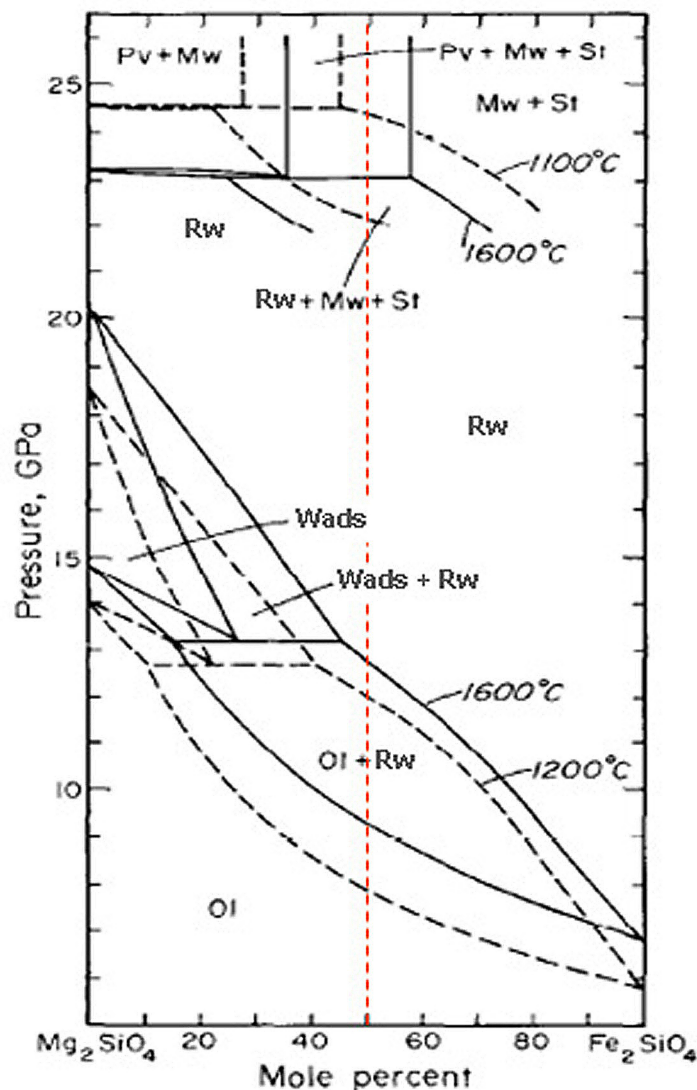


Figure 4.21: Phase diagram of the joint Mg_2SiO_4 - Fe_2SiO_4 as a function of pressure (Presnell 1995) - dashed line represents the nominal Fo_{50} bulk composition applied in this study.

Table 4.12: EPMA data of magnesiowüstite with magnesioferrite and magnetite components
(1σ standard deviation in parenthesis)

Sample	P, T	pts.	MgO [wt%]	FeO [wt%]	SiO ₂ [wt%]	Σ	Mg#	Mineral formula*
GG 2542	(18 GPa, 1150°C)	13	3.5(1)	89.8(8)	0.30(2)	93.6(8)	6.41	Mg _{0.06} Fe _{0.93} O
GG 4236	(18 GPa, 1150°C)	64	5.0(5)	88.0(6)	0.1(1)	93.1(5)	9.17	Mg _{0.09} Fe _{0.91} O
*GG 4374	(18 GPa, 1150°C)	13	7.2(3)	86.8(4)	0.10(1)	94.2(5)	12.89	Mg _{0.13} Fe _{0.87} O
GG 4374	(18 GPa, 1150°C)	12	2.6(2)	90.9(7)	0.4(4)	93.9(4)	4.88	Mg _{0.05} Fe _{0.94} O
GG 2827	(20.5 GPa, 950°C)	19	2.4(3)	89.1(4)	0.4(5)	91.8(6)	4.52	Mg _{0.05} Fe _{0.95} O
GG 2737	(20.5 GPa, 1150°C)	17	2.3(5)	92.8(9)	0.3(3)	95.4(8)	4.20	Mg _{0.04} Fe _{0.95} O
GG 2795	(20.5 GPa, 1300°C)	15	4.1(4)	87.5(7)	0.2(2)	91.7(4)	7.63	Mg _{0.08} Fe _{0.92} O
GG 4218	(20.5 GPa, 1400°C)	23	4.8(4)	86.9(5)	0.7(6)	92.5(6)	8.94	Mg _{0.09} Fe _{0.89} O
GG 2613	(23 GPa, 950°C)	10	1.5(7)	92.3(9)	0.4(2)	94.2(7)	2.86	Mg _{0.03} Fe _{0.96} O
GG 2736	(23 GPa, 1150°C)	21	2.9(2)	91.7(5)	0.2(1)	94.7(6)	5.26	Mg _{0.05} Fe _{0.94} O
GG 2793	(23 GPa, 1300°C)	15	5.1(9)	88.6(7)	0.2(1)	93.8(5)	9.24	Mg _{0.09} Fe _{0.90} O
GG 4327	(23 GPa, 1400°C)	30	7.4(5)	85.7(5)	0.50(3)	93.6(4)	13.39	Mg _{0.13} Fe _{0.86} O
GG 2800	(23 GPa, 1500°C)	10	4.7(1)	88.9(5)	0.57(4)	94.2(6)	8.69	Mg _{0.13} Fe _{0.86} O

* anhydrous MgFeSiO₄ system
 * iron assumed to be purely ferrous

The Mg-Fe oxide phases, which were analysed by EPMA, appear to be composed of magnesiowüstite, magnesioferrite and magnetite components. This is obvious from the low microprobe totals, because iron was measured as FeO and the deviation from 100% EPMA totals is the result of the ferric iron fraction (Table 4.12). However, the amount of ferric iron in the Mg-Fe oxide phases is unknown and it is difficult to determine the fraction of each component. Therefore, the Mg-Fe oxides are referred to as magnesiowüstite, since this oxide phase was observed by TEM analyses (see below).

Magnesiowüstite coexists with dense hydrous magnesium silicates (DHMS) in the pressure range of 20 - 23 GPa and temperatures between 950 - 1300°C. The chemical composition of magnesiowüstite varies from 84 - 96 mol% FeO. The structure of magnesiowüstite was examined using electron diffraction. Measured diffraction spot distances in reciprocal and real space were compared with reference data of wüstite FeO (space group $Fm\bar{3}m$, $a = 4.311 \text{ \AA}$). Within the error limits of electron diffraction, structural properties of magnesiowüstite are consistent with the reference data. Magnetite is present in sample GG 2613, GG 2793 and GG 4327 indicating oxidising run conditions, which could be due to the slightly oxidising character of the platinum capsule as well as the loss of hydrogen through the platinum capsule resulting from the dissociation of water. Ferric iron is dominantly present implying that the loss of water is not extensive. Also, the relative abundance of magnetite compared to magnesiowüstite is very small. Bright field TEM images show that magnetite crystals are small ($<2\mu\text{m}$) and appear locally in association with magnesiowüstite, hence the dimensions are too small to resolve the chemical composition of magnetite by EPMA (Figure 4.22, 4.23). It is likely that the Fe^{3+} contents of the recovered samples differ due to the extent of hydrogen loss from the capsule depending on the heating duration.

4. HYDROUS FO₅₀ SYSTEM

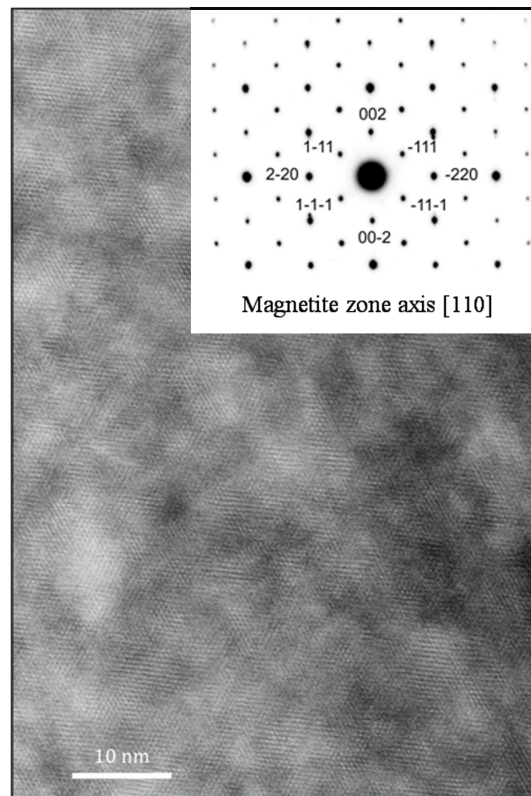


Figure 4.22: High-resolution TEM image of magnetite - zone axis [110] sample GG 2613 (23 GPa, 950°C).

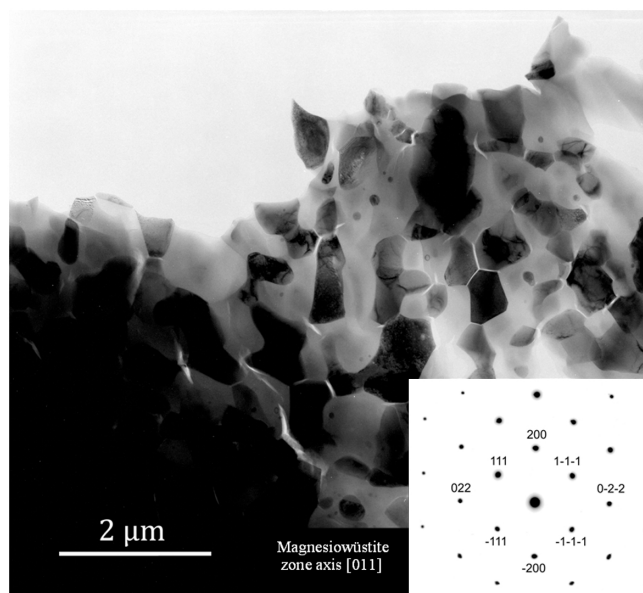


Figure 4.23: Bright-field TEM image of magnesiowüstite - enclosing magnetite grains, sample GG 2613 (23 GPa, 950°C).

4.4 Discussion and conclusions

In respect of the data presented in this study, the following conclusions are drawn concerning I. the effect of hydrogen and Fe substitution on the Mg_2SiO_4 ringwoodite structure, II. the effect of Fe-substitution on the O-H stretching mode of hydrous ringwoodite, III. the effect of hydrogen and Fe substitution on the compressibility of Mg_2SiO_4 ringwoodite, IV. water substitution mechanisms and water contents of ferroan ringwoodite and V. the stability of dense hydrous Mg-Fe silicates in iron-rich systems.

4.4.1 Effect of hydrogen and Fe substitution on the Mg_2SiO_4 ringwoodite structure

The two Fe-bearing ringwoodite samples used for this study differ not only in the water contents, but also in their $\text{Fe}^{3+}/\Sigma\text{Fe}$ ratios (Table 4.8). The large abundance of octahedral vacancies (run GG 4218) is rather the result of the oxidation of iron (defect equation 4.7), which is not balanced by the protonation of oxygen (McCammon et al. 2004), because the amount of water in sample 4218 of ~ 0.37 wt% H_2O is relatively small. The uncertainties of the microprobe analyses are such that it is difficult to discriminate whether octahedral vacancies are present, however the structural refinements (Table 4.9) clearly indicate that these are indeed more abundant in sample 4218 and cannot be exclusively due to H incorporation. The Fe^{3+} -content and vacancies, however, appear to have little effect on the unit-cell volume of ringwoodite (Figure 4.9), in contrast with what is reported for non-stoichiometric $T(\text{Mg}_{0.4}\text{Al}_{0.6})^M(\text{Al}_{1.8}\square_{0.2})\text{O}_4$ -spinel (Nestola et al. 2009), which has a much smaller unit-cell volume than stoichiometric MgAl_2O_4 -spinel (Nestola et al. 2007). There is some evidence, at least for the Mg_2SiO_4 -ringwoodite end member that H incorporation increases the unit-cell volume (Smyth et al. 2003). The hydrous ringwoodite samples (this study) lie above the straight line connecting the anhydrous end-members (Figure 4.9) suggesting that such a hypothesis also is valid for iron-rich ringwoodites. The octahedral bond distance increases with increasing iron content (Figure 4.10a) and appears to be only slightly affected by the H incorporation. In contrast the T-O distance appears to have the same value for anhydrous Mg_2SiO_4 and Fe_2SiO_4 ringwoodites but increases with increasing H content (Figure 4.10b) (Smyth et al 2003). An increase of the T-O bond distance also has been attributed by Hazen et al. (1993) to Mg / Si disorder between the octahedral and tetrahedral site. However, the water content of the samples studied by Hazen et al. (1993) was not

measured and therefore it is difficult to assess the real effect of Mg/Si disorder, given the difficulty to determine the disorder from X-ray diffraction data due to the close similarity of the scattering curves of Si and Mg.

4.4.2 Effect of Fe-substitution on the O-H stretching mode of hydrous ringwoodite

The position of the absorption maxima corresponding to the OH-stretching modes in the IR spectra of hydrous ringwoodites increases with increasing Fe-content (Figure 4.8). The OH-stretching frequency depends on the bond strength of the O-H \cdots O bond. With increasing iron content the bond strength A-H \cdots B changes from strong to weak according to the classification given by Emsley (1980). Weak bonds are defined as those with reduced proton transfer between atom A and B, i.e. with the hydrogen atom remaining covalently bond to the parent atom A. This causes the shift of the OH-stretching frequencies to higher wavenumbers since the interaction between H \cdots B is reduced. Normally, weaker hydrogen bonds, i.e. higher OH-stretching wavenumbers, are observed when the bond distance O \cdots O increases (Libowitzky and Beran 2004). The structure refinement of ferroan ringwoodite (this study) indicates no change in O-O distance of the tetrahedral site with respect to the Mg₂SiO₄-ringwoodite end-member (Sasaki et al. 1982; Kudoh et al. 2000; Smyth et al. 2003) but an increase of the O-O distance of shared and unshared edge octahedral sites (Table 4.9). Therefore both the observation of the presence of octahedral site vacancies as indicated from structural refinements and the correlation between the O-O octahedral edge and the wavenumber shift of the OH-mode (Figure 4.24) point to the octahedral site as the most favoured protonation site. This is in agreement with a recent theoretical study, which assigns the main absorption band of the OH-stretching mode to protons located between the O-O pairs shared by octahedra (Blanchard et al. 2009).

It appears also that a ferric iron plus vacancies substitution has a strong effect on the OH-stretching frequencies since the absorption maximum of run 4218 Fo₆₀-ringwoodite with 13% ferric iron is located at 3300 cm⁻¹ (Figure 4.8), i.e. at larger wavenumber than that of run 3854 Fo₅₀-ringwoodite.

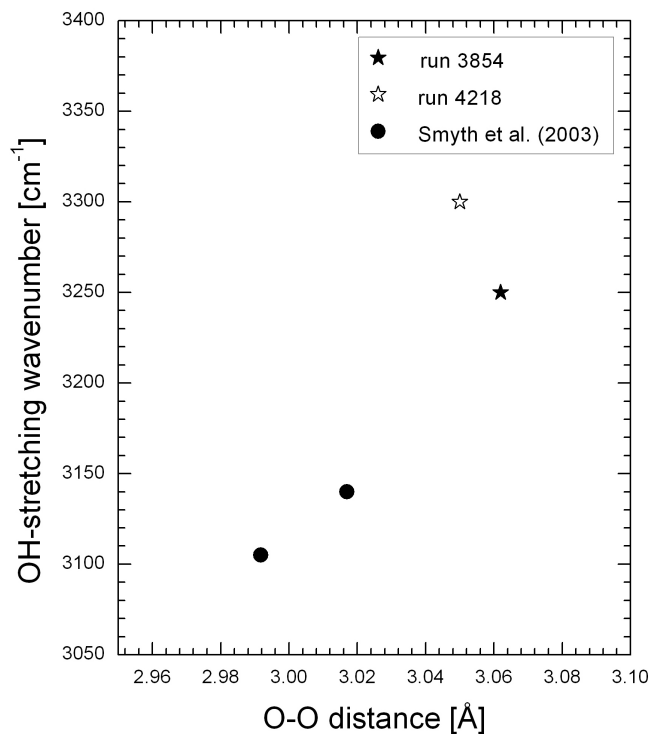


Figure 4.24: Correlation between the OH-stretching wavenumber and the O-O distance of the octahedral shared edge - solid circles - Smyth et al. (2003); solid asterisk - sample GG 3854 (this study), open asterisk - sample GG 4218 (this study).

4.4.3 Effect of hydrogen and Fe substitution on the compressibility of Mg₂SiO₄ ringwoodite

The bulk modulus of hydrous ferroan ringwoodites obtained in this study are very similar ($K_{T0} = 186.5(9)$ and $K_{T0} = 184.1(7)$ GPa for samples 3854 and 4218 respectively) and have values close to those reported for dry Mg-ringwoodite (Table 4.13). Hazen (1993) reports for Fe₆₀, Fe₈₀ and end-member Fe₂SiO₄ ringwoodites values of bulk moduli ranging between 203 and 207 GPa with a K' fixed to the value of 4.8. For comparison we have also used a Birch-Murnaghan EoS with K' fixed to the value of 4.8 to fit our P-V data with resulting EoS parameters:

$V_0 = 543.38(8) \text{ \AA}^3$ and $K_{T0} = 183.1(9)$ GPa for run 3854 and $V_0 = 539.05(6) \text{ \AA}^3$ and $K_{T0} = 181.0(7)$ GPa for run 4218. Thus, our samples appear to be more compressible than the ferroan ringwoodites studied by Hazen (2003). There is some evidence that vacancies associated with the H incorporation

4. HYDROUS FO₅₀ SYSTEM

strongly increase the compressibility of Mg₂SiO₄ ringwoodite (Table 4.13). If we assume that the samples studied by Hazen (1993) were anhydrous ferroan ringwoodites the decrease of the bulk moduli values observed in our samples may be a consequence of the presence of vacancies. This suggestion also is supported by the fact that the sample 4218, which has the larger amount of vacancies due to iron oxidation, also is slightly more compressible than sample 3854. A strong increase in compressibility associated with the presence of octahedral vacancies has also been observed for non-stoichiometric $T(\text{Mg}_{0.4}\text{Al}_{0.6})^M(\text{Al}_{1.8}\square_{0.2})\text{O}_4$ -spinel (Nestola et al. 2009). A recent theoretical study by Li et al. (2009) predicts a linear decrease of bulk modulus with increasing water content of ringwoodite, i.e. an increasing amount of octahedral vacancies. Ferroan ringwoodite with up to 0.71 wt% H₂O (this study), however, does not show the predicted increase in compressibility within the analytical accuracy. However, a recent study on Fe₂SiO₄-ringwoodite (Nestola et al., submitted to PEPI) reports a value of bulk modulus very similar to that of (Mg,Fe)₂SiO₄-ringwoodite found in this study, suggesting therefore that the Fe substitution has little effect on the compressibility of ringwoodite. This would suggest therefore that the oxygen closed-packing of the spinel structure plays a major role in determining its compressibility and this cannot be affected by the presence of less than 1% of water or of up to 0.1 atoms per formula unit of vacancies.

Table 4.13: Compressibility of ringwoodite and spinel phases.

Phase	H ₂ O [wt%]	K _{T0} [GPa]	Mg#	K' [dK/dP]	Method	P ^{max} [GPa]	Reference
ringwoodite							
—	—	100	185(3)	—	BS	0	Jackson et al. 2000
—	—	100	185(2)	4.5(2)	US	12	Li 2003
—	—	100	184(2)	—	BS	0	Weidner et al. 1984
—	—	100	199(9)	4.19	theory*	30	Kiefer et al. 1997
—	—	92	188(3)	4.1(2)	BS	16	Sinogeikin et al. 2003
—	—	100	184(2)	4.8(fixed)	XRD	5	Hazen 1993
—	—	40	203(2)	4.8(fixed)	XRD	5	Hazen 1993
—	—	20	205(2)	4.8(fixed)	XRD	5	Hazen 1993
—	—	0	207(3)	4.8(fixed)	XRD	5	Hazen 1993
—	—	0	187(2)	5.5(4)	XRD	10	Nestola et. al (submitted)
hydrous ringwoodite							
run 4218	2.3	100	165.8(5)	—	BS	0	Wang et al. 2003
run 3854	2.2	100	155(4)	—	BS	0	Inoue et al. 1998
run 4218	~1	88	176(7)	—	US	0	Jacobsen et al. 2004
run 3854	~1	88	177(4)	5.3(4)	US	9	Jacobsen and Smyth 2006
run 4218	~1	88	175(3)	6.2(6)	XRD	45	Manghani et al. 2003
run 3854	0.93	89	169(3)	7.9(9)	XRD	11.2	Smyth et al. 2004
run 4218	~0.4	61	184.1(7)	4 (fixed)	XRD	8.9	this study
run 3854	~0.7	49	186.5(9)	4 (fixed)	XRD	8.8	this study
spinel phase							
run 4218	—	185(3)	—	5.1(1)	US	8.7	Reichmann and Jacobsen 2004
run 3854	—	193(1)	—	5.6(3)	XRD	7.5	Nestola et al. 2007
run 4218	—	171(2)	—	7.3(6)	XRD	8.7	Nestola et al. 2009

* calculated values using plane-wave pseudopotential method

4.4.4 Water substitution mechanisms and water contents of ferroan ringwoodite

I. Water content of ferroan ringwoodite

Pure Mg-ringwoodite can accommodate up to 2.3 wt% H₂O (Wang et al. 2003). Ferroan ringwoodite with 12 mole% Fe₂SiO₄ incorporates about 1 wt% H₂O as reported by Jacobsen et al. (2004) and Manghnani et al. (2005). The current study showed that ferroan ringwoodite (with 25 - 50 mole% Fe₂SiO₄) synthesised in the MgFeSiO₄ + 9.5 wt% H₂O system accommodates ~0.4-0.7 wt% H₂O which is slightly less than previously reported for ferroan ringwoodite and considerably less compared to the Mg-endmember (Figure 4.25). This implies a potential inverse correlation between iron-fraction and water content of ringwoodite, i.e. the water content decreases with increasing Fe-content of ringwoodite. The effect of iron on the water storage capacity of ringwoodite appears to be clearly obvious though not continuous since ringwoodite shows strong variations in Fe-content (between FO₅₀ and FO₇₅) but similar water storage capacities between 0.4 - 0.7 wt% H₂O. The slightly lower water storage capacities were observed for ringwoodite containing Fe³⁺, which implies that the water substitution is rather diminished than enhanced by oxidation of iron (Table 4.14).

Table 4.14: Correlation of composition (Fe³⁺-content) and water-content of ringwoodite

sample	Fe# [mole%]	Fe ³⁺ /ΣFe	Fe ³⁺ content	Water content
	Fe/(Mg+Fe)*100	EELS	relative to Fe#	[wt%]
GG 3854	50.72	0.01(5)	0.05%	0.71
GG 4327	25.42	0.03(5)	0.76%	0.62
GG 2542	51.28	0.07(5)	3.59%	0.50
GG 4218	38.60	0.13(5)	5.02%	0.37

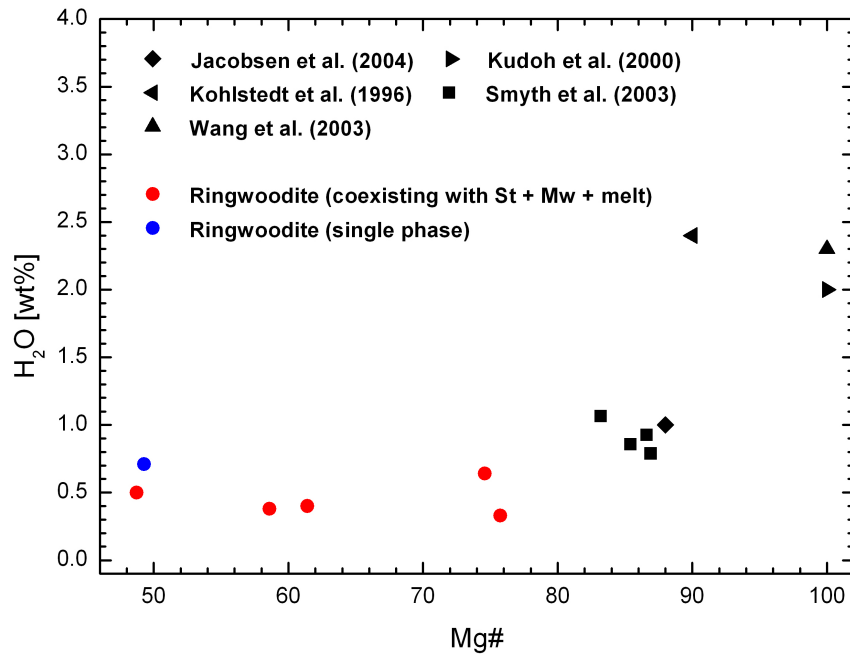


Figure 4.25: Water content of Mg- and MgFe-ringwoodite - Illustration of the inverse correlation between iron-fraction and water-content of ringwoodite; black symbols denote literature data, blue and red circles represent data obtained in this study; abbreviations are St - stishovite, Mw - magnesiowüstite.

Hirschmann et al. (2005) postulated that the water storage capacity of nominally anhydrous minerals is influenced by mineral phase assemblages and can therefore change with different coexisting phases because the water content is dependent on water- and iron-partitioning between coexisting mineral phases. According to the particular temperature, fluid or melt coexist with mineral phases due to the finite capacity of water incorporation in NAMs (Figure 4.26). The constitution of quenched material indicates that the silica-content of the melt increases with increasing temperature. This implies that the water activity decreases and consequently also the water storage capacity of present nominally anhydrous minerals. Additionally, the water partitioning coefficient between mineral and melt of $D_{\text{mineral/melt}}^{\text{water}} = 0.01$ concerning upper mantle minerals (Hirth and Kohlstedt 1996) displays the enhanced solubility of water in melt rather than in mineral phases e.g. ringwoodite. Thus, ringwoodite developed as single phase (GG 3854) is representative for comparison with literature data, since further potential influences on the water storage capacity of hydrous ferroan ringwoodite in addition to the ringwoodite-composition are eliminated such as melt occurrence.

4. HYDROUS FO₅₀ SYSTEM

Figure 4.25 shows that the water storage capacity of ringwoodite developed as three phase assemblage with melt is reduced. Even ringwoodite with lower Fe-fraction does not reach the water content values as reported for Mg₈₃₋₈₇-ringwoodite by Smyth et al. (2003) because of the presence of silicate-rich melt and the subsequently lower water activity. Ringwoodite crystals studied by Jacobsen et al. (2004) and Kohlstedt et al. (1996) coexist with stishovite. It is likely that stishovite does not influence the water storage capacity of ringwoodite since the water partitioning coefficient between ringwoodite and stishovite of about $D_{rw/st}^{water} \sim 521$ (Bolfan-Casanova et al. 2000) shows that it rather enhances the water content of ringwoodite. Ringwoodite coexists with phase B, a dense hydrous magnesium silicate, in the sample synthesised by Kohlstedt et al. (1996) which could affect the water storage capacity of ringwoodite since the water partitions preferentially in phase B. Thus, the variable water storage capacity of ringwoodite obtained in this study is a consequence of coupled effects by composition of coexisting melt, composition of ringwoodite and coexisting hydrous phases such as dense hydrous magnesium silicates.

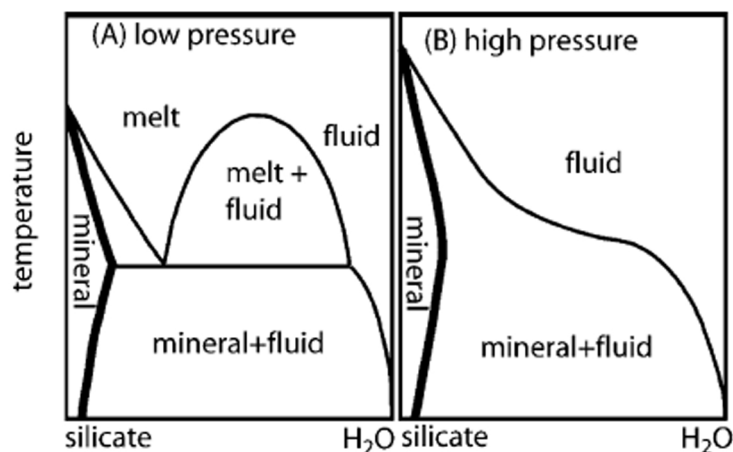
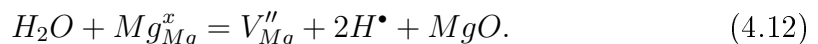


Figure 4.26: Schematic illustration of the water storage capacity of nominally anhydrous minerals - mineral phases with finite capacity to incorporate water (Hirschmann et al. 2005); (A) minerals coexists at low pressure and low temperature with H₂O-rich fluid and with hydrous silicate melt at high temperature (B) mineral phases coexist at high pressure with water-rich fluid at low temperature and silicate-rich fluid at high temperature.

II. Water substitution mechanisms of ferroan ringwoodite

The tetrahedral (Smyth et al. 2003; Chamorro Pérez et al. 2006) and octahedral edges (Kudoh et al. 2000; Ross et al. 2003) have been suggested to be the most probable protonation sites in ringwoodite. Structure refinement of hydrous ferroan ringwoodite obtained in this study indicates that octahedral site vacancies occur due to the accommodation of water (defect equation 4.12) and the oxidation of ferrous iron (defect equation 4.7). Chemical analyses and structure refinement show small concentrations of Si-site vacancies (within the analytical accuracy) which would imply the presence of $\text{Si}^{4+} = 4 \text{H}^+$ mechanism. Similar scattering factors of Mg and Si complicate the determination of Mg-Si disorder by x-ray diffraction methods. Thus, Mg-Si disorder can not be definitely excluded. However, the shifts of the OH-stretching frequency to higher wavenumbers observed in IR-spectra denote an increase of O-O bond distance which was exclusively determined for the octahedral site. This implies that the accommodation of water in ferroan ringwoodite is predominantly accomplished by protonation of octahedral sites, i.e. Mg-site vacancies (defect equation 4.12). This is consistent with recent theoretical studies based on energy considerations (Blanchard et al. 2009; Li et al 2009), suggesting that the Mg-substitution by two protons is the most favorable protonation mechanism, although Li et al. (2009) argue that both type of defects are abundant in synthetic samples. Water substitution mechanisms that create Fe-vacancies are not described in the literature, also Fe-Si disorder was not observed for hydrous ferroan ringwoodites (Hazen et al. 1993). Iron substitutes preferentially into the octahedral site by Mg-Fe substitution, and therefore the water incorporation in ferroan ringwoodite may be limited due to certain amounts of iron occupying octahedral positions, and the creation of non-protonated Mg-site vacancies as a result of the oxidation of iron. This consequently reduces the amount of possible protonation sites, i.e. the water content of ferroan ringwoodites. In summary, water is dominantly incorporated by Mg-substitution mechanisms in ferroan ringwoodite of this study:



4.4.5 The stability, iron partitioning and point defect chemistry of dense hydrous Mg-Fe silicates in iron-rich systems

The development of phase assemblages is affected by water addition since dense hydrous magnesium silicates, so called “Alphabet phases”, are stabilised and coexist with nominally anhydrous minerals such as ringwoodite. Figure 4.27 displays the observed phase assemblages of dense hydrous magnesium silicates (DHMS) and ringwoodite as well as ringwoodite without DHMS. The comparison to the diagram by Kawamoto (2004) shows that “phase E” is absent in the hydrous MgFeSiO₄ system, which also implies that phase E becomes unstable with certain iron-contents of the bulk composition. At a temperature of 750°C, ringwoodite is stable down to 9 GPa, which corresponds to the stability field of olivine and instead of phase E, ringwoodite coexists with phase A. Phase D was observed in this study at 23 GPa and 1300°C, which is at higher temperature than reported for Mg-endmember phase D synthesised from Mg₂SiO₄ bulk composition with a comparable water content of 11 wt% H₂O. However, phase D shows larger thermal stability than superhydrous B, which is contrary to data reported by Ohtani et al. (2000) and Frost (1999). The stability of phase D is extended up to the stability field of ringwoodite in comparison to the data by Ohtani et al. (1997) for Mg-endmember phase D with Mg₂SiO₄ + 11 wt% H₂O (Figure 4.28). Kawamoto (2004) showed that phase D synthesised from KLB-1 + 13.6 wt% H₂O bulk composition decomposes at around 1250°C and superhydrous B is stable up to ~1300°C at 24 GPa, which is the opposite case in the present study. However, structural properties of phase D and superhydrous B remain unaffected by the iron substitution as indicated by similar lattice parameters in comparison to the Mg-endmembers. Thus, structural reasons can be excluded to cause this observation. It remains unclear, what causes the transposition of the thermal stability of superhydrous B and phase D and whether simply the bulk iron content could be the reason for this observation.

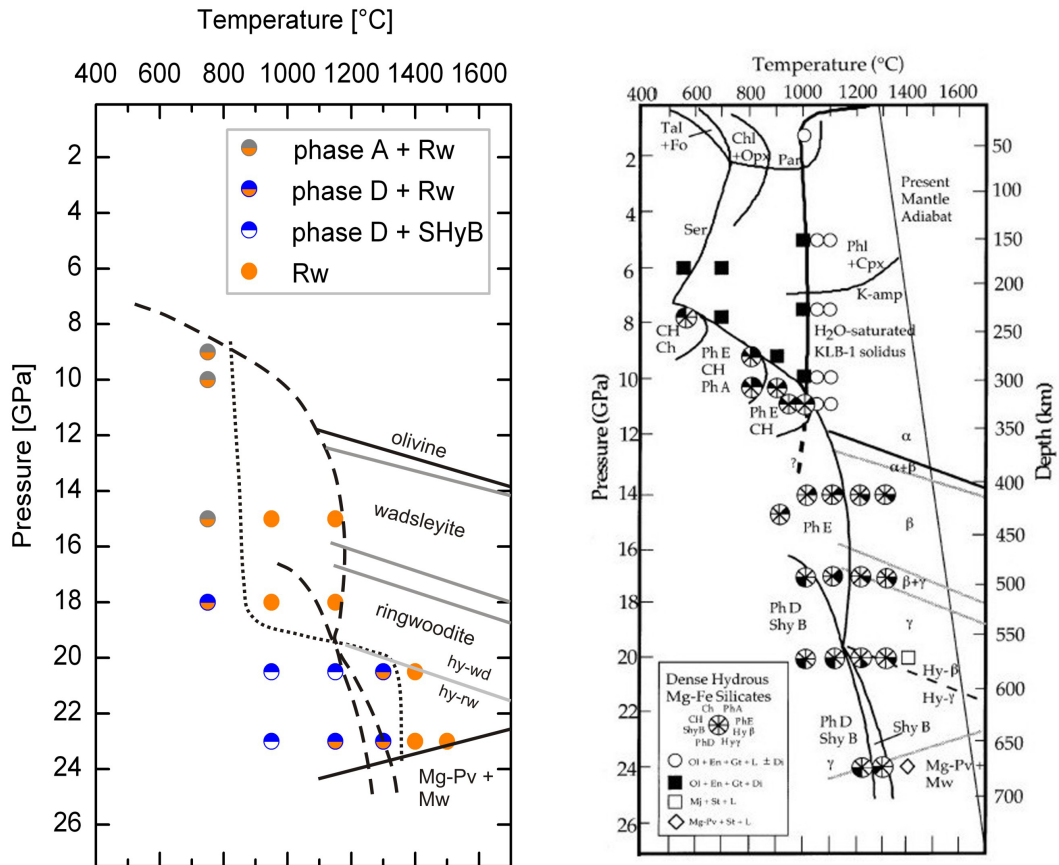


Figure 4.27: Phase assemblages as a function of pressure and temperature - right - data from Kawamoto (2004) applying KLB-1 + 13.6 wt% H_2O bulk composition, left - this study applying $\text{MgFeSiO}_4 + 9.5 \text{ wt\% H}_2\text{O}$ bulk composition; dotted line represents the temperature limit of dense hydrous Mg-Fe silicates (this study), dashed and solid lines - from Kawamoto (2004).

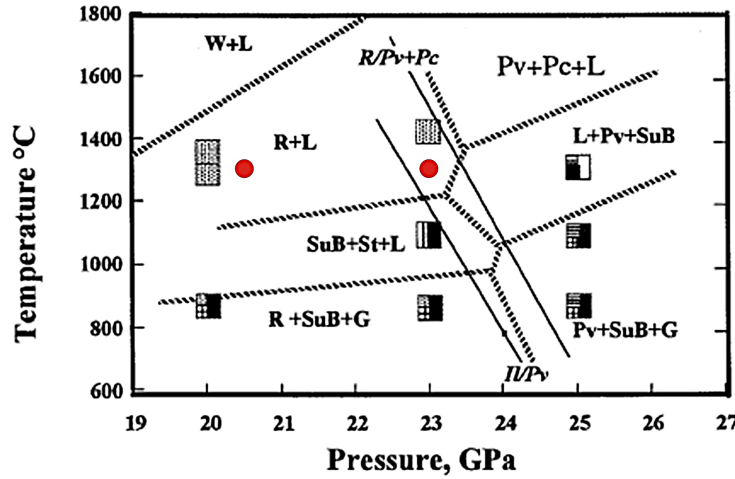
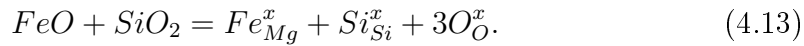


Figure 4.28: Phase relations for the $\text{Mg}_2\text{SiO}_4 + 11 \text{ wt}\% \text{ H}_2\text{O}$ bulk composition - red circles represent the maximum pressure-temperature stability of phase D obtained in this study; abbreviations are L - liquid, W - wadsleyite, St - stishovite, Pv - perovskite, R - ringwoodite, Pc - periclase, Il - ilmenite, G - phase G/D/F, SuB - superhydrous B and Bc - brucite (from Ohtani et al. 2000).

I. Point defect chemistry of dense hydrous Mg-Fe silicates and iron partitioning between DHMS and ringwoodite

The incorporation of ferrous iron in dense hydrous magnesium silicates occurs by the common Fe^{2+} -Mg substitution into octahedral sites, whereas ferric iron occupies Si- and Mg-site. The following equations represent the observed cation- and water-substitution mechanisms for phase A, superhydrous B and phase D (for notation see Kröger and Vink 1956)⁴:

Fe²⁺ in Mg-site



⁴ Mg_{Mg}^x - Mg in Mg-site, $\text{V}_\text{O}^{\bullet\bullet}$ - oxygen vacancy, $\text{O}_i^{\bullet\bullet}$ - O^{2-} on an interstitial site, Fe'_{Si} - ferric iron in Si-site, V''_{Mg} - Mg-vacancy, Fe^*_{Mg} - ferric iron in Mg-site; x - neutral site, ' - positive undercharge, • - negative undercharge

Chemical analyses of phase D showed that iron is not involved in water-substitution mechanisms, because the Fe-content is constant throughout the entire variation range of water contents. Thus, higher water contents, which are observed for phase A and phase D are mainly charge balanced by:

Mg-site vacancies

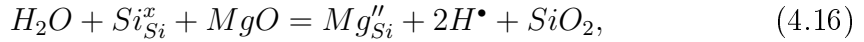


Si-site vacancies



which are dominant in phase A, minor in phase D and insignificant for superhydrous B and:

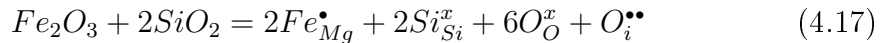
Mg-Si disorder



which is observed for phase D and superhydrous B, but when ferric iron is present in SHyB the Mg-Si disorder mechanism is eliminated.

EELS measurements of phase D and superhydrous B yield $Fe^{3+}/\Sigma Fe = 0.60(5)$ and $Fe^{3+}/\Sigma Fe = 0.29(5)$, respectively. Superhydrous B accommodates ferric iron mainly in the Mg-site (defect equation 4.17) and to a small extent in the Si-site, which results in reduced water contents (Table 4.11). On the contrary, phase D incorporates the ferric iron only in the Si-site (based on chemical analyses) resulting in slightly higher water contents compared to the ideal formula of phase D:

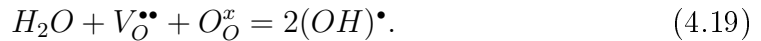
Fe³⁺ in Mg-site



Fe³⁺ in Si-site



while the created oxygen vacancy is charge balanced by hydroxyl-groups:



4. HYDROUS FO₅₀ SYSTEM

Figure 4.18 shows Mg/Si ratios versus analyses totals (assumed to correspond to the water content) of phase D, which gives information about the dominant water substitution mechanisms. Thus, according to Figure 4.18 and the calculated mineral formulae of phase D, it can be estimated that water substitution mechanisms involving the Si-site are favoured (equation 4.16). This is in agreement with Frost and Fei (1998) and Frost (1999) who reported that Si-content and water concentration of phase D are related (Figure 4.29). Yang et al. (1997) also suggested Mg-Si disorder as water substitution mechanism, which can be also observed in iron-bearing phase D (this study, Figure 4.18). Subordinate Mg- and Si-site vacancies (equation 4.14, 4.15) are also observed while Mg-Si disorder is the most common water substitution mechanism in iron-bearing phase D.

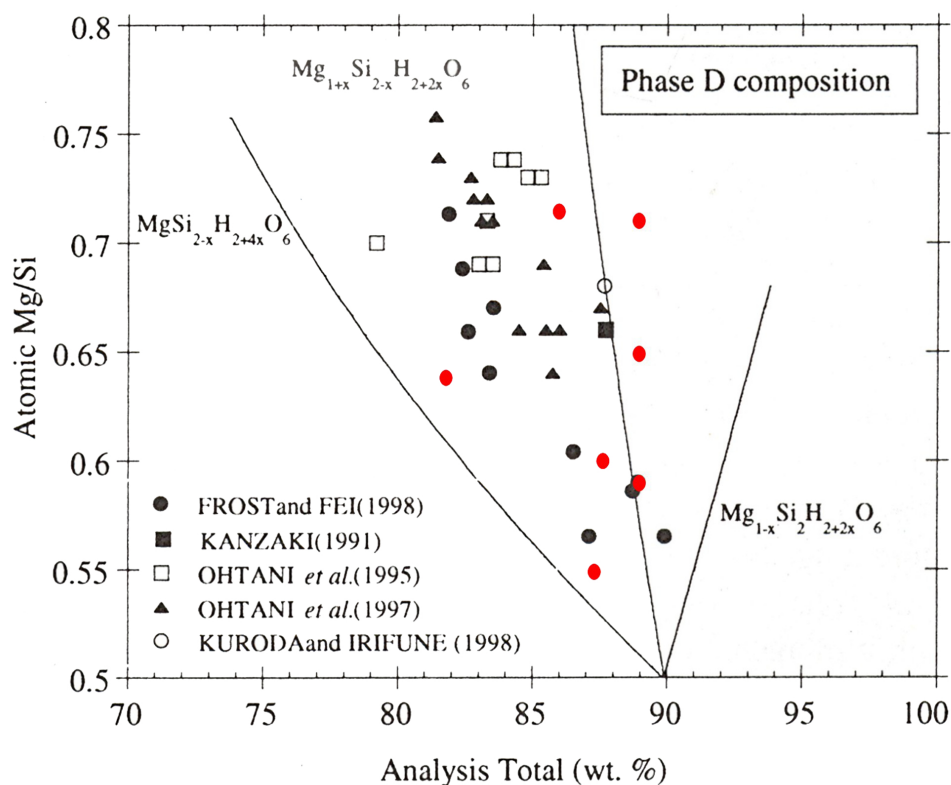


Figure 4.29: Water substitution mechanisms of phase D - modified diagram from Frost (1999); red circles represent Mg/Si ratio of iron-bearing phase D (this study).

The iron substitution into dense hydrous magnesium silicates - nominal hydrous minerals - is apparently limited to ~ 6 wt% Fe_{total} for phase D and 17-22 wt% Fe_{total} for phase A and superhydrous B, respectively. Despite the limited iron substitution of DHMS, these dense hydrous Mg-Fe silicates are stable in iron-rich systems up to at least 50 mole% Fe_2SiO_4 of the bulk composition. The iron partitions preferentially into the coexisting ringwoodite (Figure 4.30) and phase A, phase D and superhydrous B are stabilised even in iron-rich systems.

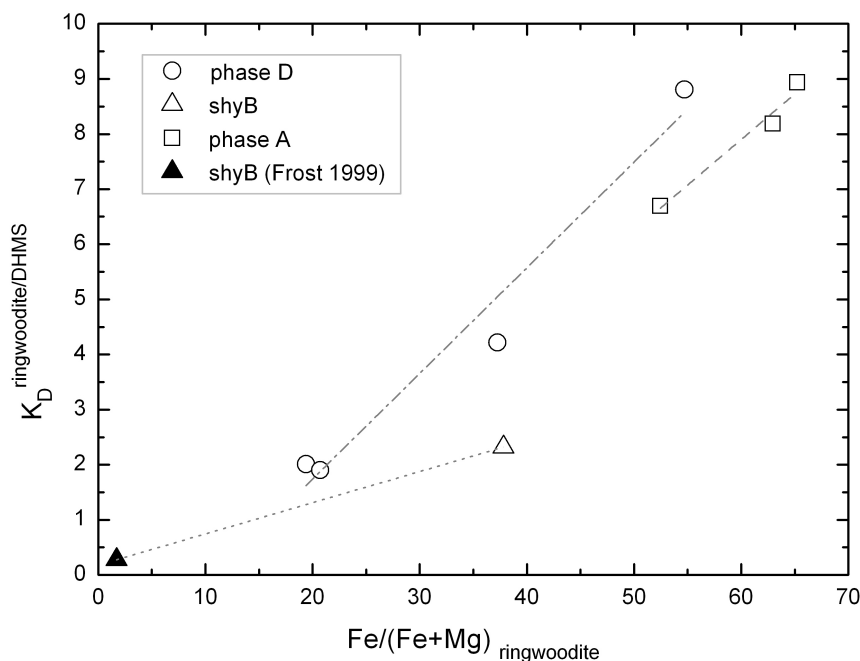


Figure 4.30: Iron partitioning between ringwoodite and dense hydrous magnesium silicates as a function of Fe_2SiO_4 mole fraction of ringwoodite - open symbols - this study, solid triangle - Frost (1999), dashed dotted line - regression line for phase D, dashed line - regression line for phase A, dotted line - regression line for superhydrous B (SHyB)

Nevertheless, the estimation of the Margules interaction parameter of the cation exchange between DHMS and ringwoodite (following the procedure presented by Frost 2003), which is based on the iron partitioning coefficient K_D between DHMS and ringwoodite, indicates that the substitution of iron in DHMS is energetically unfavored and will lead to the destabilisation of DHMS as the bulk iron content approaches the iron-endmember of the Mg_2SiO_4 - Fe_2SiO_4 system.

Chapter 5

Experimental study of hydrous silicates in the Martian mantle

5.1 Starting material and experimental conditions

The study of mineral phases relevant for the Martian interior requires a starting material containing the main chemical components in representative proportions. In this study, components ≥ 3 wt% of the bulk composition were considered, which are in this case silicon, magnesium, iron and aluminum. The starting material for the sample synthesis in a simple Martian system is based on the Martian mantle composition model after Dreibus and Wänke (1985) and Wänke and Dreibus (1988). A mixture of $\text{SiO}_2 + \text{Mg}(\text{OH})_2 + \text{FeO} + \text{Al}_2\text{O}_3$ (hydrous FMAS - **FeMgAlSi**) was prepared in order to obtain the composition (oxide wt%) after the Dreibus and Wänke model (Table 5.1). The magnesium fraction was added exclusively in the form of brucite in order to achieve a hydrous FMAS bulk composition with 12.35 wt% H_2O . Preparation of the starting material followed the identical procedure as for the hydrous Fo_{50} composition. The dried and powdered components were ground together under ethanol in an agate mortar. Fractions of the starting material were loaded into platinum capsules, which were previously sealed one-sided by electrical welding and finally closed by cold welding after loading the powder.

5. HYDROUS MARTIAN MANTLE COMPOSITION

Table 5.1: Bulk composition of the starting material - hydrous FMAS.

Martian mantle composition*		hydrous FMAS	
(Lodders & Fegley (1997)*)		normalized	
SiO ₂	wt%	44.4	40.79
MgO	wt%	30.2	27.65
FeO	wt%	17.9	16.49
Al ₂ O ₃	wt%	3.02	2.72
H ₂ O	wt%	—	12.35
CaO	wt%	2.45	—
Na ₂ O	wt%	0.5	—
TiO ₂	wt%	0.14	—
Cr ₂ O ₃	wt%	0.76	—
MnO	wt%	0.46	—
P ₂ O ₅	wt%	0.16	—
Σ	wt%	100	100

* normalised mantle and crust bulk composition
 * Dreibus & Wänke (1985), Wänke & Dreibus (1988)

Mars' thermal gradient displays the pressure-temperature path through the stability fields of mineral phases that constitute the Martian interior. The modeled thermal gradient of Mars (areotherm, Fig. 5.1) depends on the physical state and composition of the Martian core, which is still under debate. Bertka and Fei (1997) chose an areotherm for their experiments assuming a liquid Martian core (Figure 1.4). More recent publications point out that the current Martian core is potentially divided into outer liquid and inner solid core (Stevenson 2001, Yoder et al. 2003). However, the temperature of the bottom of the mantle at the core-mantle boundary is about 1800 K (Martian thermal evolution model of Williams and Nimmo 2004), which implies that the areotherm represented by line a in Figure 1.4 is an overestimation. Thus, the thermal gradient indicated by Fei and Bertka (2005) seems to be more reasonable for the experiments performed in this study (Figure 5.1). Experimental run conditions are focused on the mantle region between 18 - 23 GPa with temperatures ranging from 1150 - 1600°C in order to study the thermal stability of hydrous mantle silicates in the Martian mantle transition zone. The pressure range of experiments conducted at 1500°C is extended to upper and lower mantle conditions up to 6 and 24 GPa, respectively (Table 5.2), in order to study the entire mineralogical structure of the Martian interior with the applied chemical composition.

5.1 Starting material and experimental conditions

Table 5.2: Experimental run conditions - hydrous FMAS.

Sample	Pressure	Temperature	Heating duration	Capsule	Starting composition
GG 4380	6 GPa	1500°C	3 h	platinum	hy FMAS
GG 4381	10 GPa	1500°C	3 h	platinum	hy FMAS
GG 4464	12 GPa	1500°C	2 h	platinum	hy FMAS
GG 4383	15 GPa	1500°C	3 h	platinum	hy FMAS
GG 4376	18 GPa	1250°C	4 h	platinum	hy FMAS
GG 2960	18 GPa	1400°C	4 h	platinum	hy FMAS
GG 2990	18 GPa	1400°C	2 h	platinum	hy FMAS
GG 2987	18 GPa	1550°C	3 h	platinum	hy FMAS
GG 4345	20.5 GPa	1150°C	4 h	platinum	hy FMAS
GG 2945	20.5 GPa	1300°C	4 h	platinum	hy FMAS
GG 4348	20.5 GPa	1450°C	4 h	platinum	hy FMAS
GG 4417	20.5 GPa	1450°C	8 h	platinum	hy FMAS
GG 4389	20.5 GPa	1600°C	4 h	platinum	hy FMAS
GG 2947	23 GPa	1150°C	4 h	platinum	hy FMAS
GG 4377	23 GPa	1350°C	4 h	platinum	hy FMAS
GG 2957	23 GPa	1500°C	4 h	platinum	hy FMAS
GG 3034	24 GPa	1500°C	2 h	platinum	hy FMAS

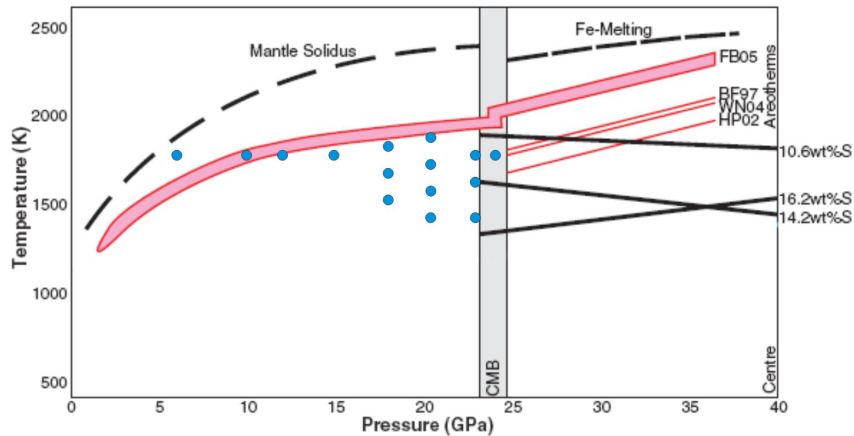


Figure 5.1: Model of the Martian thermal gradient - Core-mantle boundary (CMB) after Fei and Bertka (2005), thermal gradients (areotherms) after Fei and Bertka (2005)(FB05); black solid line - temperatures of liquidus loop intersections for sulfur contents of the core (Stewart et al. 2007); red solid lines - core areotherms of Bertka and Fei (1997)(BF97), Williams and Nimmo (2004)(WN04), Hauck and Phillips (2002)(HP02); blue circles - experiments performed in this study (Dreibus and Wänke 1985, Wänke and Dreibus 1988, Martian mantle composition)

5.2 General description of experimental run products and calculation fundamentals for presented data

Quenched melt was observed in all run products conducted above 1400°C. The size of quench crystals decreases from $\sim 20\mu\text{m}$ to $<10\mu\text{m}$ with increasing pressure, i.e. the viscosity of the melt increases as a consequence of the increasing silica content in the melt. The fine grained crystals in the quenched melt were analysed with EPMA using defocused beam ($20\mu\text{m}$); results are given in Table 5.3. The low totals are probably due to the porosity and roughness of the samples, which is caused by the limited degree of polishing. The high porosity of the quench material is an indicator for exsolution of fluid upon quenching and indicates that fluid was dissolved in the melt during the experiment. Thus, the free fluid, which was observed after quench, does not necessarily mean that a free fluid phase was present during the experiment. The absorption of iron by the platinum capsule was estimated on the basis of mass balance calculations, which yield up to 12% loss of iron ($\sim 2\text{ wt}\% \text{ Fe}_{\text{total}}$). This is reasonable because iron diffusion is faster through liquids (Merrill and Wyllie 1973) and the melt fraction is relatively high in most of the experiments (see table 5.4). However, the experimental conditions are in the dry subsolidus region of the mineral phases, so that the iron loss is inhibited by crystalline mineral phases. Figure 5.2 shows backscattered electron images of recovered samples with phase assemblages at various conditions. The relative mineral phase abundance (modal%) was determined for the recovered samples using ImageJ program and mass balance calculations (Table 5.4).

Table 5.3: EPMA data of quenched melt fraction (selected samples)

Sample	O	Al	Mg	Fe	Si	Total	
Pressure/Temp.	pts.	[wt%]	[wt%]	[wt%]	[wt%]	[wt%]	
GG 4383	16	29(3)	0.45(1)	18(2)	13.6(8)	12(1)	73(7)
15 GPa/1500°C							
GG 2960	25	31.7(9)	0.34(5)	19.7(9)	8.8(5)	13.9(5)	74(2)
18 GPa/1400°C							
GG 2990	26	33(1)	0.44(2)	19.1(8)	12.1(6)	14.7(7)	79(3)
18 GPa/1400°C							
GG 2987	20	28(3)	0.28(5)	16(2)	12(1)	12(2)	69(7)
18 GPa/1550°C							
GG 4389	37	33(1)	0.54(3)	20.0(6)	12.1(4)	13.8(8)	79(2)
20.5 GPa/1600°C							
GG 2957	25	31.4(4)	0.51(2)	20.5(4)	13.2(4)	12.0(4)	77.6(8)
23 GPa/1500°C							

5.2 General description of experimental run products

The iron partitioning coefficient K_D between ringwoodite and melt as well as garnet and melt was determined on the basis of the equation:

$$K_D = \frac{X_{\text{Mg}}^{\text{mineral}} X_{\text{Fe}}^{\text{melt}}}{X_{\text{Mg}}^{\text{melt}} X_{\text{Fe}}^{\text{mineral}}}, \quad (5.1)$$

where $X_{\text{Fe}}^{\text{mineral}}$ is the molar $\text{Fe}/(\text{Mg}+\text{Fe})$ ratio.

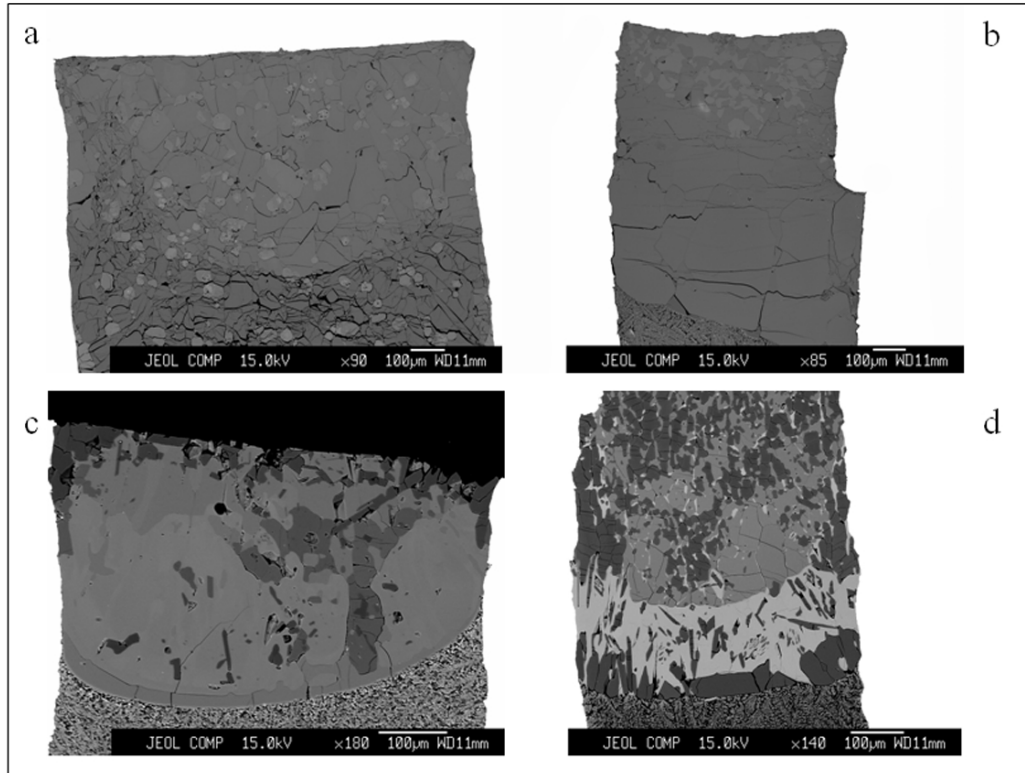


Figure 5.2: Backscattered electron images of run products - (mineral order from light grey to dark grey contrast);

(a) sample GG 4381 - 10 GPa, 1500°C - garnet, olivine, pyroxene

(b) sample GG 2987 - 18 GPa, 1550°C - ringwoodite, wadsleyite, garnet, stishovite

(c) sample GG 2957 - 23 GPa, 1500°C - ringwoodite, akimotoite, garnet, stishovite

(d) sample GG 4348 - 20 GPa, 1450°C - superhydrous B, phase D, stishovite.

5. HYDROUS MARTIAN MANTLE COMPOSITION

Table 5.4: Relative mineral phase abundances (modal%) of recovered samples

Sample	Pressure/Temp.	Dominant phase	Secondary phase	Accessory phase ($\leq 5\%$)	Melt
4380	6 GPa/1500°C	olivine	—	pyroxene (quench crystals)	90.7%
4381*	10 GPa/1500°C	olivine pyroxene	garnet	8.0%	43.0%
4464*	12 GPa/1500°C	pyroxene	wadsleyite garnet	15.0% 10.0%	50.0%
4383*	15 GPa/1500°C	pyroxene	wadsleyite garnet	13.0% 14.0%	54.0%
4376	18 GPa/1250°C	phase D superhydrous B	brucite residual phase	9.8% 12.0%	4.8%
2960	18 GPa/1400°C	garnet	ringwoodite (quench crystals)	—	71.5%
2990*	18 GPa/1400°C	garnet	ringwoodite	9.0%	2.0%
2987*	18 GPa/1550°C	garnet	ringwoodite wadsleyite	12.0% 10.0%	<1% 54.0%
4345	20.5 GPa/1150°C	phase D	superhydrous B brucite	22.5% 7.2%	2.9%
2945	20.5 GPa/1300°C	phase D	superhydrous B magnesiowüstite	26.6% 7.4%	2.2%
4348*	20.5 GPa/1450°C	phase D	superhydrous B	22.0%	3.0%
4389*	20.5 GPa/1600°C	garnet	ringwoodite	6.0%	3.0%
2947	23 GPa/1150°C	phase D brucite	superhydrous B magnesiowüstite	17.7% 6.3%	<1%
4377	23 GPa/1350°C	phase D	superhydrous B	33.2%	3.8%
2957*	23 GPa/1500°C	garnet	ringwoodite	8.0%	3.0%
				akimotoite	4.0%

relative phase abundances measured with ImageJ program;
phases were distinguished by different gray scales of backscattered electron images
* mineral phase abundance based on mass balance calculations

5.2 General description of experimental run products

The observed phase assemblages are in agreement with the Gibbs' phase rule (except sample GG 2960 and GG 4380), $F = C - P + 2$, with C - minimum number of components to create the present (mineral) phases, P - number of (mineral) phases, F - degree of freedom which is the number of intensive properties (e.g. pressure and temperature) that are independent of other intensive parameters. The observed brucite phase is probably a result of experiment quenching. However, the fluid phase, which formed brucite upon quenching, was present during the experiment and is considered as one phase. The minimum number of components, number of observed phases and the resulting degrees of freedom are given in table 5.5.

Table 5.5: Application of Gibbs' phase rule to observed phase assemblages

Component system	Present phases (P)	Sample		Number of components (C)	Degrees of freedom (F)*
A	olivine pyroxene garnet melt	GG 4381	5	MgO SiO ₂ FeO Al ₂ O ₃ H ₂ O	3
B	phase D superhydrous B brucite magnesiowüstite stishovite	GG 2947	5	MgO SiO ₂ FeO Al ₂ O ₃ H ₂ O	2
C	ringwoodite wadsleyite garnet pyroxene melt	GG 2987	5	MgO SiO ₂ FeO Al ₂ O ₃ H ₂ O	2
D	phase D superhydrous B stishovite melt	GG 4348	4	Mg(OH) ₂ SiO ₂ FeO Al ₂ O ₃	2

* $F = C - P + 2$ Gibbs' phase rule

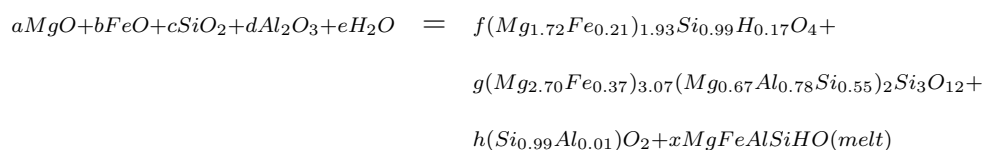
observed run products are given in table 5.4

5. HYDROUS MARTIAN MANTLE COMPOSITION

The number of components involves the components which are needed to produce the present phases of the run products. For systems A-C five components MgO, SiO₂, FeO, Al₂O₃ and H₂O are assigned to form the present phases, yielding $F = 2$ and $F = 3$ for the experimental runs. In case of system D four components are assigned to form the run products. During the experiments, temperature and pressure (intensive parameter) were constant, thus the chemical equilibrium was reached in most of the experiments with $F=0$, except for system A where one degree of freedom is remaining. This indicates that the chemical composition of the mineral phases was not fixed, yet the EPMA data show chemical uniformity of the mineral phases such as ringwoodite. However, chemical zoning was observed for garnet and pyroxenes in most of the recovered samples. The samples GG 4380 and GG 2960 were not in chemical equilibrium, since four components that build up 2 phases will yield 4 degrees of freedom, which implies that the chemical reactions would proceed further.

Mass balance calculation - an example

The modal fraction of mineral phases and melt was determined for particular samples (labeled with “asterisk” in Table 5.4) on the basis of mass balance calculations. The following reaction (sample GG 4389) is an example for the mass balance calculation, which is also the basis for the derivation of a Martian mineralogical model presented in section 5.5. Each element leads to an equation that can be solved to determine the 9 unknown mole fractions of mineral phases and melt, because the mole fractions of the bulk composition (a,b,c,d and e) are known. Assuming an approximately closed system during the experiments, the equations can be solved by transposing and interrelating the particular equations. The chemical analyses of the quenched melt have large uncertainties and therefore the melt composition was refined by adjusting the mole fraction values determined by image analyses to nearly match the measured melt composition. This mass balance calculation yields an absorption of iron by the platinum capsule of up to 12% loss of iron (2 wt% Fe_{total}).



5.2 General description of experimental run products

Table 5.6: Mass balance calculation - sample GG 4389 (exemplary for presented data)

	mole fraction [‡]	Al₂O₃	MgO	FeO	SiO₂	H₂O	Total
	mineral phase	[mol%]	[mol%]	[mol%]	[mol%]	[mol%]	
rw*	0.02 [†]	0.08	57.17	6.98	32.73	3.04	100
gt*	0.24 [†]	5.20	43.75	4.94	46.12	n.a.	100
st*	0.03 [†]	0.32	0.25	0.22	99.21	n.a.	100
melt*	0.71 [†]	0.37	30.64	8.07	18.34	42.58	100
mass balance calculation							
rw	(f) 0.06*	0.08	57.17	6.98	32.73	3.04	100
gt	(g) 0.19*	5.20	43.75	4.94	46.12	0.00	100
st	(h) 0.03*	0.32	0.25	0.22	99.21	0.00	100
melt*	(x) 0.72*	0.21	24.98	11.92	21.83	41.05	100
total		1.16	29.74	9.95	29.42	29.74	100
bulk comp.	1.0	1.16	29.74	9.95	29.42	29.74	100
residual		0.00	0.00	0.00	0.00	0.00	0.00

[‡] mole fraction \equiv modal% of the mineral phase
 * EPMA measurements
[†] ImageJ picture analysis
 * refined by mass balance calculation

The element totals in Table 5.6 are calculated by multiplying the mole fraction of each element with the modal fraction of the particular mineral phase (product), which is equivalent with the mole fractions f,g,h etc. of the products in the equation above. The element totals have to match the mole fraction of each element in the bulk composition. The residual is the difference between element total and mole fraction of the element in the bulk composition, which has to reach a minimum to determine the mass fractions of the mineral phases. This procedure was accomplished using the “solver” plug-in with excel program.

5. HYDROUS MARTIAN MANTLE COMPOSITION

Mineral formulae derivation

The mineral formulae presented in the sections below were derived following the procedure shown in Table 5.7 and 5.8.

Table 5.7: Mineral formulae calculation of wadsleyite (wd), superhydrated B (SHyB) and phase D (exemplary for presented data)

		GG 4464	GG 4348	GG 4348			
		wd	phase D	SHyB			
		(31)	(31)	(53)			
SiO ₂	[wt%]	41.0(2)	57(1)	25.5(3)			
MgO	[wt%]	45.3(2)	21(1)	53.2(3)			
FeO	[wt%]	9.0(1)	1.4(1)	1.9(1)			
Fe ₂ O ₃	[wt%]	4.3(2)	4.6(6)	11.1(9)			
Al ₂ O ₃	[wt%]	0.5(2)	5(1)	1.8(3)			
H ₂ O	[wt%]	0.49	11(1) [†]	6.5(3) [†]			
Σ	[wt%]	100.6(3)	100	100			
Cation based on		4 O	6 O	18 O			
Si ⁴⁺	} T-site	1.00	} 1.01	1.73	} 2.00	2.70	} 3.00
Al ³⁺		0.01		0.18		0.23	
Fe ³⁺		—		0.09		0.07	
Fe ³⁺	} M-site	0.08	} 1.90	0.01	} 1.03	0.82	} 9.42
Mg ²⁺		1.64		0.98		8.43	
Fe ²⁺		0.18		0.04		0.17	
H		0.08		2.21		4.64	
Σ		2.99		5.24		17.06	
Mg/Si		1.64		0.57		3.12	

[†] estimated water contents based on low microprobe totals

5.2 General description of experimental run products

Table 5.8: Mineral formulae calculation of majoritic-garnet (maj-gt) and pyroxene (exemplary for presented data)

		GG 4464			GG 2987		
		pyroxene			maj-gt		
		(37)			(31)		
SiO ₂	[wt%]	58.7(4)			51.6(7)		
MgO	[wt%]	37.6(4)			32.1(6)		
FeO	[wt%]	2.6(1)			4.7(3)		
Fe ₂ O ₃	[wt%]	1.8(1)			4.9(6)		
Al ₂ O ₃	[wt%]	0.22(2)			7.5(7)		
Σ	[wt%]	100.9(8)			100.8(4)		
Cation based on		6 O			12 O		
Si ⁴⁺	}	1.98	}	2.00	}	3.00	
Al ³⁺		0.01		—		}	3.00
Fe ³⁺		0.01		—			
Si ⁴⁺	}	—	}	1.00	}	0.56	
Fe ³⁺		0.04		0.25		}	2.00
Al ³⁺		—		0.61			
Fe ²⁺		—		—			
Mg ²⁺	}	0.96	}	}	}	0.58	
Fe ³⁺		—				—	
Mg ²⁺		0.93				1.00	2.73
Fe ²⁺	0.07	0.27	0.27				
Σ		4.00				8.00	
Mg/Si		0.95				0.93	
		En	94%	Py	14%		
		Fs	6%	Alm	16%		
				Maj	70%		

★ M1 and M2 site of pyroxene; X and Y site of garnet

5.3 Results on the particular mineral phases

5.3.1 Olivine, wadsleyite and ringwoodite - water storage capacities of nominally anhydrous minerals in a hydrous Martian model system

Water storage capacity of the Earth's upper mantle and transition zone is essentially determined by olivine and its high pressure polymorphs ringwoodite and wadsleyite. Other nominally anhydrous minerals such as garnet and pyroxene are also dominant mineral phases in the mantle region and contribute to the storage capacity even if their storage capacity is comparably lower. This subchapter deals primarily with the chemical and structural data obtained for nominally anhydrous minerals and their water storage capacity in the mantle region of the Martian interior.

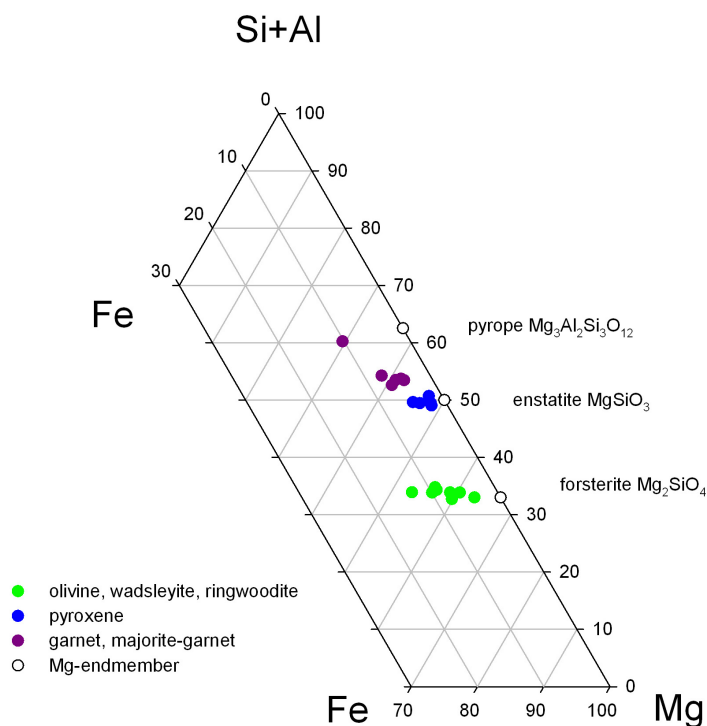


Figure 5.3: Ternary diagram showing the compositions of run products - Mg-Fe substitution in olivine, wadsleyite and ringwoodite, compositional variations of pyrope-almandine garnet and majorite-garnet; open circles denote Mg-endmember compositions of olivine, pyroxene and garnet.

Table 5.9: EPMA data of olivine, wadsleyite and ringwoodite (1σ standard deviation in parenthesis)

Sample	pts.	MgO	SiO ₂	FeO	Fe ₂ O ₃ [†]	Al ₂ O ₃	H ₂ O*	Total	\ddagger K _D ^{rw/melt}	Mineral phase	Mineral formula
Pressure/Temp.		[wt%]	[wt%]	[wt%]	[wt%]	[wt%]	[wt%]				
GG 2990	22	45.4(3)	40.7(3)	14.3(5)	n.a.	0.1(1)	1.02	101.5(4)	0.37(5)	Ringwoodite	(Mg _{1.65} Fe _{0.29}) _{1.94} Si _{0.99} H _{0.17} O ₄
18 GPa/1400°C											
GG 2987	17	41.9(6)	39.9(4)	15.8(5)	3.1(1)	0.04(2)	1.02	101.7(5)	0.32(8)	Ringwoodite	(Mg _{1.54} Fe ²⁺ _{0.32} Fe ³⁺ _{0.06}) _{1.92} Si _{0.98} H _{0.17} O ₄
18 GPa/1550°C											
GG 4389	11	48.0(2)	41.0(2)	10.5(2)	n.a.	0.16(2)	1.08	100.7(5)	0.26(2)	Ringwoodite	(Mg _{1.72} Fe _{0.21}) _{1.93} Si _{0.99} H _{0.17} O ₄
20.5 GPa/1600°C											
GG 2957	56	49.8(2)	41.4(3)	5.9(2)	2.8(2)	0.21(2)	~1	101.2(4)	0.17(1)	Ringwoodite	(Mg _{1.76} Fe ²⁺ _{0.12} Fe ³⁺ _{0.05}) _{1.93} (Al _{0.01} Si _{0.98}) _{0.99} H _{0.16} O ₄
23 GPa/1500°C											
GG 4380	35	53.6(6)	41.9(2)	6.0(7)	n.a.	0.03(1)	0.25	101.8(3)	—	Olivine	(Mg _{1.86} Fe _{0.14}) ₂ Si _{0.99} H _{0.04} O ₄
6 GPa/1500°C											
GG 4381	39	49.7(4)	40.6(2)	11.1(5)	n.a.	0.01(1)	0.25	101.7(5)	—	Olivine	(Mg _{1.79} Fe _{0.22}) _{2.01} Si _{0.99} H _{0.04} O ₄
10 GPa/1500°C											
GG 4464	31	45.3(2)	41.0(2)	9.0(1)	4.3(2)	0.5(2)	0.49	100.6(3)	—	Wadsleyite	(Mg _{1.64} Fe ²⁺ _{0.18} Fe ³⁺ _{0.08}) _{1.90} (Al _{0.01} Si _{1.00}) _{1.01} H _{0.08} O ₄
12 GPa/1500°C											
GG 4383	38	45.3(4)	40.5(3)	12.8(6)	n.a.	0.4(1)	~0.5	99.5(3)	—	Wadsleyite	(Mg _{1.67} Fe _{0.27}) _{1.94} (Al _{0.01} Si _{1.00}) _{1.01} H _{0.08} O ₄
15 GPa/1500°C											
GG 2987	16	44.7(5)	41.0(2)	9.6(6)	3.6(4)	0.2(1)	0.62	99.7(4)	—	Wadsleyite	(Mg _{1.63} Fe ²⁺ _{0.20} Fe ³⁺ _{0.07}) _{1.96} Si _{1.01} H _{0.10} O ₄
18 GPa/1550°C											

* Unpolarised infrared analyses

† Electron energy-loss spectroscopy

‡ K_D defined as (Fe/Mg)_{ringwoodite}/(Fe/Mg)_{melt} as in equ. 5.1

I. Olivine

The upper mantle region up to a pressure of 10 GPa at 1500°C is dominated by olivine coexisting with pyroxene and garnet. Relative phase abundances (regarding crystalline mineral phases only) of olivine range from 45 to 100% (Table 5.4).

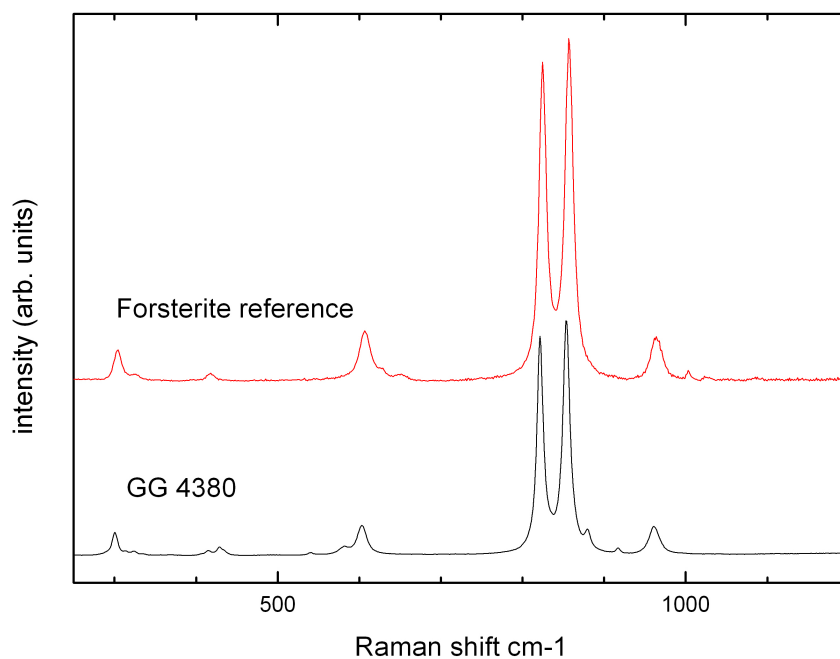


Figure 5.4: Raman spectra of olivine - $\text{Mg}_{1.86}\text{Fe}_{0.14}\text{Al}_{0.00}\text{Si}_{0.98}\text{H}_{0.05}\text{O}_4$ (GG 4380, 6 GPa and 1500°C).

Olivine can be distinguished easily from its high pressure polymorphs wadsleyite and ringwoodite by Raman spectroscopy (Figure 5.4) which allows to constrain the upper mantle - transition zone boundary. Olivine observed in this study has Fo_{93-89} composition (Table 5.9, Figure 5.3). Infrared analyses reveal a water storage capacity of olivine of about 0.3 wt% H_2O , yielding the mineral formula $(\text{Mg}_{1.79}\text{Fe}_{0.22})_{2.01}\text{Si}_{0.99}\text{H}_{0.04}\text{O}_4$ (sample GG 4381).

II. Wadsleyite

Between 10 and 12 GPa olivine transforms to its denser high pressure polymorph wadsleyite, marking the upper bound of the transition zone. The olivine-wadsleyite transition occurs at about 2 GPa lower pressure than predicted (Figure 1.6, Figure 4.21). Within the uncertainty of multi anvil pressure calibrations, the transition pressure of the olivine-wadsleyite transformation is lowered by ~ 2 GPa due to the addition of water and the ferric iron content of wadsleyite as shown by Frost and Dolejš (2007). Coexisting phases like garnet and pyroxene are also dominant in this pressure range in addition to wadsleyite. With increasing pressure wadsleyite starts to transform to ringwoodite at 1550°C forming a field of coexisting wadsleyite and ringwoodite with dominant garnet and accessory pyroxene and stishovite, respectively (Table 5.4). Mineral phases were mostly identified and distinguished using Raman spectroscopy (Figure 5.5). At 20.5 GPa and 1600°C wadsleyite transforms completely to ringwoodite.

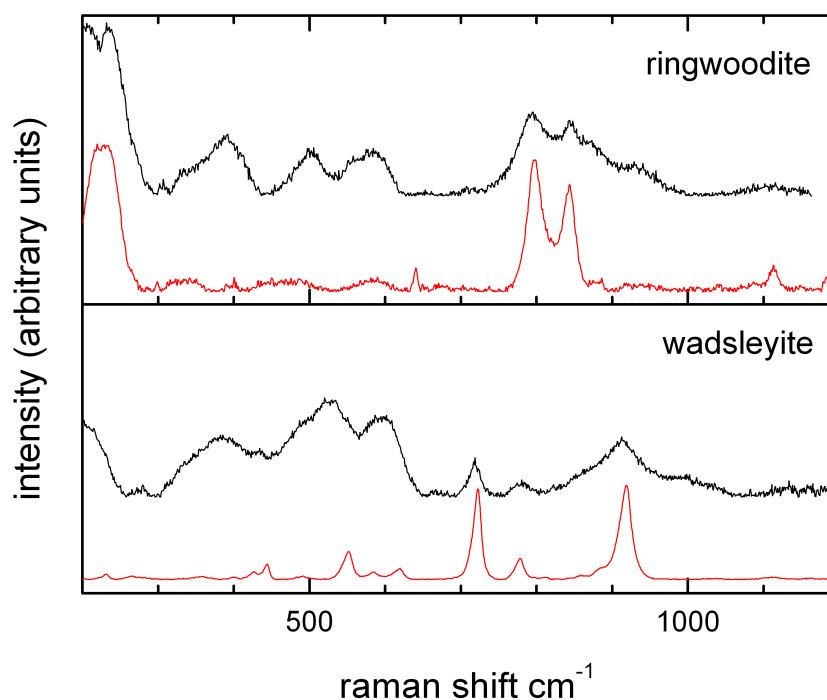


Figure 5.5: Raman spectra of coexisting mineral phases - sample GG 2987 (18 GPa, 1550°C); red spectra denoting reference Raman spectra from database.

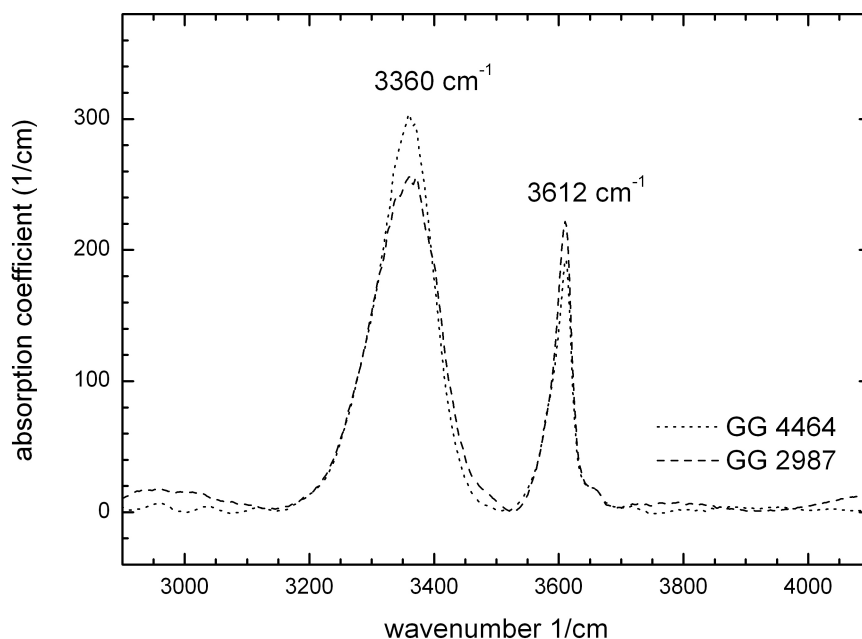


Figure 5.6: Infrared spectra of wadsleyite - two main absorption peaks at 3360 cm^{-1} and 3612 cm^{-1} ; sample GG 4464 (12 GPa, 1500°C), sample GG 2987 (18 GPa, 1550°C).

Transmission electron microscopy observations reveal a defect-free orthorhombic structure for wadsleyite (Figure 5.7) with interplanar distances close to the Mg_2SiO_4 -wadsleyite reference. Electron diffraction along the zone axis $[001]$ shows the common pattern of wadsleyite, which excludes also the occurrence of wadsleyite II. The orthorhombic structure is consistent with the findings of Smyth and Kawamoto (1997), suggesting that the monoclinic structure of hydrous wadsleyite is unlikely for compositions with <92 mole% Mg_2SiO_4 . Electron energy-loss spectroscopy (EELS) was carried out on wadsleyite in order to determine the valence state of iron, which is important for assessing the possible water incorporation mechanisms. EELS analyses resulted in an $\text{Fe}^{3+}/\Sigma\text{Fe}$ ratio of $25\pm 5\%$ (Figure 5.8). Wadsleyite has about 14 mole% Fe_2SiO_4 yielding the mineral formula $(\text{Mg}_{1.63}\text{Fe}^{2+}_{0.20}\text{Fe}^{3+}_{0.07})_{1.90}\text{Si}_{1.01}\text{H}_{0.10}\text{O}_4$ with 0.6 wt% H_2O (Figure 5.6) when coexisting with ringwoodite, garnet and pyroxene at 18 GPa and 1550°C (Table 5.9).

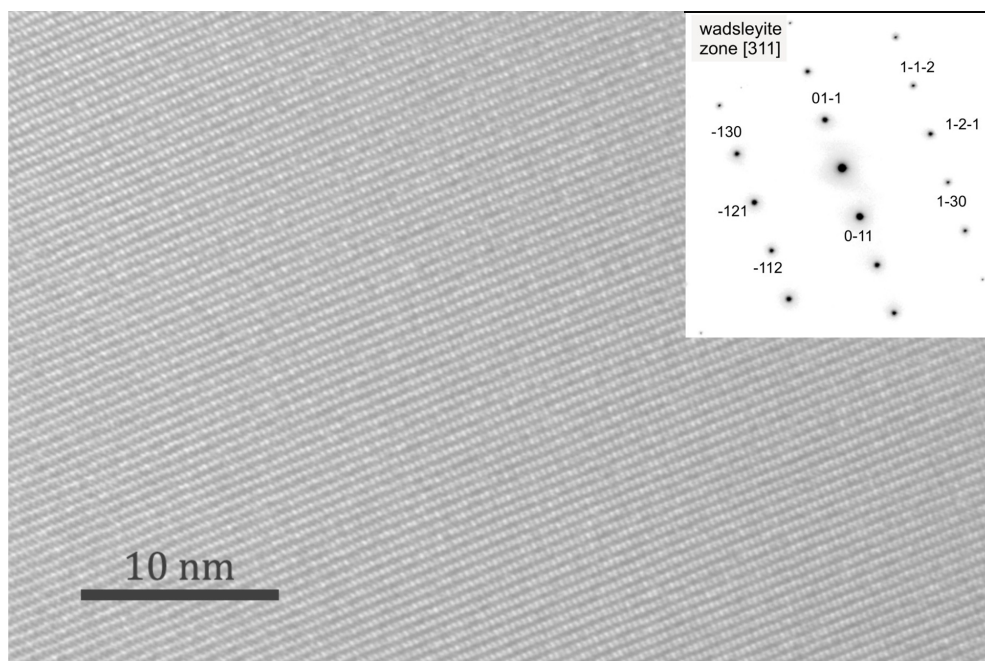


Figure 5.7: High-resolution TEM image of wadsleyite - zone axis [311], sample GG 2987 (18 GPa, 1550°C).

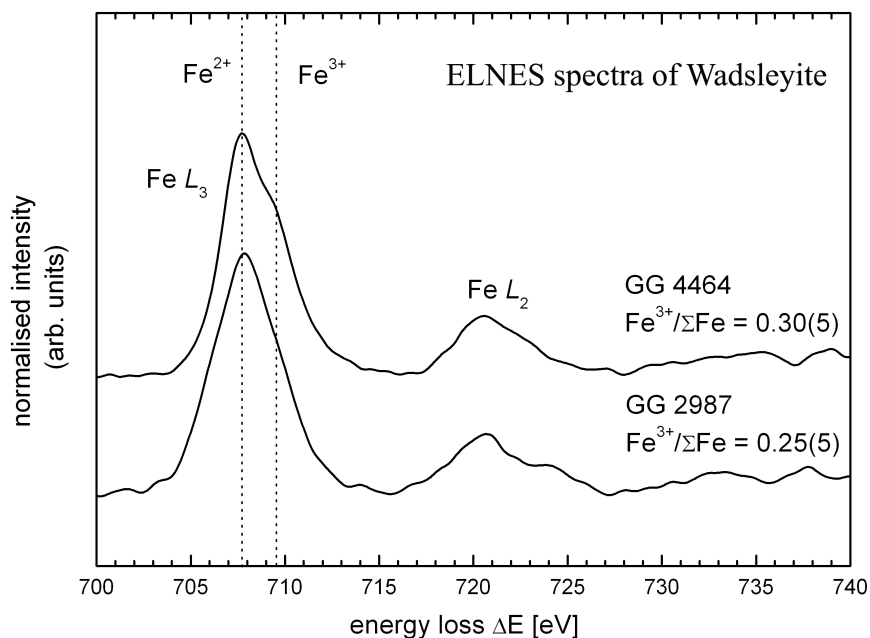


Figure 5.8: Iron $L_{2,3}$ electron energy-loss near-edge structure (ELNES) spectra of Mg,Fe-wadsleyite - GG 4464 (12 GPa, 1200°C), GG 2987 (18 GPa, 1550°C).

III. Ringwoodite

The highest pressure polymorph of olivine, ringwoodite, appears at 18 GPa and 1400°C as well as 1550°C and is stable up to 23 GPa, corresponding to 1800 km depth in the Martian interior. Dominant garnet and accessory stishovite accompanies ringwoodite through its entire stability field (Table 5.4). At 18 GPa and 1550°C ringwoodite coexists with wadsleyite, representing the gradual change from upper to lower Martian transition zone. Iron content of ringwoodite reaches a maximum with 20 mole% Fe_2SiO_4 coexisting with wadsleyite, while the lowest Fe-content of ringwoodite of about 9 mole% Fe_2SiO_4 appears at 23 GPa when ringwoodite coexists with akimotoite and garnet as well as minor stishovite (Table 5.9, sample GG 2957). Water content of ringwoodite reaches up to 1.08 wt% H_2O at 20.5 GPa and 1600°C (sample GG 4389, Figure 5.9). The main absorption band of ringwoodite is very broad (FWHM $\sim 700\text{ cm}^{-1}$) and centered at 3140 cm^{-1} (sample GG 2990) as well as 3250 cm^{-1} (sample GG 2987). The weaker absorption bands at 2900 cm^{-1} and 3700 cm^{-1} are assigned to different OH-groups (Bolfan-Casanova et al. 2000), while the main absorption feature represents the predominant OH-group probably connected to the octahedral site (see chapter 4.4).

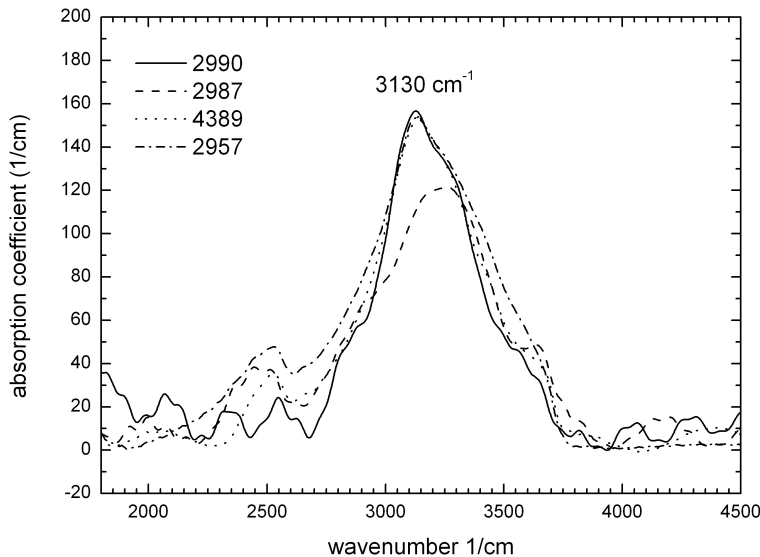


Figure 5.9: Infrared spectra of ringwoodite - synthesised at different pressure-temperature conditions GG 2990 (18 GPa, 1400°C), GG 2987 (18 GPa, 1550°C), GG 4389 (20.5 GPa, 1600°C) and GG 2957 (23 GPa, 1500°C); main absorption peak at 3140 cm^{-1} (sample GG 2990) as well as 3250 cm^{-1} (sample GG 2987).

The water content of ringwoodite is again higher than the water storage capacity of wadsleyite at lower pressure (Table 5.9, Figure 5.9). Transmission electron microscope observations reveal a defect-free ringwoodite structure. Analyses of diffraction patterns are consistent with the cubic structure of ringwoodite without major deviations of lattice parameters from the reference data. The amounts of ferric and ferrous iron, respectively, were determined using electron energy loss spectroscopy, yielding up to $\sim 30 \pm 5\%$ $\text{Fe}^{3+}/\Sigma\text{Fe}$ (Figure 5.10) with the resulting mineral formula $(\text{Mg}_{1.76}\text{Fe}^{2+}_{0.12}\text{Fe}^{3+}_{0.05})_{1.93}(\text{Al}_{0.01}\text{Si}_{0.98})_{0.99}\text{H}_{0.16}\text{O}_4$ (sample GG 2957).

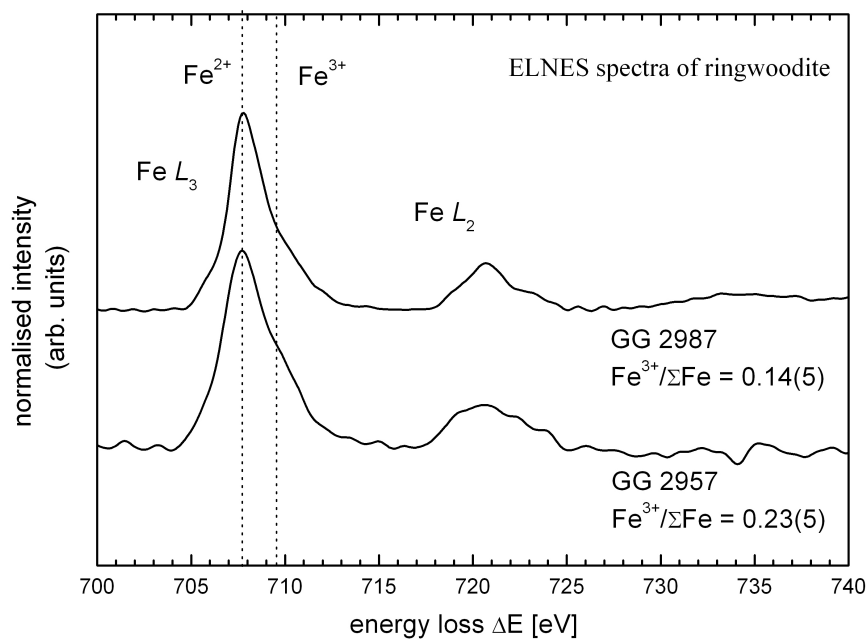


Figure 5.10: Iron $L_{2,3}$ electron energy-loss near-edge structure (ELNES) spectra of Mg,Fe-ringwoodite - samples GG 2987 (18 GPa, 1550°C) and GG 2957 (23 GPa, 1500°C).

5.3.2 Pyroxene, garnet and (Mg,Fe)SiO₃ (ilmenite-structure) - coexisting mantle minerals

I. Pyroxene

The upper Martian mantle and the Martian transition zone consist also of pyroxene and garnet in addition to olivine and its high pressure polymorphs ringwoodite and wadsleyite. At 10 GPa and 1500°C olivine and pyroxene (enstatite) represent the dominant mineral phases with minor amounts of garnet (Table 5.4). Raman spectroscopy and microprobe analyses reveal the presence of pyroxene (enstatite) and garnet with pyrope, almandine and majorite components at 15 GPa and 1500°C (Table 5.10). Pyroxene was still observed as an accessory phase at 18 GPa and 1550°C, which marks the highest pressure at which pyroxene is stable. According to the phase diagram of the join MgSiO₃-FeSiO₃ (Ohtani et al. 1991) pyroxene with ~5 mol% ferrosillite component is stable up to about ~17 GPa, which is consistent with data obtained in this study (sample GG 2987). Pyroxene synthesised in this study has up to 7 wt% Fe_{total}, with ferric iron contents of up to $\text{Fe}^{3+}/\Sigma\text{Fe} = 0.43(5)$ determined by electron energy-loss spectroscopy (Figure 5.11). The resulting mineral formulae are given in Table 5.10. Recovered pyroxene crystals contain several cracks and optical impurities, which influence infrared analyses and yield poor data.

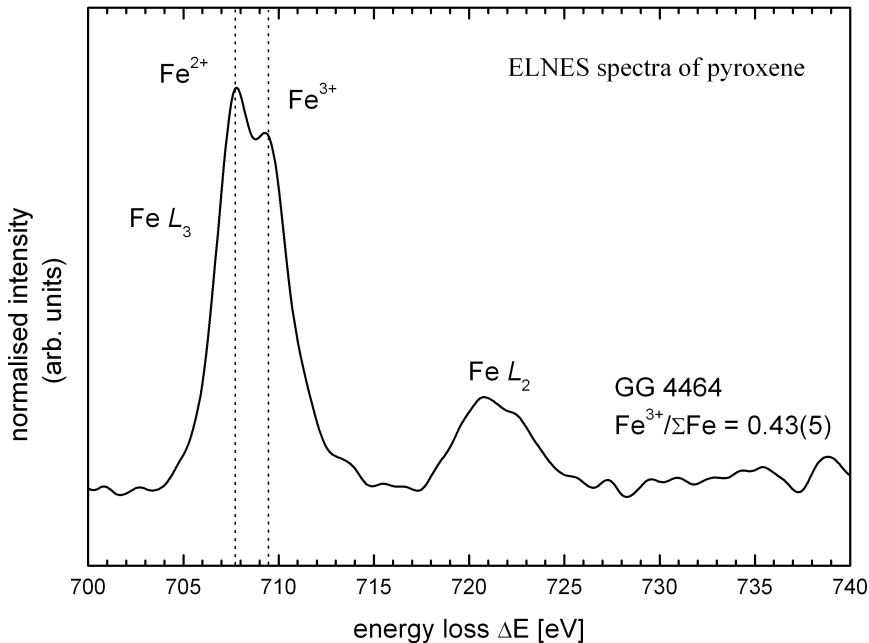


Figure 5.11: Iron $L_{2,3}$ electron energy-loss near-edge structure (ELNES) spectra of pyroxene - GG 4464 (12 GPa, 1200°C).

Table 5.10: EPMA data of akimotoite, garnet and pyroxene (1σ standard deviation in parenthesis)

Sample	pts.	MgO	SiO ₂	FeO	Fe ₂ O ₃ [†]	Al ₂ O ₃	Total	Mineral formula
Pressure, Temp.		[wt%]	[wt%]	[wt%]	[wt%]	[wt%]		
Garnet - ideal formula X ₃ Y ₂ T ₃ O ₁₂								
GG 4381	27	23.4(7)	43.7(6)	13(1)	n.a.	21(1)	101.5(4)	(Mg _{2.29} Fe _{0.76}) _{3.05} (Mg _{0.16} Al _{1.77} Si _{0.07}) ₂ Si ₃ O ₁₂
10 GPa, 1500°C								
GG 4464	11	28.1(3)	47.7(3)	2.0(1)	7.5(6)	16.8(4)	102.1(5)	(Mg _{2.79} Fe _{2⁺⁺0.11}) _{2.90} (Mg _{0.05} Fe _{3⁺⁺0.38} Al _{1.34} Si _{0.23}) ₂ Si ₃ O ₁₂
12 GPa, 1500°C								
GG 4383	18	28.2(5)	48.8(8)	11.5(7)	n.a.	12.6(7)	101.1(4)	(Mg _{2.39} Fe _{0.68}) _{3.07} (Mg _{0.55} Al _{1.04} Si _{0.41}) ₂ Si ₃ O ₁₂
15 GPa, 1500°C								
GG 2960	106	33.6(5)	53.0(5)	6.5(5)	n.a.	7.4(7)	100.5(3)	(Mg _{2.68} Fe _{0.37}) _{3.05} (Mg _{0.76} Al _{0.60} Si _{0.64}) ₂ Si ₃ O ₁₂
18 GPa, 1400°C								
GG 2990	22	32.4(3)	52.0(5)	7.7(3)	n.a.	8.6(8)	100.7(3)	(Mg _{2.62} Fe _{0.45}) _{3.07} (Mg _{0.71} Al _{0.70} Si _{0.59}) ₂ Si ₃ O ₁₂
18 GPa, 1400°C								
GG 2987	31	32.1(6)	51.6(7)	4.7(3)	4.9(6)	7.4(7)	100.7(4)	(Mg _{2.73} Fe _{2⁺⁺0.27}) ₃ (Mg _{0.58} Fe _{3⁺⁺0.25} Al _{0.61} Si _{0.56}) ₂ Si ₃ O ₁₂
18 GPa, 1550°C								
GG 4389	35	33.0(3)	51.7(3)	6.4(3)	n.a.	9.6(4)	100.7(4)	(Mg _{2.70} Fe _{0.37}) _{3.07} (Mg _{0.67} Al _{0.78} Si _{0.55}) ₂ Si ₃ O ₁₂
20.5 GPa, 1600°C								
GG 2957	51	33.3(5)	51.2(5)	3.1(3)	3.4(3)	10(1)	101.1(3)	(Mg _{2.85} Fe _{2⁺⁺0.18}) _{3.03} (Mg _{0.53} Fe _{3⁺⁺0.18} Al _{0.81} Si _{0.48}) ₂ Si ₃ O ₁₂
23 GPa, 1500°C								
Pyroxene - ideal formula M ₂ MT ₂ O ₆								
GG 4380	14	35.9(2)	54.8(7)	7.0(5)	n.a.	3.1(3)	100.8(3)	(Mg _{0.86} Fe _{0.20}) _{1.06} (Al _{0.02} Mg _{0.98}) ₁ (Al _{0.11} Si _{1.89}) ₂ O ₆
6 GPa, 1500°C								
GG 4381	63	36.9(2)	58.2(4)	5.6(2)	n.a.	0.21(2)	100.9(6)	(Mg _{0.87} Fe _{0.16}) _{1.03} (Mg _{1.00}) ₁ (Al _{0.01} Si _{1.98}) _{1.99} O ₆
10 GPa, 1500°C								
GG 4464	37	37.6(4)	58.7(4)	2.6(1)	1.8(1)	0.22(2)	100.9(8)	(Mg _{0.93} Fe _{2⁺⁺0.07}) ₁ (Mg _{0.96} Fe _{3⁺⁺0.04}) ₁ (Fe _{3⁺⁺0.01} Al _{0.01} Si _{1.98}) _{2.00} O ₆
12 GPa, 1500°C								
GG 4383	101	38.5(4)	58.7(9)	3.3(7)	n.a.	0.15(3)	100.7(4)	(Mg _{0.94} Fe _{0.09}) _{1.03} (Mg _{1.00}) ₁ (Al _{0.01} Si _{1.98}) _{1.99} O ₆
15 GPa, 1500°C								
GG 2987	02	38.2(1)	57.5(4)	3.41(1)	n.a.	0.11(3)	99.3(3)	(Mg _{0.95} Fe _{0.10}) _{1.05} (Mg _{1.00}) ₁ (Al _{0.00} Si _{1.97}) _{1.97} O ₆
18 GPa, 1550°C								
Akimotoite - ideal formula (Mg,Fe)(Al,Si)O ₃								
GG 2957	35	38.2(5)	56.9(4)	2.3(1)	0.6(1)	0.8(1)	98.8(6)	(Mg _{0.98} Fe _{2⁺⁺0.03} Fe _{3⁺⁺0.01}) _{1.02} (Al _{0.02} Si _{0.98}) ₁ O ₃
23 GPa, 1500°C								

† Electron energy-loss spectroscopy

5. HYDROUS MARTIAN MANTLE COMPOSITION

Table 5.11: Garnet-melt partitioning ratios of Fe and Al

Sample	Pressure/Temp.	$\dagger K_D^{\text{gt/melt}}$	$*D_{\text{Al}}^{\text{gt/melt}}$
GG 4381	10 GPa/1500°C	—	42(2)
GG 4464	12 GPa/1500°C	—	20(2)
GG 4383	15 GPa/1500°C	—	14(3)
GG 2990	18 GPa/1400°C	0.29(4)	15(2)
GG 2987	18 GPa/1550°C	0.22(6)	24(6)
GG 4389	20.5 GPa/1600°C	0.24(3)	24(2)
GG 2957	23 GPa/1500°C	0.19(2)	16(2)

$\dagger K_D$ defined as $(\text{Fe/Mg})_{\text{garnet}}/(\text{Fe/Mg})_{\text{melt}}$ as in equ. 5.1
 $* D$ defined as $D_i = (i)_{\text{garnet}}/(i)_{\text{melt}}$ with $i = \text{Al}$ [mole%]

II. Majoritic-garnet

The decomposition of pyroxene, beginning at pressures >15 GPa, is followed by an increasing majorite-garnet fraction in pyrope-almandine garnet with increasing pressure. The almandine component of majoritic-garnet reaches a maximum of 31% at 10 GPa and 1500°C and decreases with increasing pressure. The increasing majorite component (Figure 5.12) results in decreasing Al-contents of majoritic-garnet (Table 5.10). Majoritic-garnet is stable up to 23 GPa and 1500°C with a maximum majorite component ($\text{Mg}_4\text{Si}_4\text{O}_{12}$) of 70%. This maximum is reached at a pressure corresponding to the upper bound of the transition zone, when clinopyroxene disappears and entirely enters into the garnet structure. The obtained compositional data of garnet is in agreement with thermodynamical calculations (Gasparik 2003), while small deviations may result from analytical inaccuracy and the distinct bulk composition containing iron and water (Figure 5.12). The element partitioning of iron and aluminium between garnet and melt (Table 5.11) is relevant for the interpretation of differentiation processes during e.g. magma ocean solidification and the estimation of resulting changes in chemical composition of the crystallising mineral phases and the residual melt (see general conclusions).

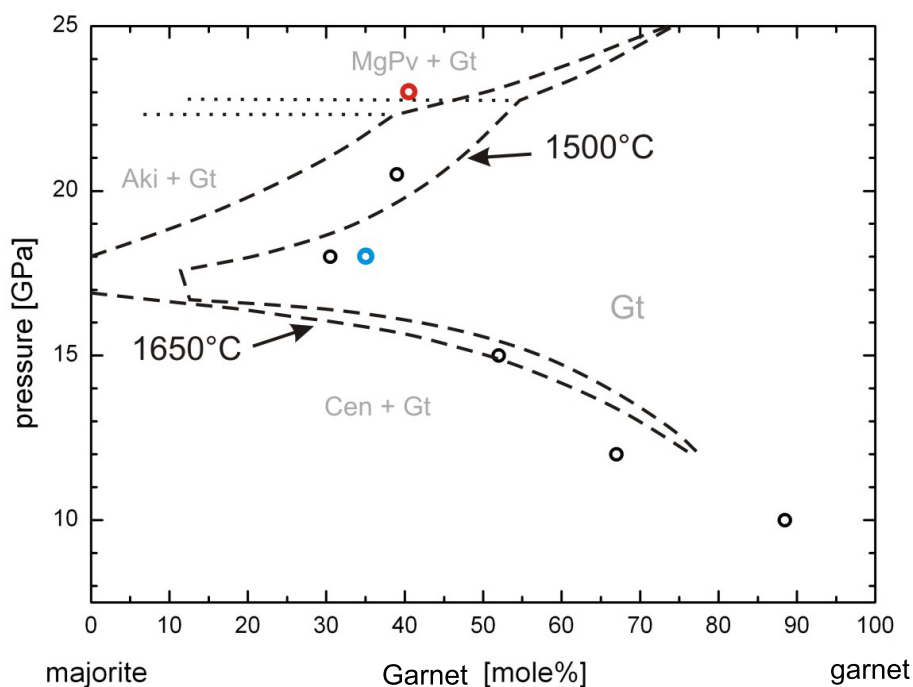


Figure 5.12: Chemical composition of garnet (pyrope with up to 31% almandine) as a function of pressure - indicating the increase of majorite component in garnet with increasing pressure as well as the decreasing majorite component due to the appearance of akimotoite at >20 GPa; black circles - experiments at 1500°C, blue and red circle denote experiments at lower (1400°C) and higher (1600°C) temperature, respectively; dashed lines - thermodynamic calculations for the enstatite-pyrope join at 1500°C and 1650°C from Gasparik (2003); abbreviation: Gt - garnet, Aki - akimotoite, MgPv - Mg-perovskite, Cen - clinoenstatite.

5. HYDROUS MARTIAN MANTLE COMPOSITION

Electron energy-loss near-edge structure (ELNES) spectra of garnet yield $\text{Fe}^{3+}/\Sigma\text{Fe} = 0.48(5)$ - $0.77(5)$ (Figure 5.13). The highest amount of ferric iron (7.5 wt% Fe_2O_3) was observed at 12 GPa and 1500°C (sample GG 4464), while garnet with increased majoritic-component shows constantly $\sim 50\%$ ferric iron. The resulting majorite-garnet formula (according to the mineral formulae calculation presented in Table 5.8 based on 12 oxygen) is: $(\text{Mg}_{2.73}\text{Fe}^{2+}_{0.27})_3(\text{Mg}_{0.58}\text{Fe}^{3+}_{0.25}\text{Al}_{0.61}\text{Si}_{0.56})_2\text{Si}_3\text{O}_{12}$ (sample GG 2987). Infrared analyses, however, yield water contents below the detection limit of FTIR spectroscopy.

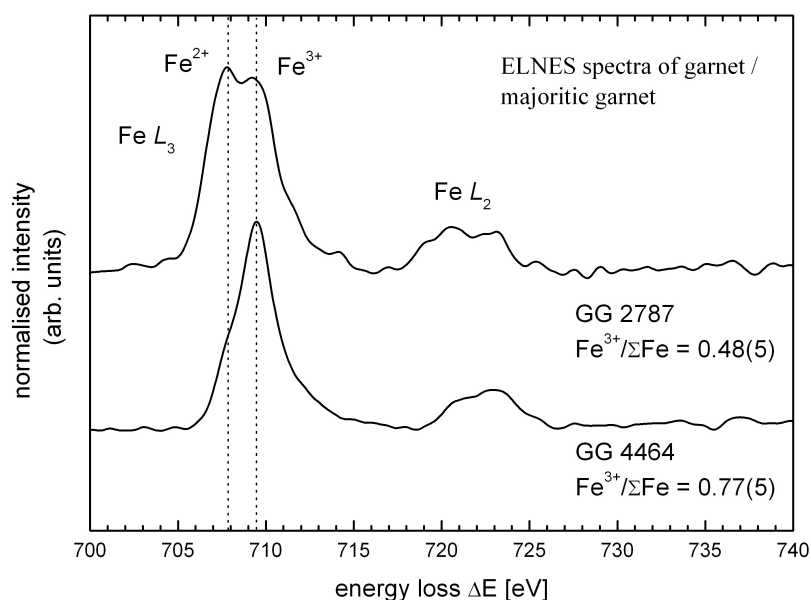


Figure 5.13: Iron $L_{2,3}$ electron energy-loss near-edge structure (ELNES) spectra of garnet/majoritic-garnet - GG 4464 (12 GPa, 1200°C), GG 2987 (18 GPa, 1550°C).

III. Akimotoite

At Martian core-mantle boundary conditions (23 GPa and 1500°C), ringwoodite coexists with majorite garnet, stishovite and ilmenite-structured (Mg,Fe)SiO₃, so-called akimotoite (Figure 5.14). This ilmenite-type (Mg,Fe)SiO₃ polymorph, which forms by the partial transformation of garnet at high pressure and incorporates ~1 wt% Al by Al-Si substitution and ~2 wt% FeO as well as 0.6 wt% Fe₂O₃ by Mg-Fe substitution. The ferric iron content was determined using electron energy-loss spectroscopy revealing Fe³⁺/ΣFe = 0.20(5). The resulting mineral formula of akimotoite is as follows (according to the mineral formulae calculation presented in Table 5.8 based on 3 oxygen): (Mg_{0.98}Fe²⁺_{0.03}Fe³⁺_{0.01})_{1.02}(Al_{0.02}Si_{0.98})₁O₃. The akimotoite crystals were not suited for infrared analyses in this study because of optical impurities and cracks. Pure Mg-akimotoite, however, can accommodate up to 0.045 wt% H₂O (Bolfan-Casanova et al. 2000) which could be enhanced by Al-substitution for octahedral silicon (Smyth 2006).

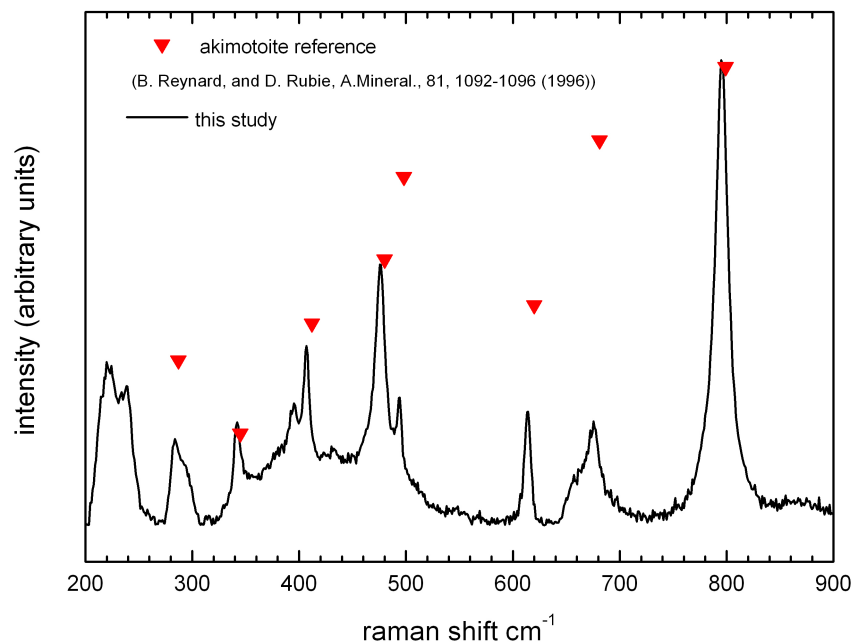


Figure 5.14: Raman spectra of Akimotoite - sample GG 2957 (23 GPa, 1500°C).

5.3.3 Stability and characteristics of DHMS in the Martian mantle between 18-23 GPa

Analytical results for potential dense hydrous phases in the Martian mantle will be presented in the following subchapter. The potential occurrence of hydrous phases in the Martian interior was investigated at transition zone pressures of 18 - 23 GPa and at temperatures between 1150°C up to 1450°C. According to the study of hydrous phases in the MgFeSiO₄ system, the stability of ferroan dense hydrous phases is extended to higher temperatures at higher pressures.

Phase D and superhydrous B are stable up to 1450°C at 20.5 GPa. At higher and lower pressures the maximum stability temperature of phase D and superhydrous B decreases, reaching 1250°C at 18 GPa and 1350°C at 23 GPa.

I. Phase D

The water content of phase D varies less than that described for pure Mg-phase D while magnesium, silicon and aluminium contents show significant variations (Table 5.12). Silicon and magnesium contents vary within a difference of about 5 wt% for all samples, whereas the water content ranges from 11 - 14 wt% H₂O (estimated water content from low totals of microprobe analyses). The aluminium contents range from 1.5 - 5 wt% Al₂O₃, while the iron contents show the smallest variability throughout the samples synthesised at different conditions (Figure 5.17). Electron energy-loss spectroscopy of phase D yield Fe³⁺/ΣFe = 0.74(5) (Figure 5.16), thus ferrous and ferric Fe-content of phase D (sample GG 4348) is 1.4 wt% FeO and 4.6 wt% Fe₂O₃. It is likely that ferrous iron occupies Mg-positions and ferric iron as well as aluminium fills the Si-site, while the common water substitution mechanisms for phase D, Mg-substitution and Mg-Si disorder, are maintained. Figure 5.15 shows the Mg/Si ratio versus analysis totals of phase D. The substitution mechanisms are indicated by dashed lines. The composition of phase D analysed in this study lies between the Si⁴⁺ = 4H⁺ (MgSi_{2-x}H_{2+4x}O₆) and Si⁴⁺ = 2H⁺ + Mg²⁺ (Mg_{1+x}Si_{2-x}H_{2+2x}O₆) mechanisms, which implies the combination of both mechanisms with preference to the latter. This result is consistent with the results for the pure Mg-endmember phase D. However, due to the accommodation of ferric iron and aluminium in the Si-site the water content of phase D is reduced compared to the pure Mg-endmember phase D, showing Mg-Si disorder and Si-vacancies charge balanced by hydrogen.

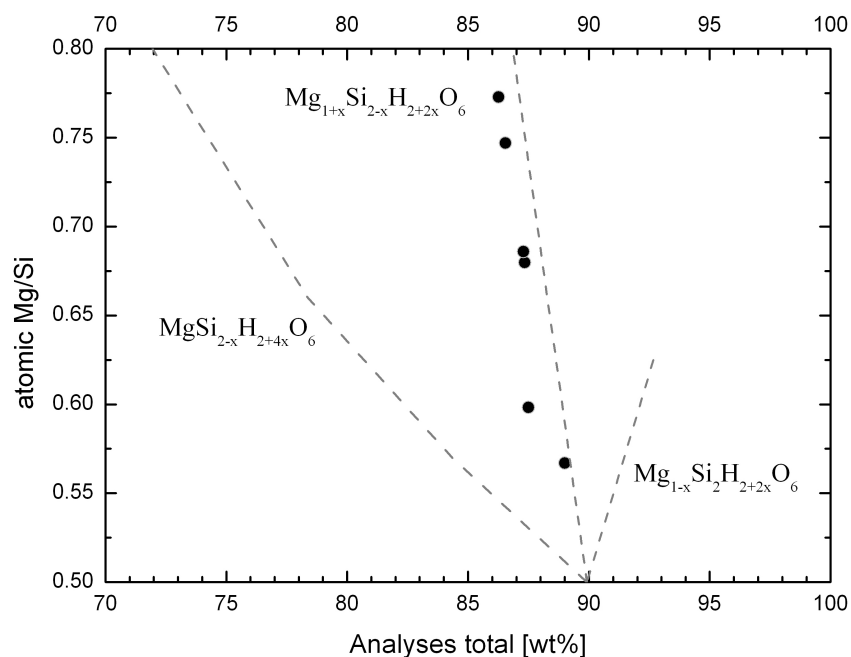


Figure 5.15: Water substitution mechanisms of phase **D** - according to the Mg/Si ratios, dashed lines represent water substitution mechanisms.

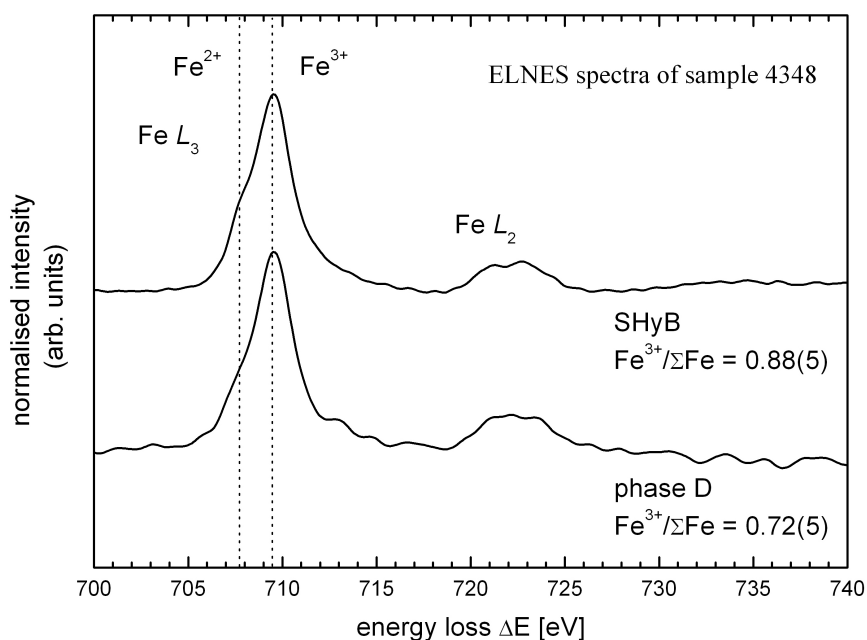


Figure 5.16: Iron $L_{2,3}$ electron energy-loss near-edge structure (ELNES) spectra of superhydrous **B** and **Phase D** - sample 4348 (20.5 GPa, 1450°C).

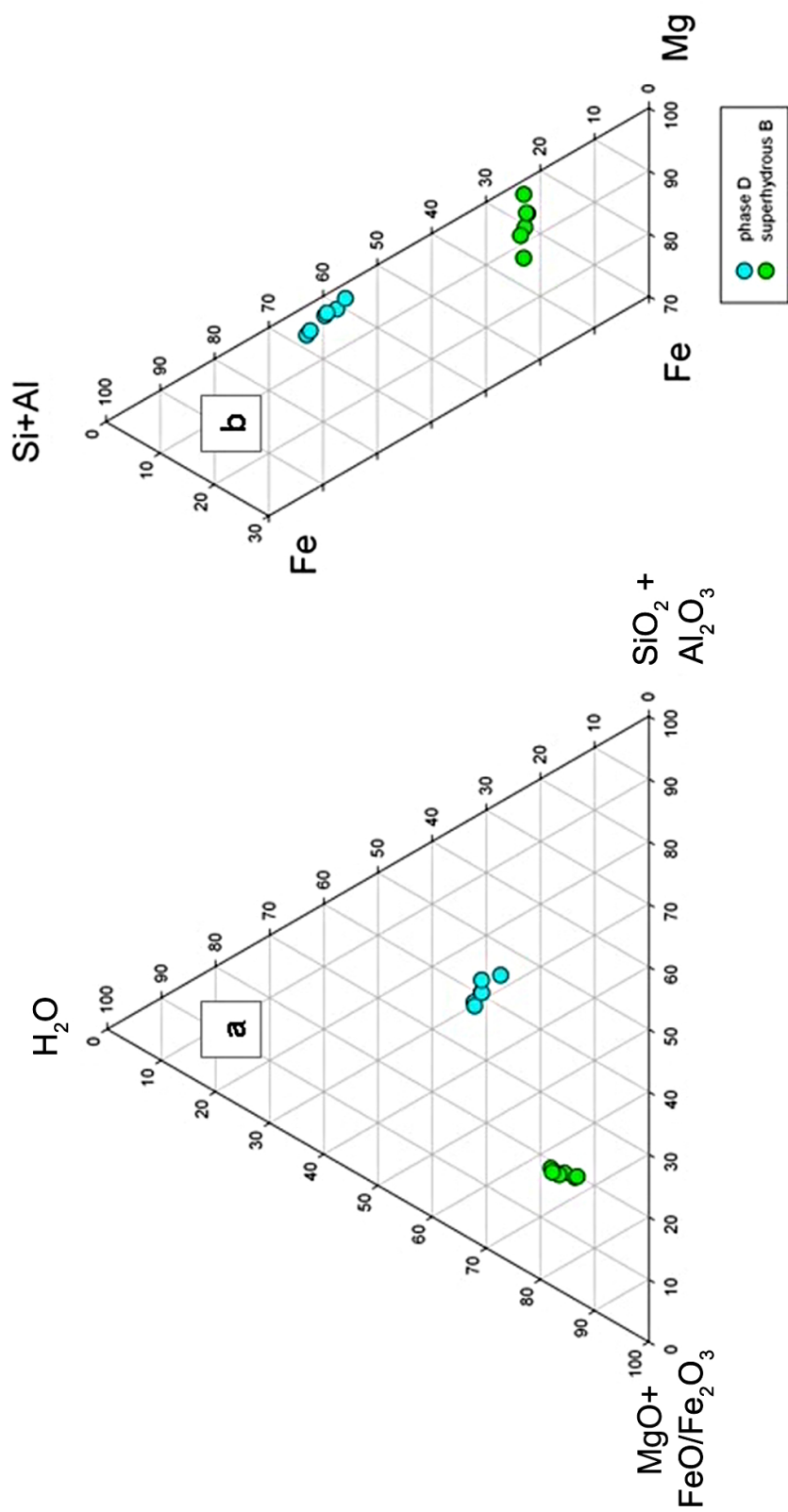


Figure 5.17: Ternary diagram of composition of phase D and superhydrous B - showing a) variations in water content, b) variations in Si+Al-content and Fe-content, respectively.

Table 5.12: EPMA data of phase D and superhydrous B (1σ standard deviation in parenthesis)

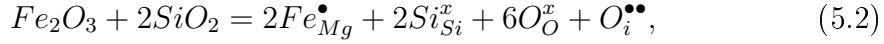
Sample Pressure, Temp	pts.	MgO [wt%]	SiO ₂ [wt%]	FeO [wt%]	Fe ₂ O ₃ [†] [wt%]	Al ₂ O ₃ [wt%]	Total	Mineral formula*
phase D - ideal formula MgSi₂H₂O₆								
GG 4345	47	24.6(6)	54.0(6)	3.8(2)	n.a.	4(1)	87.3(9)	(Mg _{0.91} Fe ²⁺ _{0.10}) _{1.01} (Mg _{0.20} Al _{0.16} Si _{1.64}) ₂ H _{2.56} O ₆
20.5 GPa, 1150°C								
GG 2947	39	27.9(9)	54(1)	2.9(6)	n.a.	1(1)	86.3(5)	(Mg _{0.91} Fe ²⁺ _{0.07}) _{0.98} (Mg _{0.34} Al _{0.05} Si _{1.61}) ₂ H _{2.75} O ₆
23 GPa, 1150°C								
GG 4376	39	25(1)	55(1)	3.6(6)	n.a.	4(1)	87.3(9)	(Mg _{0.91} Fe ²⁺ _{0.09}) _{1.00} (Mg _{0.22} Al _{0.13} Si _{1.65}) ₂ H _{2.56} O ₆
18 GPa, 1250°C								
GG 2945	69	26(1)	52(2)	4.0(2)	n.a.	4(2)	86.5(7)	(Mg _{0.90} Fe ²⁺ _{0.10}) _{1.00} (Mg _{0.27} Al _{0.15} Si _{1.58}) ₂ H _{2.71} O ₆
20.5 GPa, 1300°C								
GG 4377	42	22.2(5)	55.4(8)	5.1(3)	n.a.	4.4(7)	87.5(6)	(Mg _{0.85} Fe ²⁺ _{0.13}) _{0.98} (Mg _{0.16} Al _{0.16} Si _{1.68}) ₂ H _{2.53} O ₆
23 GPa, 1350°C								
GG 4348	31	21(1)	57(1)	1.4(1)	4.6(6)	5(1)	89(1)	(Mg _{0.98} Fe ²⁺ _{0.04} Fe ³⁺ _{0.01}) _{1.03} (Fe ³⁺ _{0.09} Al _{0.18} Si _{1.73}) ₂ H _{2.21} O ₆
20.5 GPa, 1450°C								
superhydrous B - ideal formula Mg₁₀Si₃H₄O₁₈								
GG 4345	56	50.6(6)	26.5(3)	17.3(7)	n.a.	0.4(1)	96.3(4)	(Mg _{8.72} Fe ²⁺ _{1.67} Si ⁴⁺ _{0.06} Al _{0.05}) _{10.5} Si _{3.00} H _{2.85} O ₁₈
20.5 GPa, 1150°C								
GG 2947	17	61.7(7)	27.7(9)	3.3(5)	n.a.	0.5(2)	93.5(7)	(Mg _{9.55} Fe ²⁺ _{0.29}) _{9.84} (Mg _{0.04} Al _{0.07} Si _{2.89}) ₃ H _{4.49} O ₁₈
23 GPa, 1150°C								
GG 4376	11	58.1(6)	26.3(3)	8.1(9)	n.a.	0.5(1)	93.6(5)	(Mg _{9.15} Fe ²⁺ _{0.73}) _{9.88} (Mg _{0.13} Al _{0.06} Si _{2.81}) ₃ H _{4.55} O ₁₈
18 GPa, 1250°C								
GG 2945	42	56(2)	26.8(5)	11(2)	n.a.	0.5(3)	95.4(5)	(Mg _{9.25} Fe ²⁺ _{1.01} Al _{0.03}) _{10.29} (Al _{0.04} Si _{2.96}) ₃ H _{3.42} O ₁₈
20.5 GPa, 1300°C								
GG 4377	20	57.7(6)	26.0(3)	7.8(5)	n.a.	0.8(1)	93.0(4)	(Mg _{9.01} Fe ²⁺ _{0.69}) _{9.70} (Mg _{0.14} Al _{0.10} Si _{2.76}) ₃ H _{4.96} O ₁₈
23 GPa, 1350°C								
GG 4348	53	53.2(3)	25.5(3)	1.9(1)	11.1(9)	1.8(3)	93.5(3)	(Mg _{8.43} Fe ²⁺ _{0.17} Fe ³⁺ _{0.82}) _{9.42} (Fe ³⁺ _{0.07} Al _{0.23} Si _{2.70}) ₃ H _{4.64} O ₁₈
20.5 GPa, 1450°C								

* water contents estimated based on low microprobe totals

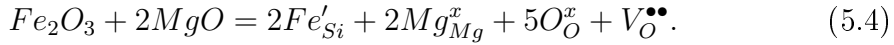
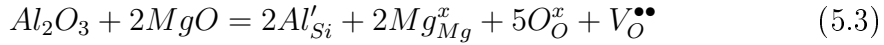
† Electron energy-loss spectroscopy

II. Superhydrous B

In contrast to phase D, which accommodates up to ~ 5 wt% Al_2O_3 in its structure, superhydrous B incorporates < 1.5 wt% Al_2O_3 . Magnesium contents of superhydrous B show significant variations of up to 12 wt% MgO and are inversely proportional to the total iron (Table 5.12; Figures 5.17, 5.18). Superhydrous B shows high amounts of ferric iron of about $\text{Fe}^{3+}/\Sigma\text{Fe} = 0.84(5)$ determined by electron energy-loss spectroscopy (Figure 5.16). Ferrous iron is incorporated by Mg-Fe substitution and ferric iron substitutes into the Mg- and the Si-sites while aluminium occupies the Si-site. The substitution of ferric iron into the Mg-site inhibits the water substitution by following equation:



whereas ferric iron and aluminum occupying the Si-site enhances the water substitution according to equation 5.6:



However, water contents are higher or lower compared to the ideal mineral formula ($\text{Mg}_{10}\text{Si}_3\text{H}_4\text{O}_{18}$) with changing amounts of ferric iron and aluminum in the Si-site and ferric iron in the Mg-site, respectively (Table 5.12).

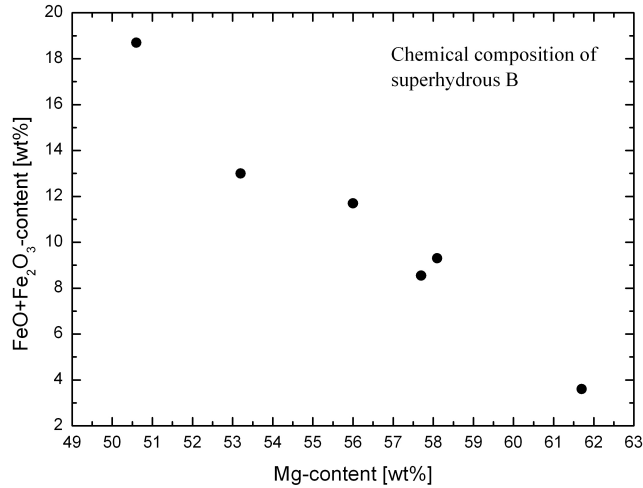
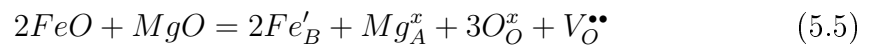


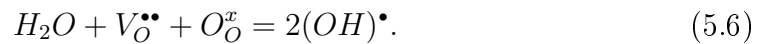
Figure 5.18: Chemical composition of ferroan superhydrous B - based on EPMA and EELS measurements; showing the inverse correlation of Mg- and total Fe-content corresponding to the common Mg-Fe substitution mechanism.

5.3.4 Point defect chemistry of nominally anhydrous mantle minerals - Water substitution mechanisms and potential water contents of garnet and pyroxene

Element substitutions of ferric iron and aluminum may enhance the incorporation of water in nominally anhydrous minerals by creation of point defects. On the basis of chemical analyses and electron energy loss spectroscopy potential water contents can be estimated and possible water substitution mechanisms can be assigned. Infrared analyses of garnet as well as majoritic-garnet yield water contents below the detection limit. However, potential water content of garnet was estimated by oxygen defect calculations (Table 5.13) based on the general majoritic-garnet formula $A_3B_2(\text{Si,Al})_3\text{O}_{12}$ with $A = \text{Mg}^{2+}, \text{Fe}^{2+}$ and $B = \text{Al}^{3+}, \text{Fe}^{3+}, \text{Si}^{4+}$. The calculations are based on the following equation as an example for A-site atoms in the B-site of garnet (for notation see Kröger and Vink 1956)⁵:



with magnesium and/or ferrous iron in the B-site. The oxygen vacancy is balanced by the hydration mechanism:



This implies that an oxygen vacancy equals two hydroxyl-groups that can be potentially incorporated. According to the calculated oxygen-vacancies of up to 0.08 p.f.u., which corresponds at most to 0.67% of oxygen sites being vacant, ~ 0.32 wt% H_2O (~ 0.05 H/Si) can be accommodated potentially in majoritic-garnet.

⁵ Mg^x_{Mg} - Mg in Mg-site, $\text{V}^{\bullet\bullet}_O$ - oxygen vacancy, $\text{O}^{\bullet\bullet}_i$ - O^{2-} on an interstitial site, Fe'_{Si} - ferric iron in Si-site, V''_{Mg} - Mg-vacancy, Fe^\bullet_{Mg} - ferric iron in Mg-site; x - neutral site, $'$ - positive undercharge, \bullet - negative undercharge

5. HYDROUS MARTIAN MANTLE COMPOSITION

Table 5.13: Calculated oxygen defects in majoritic-garnet and associated water contents

Sample	A_{total} = x	A'_B = x-3	Si_{Al}^\bullet = y	Oxygen defects a.p.f.u.	Water content [[OH]•] wt%
GG 4381	2.85(8)	-0.15(2)	0.07(4)	-0.2(2)	0
GG 4464	2.96(3)	-0.040(3)	0.23(1)	-0.28(6)	0
GG 4383	3.29(8)	0.29(3)	0.41(5)	-0.12(2)	0
GG 2960	3.6(1)	0.63(7)	0.64(3)	-0.008(1)	0
GG 2990	3.56(7)	0.56(4)	0.59(3)	-0.030(3)	0
GG 2987	3.6(1)	0.59(6)	0.56(4)	0.030(4)	0.11(2)
GG 4389	3.56(7)	0.56(4)	0.55(2)	0.010(1)	0.05(1)
GG 2957	3.59(9)	0.59(5)	0.51(4)	0.08(1)	0.32(5)

$A_{total} = x$ denotes A-site occupied by Mg and Fe^{2+}

A'_B denotes Mg and/or Fe^{2+} in the B-site

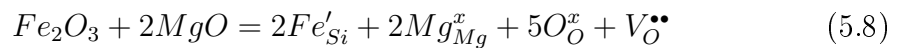
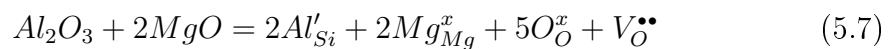
$Si_{Al}^\bullet = y = X_{Si} - 3$ with X_{Si} being the fraction of Si in a.p.f.u.

Fe^{3+} occupies exclusively B-site

$[(OH)^\bullet] = 2[V_O^\bullet]$ (see eq. 5.6)

The potential water content of pyroxene (ideal Mg-endmember $\text{Mg}_2\text{Si}_2\text{O}_6$) was estimated with an analogue calculation as for majoritic-garnet based on the assumption that Fe^{3+} substitutes in the Mg-site and the Si-site, Fe^{2+} is incorporated merely in the Mg-site and Al^{3+} goes into the Si-site (Table 5.14). According to the following defect equation, these substitution mechanisms cause either oxygen vacancies or interstitial oxygens, since octahedral site vacancies are excluded by chemical analyses:

Trivalent ion in Si-site



Fe^{3+} in Mg-site

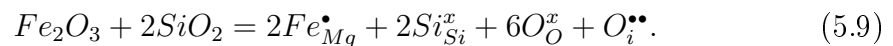


Table 5.14: Calculated oxygen defects in pyroxene and associated water content

Sample	M_{total} = x	Fe^{3+} = y	Fe'_{Si} = x-2	$\text{Fe}^{\bullet}_{\text{Mg}}$ = u	Al'_{Si} = z	Oxygen defects a.p.f.u.	Water cont. [(OH)•] wt%
GG 4381	2.03(1)	0.07(1)	0.030(5)	0.04(1)	0.010(1)	-0.0004(1)	0(0)
GG 4464	2.01(1)	0.05(1)	0.010(2)	0.03(1)	0.010(1)	-0.023(5)	0
GG 4383	2.03(4)	0.04(05)	0.03(2)	0.01(05)	0.010(1)	0.03(2)	0.3(1)
GG 2987	2.05(1)	0.04(1)	0.05(1)	-0.01(1)	0.00(0)	0.06(1)	0.5(1)

$M_{\text{total}} = x$ denotes M-site occupied by Mg and Fe_{total}

$\text{Fe}^{\bullet}_{\text{Mg}} \text{ u} = y - (x-2)$

$z = X_{\text{Al}}$ which corresponds to the fraction of Al in a.p.f.u.

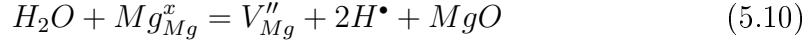
water content calculation [(OH)•] = $2[\text{V}_{\text{O}}^{\bullet\bullet}]$ (see eq. 5.6)

The oxygen-defects of up to 0.06 p.f.u. correspond to about 1% of oxygen site being vacant, which yields a potential water content of ~ 0.5 wt% H_2O (~ 0.06 H/Si) of pyroxene.

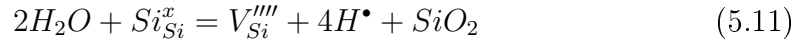
5. HYDROUS MARTIAN MANTLE COMPOSITION

Common water substitution mechanisms reported for Al-free nominally anhydrous minerals such as Mg_2SiO_4 -polymorphs including the presence of ferric iron are as follows:

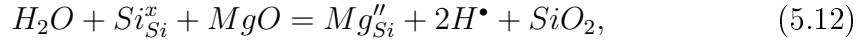
Mg-site vacancies



Si-site vacancies

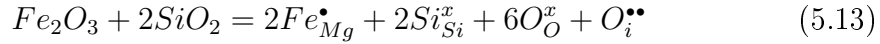


Mg-Si disorder



while Mg-Si disorder is difficult to determine by EPMA. Thus, dominant water substitution mechanism are accomplished by Mg-substitutions. The substitution of ferric iron for magnesium creates an interstitial oxygen or an octahedral site vacancy:

Fe^{3+} in Mg-site



Mg-site vacancy gives in combination with equation 5.13 the resulting equation 5.15, i.e. creation of octahedral-site vacancies without hydration:



5.4 Discussion

5.4.1 Water substitution mechanisms and water contents of iron-bearing nominally anhydrous minerals in the Martian mantle

I. Olivine

Olivine, the major Martian upper mantle mineral, with Fo_{93–89} composition incorporates 0.3 wt% H₂O, which is considerably less than the maximum solubility of water in Mg₂SiO₄ olivine of up to 0.89 wt% H₂O reported by Smyth et al. (2006). However, olivine determines the water storage capacity of the upper Martian mantle and thus contributes to the bulk storage capacity of the entire Martian mantle. According to the point defect chemistry based on chemical analyses, water in olivine is accommodated by Si-site vacancies:



II. Wadsleyite

The water storage capacity of Fe-bearing wadsleyite of 0.6 wt% H₂O is higher than that of olivine which implies an enlarged water storage capacity of the upper Martian transition zone. However, the water content of Mg₈₆-wadsleyite determined in this study is significantly reduced compared to the data of Kohlstedt et al. (1996) and Hirschmann et al. (2005). Several publications predict higher water contents in Mg,Fe-wadsleyite with increasing Fe-fraction compared to Mg-wadsleyite as summarised in Hirschmann et al. (2005). On the contrary, studies by Inoue et al. (1995) and Kohlstedt et al. (1996) report water contents of up to 3.1 wt% H₂O for Mg₁₀₀-wadsleyite and up to 2.4 wt% H₂O for Mg₉₀-wadsleyite. This implies an inverse correlation of iron and water contents, i.e. iron substitution in wadsleyite might be one parameter which diminishes the water content. Water substitution mechanisms for wadsleyite are reported by Smyth (1987), who specified M(3)-site Mg-vacancies as well as Si-vacancies to charge balance the protonation of a non-silicate oxygen O(1) site by the following substitution mechanisms $Mg^{2+} = 2 H^+$ and $Si^{4+} = 4 H^+$. Kohlstedt et al. (1996) suggested also Fe³⁺-Si disorder and Me-site vacancies as possible hydration mechanism. Downs (1989) proposed that also the O(2)-site is a possible protonation site in wadsleyite. The O(1)-site is bonded to five

5. HYDROUS MARTIAN MANTLE COMPOSITION

Mg-atoms and the O(2)-site is connected to two silicon and one magnesium atom (Ross et al. 2003), whereas protonation is assumed to be possible for all O atoms in wadsleyite. The lower amounts of octahedral site cations compared to ideal stoichiometry represent cation vacancies, which confirms the $Mg^{2+} = 2 H^+$ mechanism, while octahedral site vacancies can also be created when ferric iron substitutes into the Mg-site by defect equation 5.14. Uncertainties of chemical analyses, however, are such that it is difficult to resolve small amounts of cation vacancies such as silicon vacancies, which are charge balanced by protonation. Thus, no evidence was found for the $Si^{4+} = 4 H^+$ mechanism in wadsleyite. The infrared spectrum of wadsleyite (Figure 5.6) shows two main absorption peaks near 3360 cm^{-1} and 3612 cm^{-1} which are assigned to reflect the vibrational modes of two distinct protonation sites in wadsleyite (Figure 5.6). Cynn and Hofmeister (1994) suggest that the absorption peak near 3330 cm^{-1} is attributable to protonation of the O(2) site, while the weaker absorption peak near 3600 cm^{-1} corresponds to protonation of the O(1) site. Chemical analyses yield to fully occupied Si-site within the analytical accuracy which excludes water substitution mechanisms involving Si-site vacancies. Thus, obtained spectra imply that hydration of wadsleyite occurs by protonation of the O(2) site connected to the Si-site but likely substituting the adjacent Mg-atom and also by protonation of the O(1) site bonded to the M(3) site corresponding to defect equation 5.10. The absorption peaks corresponding to O(1) and O(2) site are shifted to higher wavenumber, i.e. the hydrogen bond is stiffer which may be caused by increasing O-O bond distances of the octahedra edge due to Fe-substitution. Cynn and Hofmeister (1994) argued that the absorption peak may be correlated to the O(2) site since it does not shift significantly due to iron substitution, i.e. the nearest cations are silicon atoms. Wadsleyite synthesised in this study has ferric iron content in contrast to the sample analysed by Cynn and Hofmeister (1994). Ferric iron might affect the OH-stretching frequencies due to modified bond distances as well as distinct atomic environments and may shift the absorption maximum of the O(1) and O(2) site to higher wavenumber. Thus, water is preferentially accommodated in wadsleyite by the following mechanism:

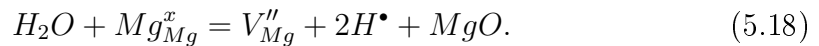
Mg-site vacancies



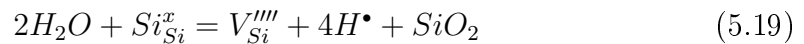
III. Ringwoodite

The water storage capacity of ferroan ringwoodite of about 1.1 wt% H₂O in a simple Martian bulk system is still significantly lower compared to Mg-ringwoodite, but higher than the water content of ferroan wadsleyite. Small amounts of octahedral and tetrahedral site vacancies, evident from mineral formula calculations based on chemical analyses determined by EPMA measurements, assign $Mg^{2+} = 2 H^+$ (defect equation 5.18) and $Si^{4+} = 4 H^+$ (defect equation 5.19) substitutions as protonation mechanisms in ringwoodite. As described above, Fe³⁺-Mg substitutions also create octahedral site vacancies without protonation, which rather diminishes the water content of ringwoodites. Infrared spectra of ferroan ringwoodite indicate increasing O-O distances of the protonated site by the shift of the absorption maximum to higher wavenumbers, which was described previously for iron-rich ringwoodite. This shift is probably related to the protonation of the octahedral site:

Mg-site vacancies



Si-site vacancies



McCammon et al. (2004) suggest that the water content of wadsleyite and ringwoodite is enhanced by the corresponding ferric iron (Figure 5.19). The data of majoritic-garnet obtained in this study follow the indicated trend for majorite, especially because the water content is estimated to be below 0.2 wt% H₂O. However, the data of wadsleyite and ringwoodite differ from previous data, particularly it appears that the ferric iron and water content of wadsleyite analysed in this study do not correlate.

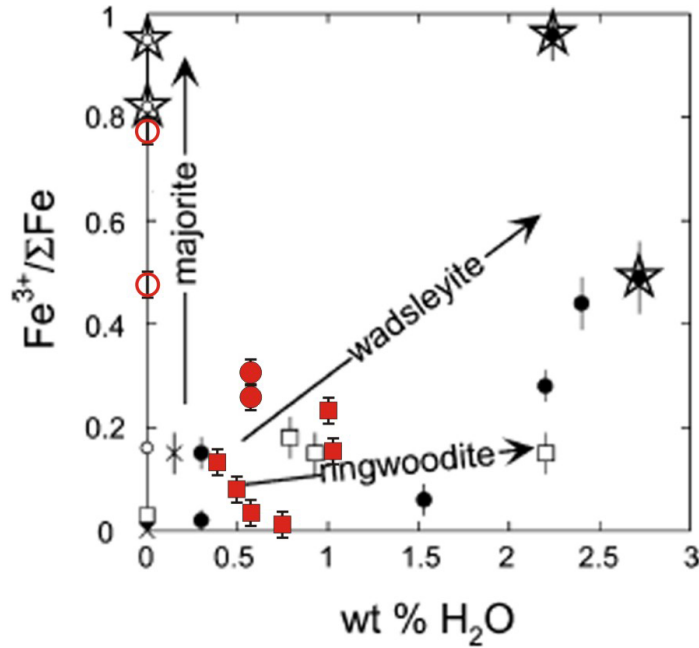
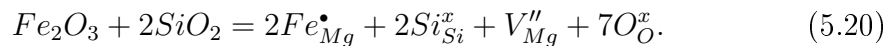


Figure 5.19: Ferric iron fraction versus water content (McCammon et al. 2004) - olivine - crosses, wadsleyite - solid circles, ringwoodite - open squares, majorite - open circles; stars indicate the runs carried out under extremely oxidizing conditions (AuPd capsules); trend of $Fe^{3+}/\Sigma Fe$ with OH concentration is indicated by annotated lines for each mineral; this study: red solid circles - wadsleyite, red solid squares - ringwoodite and red open circles (majoritic-garnet).

Ferroan ringwoodite shows even an inverse correlation of ferric iron and water content, which is in contradiction to the data displayed in Figure 5.19. This trend supports the Fe^{3+} -Mg substitution, which forms Mg-vacancies without protonation by the defect mechanism:



The presentation of these data in comparable units (wt%), concerning the water and ferric iron content of ringwoodite and wadsleyite, indicates the inverse correlation of ferric iron and water content (dashed line, Figure 5.20). The water content of ringwoodites synthesised in the hydrous FMAS system, however, show small variations in ferric iron content but similar hydrogen content (solid rectangle).

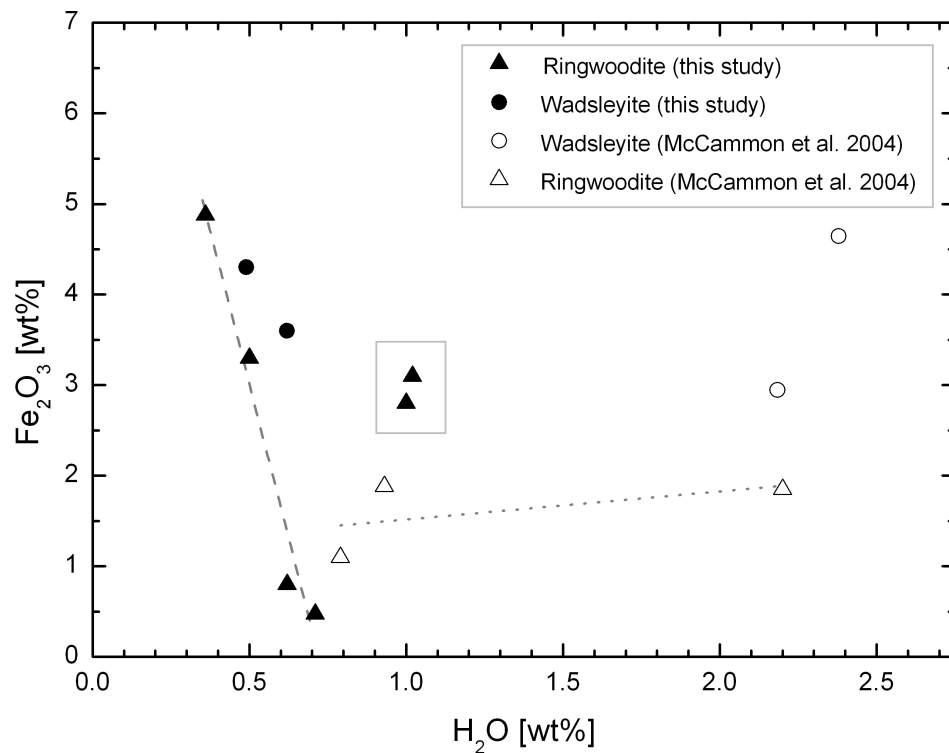


Figure 5.20: Ferric iron (wt%) versus water content (wt%) of ringwoodite and wadsleyite - open symbols - McCammon et al. (2004) with comparable synthesis conditions (Pt-capsules), solid symbols - this study; dashed line - linear fit of ringwoodite data ($\text{MgFeSiO}_4 + 9.5 \text{ wt\% H}_2\text{O}$ system), dotted line - linear fit of ringwoodite data (McCammon et al. 2004), solid line - ringwoodite data (hydrous FMAS system).

The ringwoodite data (McCammon et al. 2004) with 0.8-0.9 wt% H_2O is in the range of the data obtained in this study and may follow the trend indicated by the dashed line. The ringwoodite with 2.2 wt% H_2O has about the same ferric iron content as the other two samples (McCammon et al. 2004), thus the distinctly higher water content is not correlated with the ferric iron content. Despite the indication that ferric iron diminishes the water substitution in ringwoodite, the existing dataset is too inconsistent and insufficient to define general correlations of ferric iron and water content. This also shows that water storage capacities of wadsleyite and ringwoodite are more probably affected by multiple parameters such as phase assemblages, oxidation state of iron, composition of coexisting phases and melt composition. Further possible impact factors on the water storage capacity of nominally anhydrous minerals are described by Hirschmann et al. (2005).

IV. Garnet and pyroxene

The water contents of garnet and pyroxene are probably below the detection limit of infrared analyses, because the IR-spectra show no water absorption peaks. Calculation of oxygen vacancies based on chemical analyses indicate theoretical water contents of garnet up to 0.32(5) wt% H₂O and pyroxene up to 0.5(1) wt% H₂O. This water content should be detectable by IR-analyses. The absence of detectable water contents is probably due to the water partitioning between ringwoodite (rw) - garnet (gt) and wadsleyite (wd) - garnet of $D_{Rw/Gt}^{water} \gg 1$ and $D_{Wd/Gt}^{water} \gg 1$ as well as wadsleyite and pyroxene (cen - clinoenstatite; orthoenstatite in this study) of $D_{Wd/Cen}^{water} \sim 3.8$ (Bolfan-Casanova et al. 2000).

5.4.2 Dense hydrous Mg-Fe silicates in the Martian mantle

Phase D and superhydrous B could be relevant dense hydrous Mg-Fe silicates in the lower transition zone of the Martian mantle at 18-20.5 GPa (Figure 5.21). Both hydrous phases show thermal stability up to 1450°C at 20.5 GPa, which is at elevated temperatures compared to the previously reported thermal stability of phase D (at 1250°C and 25 GPa, Kawamoto 2004 and at 1300°C and 23 GPa, Ohtani et al. 2000). At higher and lower pressures the stability temperature of phase D and superhydrous B decreases reaching 1250°C at 18 GPa and 1350°C at 23 GPa, which is again comparable to the stability of superhydrous B obtained by previous experiments (Kawamoto 2004, Ohtani et al. 2000), while phase D is stable at higher temperature than reported for bulk compositions with comparable water content.

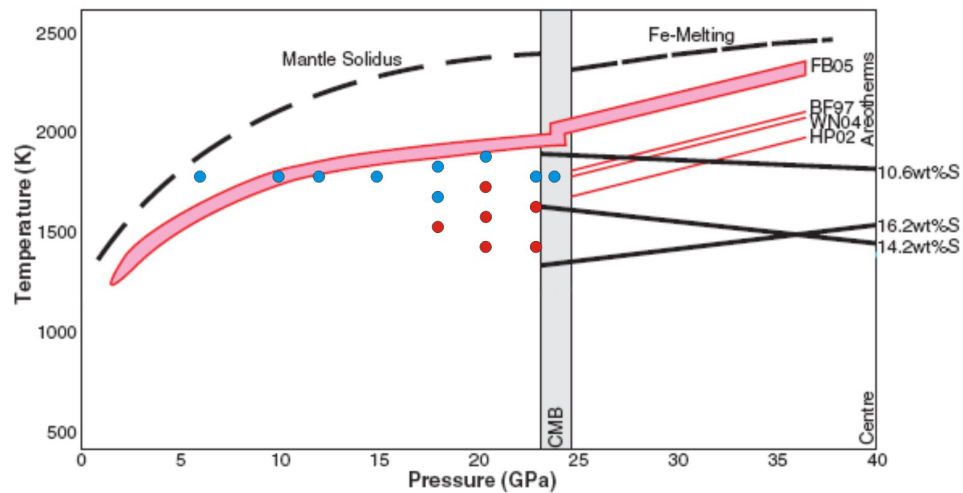


Figure 5.21: Model of the Martian thermal gradient - Core-mantle boundary (CMB) after Fei and Bertka (2005), thermal gradients (areotherms) after Fei and Bertka (2005)(FB05); black solid line - temperatures of liquidus loop intersections for sulfur contents of the core (Stewart et al. 2007); red solid lines - core areotherms of Bertka and Fei (1997)(BF97), Williams and Nimmo (2004)(WN04), Hauck and Phillips (2002)(HP02); blue circles - experiments performed in this study (Dreibus and Wänke [1985], Wänke and Dreibus [1988] Martian mantle composition); red circle - experimental runs containing superhydrous B and phase D.

5.5 Conclusions - Implications for the water storage capacity of the Martian interior

The mineralogical structure (hydrous mantle) of planet Mars according to the areotherm of Fei and Bertka (2005) is composed of an upper mantle dominated by olivine, pyroxene and garnet extending up to 11.5 GPa (~ 900 km depth). The upper transition zone consists of pyroxene, wadsleyite and garnet and is extended by ~ 2 GPa (~ 11.5 -19 GPa, about 900-1475 km depth) compared to the anhydrous mantle (Bertka and Fei 1997). Pyroxene decomposes at the transition from the upper to lower transition zone, which results in an increased majorite component of garnet in the lower transition zone. Akimotoite forms nearby the core-mantle boundary in the lower transition zone at around 23 GPa and 1500°C by partial transformation of majoritic-garnet (Figure 5.22).

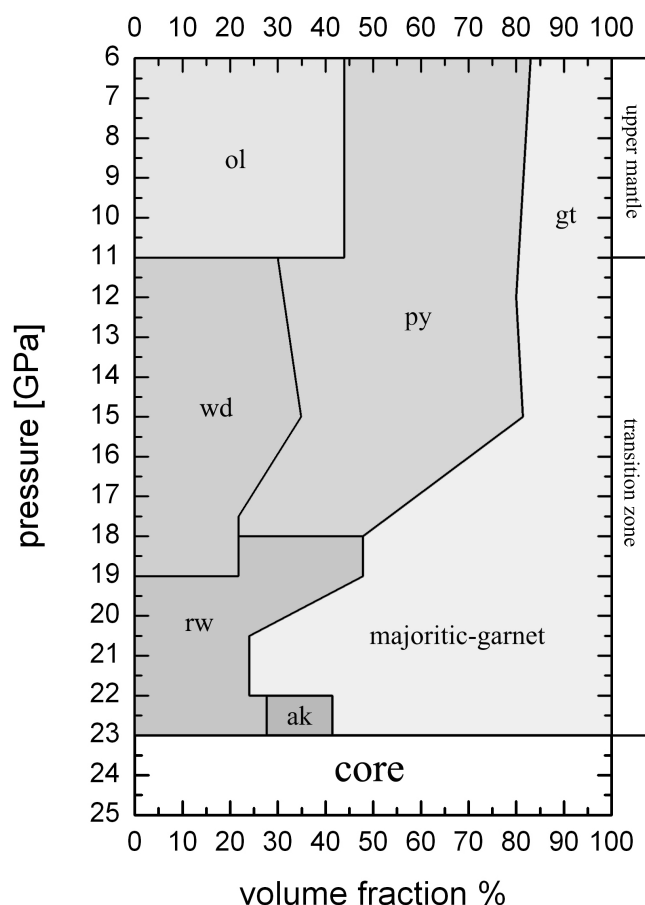


Figure 5.22: Mineralogical model of a hydrous Martian interior - derived on the basis of mass balance calculations (section 5.2).

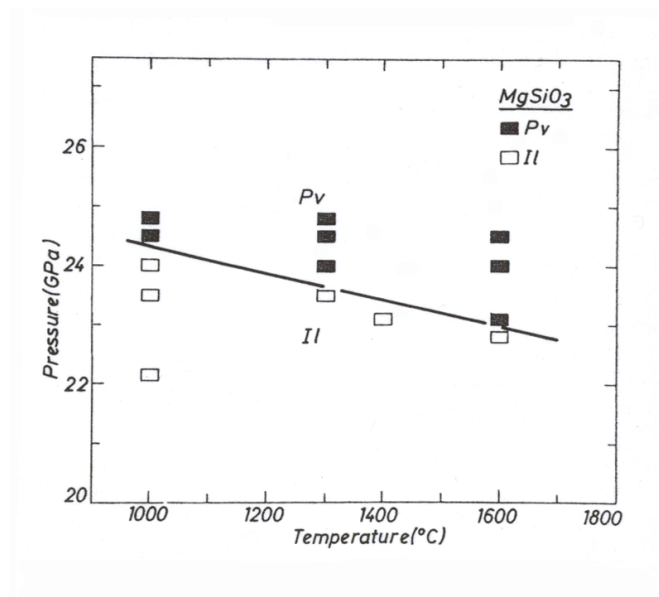


Figure 5.23: MgSiO_3 Ilmenite-perovskite transition boundary as a function of pressure and temperature - Ito & Takahashi (1989).

The pressure-temperature conditions at the core-mantle boundary (1800 K and 23 GPa; Williams and Nimmo 2004, Fei and Bertka 2005) are insufficient to stabilise a perovskite phase according to data on the MgSiO_3 system (Ito and Takahashi 1989, Figure 5.23). The experiment at 23 GPa and 1500°C performed in this study also confirms that perovskite is absent in the mantle at the Martian core-mantle boundary (CMB). The perovskite phase occurs at 24 GPa and 1500°C, which corresponds to pressure-temperature conditions beyond the Martian CMB. This implies that a lower Martian mantle is absent in the present mineralogical model of Mars. The water storage capacity of the Martian interior is mainly determined by the amount of water stored in olivine (~ 0.3 wt% H_2O), wadsleyite (~ 0.6 wt% H_2O) and ringwoodite (~ 1.1 wt% H_2O). This implies that the water storage capacity of the Martian mantle increases from upper mantle to lower transition zone. Table 5.15 shows the amount of water that can be stored in the upper Martian mantle and Martian mantle transition zone. Akimotoite may subordinately contribute to the water storage capacity of the deep Martian mantle region. However, according to the water content and the mass fraction of olivine as well as wadsleyite and ringwoodite, about 6.94×10^{20} kg H_2O can be potentially stored in a water-saturated model Martian mantle (Table 5.15).

5. HYDROUS MARTIAN MANTLE COMPOSITION

Table 5.15: Estimated water content of a saturated Martian mantle.

		upper mantle	transition zone	
			upper	lower
depth	km	50 [‡] -900	900-1475	1475-1900
		olivine	wadsleyite	ringwoodite
average mole fraction [†]		45%	27.5%	37.5%
volume*	km ³	3.45x10 ¹⁰	5.65x10 ⁹	5.51x10 ⁹
mass	kg	1.11x10 ²³	1.95x10 ²²	1.95x10 ²²
amount water	ppm wt	~3000	~6000	~11000
	kg	3.34x10 ²⁰	1.17x10 ²⁰	2.14x10 ²⁰
Σ	kg		6.65x10 ²⁰	
		~50% of the Earth's ocean water mass*		

† based on mass balance calculation / hydrous Mars model (Figure 5.22)

‡ average crustal thickness (Zuber et al. 2000)

* modal fraction of particular mineral phase of upper mantle and upper and lower transition zone volume, respectively

* Mass of the oceans (Earth) = 1.4x10²¹ kg (Yoder 1995)

Chapter 6

General conclusions

I. The potential existence of hydrous mantle silicates in the Martian interior

Geochemical analyses imply that Mars is a more volatile rich planet than Earth, since solar formation models predict an increase of volatile components with increasing distance from the Sun (Dreibus & Wänke 1985). Several formation models of planet Mars predict the preservation of water during the accretion as well as the delivery of water by impactors after accretion. During the planetary cooling and differentiation processes, accreted water may have been liberated from the interior and contributed to the early atmosphere or lost to space. However, the scenario of a magma ocean solidification in the early history of Mars postulated by Elkins-Tanton (2008) indicates the possible enrichment of water in the Martian mantle. As solidification of the magma ocean proceeded and mineral phases crystallised, iron and volatiles partitioned preferentially into the residual melt. The $\text{MgFeSiO}_4 + \text{H}_2\text{O}$ system (this study) may therefore be considered as a model system for this iron-rich residual melt. This study has shown that dense hydrous Mg-Fe silicates in the Fe-rich system are stable at higher temperatures than in a magnesium-rich system relevant for the Earth (Figure 6.2). However, it is assumed that the solidification took place in the early Noachian epoch within up to 5 Ma after planet formation, which indicates temperatures above the stability of dense hydrous magnesium silicates according to the thermal history models of Spohn et al. (2001)(Figure 1.1). Nevertheless, it is likely that nominally anhydrous minerals such as ringwoodite and wadsleyite incorporated significant amounts of water during magma ocean solidification.

According to the present Martian mantle areotherms (Sohl and Spohn 1997, Fei and Bertka 2005), with optimised model parameters to satisfy the geochemical

6. GENERAL CONCLUSIONS

data based on SNC meteorites and the maximum value of the polar moment of inertia, the temperatures at the Martian CMB would be above the thermal stability of dense hydrous Mg-Fe silicates. However, thermal history models of Mars (Spohn et al. 2001, Figure 1.1) predict current mantle temperatures of 1650 K and 1500 K (lithosphere growth model and plate tectonic model, respectively), which is in the stability range of dense hydrous Mg-Fe silicates. Matsukage et al. (2005) showed that the density of hydrous silicate melts with 5 wt% H₂O increases with increasing iron content and that the decrease of the density of the silicate melt due to water is diminished at high pressures. Therefore, the density of iron-rich hydrous silicate melts could have been high enough for them to sink to the Martian core-mantle boundary, while ringwoodite and garnet floated. Such a scenario was also proposed for the Earth, with descending dense hydrous melts that finally solidified, and which may form the D" layer (Elkins-Tanton 2008, Boyet and Carlson 2005). The dense hydrous Mg-Fe silicate, phase D, formed as liquidus phase in the experimental run at 23 GPa and 1350°C. Thus, if a dense water rich reservoir was preserved during the magma ocean solidification of Mars, the appearance of dense hydrous Mg-Fe silicates is possible in the deep mantle at a depth of 1900 km close to the core mantle boundary.

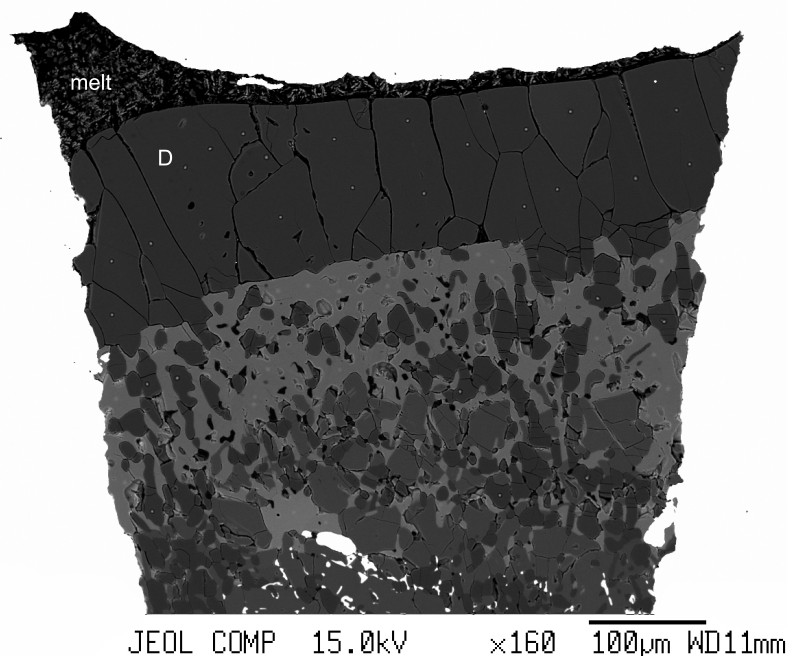


Figure 6.1: Backscattered electron image of sample GG 4377 - 23 GPa, 1350°C, phase D is the liquidus phase (D) in contact with the melt.

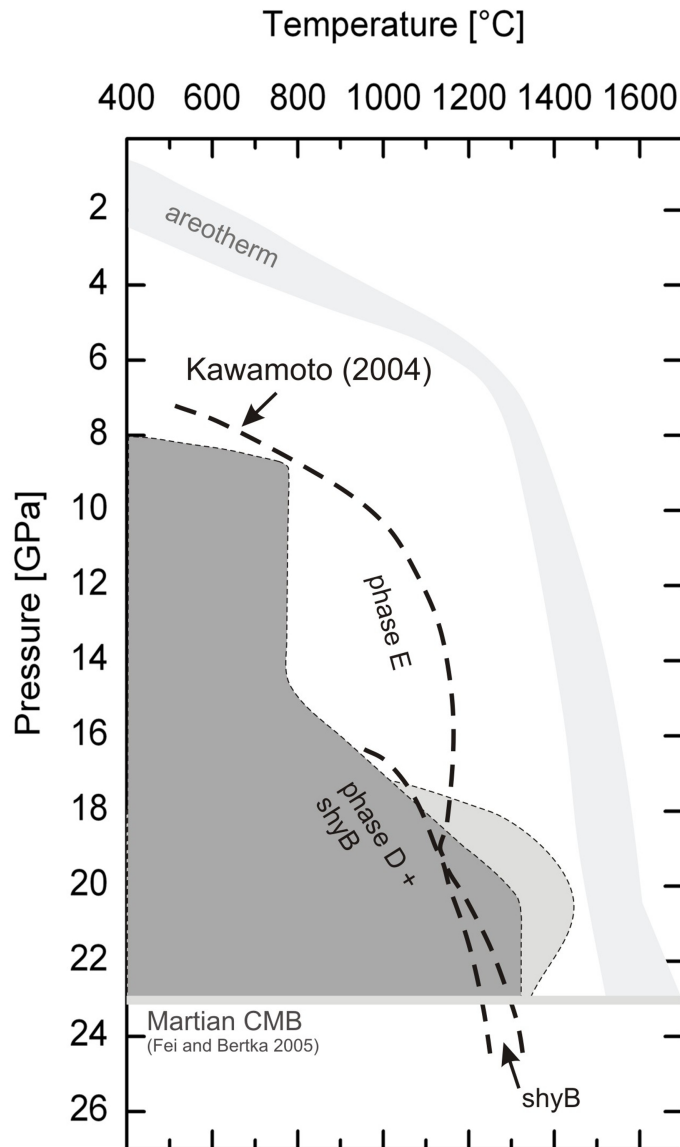


Figure 6.2: Stability regions of dense hydrous magnesium silicates as function of pressure and temperature - for KLB-1 + 13.6 wt% H₂O bulk composition (Kawamoto 2004), bold dashed line; MgFeSiO₄ + 9.5 wt% H₂O bulk composition (this study), gray area; simple hydrous Martian mantle bulk composition (FMAS + 12.35 wt% H₂O, this study), light gray area; range of the present Martian mantle areotherm based on two different models from Sohl and Spohn (1997).

II. The water storage capacity of the Earth's and Martian mantles - A comparison

Multiple parameters account for the water storage capacity of nominally anhydrous minerals as presented in chapter 4.4. Despite several influencing factors, the water content of ringwoodite is determined by its iron content and the temperature. The water content of ringwoodite decreases with increasing iron fraction and with increasing temperature (Figure 6.3), yet an increase in the iron content has a stronger effect on the water contents than the temperature. This implies that the iron-rich nominally anhydrous minerals in the Martian interior could store less water than those in the Earth's interior, although the assumed mantle temperature of the Earth is higher than that of Mars (Figure 6.3).

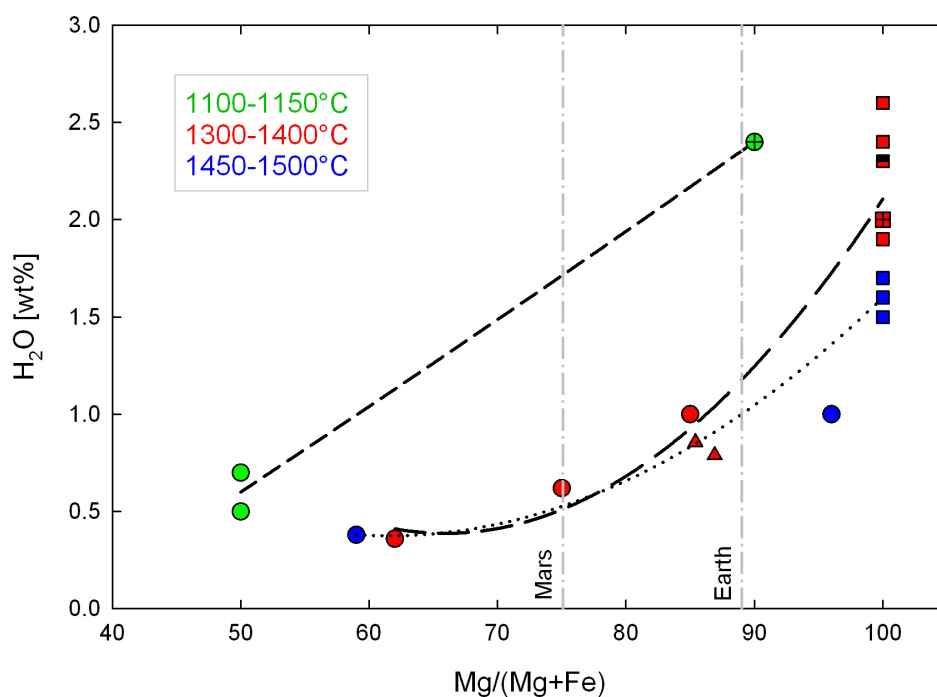


Figure 6.3: Water contents of ringwoodite as a function of the iron content - green symbols - 1100-1150°C isotherm, red symbols - 1300-1400°C isotherm, 1450-1500°C isotherm; circles - this study, squares - Ohtani et al. (2000), triangles - Smyth et al. (2003), crossed square - Kudoh et al. (2000), semi-filled square - Wang et al. (2003), crossed circle - Kohlstedt et al. (1996); short dashed line - regression line 1100-1150°C isotherm, dashed line - regression line 1300-1400°C, dotted line - regression line 1450-1500°C isotherm, dotted dashed lines represent the Mg# of the Martian mantle (Dreibus & Wänke 1985, Wänke & Dreibus 1988) and the Earth's mantle (Kargel & Lewis 1993).

The effect of temperature on the water storage capacity of ringwoodite is diminished and becomes less obvious with increasing iron content and lower water contents, respectively (Figure 6.3). The schematic diagram of the water storage capacity of nominally anhydrous minerals (Figure 4.26, Hirschmann et al. 2005) shows that the water contents of nominally anhydrous minerals are expected to increase with temperature up to the water saturated solidus, reaching a maximum and then decrease up to the dry melting temperature of the mineral phase. However, if this water content maximum is small, then the water content would appear to be approximately constant over a wide temperature range because the decrease of the water content with increasing temperature (after reaching water saturation) would be probably within the analytical error of IR analyses. Despite the probable decrease of the water storage capacity with increasing temperature, the water contents of ringwoodite would be approximately constant (within analytical accuracy) in the Martian transition zone. Thus, ringwoodite may store about 1 wt% H₂O in the lower Martian transition zone at 23 GPa and ~1500°C, which may correspond to the water storage capacity of ringwoodite at higher temperature (~1600°C at 23 GPa) in the Earth's lower transition zone.

III. Iron and aluminium partitioning between mantle minerals and melt - Implications for the chemical differentiation of an early hydrous Martian mantle

According to the iron partitioning coefficient K_D between ringwoodite and the coexisting melt and garnet and coexisting melt, respectively, iron partitions preferentially into the melt, which is enhanced with increasing pressure in case of ringwoodite (Figure 6.4a). Additionally, the partitioning behavior of iron is relatively independent of the melt compositions (Figure 6.4b).

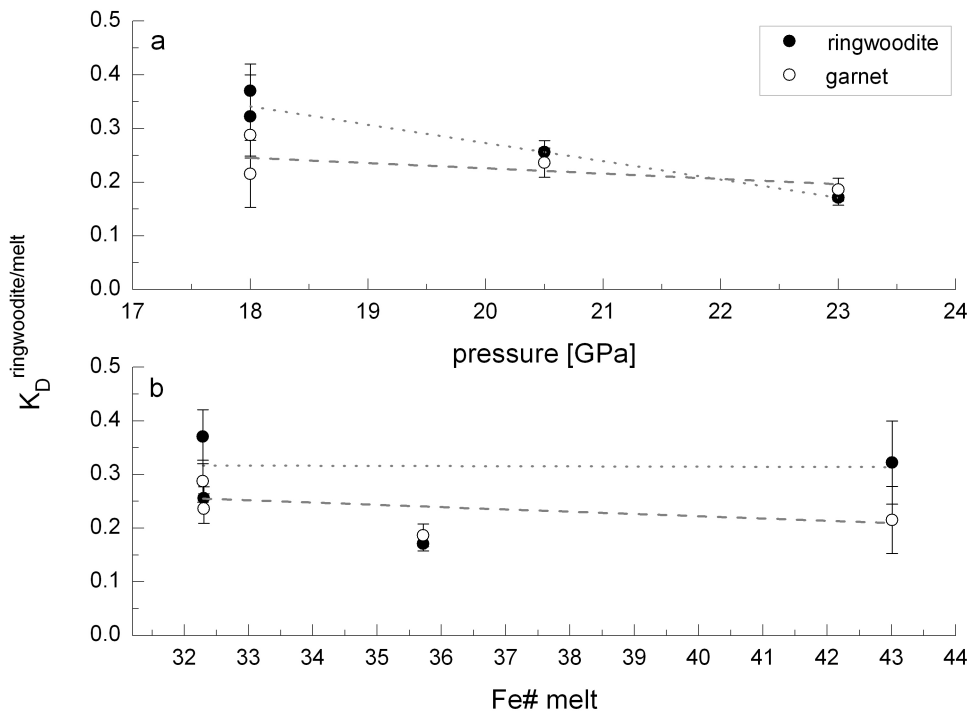


Figure 6.4: Iron partitioning coefficient K_D between ringwoodite and coexisting melt as well as garnet and coexisting melt - as function of pressure (a) and melt composition (Fe#) (b), K_D defined as $(Fe/Mg)_{\text{mineral}}/(Fe/Mg)_{\text{melt}}$; error bars denote 1σ standard deviation.

This implies that ringwoodite, which initially crystallised together with garnet from a cooling Martian magma ocean, was Mg-rich compared to the Martian bulk composition and the Mg-content of ringwoodite would increase with increasing depth of crystallisation. These Mg-rich mineral phases are possibly buoyant relative to the melt at high pressure (Matsukage et al. 2005) and float by forming mantle cumulates of ringwoodite, garnet and wadsleyite, which have the

potential to store significant amounts of water. In the course of magma ocean crystallisation, the fractionation of garnet and ringwoodite increased successively the iron-content of the melt so that the subsequently-crystallised mineral phases were iron-rich. These iron-rich minerals may have a higher density than the melt and the surrounding cumulates and sink deeper to form the lower transition zone. These cumulates at greater depth may store smaller amounts of water due to the higher iron-content of the mineral phases and the higher temperature. This implies that the Martian mantle may be heterogeneous in terms of Fe- and H₂O-contents of the constituent mineral phases, with Mg-rich cumulates at the lower pressure (~15-18 GPa) and Fe-rich cumulates at higher pressure (~18-23 GPa) in the lower Martian transition zone. However, these heterogeneities may have been averaged out by convective stirring of the mantle over the Martian history.

The high Al partitioning values between garnet and melt (Table 5.11, Figure 6.5) are caused by the low Al contents in the melt fraction, whereas the data by Trønnes and Frost (2002) using a pyrolitic and KLB-1 bulk composition indicate a high Al content of the melt and thus $D_{\text{Al}}^{\text{gt/melt}}$ values of about 2. Both data sets show small variations with pressure, and the errors (this study) result from the melt composition, which was measured with EPMA using a defocused electron beam of 20 μm . The garnets analysed in this study have an almandine component of up to 31%, which may retain the aluminum in the structure of garnet and inhibit the Al partitioning into the melt. This implies, that the fractionation of garnet from a deep iron-rich magma ocean would decrease the Al content of the residual melt and subsequently crystallising minerals would be poor in aluminium. This may be a plausible explanation for the apparent low Al content assumed for the Martian mantle from analyses of crust rocks (SNC meteorites, Wänke and Dreibus 1988).

6. GENERAL CONCLUSIONS

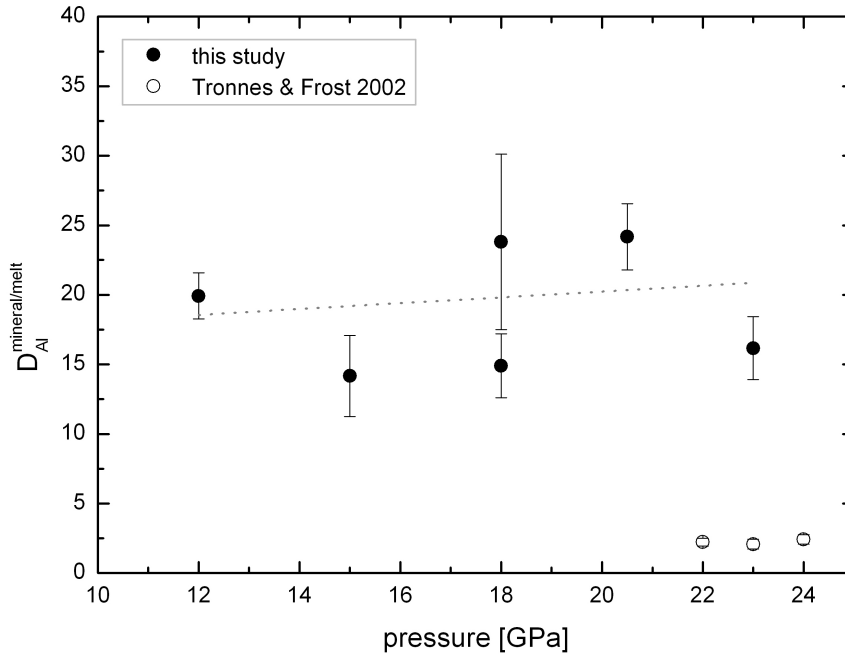


Figure 6.5: Aluminium partitioning between garnet and melt as function of pressure - D is defined as $D_{Al} = (Al)_{\text{garnet}} / (Al)_{\text{melt}}$, solid circles - this study, open circles - Trønnes and Frost (2002); error bars denote 1σ standard deviation.

IV. The effect of iron on the compressibility of hydrous ringwoodite

This study showed that the bulk modulus of ringwoodite, which is one of the parameters that determine the velocities of compressional waves in the lower transition zone, is not a function of the iron-content of ringwoodite. The bulk modulus of iron-rich ringwoodites is close to values reported for anhydrous Mg-endmember ringwoodites ($K \sim 185$ GPa). However, this conclusion is only valid up to the value of 0.1 a.p.f.u. of cation vacancies that result from the oxidation of iron and/or the accommodation of water. Above this concentration of cation vacancies, the bulk modulus of ringwoodite decreases, i.e. with increasing water and/or ferric iron content ringwoodite becomes more compressible.

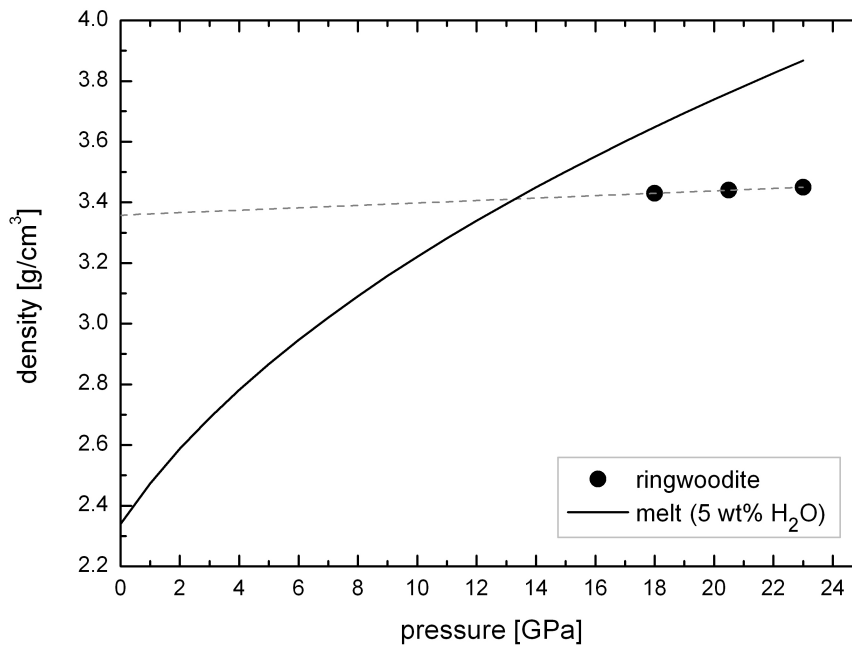


Figure 6.6: Density of a hydrous Martian melt and ringwoodite as function of pressure at 2170 K - calculations of the density of ringwoodite are based on equation of state and iron partitioning data (this study), dashed line - polynomial fit of ringwoodite data; calculations of the density of the hydrous melt are based on Ita and Stixrude (1992), Matsukage et al. (2005) and Xu et al. (2008).

The combination of the presented equation of state and the iron partitioning data of ringwoodite yields a first order approximation for the density of ringwoodite that crystallised from a hydrous Martian magma ocean. The iron partitioning data between ringwoodite and melt, obtained on the simple hydrous Martian mantle composition was applied to the actual Martian mantle composition (Table 5.1), which yield the iron content of ringwoodite according to equation 5.1 (Table 6.1). In order to determine the density of ringwoodite, the volume of the Mg- and Fe-endmember ringwoodite was calculated at 18, 20.5 and 23 GPa at 2170 K using a P-V-T equation of state (Ita and Stixrude 1992, Xu et al. 2008). The density of the ringwoodite crystals are the product of the density fraction of the endmember components (Table 6.1). The density of a Martian melt (with 5 wt% H₂O) as a function of pressure at 2170 K was calculated from estimated results of Matsukage et al. (2005). These results provide evidence that ringwoodite, which crystallises ≥ 15 GPa from a hydrous Martian magma ocean, will be Mg-rich and less dense in respect to the melt and will therefore float. In addition, the high Mg-content would imply a high water storage capacity of ringwoodite (see above), and consequently large amounts of water that can be

6. GENERAL CONCLUSIONS

stored in the Martian mantle. Furthermore, this confirms that iron-rich hydrous melt will be denser than the surrounding cumulates and sink to the Martian CMB. Therefore, depending on the thermal evolution and on the mantle temperatures of Mars, respectively, dense hydrous Mg-Fe silicates may crystallise under suitable conditions (1450°C and 23 GPa) in the Martian mantle.

Table 6.1: Density and iron content calculation of ringwoodite (rw) at 2170 K.

Pressure [GPa]	18	20.5	23	
K_D	0.32	0.26	0.17	
Fe/(Fe+Mg)	0.09	0.07	0.05	
Mg/(Mg+Fe)	0.91	0.93	0.95	
density [g/cm ³]*	Mg-endmember	3.31	3.35	3.39
	Fe-endmember	4.67	4.73	4.78
density [g/cm ³]	Mg-Fe rw	3.43	3.44	3.45

actual Martian mantle composition $X_{Fe}^{melt} / X_{Mg}^{melt} = 0.26$
 X_{Fe}^{melt} is the molar Fe/(Mg+Fe) ratio
 K_D defined as $(Fe/Mg)_{ringwoodite} / (Fe/Mg)_{melt}$ as in equ. 5.1
* from volume data of thermal equation of state $K_0 = 185$ GPa (Mg-rw),
 $K_0 = 186$ GPa (Fe-rw)

References

- Anderson, D.L. (2007) *New theory of the earth*. Cambridge, UK; New York: Cambridge University Press, 408 pp.
- Angel, R.J., Finger, L.W., Hazen, R.M., Kanzaki, M., Weidner, D.J., Liebermann, R.C. and Veblen, D.R. (1989) Structure and twinning of single-crystal MgSiO₃ garnet synthesized at 17 GPa and 1800°C. *American Mineralogist*, **74**, 509–512.
- Angel R. J. (2000) Equations of state. In: Hazen, R. M. and Downs, R. T. (eds.) *High-Temperature and High-Pressure Crystal Chemistry*. Reviews in Mineralogy and Geochemistry, vol. 41, Mineralogical Society of America and Geochemical Society, Washington, USA, 35–59.
- Angel, R.J. (2002) EoS-Fit V5.2 program. Crystallography Laboratory, Virginia Tech, Blacksburg, U.S.A.
- Armbruster, T., Geiger, C.A. and Lager, G. (1992) Single crystal X-ray study of synthetic pyrope almandine garnets at 100 and 293 K. *American Mineralogist*, **77**, 512–521.
- Bertka, C.M. and Fei, Y. (1997) Mineralogy of the Martian interior up to core-mantle boundary pressures, *Journal of Geophysical Research*, **102**, 5251–5264.
- Bertka, C.M. and Fei, Y. (1998) Density profile of an SNC model martian interior and the moment-of-inertia factor of Mars. *Earth and Planetary Science Letters*, **157**, 79–88.
- Blanchard, M., Balan, E. and Wright, K. (2009) Incorporation of water in iron-free ringwoodite: A first-principles study. *American Mineralogist*, **94:1**, 83–89.
- Bolfan-Casanova, N., Keppler, H. and Rubie, D.C. (2000) Partitioning of water between mantle phases in the system MgO-SiO₂-H₂O up to 24 GPa: Implications for the distribution of water in the Earth's mantle. *Earth and Planetary Science Letters*, **182**, 209–221.

- Boyet, M. and Carlson, R.W. (2005) ^{142}Nd evidence for early (>4.53 Ga) global differentiation of the silicate Earth. *Science*, **309**, 576–581.
- Chamorro Pérez, E.M., Daniel, I., Chervin, J.-C., Dumas, P., Bass, J.D., and Inoue, T. (2006) Synchrotron IR study of hydrous ringwoodite ($\gamma\text{-Mg}_2\text{SiO}_4$) up to 30 GPa. *Physics and Chemistry of Minerals*, **33**, 502–510.
- Crichton, W.A. and Ross, N.L. (2005) Equations of state of dense hydrous magnesium silicates: results from single crystal X-ray diffraction. *Mineralogical Magazine*, **69**, 273–287.
- Cynn, H. and Hofmeister, A.M. (1994) High-pressure IR spectra of lattice modes and OH vibrations in Fe-bearing wadsleyite. *Journal of Geophysical Research*, **99**, 17'717–17'727.
- Downs, J.W. (1989) Possible sites for protonation in $\beta\text{-Mg}_2\text{SiO}_4$ from an experimentally derived electrostatic potential. *American Mineralogist*, **74**, 1124–1129.
- Dreibus, G. and Wänke, H. (1985) Mars, a volatile-rich planet. *Meteoritics*, **20**, 367–381.
- Dreibus, G., Jagoutz, E., and Wänke, H. (1997) Water in the Earth's mantle. *Geologiya i Geofizika*, **38**, 269–275.
- Dziewonski, A.M. and D.L. Anderson (1981) Preliminary Reference Earth Model (PREM). *Physics of the Earth and Planetary Interiors*, **25**, 297–356.
- Elkins-Tanton, L.T. (2008) Linked magma ocean solidification and atmospheric growth for Earth and Mars. *Earth and Planetary Science Letters*, **271**, 181–191.
- Emsley, J. (1980) Very strong hydrogen bonding. *Chemical Society Reviews*, **9**, 91–124.

- Farrugia, L.J. (1999) WinGX suite for small-molecule single-crystal crystallography. *Journal of Applied Crystallography*, **32**, 837–838.
- Fei, Y. and Bertka, C.M. (1996) The State of the Martian Core. *Lunar and Planetary Science*, **27**, 351–352.
- Fei, Y. and Bertka, C. (2005) The interior of Mars. *Science*, **308**, 1120–1121.
- Fei, Y., Mao, H. and Mysen, B.O. (1991) Experimental determination of element partitioning and calculation of phase relations in the MgO-FeO-SiO₂ system at high pressure and high temperature. *Journal of Geophysical Research*, **96**, 2157–2169.
- Fei, Y., Prewitt, C.T., Mao, H. and Bertka, C.M. (1995) Structure and density of FeS at high pressure and high temperature and the internal structure of Mars. *Science*, **268**, 1892–1894.
- Fei, Y., Van Orman, J., Li, J., van Westrenen, W., Sanloup, C., Minarik, W., Hirose, K., Komabayashi, T., Walter, M. and Funakoshi, K. (2004b) Experimentally determined postspinel transformation boundary in Mg₂SiO₄ using MgO as an internal pressure standard and its geophysical implications. *Journal of Geophysical Research*, **109**, B02305.
- Finger, L.W., Hazen, R.M., Zhang, J., Ko, J., and Navrotsky, A. (1993) The effect of Fe on the crystal structure of wadsleyite β -(Mg_{1-x}Fe_x)₂SiO₄, 0.00 < x < 0.40. *Physics and Chemistry of Minerals*, **19**, 361–368.
- Fleet, M.E. (1981) The structure of magnetite. *Acta Crystallographica*, **B37**, 917–920.
- Frost, D.J. (1999) The stability of dense hydrous magnesium silicates in Earth's transition zone and lower mantle. In: Fei, Y., Bertka, C.M., Mysen, B.O. (Eds.), *Mantle Petrology, Field Observation and High Pressure Experimentation, vol. 6. The Geochemical Society*, 283–296.

- Frost, D.J. (2003) Fe²⁺-Mg partitioning between garnet, magnesiowüstite, and (Mg,Fe)₂SiO₄ phases of the transition zone. *American Mineralogist*, **88**, 387–397.
- Frost, D.J. (2008) The Upper Mantle and Transition Zone. *Elements*, **4:3**, 171–176.
- Frost, D.J. and Fei, Y. (1998) Stability of phase D at high pressure and high temperature. *Journal of Geophysical Research*, **103**, 7463–7474.
- Frost, D.J. and Dolejš, D. (2007) Experimental determination of the effect of H₂O on the 410-km seismic discontinuity. *Earth and Planetary Science Letters*, **256**, 182–195.
- Gasparik, T. (1990) Phase relations in the transition zone. *Journal of Geophysical Research*, **95**, 15'751–15'769.
- Gasparik, T. (2003) Phase diagrams for geoscientists - An atlas of the Earth's interior. Springer-Verlag, Berlin, Heidelberg, New York, 462 pp.
- Hauck, S.A. and Phillips, R.J. (2002) Thermal and crustal evolution of Mars, *Journal of Geophysical Research*, **107**, 5052.
- Hazen, R.M. (1981) Systematic variation of bulk modulus of wüstite with stoichiometry. *Carnegie Institute of Washington Yearbook*, **80**, 277–280.
- Hazen, R.M. (1993) Comparative compressibilities of silicate spinels: anomalous behavior of (Mg,Fe)₂SiO₄. *Science*, **259**, 206–209.
- Hazen, R.M., Downs, R.T., Finger, L.W. and Ko, J. (1993) Crystal chemistry of ferromagnesian silicate spinels: evidence for Mg-Si disorder. *American Mineralogist*, **78**, 1320–1323.
- Heinemann, S., Seifert, F., Sharp, T.G., Rubie, D.C. and Angel, R. (1994) Cubic-tetragonal symmetry change in garnets of the majorite-pyrope solid solution. *Zeitschrift für Kristallographie, Supplement* **8**, 708.

- Hirschmann, M.M., Aubaud, C. and Withers, A.C. (2005) Storage capacity of H₂O in nominally anhydrous minerals in the upper mantle. *Earth and Planetary Science Letters*, **236**, 167–181.
- Hirth, G. and Kohlstedt, D.L. (1996) Water in the oceanic upper mantle: implications for rheology, melt extraction and the evolution of the lithosphere. *Earth Planetary Science Letters*, **144**, 93–108.
- Horiuchi, H., Morimoto, N., Yamamoto, K. and Akimoto, S. (1979) Crystal structure of 2Mg₂SiO₄ · 3Mg(OH)₂, a new high-pressure structure type. *American Mineralogist*, **64**, 593–598.
- Horiuchi, H., Hirano, M., Ito, E., and Matsui, Y. (1982) MgSiO₃ (ilmenite-type): Single crystal X-ray diffraction study. *American Mineralogist*, **67**, 788–793.
- Ibers, J.A. and Hamilton, W.C., Eds. (1974) *International tables for X-ray crystallography*, vol. IV, Kynoch, Birmingham, U.K.
- Inoue, T., Yurimoto, H., and Kudoh, Y. (1995) Hydrous modified spinel, Mg_{1.75}SiH_{0.5}O₄: a new water reservoir in the mantle transition region. *Geophysical Research Letters*, **22**, 117–120.
- Inoue, T., Weidner, D.J., Northrup, P.A. and Parise, J.B. (1998) Elastic properties of hydrous ringwoodite (γ -phase) in Mg₂SiO₄. *Earth and Planetary Science Letters*, **160**, 107–113.
- Ita, J.J. and Stixrude, L. (1992) Petrology, elasticity and composition of the transition zone. *Journal of Geophysical Research*, **97**, 6849–6866.
- Ito, E. and Takahashi, E. (1989) Postspinel transformations in the system Mg₂SiO₄-Fe₂SiO₄ and some geophysical implications, *Journal of Geophysical Research*, **94**, 10'637–10'646.
- Jackson, J.M., Sinogeikin, S.V. and Bass, J.D. (2000) Sound velocities and elastic properties of γ -Mg₂SiO₄ to 873 K by Brillouin spectroscopy. *American Mineralogist*, **85**, 296–303.

- Jacobsen, S.D., Smyth, J.R., Spetzler, H., Holl, C.M. and Frost, D.J. (2004) Sound velocities and elastic constants of iron-bearing hydrous ringwoodite. *Physics of the Earth and Planetary Interiors*, **143–144**, 47–56.
- Jacobsen, S.D. and Smyth, J.R. (2006) Effect of water on the sound velocities of ringwoodite in the transition zone. *In: S.D. Jacobsen and S. van der Lee (Eds.) Earth's Deep Water Cycle*, American Geophysical Union, Geophysical Monograph, **168**, 131–145.
- Jakosky, B.M. and Phillips, R.J. (2001): Mars' volatile and climate history. *Nature*, **412**, 237–244.
- Kagi, H., Parise, J.B., Cho, H., Rossman, G.R. and Loveday, J.S. (2000) Hydrogen bonding interactions in Phase A ($\text{Mg}_7\text{Si}_2\text{O}_8(\text{OH})_6$) at ambient and high pressure. *Physics and Chemistry of Minerals*, **27**, 225–233.
- Kargel, J.S. and Lewis, J.S. (1993) The composition and early evolution of Earth. *Icarus*, **105**, 1–25.
- Kawamoto, T. (2004) Hydrous phase stability and partial melt chemistry in H_2O -saturated KLB-1 peridotite up to the uppermost lower mantle conditions. *Physics of the Earth and Planetary Interiors*, **143–144**, 387–395.
- Keppler, H. and Frost, D.J. (2005) Introduction to minerals under extreme conditions. *In: R. Miletich, Editor, Mineral Behavior at Extreme Conditions, Lecture Notes in Mineralogy*, vol. 7, European Mineralogical Union, 1–30.
- Kerschhofer, L., Sharp, T.G., and Rubie, D.C. (1996) Intracrystalline transformation of olivine to wadsleyite and ringwoodite under subduction zone conditions. *Science*, **274**, 79–81.
- Kiefer, B., Stixrude, L., and Wentzcovitch, R.M. (1997) Calculated elastic constants and anisotropy of Mg_2SiO_4 spinel at high pressure. *Geophysical Research Letters*, **24**, 2841–2844.
- King, H.E. and Finger, L.W. (1979) Diffracted beam crystal centering and its application to high-pressure crystallography. *Journal of Applied*

Crystallography, **12**, 374-378.

- Koch, M., Woodland, A.B. and Angel, R.J. (2004) Stability of spinelloid phases in the system $\text{Mg}_2\text{SiO}_4\text{-Fe}_2\text{SiO}_4\text{-Fe}_3\text{O}_4$ at 1100°C and up to 10.5 GPa. *Physics of the Earth and Planetary Interiors*, **143–144**, 171–183.
- Kogure, T. (2003) A program to assist Kikuchi pattern analysis. *Journal of the Crystallographic Society of Japan*, **45**, 391–395 (in Japanese with English abstract, the program is available from <http://www-gbs.eps.s.u-tokyo.ac.jp/kogure/edana>).
- Kohlstedt, D.L., Keppler, H. and Rubie, D.C. (1996) Solubility of water in the α , β and γ phases of $(\text{Mg,Fe})_2\text{SiO}_4$. *Contributions to mineralogy and petrology*, **123**, 345–357.
- Kohn, S.C., Brooker, R.A., Frost, D.J., Slesinger, A.E., and Wood, B.J. (2002) Ordering of hydroxyl defects in hydrous wadsleyite ($\beta\text{-Mg}_2\text{SiO}_4$). *American Mineralogist*, **87**, 293–301.
- Kröger, F. A. and Vink, H. J. (1956) Relations between the concentrations of imperfections in crystalline solids. In *Solid State Physics - Advances in Research and Applications*, Academic Press, New York, **3**, 307–435.
- Kudoh, Y., Inoue, T. and Arashi, H. (1996) Structure and crystal chemistry of hydrous wadsleyite, $\text{Mg}_{1.75}\text{SiH}_{0.5}\text{O}_4$: possible hydrous magnesium silicates in the mantle transition zone. *Physics and chemistry of minerals*, **23**, 461–469.
- Kudoh, Y., Kuribayashi, T., Mizobata, H. and Ohtani, E. (2000) Structure and cation disorder of hydrous ringwoodite, $\gamma\text{-Mg}_{1.89}\text{Si}_{0.98}\text{H}_{0.30}\text{O}_4$. *Physics and chemistry of minerals*, **27**, 474–479.
- Li, B. (2003) Compressional and shear wave velocities of ringwoodite $\gamma\text{-Mg}_2\text{SiO}_4$ to 12 GPa. *American Mineralogist*, **88**, 1312–1317.
- Li, L., Brodholt, J., and Alfè, D. (2009) Structure and elasticity of hydrous ringwoodite: A first principle investigation. *Physics of the Earth and Planetary Interiors*, **177**, 103–115.

- Libowitzky, E. and Beran, A. (2004) IR spectroscopic characterisation of hydrous species in minerals, In: A Beran, E Libowitzky (eds), *EMU Notes in Mineralogy*, Vol. 6, Chapter 6, Budapest: Eötvös Univ Press, 227–279.
- Liu, L. (1986) Phase transformations in serpentine at high pressures and temperatures and implications for subducting lithosphere. *Physics of the Earth and Planetary Interiors*, **42**, 255–262.
- Lodders, K. and Fegley, B. (1997) An oxygen isotope model for the composition of Mars. *Icarus*, **126**, 373–394.
- Lodders, K. and B. Fegley (1998) *The planetary scientist's companion*. New York, Oxford University Press.
- Longhi, J., Knittle, E., Holloway, J.R. and Wänke, H. (1992) The bulk composition, mineralogy and internal structure of Mars. in: H.H. Kieffer. B.M. Jakosky. C.W. Snyder, M.S. Matthews (Eds.). *Mars*. The University of Arizona Press, Tucson. AZ., 184–208.
- Manghnani, M.H., Amulele, G., Smyth, J.R., Holl, C.M., Chen, G., Prakapenka, V. and Frost, D.J. (2005) Equation of state of hydrous Fo₉₀ ringwoodite to 45 GPa by synchrotron powder diffraction. *Mineralogical Magazine*, **69**, 317–323.
- Mao, H.K., Xu, J., and Bell, P.M. (1986) Calibration of the ruby pressure gauge to 800-kbar under quasi-hydrostatic conditions. *Journal of Geophysical Research*, **91**, 4673–4676.
- Matsukage, K.N., Jing, Z., and Karato, S. (2005) Density of hydrous silicate melt at the conditions of Earth's deep upper mantle. *Nature*, **438**, 488–491.
- McCammion, C.A., Frost, D.J., Smyth, J.R., Laustsen, H.M.S., Kawamoto, T., Ross, N.L., and van Aken, P.A. (2004) Oxidation state of iron in hydrous mantle phases: implications for subduction and mantle oxygen fugacity. *Physics of the Earth and Planetary Interiors*, **143**, 157–169.

- Merrill, R.B. and Wyllie, P.J. (1973) Absorption of iron by platinum capsules in high pressure rock melting experiments. *American Mineralogist*, **58**, 16–20.
- Morishima, H., Kato, T., Suto, M., Ohtani, E., Urakawa, S., Utsumi, W., Shimomura, O. and Kikegawa, T. (1994) The phase boundary between α and β -Mg₂SiO₄ determined by in situ X-ray observation. *Science*, **265**, 1202–1203.
- Nestola, F., Boffa Ballaran, T., Balić-Žunić, T., Princivalle, F., Secco, L. and Dal Negro, A. (2007) Comparative compressibility and structural behavior of spinel MgAl₂O₄ at high pressures: the independency on the degree of cation order. *American Mineralogist*, **92**, 1838–1843.
- Nestola, F., Smyth, J.R., Parisatto, M., Secco, L., Princivalle, F., Bruno, M., Prencipe, M. and Dal Negro, A. (2009) The effect of non-stoichiometry on the spinel structure at high-pressure: Implications for the Earth's mantle mineralogy. *Geochimica et Cosmochimica Acta*, **73**, 489–492.
- Ohtani, E., Kagawa, N., and Fujino, K. (1991) Stability of majorite (Mg, Fe)SiO₃ at high pressures and 1800°C. *Earth and Planetary Science Letters*, **102**, 158–166.
- Ohtani, E., Mizobata, H., Kudoh, T., Nagase, T., Arashi, H., Yurimoto, H., and Miyagi, I. (1997) A new hydrous silicate, a water reservoir, in the upper part of the lower mantle. *Geophysical Research Letters*, **24**, 1047–1050.
- Ohtani, E., Mizobata, H., and Yurimoto, H. (2000) Stability of dense hydrous magnesium silicate phases in the system Mg₂SiO₄-H₂O and MgSiO₃-H₂O at pressures up to 27GPa, *Physics and Chemistry of Minerals*, **27**, 533–544.
- Pacalo, R.E.G., and Parise, J.B. (1992) Crystal structure of superhydrous B, a hydrous magnesium silicate synthesized at 1400°C and 20 GPa. *American Mineralogist*, **77**, 681–684.
- Paterson, M.S. (1982) The determination of hydroxyl by infrared absorption in quartz, silicate glasses and similar materials. *Bulletin de Minéralogie*, **105**, 20–29.

- Presnell, D.C. (1995) Phase diagrams of earth-forming minerals. In: Ahrens, T. J., Ed. / AGU reference shelf 2: *Mineral physics and crystallography - A handbook of physical constants*, Washington, D. C., 248–268.
- Ralph, R.L. and Finger, L.W. (1982) A computer program for refinement of crystal orientation matrix and lattice constraints from diffractometer data with lattice symmetry constraints. *Journal of Applied Crystallography*, **15**, 537–539.
- Reynard, B. and Rubie, D.C. (1996) High-pressure, high-temperature Raman spectroscopic study of ilmenite-type MgSiO_3 , *American Mineralogist*, **81**, 1092–1096.
- Ringwood, A.E. and Major, A. (1967) High-pressure reconnaissance investigations in the system Mg_2SiO_4 - MgO - H_2O . *Earth and Planetary Science Letters*, **2**, 130–133.
- Ross, N.L., Gibbs, G.V. and Rosso, K.M. (2003) Potential docking sites and positions of hydrogen in high-pressure silicates. *American Mineralogist*, **88**, 1452–1459.
- Sasaki, S., Prewitt, C.T., Sato, Y. and Ito, E. (1982) Single-crystal X-ray study of γ - Mg_2SiO_4 . *Journal of Geophysical Research*, **87**, 7829–7832.
- Sheldrick, G.M. (1997) SHELXL-97 A program for crystal structure refinement. University of Goettingen, Germany, release 97-2.
- Shieh, S.R., Mao, H.K., Hemley, R.J. and Ming, L.C. (1998) Decomposition of phase D at lower mantle and the fate of dense hydrous magnesium silicates in subducting slabs. *Earth and Planetary Science Letters*, **159**, 13–23.
- Siesler, H.W., Ozaki, Y., Kawata, S. and Heise, M.H. (2002) Near-Infrared spectroscopy - Principles, Instruments, Applications. Wiley-VCH, Weinheim, Germany.

- Sinogeikin, S.V., Bass, J.D. and Katsura, T. (2003) Single-crystal elasticity of ringwoodite to high pressures and high temperatures: implications for 520 km seismic discontinuity. *Physics of the Earth and Planetary Interiors*, **136**, 41–66.
- Smith, W.E. and Dent, G.(2005) *Modern Raman Spectroscopy - A Practical Approach*. Wiley-VCH, England.
- Smyth, J.R. (1987) β -Mg₂SiO₄: a potential host for water in the mantle? *American Mineralogist*, **72**, 1051–1055.
- Smyth, J.R. (1994) A crystallographic model for hydrous wadsleyite (β -Mg₂SiO₄) - An ocean in the Earth's interior. *American Mineralogist*, **79**, 1021–1024.
- Smyth, J.R. (2006) Hydrogen in high pressure silicate and oxide mineral structures. *Reviews in Mineralogy and Geochemistry*, **62**, 85–116.
- Smyth, J.R. and Kawamoto, T. (1997) Wadsleyite II: A new high pressure hydrous phase in the peridotite-H₂O system. *Earth and Planetary Science Letters*, **146**, E9–E16.
- Smyth, J.R. and S.D. Jacobsen (2006) Nominally anhydrous minerals and Earth's deep water cycle. In: S.D. Jacobsen and S. van der Lee (Eds.) *Earth's Deep Water Cycle*, American Geophysical Union, Geophysical Monograph 168, 1–11.
- Smyth, J.R., Kawamoto, T., Jacobsen, S.D., Swope, J.R., Hervig, R.L., and Holloway, J.R. (1997) Crystal structure of monoclinic hydrous wadsleyite β -(Mg,Fe)₂SiO₄. *American Mineralogist*, **82**, 270–275.
- Smyth, J.R., Holl, C.M., Frost, D.J., Jacobsen, S.D., Langenhorst, F. and McCammon, C. (2003) Structural systematics of hydrous ringwoodite and water in Earth's interior. *American Mineralogist*, **88**, 1402–1407.

- Smyth, J.R., Holl, C.M., Frost, D.J. and Jacobsen, S.D. (2004) High pressure crystal chemistry of hydrous ringwoodite and water in the Earth's interior. *Physics of the Earth and Planetary Interiors*, **143–144**, 271–278.
- Smyth, J. R., Holl, C. M., Langenhorst, F., Laustsen, H. M. S., Rossman, G. R., Kleppe, A. K., McCammon, C. A., Kawamoto, T. and van Aken, P. A. (2005) Crystal chemistry of wadsleyite II and water in the Earth's interior. *Physics and Chemistry of minerals*, **31**, 691–705.
- Smyth, J.R., Frost, D.J., Nestola, F., Holl, C.M. and Bromiley, G. (2006) Olivine hydration in the deep upper mantle: Effects of temperature and silica activity. *Geophysical Research Letters*, **33**, L15301.
- Sohl, F. and Spohn, T. (1997) The internal structure of Mars: Implications of SNC meteorites. *Journal of Geophysical Research*, **102**, 1613–1635.
- Spohn, T., Acuña, M.H., Breuer, D., Golombek, M., Greeley, R., Halliday, A., Hauber, E., Jaumann, R., and Sohl, F. (2001) Geophysical constraints on the evolution of Mars. *Space Science Reviews*, **96**, 231–262.
- Stevenson, D.J. (2001) Mars' core and magnetism. *Nature*, **412**, 214.
- Stewart, A.J., Schmidt, M.W., van Westrenen, W. and Lieske, C. (2007) Mars: A new core-crystallization regime. *Science*, **316**, 1323–1325.
- Suzuki, A., Ohtani, E., Morishima, H., Kubo, T., Kanbe, Y. and Kondo, T. (2000) In situ determination of the phase boundary between wadsleyite and ringwoodite in Mg_2SiO_4 . *Geophysical Research Letters*, **27**, 803–806.
- Tokonami, M. (1965) Atomic scattering factor for O^{2-} . *Acta Crystallographica*, **19**, 486.
- Trønnes, R.G. and Frost D.J. (2002) Peridotite melting and mineral-melt partitioning of major and minor elements at 22–24.5 GPa. *Earth and Planetary Science Letters*, **197**, 117–131.

- van Aken, P.A., Liebscher, B. And Styrsa, V.J. (1998) Quantitative determination of iron oxidation states in minerals using Fe $L_{2,3}$ -edge electron energy-loss near-edge structure spectroscopy. *Physics and chemistry of minerals*, **25**, 323–327.
- Wang, J., Sinogeikin, S.V., Inoue, T. and Bass, J.D. (2003) Elastic properties of hydrous ringwoodite. *American Mineralogist*, **88**, 1608–1611.
- Wänke, H. and Dreibus, G. (1988) Chemical composition and accretion history of terrestrial planets. *Philosophical Transactions of the Royal Society of London*, **A325**, 545–557.
- Weidner, D.J., Sawamoto, H., Sasaki, S., and Kumazawa, M. (1984) Single-crystal elastic properties of the spinel phase of Mg_2SiO_4 . *Journal of Geophysical Research*, **89**, 7852–7860.
- Williams, K.L. (1987) *Introduction to X-ray Spectrometry*, Allen & Unwin, 370 pp.
- Williams, J.-P. and Nimmo, F. (2004) Thermal evolution of the Martian core: implications for an early dynamo. *Geology*, **32**, 97–100.
- Xu, W., Lithgow-Bertelloni, C., Stixrude, L., and Ritsema, J. (2008) The effect of bulk composition and temperature on mantle seismic structure. *Earth and Planetary Science Letters*, **275**, 70–79.
- Yagi, T., Marumo, F. and Akimoto, S. (1974) Crystal structures of spinel polymorphs of Fe_2SiO_4 and Ni_2SiO_4 . *American Mineralogist*, **59**, 486–490.
- Yamamoto, K. and Akimoto, S. (1974) High-pressure and high-temperature investigations in the system $MgO-SiO_2-H_2O$. *Journal of Solid State Chemistry*, **9**, 187–195.

- Yamamoto, K. and Akimoto, S. (1977) The system MgO-SiO₂-H₂O at high pressures and temperatures - stability field for hydroxyl-chondrodite, hydroxyl-clinohumite and 10 Å-phase. *American Journal of Science*, **277**, 285-312.
- Yang, H., Prewitt, C.T. and Frost, D.J. (1997) Crystal structure of the dense hydrous magnesium silicate, phase D. *American Mineralogist*, **82**, 651-654.
- Yoder C. F. (1995) Astrometric and geodetic properties of Earth and the solar system. In: Ahrens, T.J. (eds.) *Global Earth Physics: A Handbook of Physical Constants*, Vol. 1, American Geophysical Union, Washington DC, 1-31.
- Yoder, C.F., Konopliv, A.S., Yuan, D.N., Standish, E.M. and Folkner, W.M. (2003) Fluid core size of Mars from detection of the solar tide. *Science*, **300**, 299-303.
- Yusa, H., Inoue, T. and Ohishi, Y. (2000) Isothermal compressibility of hydrous ringwoodite and its relation to the mantle discontinuities. *Geophysical Research Letters*, **27**, 413-416.
- Zhang, J., Li, B., Utsumi, W. and Liebermann, R.C. (1996) In situ X-ray observations of the coesite-stishovite transition: reversed phase boundary and kinetics. *Physics and Chemistry of Minerals*, **23**, 1-10.
- Zuber, M.T., Solomon, S.C., Phillips, R.J., Smith, D.E., Tyler, G.L., Aharonson, O., Balmino, G., Banerdt, W.B., Head, J.W., Johnson, C.L., Lemoine, F.G., McGovern, P.J., Neumann, G.A., Rowlands, D.D., and Zhong, S. (2000) Internal structure and early thermal evolution of Mars from Mars Global surveyor topography and gravity. *Science*, **287**, 1788-1793.

Ich erkläre hiermit, dass ich die vorliegende Arbeit ohne unzulässige Hilfe Dritter und ohne Benutzung anderer als der angegebenen Hilfsmittel angefertigt habe. Die aus fremden Quellen direkt oder indirekt übernommenen Gedanken sind als solche kenntlich gemacht.

Die Arbeit wurde bisher weder im Inland noch im Ausland in gleicher oder ähnlicher Form als Dissertation eingereicht und ist als Ganzes auch noch nicht veröffentlicht.

Ferner erkläre ich hiermit, dass ich nicht bereits anderweitig mit oder ohne Erfolg versucht habe, eine Dissertation einzureichen oder mich der Doktorprüfung zu unterziehen.

Bayreuth, 17. März 2010

Geertje Ganskow